A JWST investigation into barred galaxies at $1 < z < 4$

Zoe A. Le Conte

A JWST investigation into barred galaxies at $1 < z < 4$

Zoe A. Le Conte

A Thesis presented for the degree of
Doctor of Philosophy

Department of Physics
Durham University
United Kingdom
March 2026

Abstract

Galaxies are complex systems that preserve the history of the Universe, revealing a violent, chaotic phase in the early Universe. During this phase, galaxies frequently interacted and merged, laying the foundations for the Universe's hierarchical structure. As the Universe expanded, galaxy interactions became less frequent and internal evolutionary processes dominated. It is unknown when this second evolutionary phase commences; however, stellar structures in nearby galaxies have revealed the driving mechanism behind it. In dynamically cold and rotationally supported disc galaxies, a non-axisymmetric potential will propagate and trap stars onto elongated stellar orbits. A disc galaxy with this central stellar structure is known as a barred galaxy, and they are one of the most common features found in nearby discs. However, their frequency decreases as we look back to earlier epochs in the Universe, demonstrating that internal galaxy evolution dominates at $z < 1$. This thesis presents one of the first studies of barred galaxies at $z \geq 1$ using the improved sensitivity and longer wavelength range of the James Webb Space Telescope (JWST) to identify the onset of bar formation and, if present, whether these barred structures differ from those in nearby galaxies.

I investigate the evolution of the bar fraction by selecting a nearly mass-complete disc galaxy sample in the redshift range $1 \leq z \leq 4$ from the JWST Cosmic Evolution Early Release Science (CEERS) survey. The barred galaxies were identified via visual classification. To understand instrumental biases and wavelength dependence, the methodology was repeated for the same sample of galaxies imaged with the Hubble Space Telescope (HST), and in different JWST filters. For the first time, a population of high-redshift barred galaxies was identified with JWST, yielding a bar fraction twice that from HST images. Additionally, the bar fraction was consistent across the observed JWST wavelengths. Thus, the bar fraction can be limited by instrument sensitivity, and the bar fraction reported here could still be a lower limit.

In addition, I employ image analysis techniques to measure the evolution of bar structural properties. This includes ellipse fitting and photometric decompositions to obtain the bar length, ellipticity, Sérsic index and bar-to-total luminosity ratio. I verify that ellipse-fitting techniques yield shorter, rounder bars than photometric decomposition, and that bluer-wavelength images yield shorter bars than redder-wavelength images. Overall, the bars at $z \geq 1$ have a similar distribution in bar lengths to those in nearby galaxies, but lack a longer population of ≥ 8 kpc bars which exist at $z < 1$. Overall, these bars reside in smaller disc galaxies; thus, the bar length normalised by disc size is constant from the local Universe out to Cosmic Noon. This remarkable result demonstrates that bars grow in tandem with their discs. Furthermore, the distributions of other structural properties, such as ellipticity, Sérsic index, and bar-to-total luminosity, are similar to those of nearby and intermediate redshift barred galaxies.

One of the most exceptional results of this thesis was the discovery of a nuclear disc in a strongly barred galaxy at $z \approx 1.5$. Nuclear discs form shortly after the bar and are key indicators that bar-driven evolution has commenced. Using image analysis techniques, I measure the radial extent of this nuclear disc to be ≈ 1 kpc, comparable to the largest nuclear discs in nearby galaxies. I identify possible features of a nuclear bar and spiral arms. This is the first evidence of a nuclear disc beyond the local Universe and reinforces the idea that bar-driven evolution must be rapid to form the structures we observe in nearby galaxies.

This thesis presents evidence that bar formation occurs much earlier than previously thought, as early as a few billion years after the Big Bang. Additionally, for bars in young galaxies to develop properties that are consistent with those we observe in nearby galaxies, bar-driven galaxy evolution must be rapid. In general, we must re-evaluate our understanding of disc settling, bar formation, and bar-driven evolution in the early Universe.

Declaration

The work in this thesis is based on research carried out at the Department of Physics, Durham University, United Kingdom. No part of this thesis has been submitted elsewhere for any other degree or qualification and it is all my own work unless referenced to the contrary in the text.

Publications

Some of the work presented in this thesis has been published in journals and conference proceedings - the relevant publications are listed below.

Le Conte et al. (2026) "A nuclear disc at Cosmic Noon: evidence of early bar-driven galaxy evolution", MNRAS letters, submitted, arXiv:2601.18871

Le Conte et al. (2026) "The evolution of the bar fraction and bar lengths in the last 12 billion years", MNRAS, 545, 18

Le Conte et al. (2024) "A JWST investigation into the bar fraction at redshifts 1 $\leq$ z $\leq$ 3", MNRAS, 530, 1984

Chattopadhyay et al. (2026) "Evolution of bar-induced dark gaps in galaxy discs: evidence of strong bar-driven effects already at z $<$ 2", MNRAS, subm.

Acknowledgements

A PhD is far more than an individual pursuit of research; it is a journey shaped by the people who accompany you along the way. While this thesis bears my name, it is the product of remarkable minds, countless conversations, and immense kindness. I would like to express my sincere gratitude to those who have inspired, challenged, and sustained me throughout this journey.

To an inspiring and passionate supervisor, *Dimitri Gadotti*, for guiding me through this PhD with such enthusiasm. Thank you for deepening my knowledge and fuelling my excitement and love for barred galaxies and extragalactic research. My time at Durham was truly shaped by your support.

To *Francesca Fragkoudi* for your invaluable contributions to my PhD, through your devotion of time, enthusiasm, and support. To the unforgettable members of the bar dynamics group, *Thomas, Martyna, Camila, Tutku, Luiz, Paula, Alex, Emma, Paula,* and *Soiree* for riveting discussions.

To the person who keeps the department running smoothly, *Shufei*, I will miss our chats and your lively spirit.

I am very fortunate to have developed lifelong friendships with remarkable, incredibly talented people. To *Sarah* and *Ciera*, you have been with me through every step of this PhD, from the major achievements to daily procrastination, and it has made every moment worthwhile. I will miss our walks to White Church.

To the close friends who brought me much amusement during my time at Durham. *Makun*, you set the standards high for office mates; *Emmy*, you filled the department with amazing energy and impeccable fashion; *Marcus*, your lunch schedule was

inspirational, and your enthusiasm for astronomy is unmatched; *Sutti*, your comedic timing brought much joy.

To the wonderful astronomy PhD students at Durham, *Joaquin, Zane, Bjarki, Mac, Michael, Sam, Scott,* and *Duncan*, who kept the department a great place to be.

With your unwavering support, *Jan*, you have shown me how to believe in myself and grow into a confident and passionate person. Eight years of working together have flown by, and it is amazing to think of where we started.

Thank you to my loving family, *Mum, Dad,* and *Emily*, for your incredible support. You gave me the most wonderful start to life and provided a creative, happy and adventurous home. I am so grateful for the opportunities you created for me, and my achievements are a credit to you.

To my beautiful *Grandma* and *Nan*, for taking such an interest in my studies and being constant champions of my work.

To the entirety of my second family, *the Whites and Turners*, I have felt incredible love throughout our time in Durham, and I appreciate all your encouragement for Tim and me to pursue our dreams.

Above all, to my incredible Fiancé *Tim*. I can wholeheartedly say this journey wouldn't have been possible without you. Throughout our 10 years together, my pursuit of astronomy has shaped our lives, from Southampton to Boston and now Durham, and you have shown unwavering support and have always made me feel proud of what I have achieved. Your endless love, excitement and drive for life have inspired me to keep dreaming big. I am forever grateful to have been so lucky to go on this journey with you by my side.

Contents

Abstract ii

Declaration iv

Acknowledgements vi

List of Figures xii

List of Tables xv

Dedication xvi

1 Introduction 1

1.1 The Hubble Sequence 2

1.2 Bar formation 6

1.2.1 Formation mechanisms 6

1.2.2 Orbital structure 8

1.2.3 The bar fraction 10

1.2.4 Structural properties 15

1.3 Bar-driven evolution 20

1.3.1 Angular momentum . . . 21
1.3.2 Gas dynamics . . . 21
1.3.3 Boxy/Peanut structures . . . 22
1.3.4 Nuclear stellar structures . . . 24
1.3.5 AGN fuelling . . . 27
1.4 Thesis structure . . . 27

2 A JWST investigation into the bar fraction at redshifts $1 \leq z \leq 3$ 31
2.1 Introduction . . . 33
2.2 The parent sample . . . 34
2.2.1 Data reduction pipeline . . . 34
2.2.2 Sample selection . . . 35
2.3 Bar identification . . . 36
2.3.1 Sample optimisation . . . 36
2.3.2 Disc identification . . . 41
2.3.3 Bar visual classifications . . . 43
2.4 The bar fraction . . . 47
2.5 Discussion . . . 56
2.6 Summary and conclusions . . . 61

3 The evolution of the bar fraction and bar lengths in the last 12 billion years 64
3.1 Introduction . . . 66
3.2 The sample . . . 68
3.2.1 Data reduction pipeline . . . 69
3.2.2 Sample selection . . . 69
3.3 Methodology . . . 70
3.3.1 NIRCam imaging . . . 71
3.3.2 Sample optimisation . . . 72
3.3.3 Morphological classification . . . 75
3.4 The bar fraction . . . 81
3.5 Bar properties . . . 85

3.5.1 Mass dependence . . . 85
3.5.2 The bar length . . . 87
3.5.3 The bar ellipticity . . . 95
3.6 Discussion . . . 97
3.6.1 Capturing short bars with the F200W filter . . . 97
3.6.2 Bar length-stellar mass relation . . . 100
3.6.3 The "downsizing" scenario . . . 103
3.6.4 Co-evolution of the bar and disc . . . 104
3.6.5 Bar ellipticity correction . . . 105
3.7 Summary and conclusions . . . 106

4 Structural properties of barred galaxies at $z \geq 1$ 109
4.1 Introduction . . . 111
4.2 Data and sample selection . . . 111
4.3 Photometric decomposition . . . 114
4.3.1 Image preparation . . . 117
4.3.2 Differential evolution . . . 118
4.4 Structural properties . . . 119
4.4.1 The disc galaxies that host bars . . . 121
4.4.2 Structural properties of bars . . . 124
4.4.3 Central component contribution . . . 133
4.5 Discussion . . . 134
4.5.1 Challenges at high-z . . . 135
4.5.2 Dark gaps as a proxy for bar strength . . . 137
4.5.3 Cosmic Noon bars in simulations . . . 140
4.5.4 Rethinking bar-driven secular evolution . . . 141
4.6 Summary and conclusions . . . 141

5 A nuclear disc at Cosmic Noon: evidence of early bar-driven galaxy evolution 144
5.1 Introduction . . . 146
5.2 Data analysis . . . 146

5.2.1 Data . . . 146
5.2.2 Unsharp masking . . . 147
5.2.3 Photometric decompositions . . . 147
5.2.4 Isophotal analysis . . . 148
5.2.5 SED fitting . . . 148
5.3 Results . . . 149
5.4 Discussion . . . 154
5.5 Conclusions . . . 157

6 Conclusions and outlook **158**
6.1 Future investigations . . . 161
6.1.1 The radio signatures of barred galaxies . . . 161
6.1.2 The slowing down of barred galaxies . . . 162
6.1.3 Bar-driven quenching and star formation . . . 163
6.1.4 The bars' role in fuelling AGN . . . 164

List of Figures

1.1 The Hubble Tuning Fork 3
1.2 The barred galaxy NGC 1300. 4
1.3 Illustration of a barred galaxy. 5
1.4 Orbital structure of the stellar bar. 9
1.5 Wavelength dependence of the stellar bar in NGC 1097. 12
1.6 Examples of ellipse-fitting and Fourier analysis techniques. 13
1.7 Four types of bar surface-brightness profiles. 16
1.8 Photometric decomposition technique on NGC 5101. 18
1.9 The $z = 0$ bar fraction - stellar mass relation. 19
1.10 The boxy/peanut galaxy ESO 597-G036. 23
1.11 The zoomed-in nuclear disc in the barred galaxy NGC 1097. 25

2.1 Ellipse fitting to the barred galaxy EGS 23205. 37
2.2 Examples of 3 disc and 3 non-disc galaxies at $z \geq 1$. 43
2.3 Distribution of visual classification votes. 44
2.4 HST and JWST images of the barred galaxy EGS 31125. 45
2.5 Examples of HST classified barred galaxies, deemed unbarred in JWST. 46
2.6 Examples of strongly barred, weakly barred, and unbarred galaxies. . 48

2.7 Images of the strongly barred galaxy sample at $1 \leq z \leq 3$. 49
2.8 Images of the weakly barred galaxy sample at $1 \leq z \leq 3$. 50
2.9 Stellar mass distribution of the $1 \leq z \leq 3$ disc sample. 52
2.10 Evolution of the bar fraction. 55

3.1 Stellar mass-redshift distribution of CEERS galaxies in the redshift range $1 \leq z \leq 4$. 70
3.2 Application of SExtractor on EGS 1246. 73
3.3 Distribution of structural parameters from a single 2D Sérsic function fitting using IMFIT. 77
3.4 Evolution of the bar fraction 83
3.5 Stellar mass - redshift distribution of barred galaxies at $1 \leq z \leq 4$. . . 86
3.6 Bar fraction - stellar mass relation at $z \geq 1$. 88
3.7 Evolution of the deprojected bar length over $0 \leq z \leq 4$. 90
3.8 Evolution of the projected bar length over $0 \leq z \leq 4$. 94
3.9 Distribution of the projected bar ellipticity at $1 \leq z \leq 4$. 96
3.10 Wavelength dependence of the bar length for the galaxy EGS 23205. . 99
3.11 Bar length versus stellar mass at $1 \leq z \leq 4$. 101
3.12 Distribution of the corrected bar ellipticity at $1 \leq z \leq 4$. 106

4.1 Images of strongly barred galaxy sample at $z \geq 1$. 112
4.2 Continuation of 4.1. 113
4.3 Photometric decomposition of the galaxy CEERS 3924 at $z = 1.58$. . 120
4.4 Disc scale length versus disc size of strongly barred galaxies at $z \geq 1$. 121
4.5 Specific star formation rate of disc galaxies at $z > 1$. 123
4.6 Photometrically decomposed structural properties of strongly barred galaxies at $z \geq 1$. 125
4.7 Structural properties of bars derived by ellipse fitting techniques versus photometric decomposition. 127
4.8 Structural properties of bars derived for F200W versus F356W+F444W. 130
4.9 Structural properties of the bar in star-forming (blue) and quiescent (red) strongly barred galaxies at $z \geq 1$. 132

4.10 Evolution of bar structural properties for three central component candidates. 134
4.11 Photometric decomposition of the galaxy CEERS 5241 with a strong dark gap at $z = 1.18$. 139

5.1 The galaxy CEERS 4031 in JWST NIRCam filters. 150
5.2 Image analysis of the galaxy CEERS 4031 in two NIRCam filters. . . 151
5.3 Resolved property maps of CEERS 4031 from NIRCam SED fitting. . 154

List of Tables

2.1 Galaxy sample sizes during optimisation phase. 40
2.2 The 39 visually classified strongly and weakly barred galaxies at $1 \leq z \leq 3$. . . . 51
2.3 Galaxy sample sizes after selection and classification criteria are applied. 53

3.1 Sample sizes of barred and unbarred disc galaxies in NIRCam filters. 80
3.2 Detailed bar fractions for NIRCam filters. 84

4.1 Photometrically decomposed structural properties of strongly barred galaxies at $z \geq 1$. 122

5.1 Main properties of CEERS-4031. 153

Dedication

To Tim, who kept me fed and sane throughout this process.

CHAPTER 1

Introduction

As a civilisation, we are fascinated by our existence and how unique we are within the Universe. Our ancestors searched the night skies, imbuing them with spiritual significance and using them as their greatest tools for navigation, timekeeping, and scientific exploration.

The current understanding of our place in the Universe was first theorised by the Ancient Greeks, who created myths about the Milky Way to signify its importance, whilst believing that it was a collection of stars. It wasn't until 1610 that Galileo used a telescope and discovered thousands of faint stars in the Milky Way. A century later, Immanuel Kant hypothesised the dynamics of the Milky Way. He determined that the Milky Way is a disc and that other nebulae are "island universes". However, it was only in the past century that astronomers were able to comprehend the Milky Way's immense size and pinpoint Earth's location within it.

With our growing understanding that the Milky Way is a massive barred spiral galaxy spanning 100,000 light-years, astronomers have turned their focus to its evolutionary track. This has relied on the rapid emergence of extragalactic astronomy. Since the conclusive evidence of extragalactic sources from Hubble in 1925, as-

tronomers have excelled at developing powerful observing techniques and telescopes to classify and model these wondrous objects across the electromagnetic spectrum and out to great distances, helping to formulate how galaxies form and evolve.

In this thesis, I use novel imaging data to classify barred galaxies at the farthest distances ever observed and to measure their structural properties. Through this, I unveil the mechanisms driving galaxy evolution at the earliest epochs and discover that galaxies form much earlier than previously thought. My research contributes to our understanding of galaxy evolution by placing it within the broader context of theoretical work. In this introductory chapter, I provide the context for understanding my thesis.

1.1 The Hubble Sequence

Over the past century, the most wondrous objects observed in our skies have been galaxies. Their drastically different morphologies, sizes, and compositions have driven the underlying question of how galaxies evolve. Galaxy evolution is a focus across all of astronomy, from Galactic archaeology to supermassive black holes (SMBH), and researchers are working to advance our understanding of how galaxies form and how their environments shape their morphology. Galaxies vary by more than seven orders of magnitude, ranging from 10^5 to 10^{12} stars. Their composition depends on environmental factors: those in denser environments, such as galaxy clusters, experience frequent mergers and, in extreme cases, undergo drastic gas stripping. In contrast, isolated systems will exhibit secular evolution driven by their own instabilities. This has led galaxies to exhibit a broad range of morphologies, with some more complex and others relatively simple.

Bars are elongated, non-axisymmetric structures composed of stars, typically found at the centres of spiral galaxies. The first barred galaxy discovered was NGC 613 by William Herschel [Herschel, 1802], at a distance of 67 million light-years away in the Southern constellation of Sculptor. Whilst individual systems were recorded earlier, the classification of 'barred' was coined only in the 20th century. Curtis [1918] first drew attention to the "band of matter extending diametrically across the

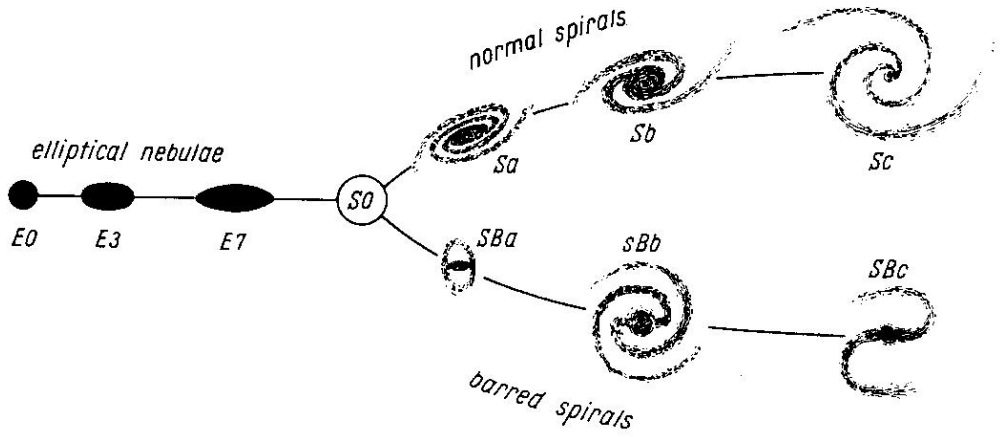

Figure 1.1: Illustration of the Hubble Tuning Fork Hubble [1936].

inner parts" in the galaxies NGC 1300, NGC 1530, NGC 3351, and NGC 5921, which he described as, for the lack of a better word, 'ϕ-type galaxies'. Shortly thereafter, Hubble grouped galaxies by appearance and structure to better understand their evolutionary tracks, as illustrated in the Hubble Tuning Fork [Figure 1.1; Hubble, 1936]. Simplistically, galaxies can be divided into three classes: ellipticals, discs, and a transitional category between them, lenticulars, which are discy but lack stellar structures. Not all galaxies can be easily classified into these three categories, for example, dwarf galaxies with masses of only a few billion solar masses, irregular galaxies with abnormal structures and shapes, and giant elliptical galaxies at the centres of clusters.

Within a dark-matter halo, a disc forms through the gravitational collapse of cooling gas, conserving angular momentum and maintaining orbital motion. Eventually, the stable, rotationally supported system will undergo disc instabilities due to a non-axisymmetric potential. This process forms stellar structures in the disc, which are observed as stellar spiral arms. Hubble characterised these disc galaxies by the compactness and openness of their spiral arms, i.e., how tightly wound they are. Another prominent feature of disc galaxies is an elongated structure through the centre, often connecting two spiral arms, known as the stellar bar. Barred spiral galaxies make up the other half of the tuning fork, and form by the same mechanisms as spiral arms in dynamically cold and rotationally supported disc galaxies; an example of a barred galaxy is shown in Figure 1.2. Bars are ubiquitous features in nearby disc galaxies and indicate that a galaxy has entered a later evolution-

Figure 1.2: Barred spiral galaxy NGC 1300 captured by the NASA/ESA Hubble Space Telescope.

ary phase. An illustration of a barred galaxy in face-on and edge-on projection with labelled stellar structures is shown in Figure 1.3. The structures shown in the illustration are discussed more thoroughly throughout this thesis.

Lenticulars are gas-deprived spiral galaxies, typically found in denser environments and have experienced rapid gas stripping or encountered a merger. Major mergers of spiral galaxies disrupt organised stellar orbits, producing a featureless elliptical galaxy with older stellar populations and little gas for further star formation. Hubble characterised elliptical galaxies by their ellipticity.

Later, de Vaucouleurs et al. [1964] revised the Hubble classification and introduced "family" and "variety" characteristics for barred and unbarred spiral galaxies, to distinguish between the bar and spiral structure. He denoted strongly barred galaxies as SB, unbarred galaxies as SA, and weakly barred galaxies as SAB, whilst the spiral structure was characterised as r for a ring encompassing the bar, s for two spiral arms connecting from the bar ends, and intermediate "pseudorings" as rs. Accordingly, de Vaucouleurs [1970] classified the Milky Way as SAB(rs)bc.

The Milky Way was probably first suggested to be a barred spiral galaxy by Johnson [1957], but Earth's obscured position within the Milky Way delayed confirmation of its bar until 1991, when Binney et al. [1991] used HI, CO and CS emission.

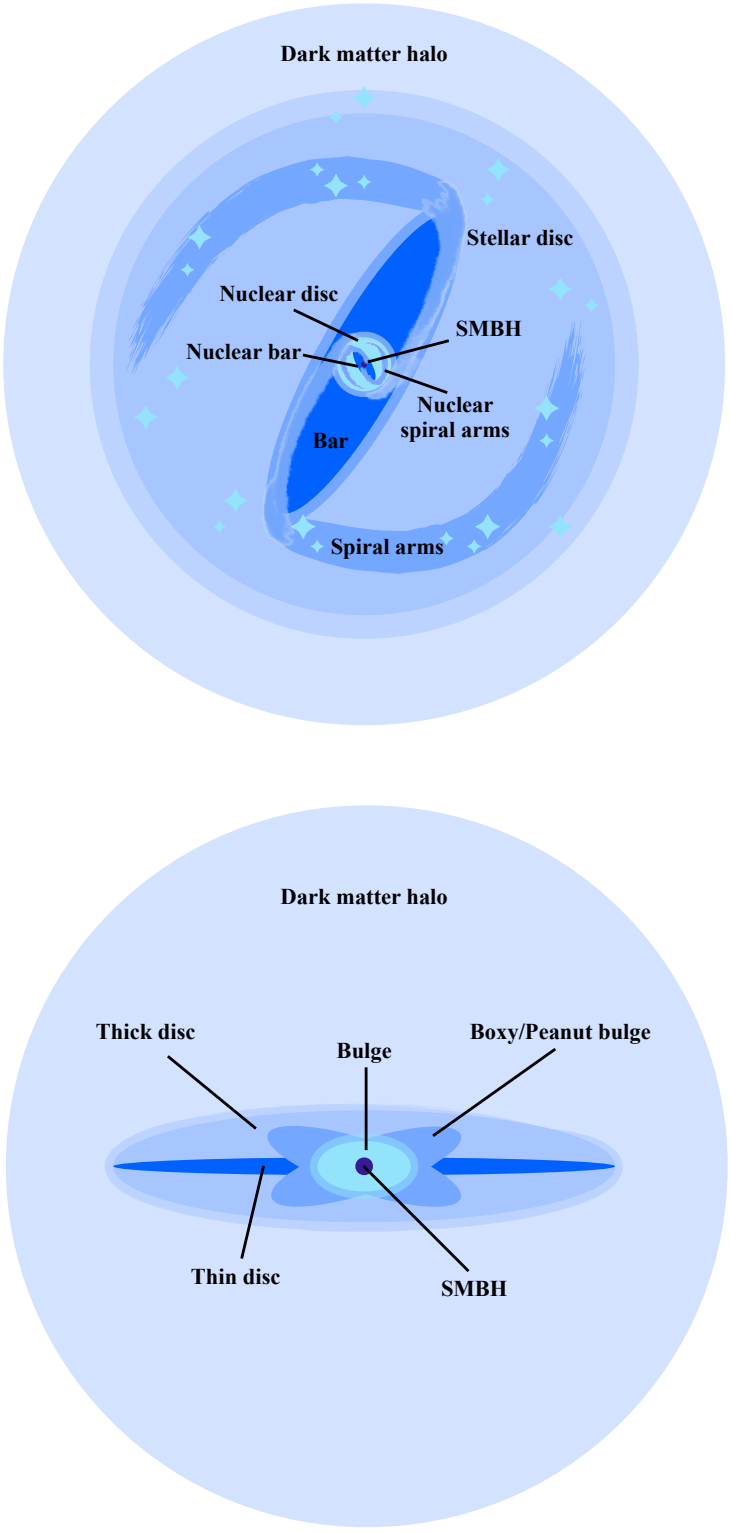

Figure 1.3: Illustration of a barred galaxy in face-on (upper) and edge-on (lower) projection. The stellar structures shown within the stellar disc are two spiral arms, connected by the stellar bar. At the centre, nuclear structures can form, such as the nuclear disc, nuclear spiral arms and a nuclear bar. Note that not all of these structures are present in every observed barred galaxy.

Barred galaxies provide insight into the mechanisms that drive galaxy evolution and are crucial for understanding how galaxies transform over time, thereby informing our picture of the Milky Way's formation.

1.2 Bar formation

Stellar bars are among the most abundant features in local disc galaxies [e.g., Aguerri et al., 2009, Buta et al., 2015, Eskridge et al., 2000, Marinova and Jogee, 2007], providing insight into the internal evolutionary processes at work in these galaxies. The occurrence and mechanisms under which bars form have been observed and tested in many observational [e.g., Aguerri et al., 2009, Buta et al., 2015, Gadotti et al., 2015, Jogee et al., 2004, Marinova and Jogee, 2007] and theoretical works [e.g., Athanassoula, 1992, Athanassoula et al., 1990, Fragkoudi et al., 2025, Rosas et al., 2022, Sellwood and Wilkinson, 1993]. Recently, investigations into younger bars at early epochs [e.g., Espejo Salcedo et al., 2025, Guo et al., 2023, 2025, Géron et al., 2025] have begun to bridge the gap between observational and theoretical research to elucidate the environments and conditions required for bar formation. In this section, I describe the interplay between the environment, stellar populations, and structural properties that promote bar formation and evolution, as well as the stellar dynamics that underpin these long-lived structures.

1.2.1 Formation mechanisms

Bar formation in disc galaxies is attributed to two main mechanisms: internal disc instabilities and the enhancement of non-axisymmetric features through interactions, including mergers and flyby encounters. Disc galaxies in less-dense environments evolve secularly, and simulations find that long-lived bars form by growing non-axisymmetric perturbations in the disc [e.g., Efstathiou et al., 1982, Fujii et al., 2018, Hohl, 1971]. However, Rosas-Guevara et al. [2022] using the magnetic-hydrodynamical simulation TNG50, demonstrated that these elongations are very small at early times, meaning the bars are on sub-kiloparsec scales. However, longer bars are shown to be produced through interactions and mergers.

In the literature, interactions have been extensively studied as a mechanism for bar formation [e.g., Berentzen et al., 2004, Gerin et al., 1990, Łokas, 2018, Łokas et al., 2014, 2016, Noguchi, 1987], with several studies demonstrating bar formation in the more extreme case of mergers [e.g., Cavanagh and Bekki, 2020, Łokas, 2025, Zhou et al., 2025]. Despite being a possible cause at all times, these interaction-induced bars are particularly favoured in the early Universe, as interactions were more frequent. A recent study using the IllustrisTNG simulations followed four bars that formed via mergers at $z > 3$ [Łokas, 2025]. These bars, with lengths of ~ 3 kpc, continued to grow in length and strength to the present day, despite subsequent interactions. Frosst et al. [2025] monitored the evolution of 307 disc galaxies in the TNG50 cosmological simulation and found that bars formed via tidal interactions are transient, whilst having similar properties to those formed secularly. They allude to the fact that tidal interactions can induce bar formation in a disc which would otherwise be stable against secular formation.

In summary, it remains an open question whether interactions form long-lived bars; however, this question can only be answered by considering the requirements for a disc's susceptibility to bar formation. Since the 1960s, theoretical work has sought to quantify the stability of a disc against bar formation, incorporating several crucial factors, which are discussed below.

At large scales, a disc is stabilised by random motions and rotation, and increasing surface density simultaneously leads to fragmentation. This balance was first approximated by Toomre [1964] in terms of the local stability criterion. As such, a system becomes unstable to axisymmetric perturbations when the Toomre parameter is below unity, a condition that requires a cold, dense system. Hotter, thicker discs will delay the onset of disc instability. The disc instability manifests as a bi-symmetric, two-armed spiral pattern, in which the inner region straightens and forms an elongated bar.

One of the leading physical contributors to disc susceptibility to bar formation is the dominance of the stellar disc over the dark-matter halo. In one of the earliest simulations, Hohl [1971] showed that within a few galactic rotations, in the absence of a halo, a stellar disc could form a bar. Subsequently, Ostriker and Peebles [1973]

built on the understanding that a dark-matter halo is required for disc stability. The role of the dark matter halo in bar formation and evolution is crucial, for it absorbs angular momentum. This process was emphasised in Athanassoula [2002], which showed that in a more halo-dominated system, a large population of resonant halo stars is present, sustaining bar evolution. This simulation demonstrated that the strongest bar was formed in a halo-dominated case, whilst an intermediate bar was formed in a disc-dominated case. Alternatively, in the same scenarios, however, with rigid halos, only mid-oval distortions were formed. In recent simulations, the coupling between the dark matter halo and the stellar bar has been explored. Collier and Madigan [2021] found dark matter bars can form in prograde halos, whilst retrograde orbits form a dark matter wake. Additionally, Fragkoudi et al. [2025] found that barred galaxies in the Auriga simulations are more baryon-dominated at all redshifts, and unbarred galaxies tend to be more dark matter-dominated within the central 5 kpc over all cosmic times.

Several other factors contribute to the instability threshold. One of these is that high-velocity dispersions will keep the disc dynamically hot, delay bar formation, and lead to larger gas fractions and lower surface densities. Additionally, the prevention of bar formation can be exacerbated by stellar structures, such as the presence of a compact classical bulge [Saha and Elmegreen, 2018].

There is no single prevailing factor driving bar formation; rather, the interplay among these components, along with structural properties, dictates the galaxy's evolution. With the majority of disc galaxies being barred in the local Universe, studies have refocused their investigations from why bars form to why a certain galaxy hasn't formed a bar.

1.2.2 Orbital structure

Bar formation is influenced by a variety of environmental factors, whereas the orbital dynamics that underpin the stellar structure remain constant. Whilst disc galaxies are very thin, where the outer disc has an axis ratio of ~ 10, the buckled bar is a much thicker component, modelled as a triaxial ellipsoid. The bar is a rigid rotating body, with an orbital frequency of Ω_{bar}, known as the bar pattern speed. The non-

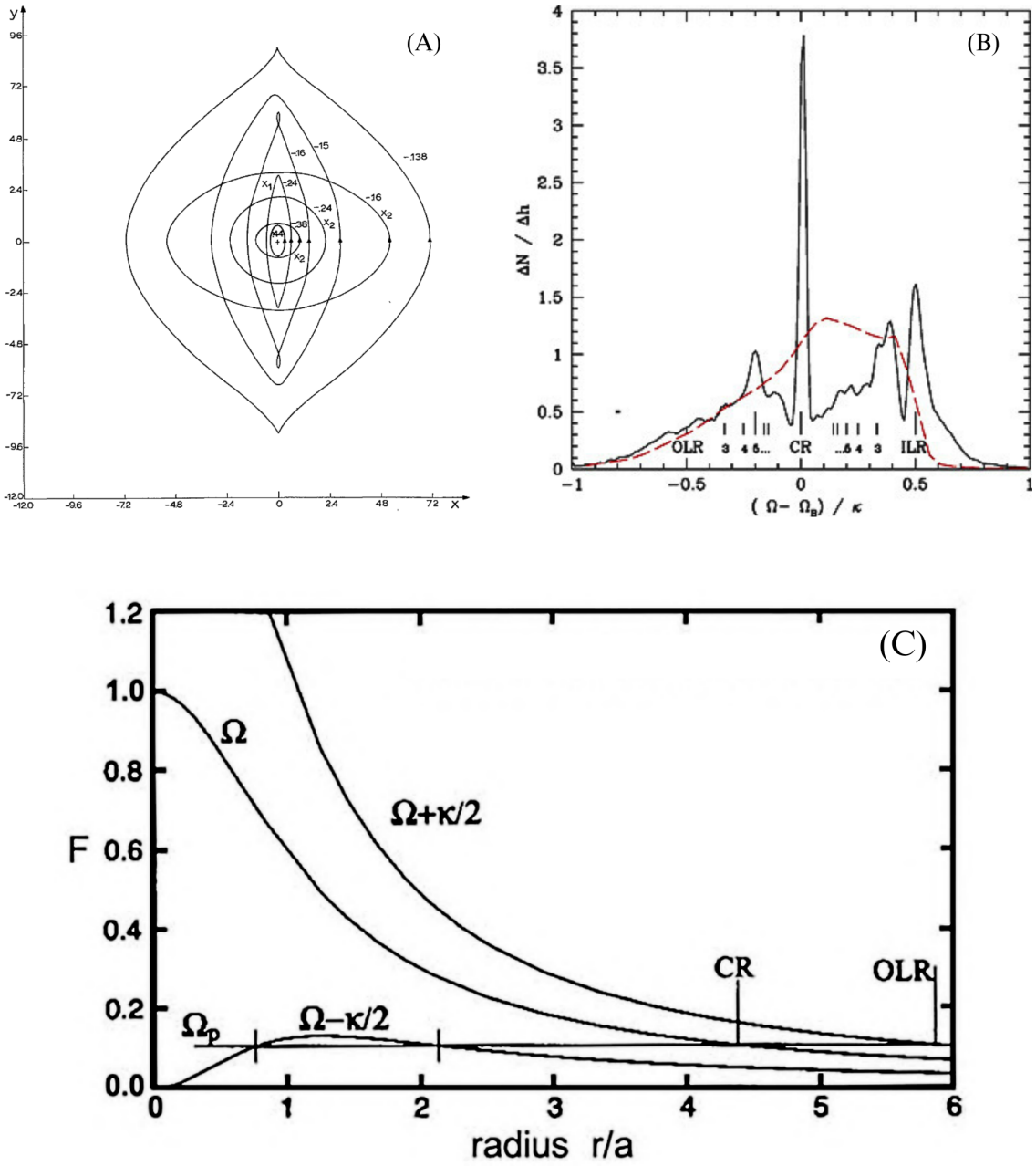

Figure 1.4: A: Examples of periodic orbits that constitute and support the bar, including the x_1, and x_2 [Fig. 7 from Contopoulos and Papayannopoulos, 1980]. B: The fraction of particles, per unit bin, at a frequency ratio after 2 Gyrs. Strong peaks at CR and ILR are clearly present [Fig. 7 from Ceverino and Klypin, 2007]. The dashed line shows the distribution 0.5 Gyr before the bar's formation. C: Angular velocity, Ω, and resonances in a Plummer potential [from Sparke and Gallagher, 2000]. For a given Ω_p, the CR occurs at $\Omega_p = \Omega$, the ILRs occurs at $\Omega_p = \Omega - k/2$, and the OLR occurs at $\Omega_p = \Omega + k/2$.

axisymmetric nature of stellar bars is due to the very elongated form of the orbits that constitute the bar, which would be the x_1 orbital family, known as the backbone of the bar, or one of the higher multiplicity families, both parallel to the semi-major axis of the bar, as shown in Figure 1.4 (a) [Contopoulos and Papayannopoulos, 1980, Wang et al., 2022], which have such properties. The x_2 orbital family is particularly important for building central nuclear structures because it is more spherical. An extensive range of orbital families and sets of families contribute to the building of the vertical component of the three-dimensional nature of bars [Patsis et al., 2002]. These are elongated orbits perpendicular to the bar, which can form a boxy/peanut (B/P; discussed in § 1.3.3) shape in edge-on galaxies. The B/P morphology is determined by the presence and stability of the supporting orbital families. Higher-order orbital families contribute to the shape of the ellipses towards the edge of the bar and determine the extent of the bar.

The elongated structure is also supported by resonant stellar orbits in the disc, which are influenced by the bar. The extent of the bar is limited by the corotation resonance (CR), which defines the corotation radius; i.e., the length of the bar cannot exceed the corotation radius. Disc stellar orbits with orbital frequencies equal to the bar orbital frequency, $\Omega = \Omega_{bar}$, are in CR with the bar. Additional critical radii, shown in Figure 1.4 (c), are the Inner Lindblad Resonance (ILR) and Outer Lindblad Resonance (OLR). Stellar orbits at these resonances strongly interact with the rotating gravity wave of the bar, thereby trapping stars and gas, creating heavily populated regions (as shown in Figure 1.4 (b)) that act as barriers to radial gas inflow. Specifically, the ILR lies within the bar and is thought to correspond to the x_2 orbital family, which forms the nuclear disc and rings (discussed in § 1.3.4). In contrast, the OLR is an important outer point of bar influence, with orbital frequencies lagging behind the bar, and it creates rings in the disc.

1.2.3 The bar fraction

In the local Universe, bars are among the most abundant stellar structures in disc galaxies, occurring in up to 80 per cent of disc galaxies when weaker bars are included [e.g., de Vaucouleurs et al., 1991, Elmegreen et al., 2004, Eskridge et al., 2000, Mari-

nova and Jogee, 2007, Menéndez-Delmestre et al., 2007]. However, results depend strongly on the observed wavelength and the identification technique employed. As discussed above, bars trap stars onto elongated, stable orbits, meaning the stellar population that bars are comprised of is predominantly older, with little to no star formation along the bar (further discussed in § 1.3.2). Hence, it is favourable to observe barred galaxies in the near-infrared (NIR), which is less affected by dust obscuration, and thus the bar fraction increases. However, quantifying the 'true' bar fraction and bar characteristics becomes challenging when the literature uses a variety of instruments and wavelengths. One of the first studies to assess the wavelength dependence of the bar fraction was Eskridge et al. [2000], which found an initial bar fraction of 56 per cent in NIR H band galaxies, which increases to 72 per cent if weakly barred galaxies are included. The optically identified bar fraction decreases to ≈ 30 per cent, demonstrating that the NIR bar fraction is nearly twice that of the optical. This result was corroborated and explored in Marinova and Jogee [2007], which found a bar fraction of 60 per cent in the NIR H band, decreasing to 40 per cent in the optical B band. Buta et al. [2015] argued that this is due to stellar structural features being more perceptible; thus, weaker bars in the optical become stronger in the NIR, so a higher bar fraction is observed. More recently, Menéndez-Delmestre et al. [2024] investigated the properties of nearby barred galaxies in the 3.6μm, R, and B bands, as shown in Figure 1.5, and reported that bars are more elliptical and 9 per cent longer in bluer wavelengths; which is as a result of star forming knots at the end of bars. These studies are critical for understanding the intrinsic evolution of bars, unbiased by band-shifting effects, by quantifying how bars vary locally due to wavelength dependence. These results can then be extrapolated to studies of bars beyond the local Universe.

The bar fraction can be derived by various bar identification techniques that are applied to images, including visual classifications [e.g., Athanassoula et al., 1990, Buta et al., 2015, Cheung et al., 2013, de Vaucouleurs et al., 1991, Eskridge et al., 2000, Nair and Abraham, 2010, Simmons et al., 2014], and more automated processes such as isophotal analysis and Fourier analysis [e.g., Buta et al., 1998, Elmegreen et al., 2004, Guo et al., 2023, 2025, Jogee et al., 2004, Marinova and Jogee, 2007,

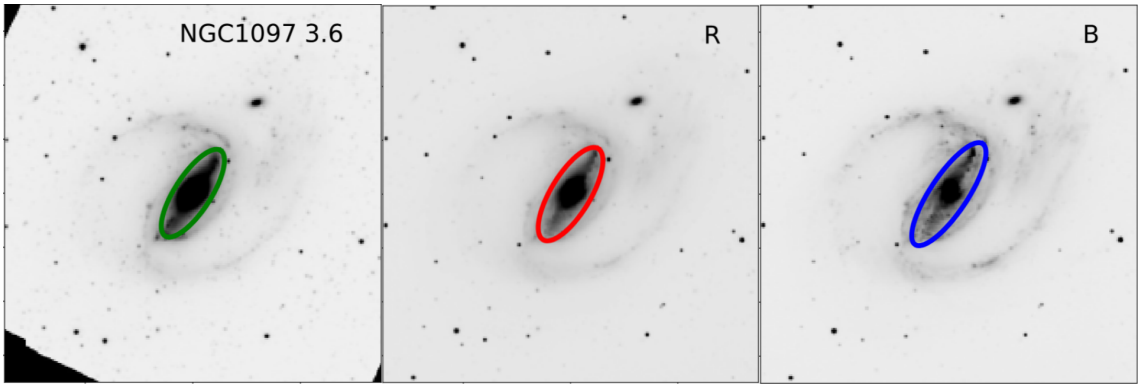

Figure 1.5: Optical through mid-infrared images of the galaxy NGC 1097 in the 3.6μm, R, and B bands with an ellipse showing the maximum ellipticity of the bar [Fig. A1 from Menéndez-Delmestre et al., 2024].

Wozniak et al., 1995]. Visual classifications are beneficial for identifying weaker bars and those in more disturbed systems; however, this method requires trained participants whom can confidently identify bar structures, and is labor expensive, especially with the recent rise in large astronomical surveys. Hence, automated techniques can aid or replace visual classification methods, which are faster and can process larger quantities of data. Automated methods can characterise signatures in the radial profiles of barred galaxies, as shown in Figure 1.6. Firstly, the ellipse-fit method fits ellipses to the image isophotes, from which position angle (PA) and ellipticity (ε) measurements are obtained; the parameter radial profiles are then used to identify a bar feature. The criteria for bar identification vary across studies, but they generally agree that, within the bar-dominated region, the PA remains constant while ε gradually increases. The end of the bar can be defined by taking the radius of either the peak ellipticity, or the one with the minimum ellipticity succeeding the peak ellipticity, or where a significant change in PA occurs, or a combination of these three metrics. Alternatively, the bar can be characterised by the $m = 2$ Fourier mode of the surface brightness distribution [Abraham et al., 1999], which is particularly beneficial for the method's sensitivity to weaker and smaller bars.

However, these techniques have their limitations: ellipse-fits are limited to well-resolved stellar structures and are sensitive to star-forming regions, interactions, and foreground sources; Fourier analysis requires deprojecting galaxy images, which becomes challenging for galaxies beyond the local Universe. In a $z \leq 0.01$ sample

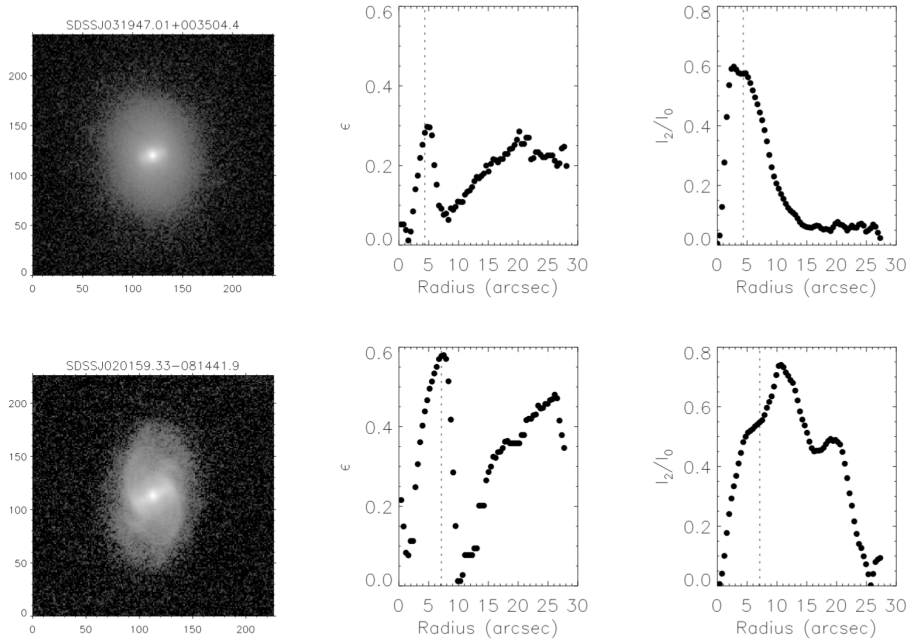

Figure 1.6: Bar lengths (vertical dashed lines) measured on r-band images (left panels) via the method of ellipticity radial profiles from fixed ellipse fits (middle panel), and $m = 2$ Fourier amplitude radial profiles (right panels) [Fig. 6 from Aguerri et al., 2009].

with galaxies $M_r \leq$ -15.2, Lee et al. [2019] found the bar fractions for three different identification techniques: 63 per cent by visual inspection; 48 per cent by ellipse fitting; 36 per cent by Fourier analysis. Additionally, in their study, they concluded that ellipse fitting techniques could miss $\sim$ 15 per cent of visually classified bars due to large bulges in early-type spirals. Using a deep convolutional neural network, Abraham et al. [2018] identified bars with good accuracy. Surveys are now conducted at remarkably large scales, so automated techniques and machine learning [e.g., Cheng et al., 2021] will become vital for morphological classification, but corrections to account for biases in the bar fraction and bar properties must be determined.

Observational investigations into the abundance of stellar bars in disc galaxies up to $z \simeq 1$ found a linear decrease in their frequency with increasing redshift [Abraham et al., 1999, Jogee et al., 2004, Melvin et al., 2014, Sheth et al., 2003, 2008]. This declining trend is observed across all these studies, which employ different identification techniques, samples, and instruments. For the broad redshift range $0.0 < z < 1.5$, Abraham et al. [1999] found a decline in the Hubble Deep Field-North and -South bar fraction. For the more constrained redshift range $0.20 < z < 0.84$,

Sheth et al. [2008] found a decrease in the bar fraction from the 2 deg^2 Cosmic Evolution Survey (COSMOS), for which both visual and ellipse-fitting techniques were employed. From $z \sim 0.4$ to $z \sim 1.0$, Melvin et al. [2014] found the COSMOS bar fraction to decrease by a factor of two, using visual classifications. In the high redshift regime of $z \simeq 1$, Simmons et al. [2014] discovered prominent bars using Galaxy Zoo, and reported that the bar fraction remains at 10 per cent for $z \geq 1$. Two observational studies of the evolution of the bar fraction with redshift find no sign of a sharp decline at $z > 0.7$: Elmegreen et al. [2004] found a near constant bar fraction of 0.23 ± 0.03 at redshifts from $z = 0$ up to $z \simeq 1.1$ for a sample of 186 disc galaxies; Jogee et al. [2004] found the optical bar fraction for a sample of galaxies in the Galaxy Evolution from Morphologies and SEDs (GEMS) survey to be $\sim 0.3 \pm 0.06$ which remains constant at redshifts $0.2 < z < 1.0$. These studies required high-resolution, sensitive imaging across a large sky area, which the Hubble Space Telescope (HST) has achieved; however, to investigate bars at earlier epochs, further instrumental improvements are necessary. These observational studies at the redshift range $0 \leq z \leq 1$ imply that bar features cease to exist at greater lookback times, suggesting that bar-driven evolutionary processes do not commence until ~ 6 Gyr after the Big Bang.

Studies based on cosmological simulations yield heterogeneous results for the bar fraction, with some agreeing with observations and others contradicting them. Kraljic et al. [2012] found a depletion in the number of bars in present-day spiral progenitors at $0 < z < 2$, implying a violent phase of galaxy evolution where discs are dynamically hot, and there are excessive merger events. However, Athanassoula et al. [2016] followed the merging of two disc galaxies and found that the merger remnant starts forming a bar before the disc is fully developed. Rosas-Guevara et al. [2022] used TNG50 simulations [Nelson et al., 2019] to trace the bar fraction evolution with redshift and showed that the bar fraction increased to ~ 50 per cent at $z \simeq 1$ and only significantly decreased at $\sim z > 2$. Even at $z \simeq 6$, the simulated bar fraction, at a minimum, reached ~ 25 per cent. The bar fraction found in the Auriga cosmological zoom-in simulations from Fragkoudi et al. [2020] are in good agreement with observational studies, where for redshifts $0 \leq z \leq 1.5$

the bar fraction decreased from ~ 70 per cent to ~ 20 per cent.

The advent of the James Webb Space Telescope (JWST) has enabled bar-fraction studies to extend to $z \approx 4$ owing to its improved sensitivity and extended wavelength range. Recently, several studies of bar fractions using visual and ellipse-fitting techniques have identified barred galaxies at this early epoch. The first JWST bar fraction study, [Le Conte et al., 2024], observed a decrease in the visually classified bar fraction from ≈ 18 per cent at $z \approx 1.5$ to ≈ 14 at $z \approx 2.5$. This result was later verified by Le Conte et al. [2026] in a range of NIRCam wavelengths and for the extended redshift range $1 \leq z \leq 4$, which measured a bar fraction of ≈ 7 per cent at $z \approx 3.5$. For the redshift range $0.5 \leq z \leq 4$, Guo et al. [2023, 2025] used ellipse fits for bar identification, and found the fraction to decrease from 28.2 ± 3.6 per cent to 6.4 ± 2.4 per cent across the redshift range. For the same redshift range, Géron et al. [2025] found the Galaxy Zoo bar fraction to decrease from 25 per cent to 3 per cent. At the two redshift bins of $0.8 < z < 1.3$ and $2.0 < z < 2.5$, Espejo Salcedo et al. [2025] determined that the bar fraction decreases from 16 per cent to 3 per cent. Such studies indicate that bar-driven internal evolution began ~ 11 Gyrs ago, but only in a small fraction of disc galaxies. To fully understand the evolution of the bar fraction, it is necessary to investigate the wavelength dependence in this high-redshift regime and to correct for observational biases.

1.2.4 Structural properties

Bar characteristics reveal the formation mechanisms and evolutionary tracks of these settled, rotationally supported disc galaxies. Below, I describe the structural properties of stellar bars, their relationship with the host disc galaxy, and their evolution over cosmic time.

The distinct radial light profile of a bar is brightest along the bar major axis and is fainter along the bar minor axis [Sellwood and Wilkinson, 1993]. The surface brightness profile can be described by different parametric laws, for example, as a flat profile, as shown in Figure 1.7. The flat-bar profile was found to be preferentially observed in higher-mass galaxies, which are early Hubble types, redder in colour, and have lower gas fractions [Erwin et al., 2023]. The surface-brightness profile of a bar

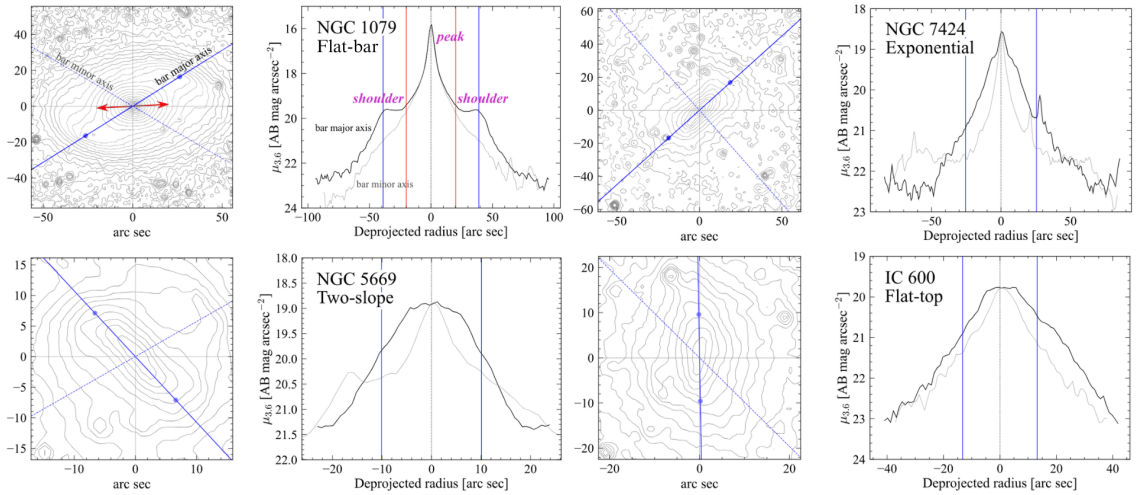

Figure 1.7: Plots of bar isophotes and profiles for four types of bar surface-brightness profiles [Fig. 1, 2, 3 & 4 from Erwin et al., 2023]. The top-left panel shows the classic 'flat bar' profile with peak and shoulders. The other panels show three subtypes of the classic exponential profile, from top right to bottom right: true exponential; 'Two-Slope' with a shallow inner slope and a steeper outer slope; and 'Flat-Top' with a constant inner region and a steep outer slope. Images show the bar position angle with solid blue lines, the bar radius with blue dots, and the dashed lines show the bar minor axis. The profile along the bar major axis is shown in black lines, and the minor axis in grey lines. Vertical blue lines mark the bar radius, and red lines show the position angle and extent of the B/P bulge.

was found to correlate with the Hubble type of the disc galaxy in an earlier study, where Elmegreen and Elmegreen [1985] observed flat surface-brightness profiles in early types and exponential profiles in late-type discs. The bar follows a Sérsic profile, characterised by the Sérsic index n_{bar}, that controls its shape. Low Sérsic index values correspond to flatter profiles, and as n_{bar} increases, they become more centrally concentrated. For nearby galaxies, Gadotti [2011] found the bar profile lies halfway between a Gaussian and an exponential, with $n_{bar} \approx 0.7$. The radially bright light profile of the bar causes a prominent light deficit along the bar's minor axis, known as the 'dark gap' [e.g., Aguerri et al., 2023, Ghosh and Di Matteo, 2024, Kim et al., 2016]. The extent and strength of dark gaps strongly correlate with the length of the bar; however, the location of dark gaps is only weakly correlated and therefore cannot be used as a robust proxy to determine the bar length measurements [Ghosh and Di Matteo, 2024].

Deciphering the bar's profile becomes challenging because the surface-brightness

profile includes central stellar structures, such as the bulge, which distort the bar from a perfect ellipse. To address this difficulty, the photometric decomposition procedure is used to separate components in galaxy images and derive the light contributions of each component. Once the morphological classification of a galaxy is determined, photometric decomposition can be employed to unveil the structural properties of each component. In the last two decades, multiple algorithms have been developed to perform 2D image decompositions, namely Galaxy Fitting [GALFIT Peng et al., 2002], Bulge/Disk Decomposition Analysis [BUDDA de Souza et al., 2004, Gadotti, 2008, ; although bars were later introduced to the model fitting in version 2], and Image Fitting [IMFIT Erwin, 2015, ; which is used in this thesis]. Figure 1.8 presents the employment of GALFIT on the nearby galaxy NGC 5101, showing the original and masked galaxy image, the fitted models, and the residual image. Models derive the structural properties of the component, whilst the residual image reveals unmodelled substructures. Despite photometric decompositions being robust, studies use a variety of techniques, including ellipse fits and Fourier analysis, to determine bar properties.

Bars have been found to form in a variety of disc galaxies, including dwarf galaxies; however, the highest incidence of bars is in $M_\star = 3 \times 10^9 M_\odot$ to $10^{10} M_\odot$ disc galaxies, and as shown in Figure 1.9, declines for higher and lower mass galaxies Erwin [2018]. Nearby studies have identified bars to be in preferentially massive, gas-poor and red discs [e.g., Cervantes Sodi, 2017, Gavazzi et al., 2015, Masters et al., 2011], but Erwin [2018] contradicted this by suggesting that SDSS samples under-predicted the bar fraction at lower stellar masses, preferentially missing blue gas-rich galaxies.

Despite bars being relatively compact features at the centres of galaxies, their shapes and sizes can vary substantially with host galaxy and viewing angle. The shape of a bar is commonly determined by fitting elliptical isophotes to the galaxy's surface-brightness profile and can range from elliptical to more rectangular, known as a boxy bar. Nearby bars have a range of ellipticities, $\varepsilon = 1 - b/a$, where b/a is the bar axis ratio, typically between 0.4 and 0.8 and peaking at 0.6 [Gadotti, 2011]. These bars have boxiness values, c, between 2 and 3.5 [Gadotti, 2011], where $c = 2$

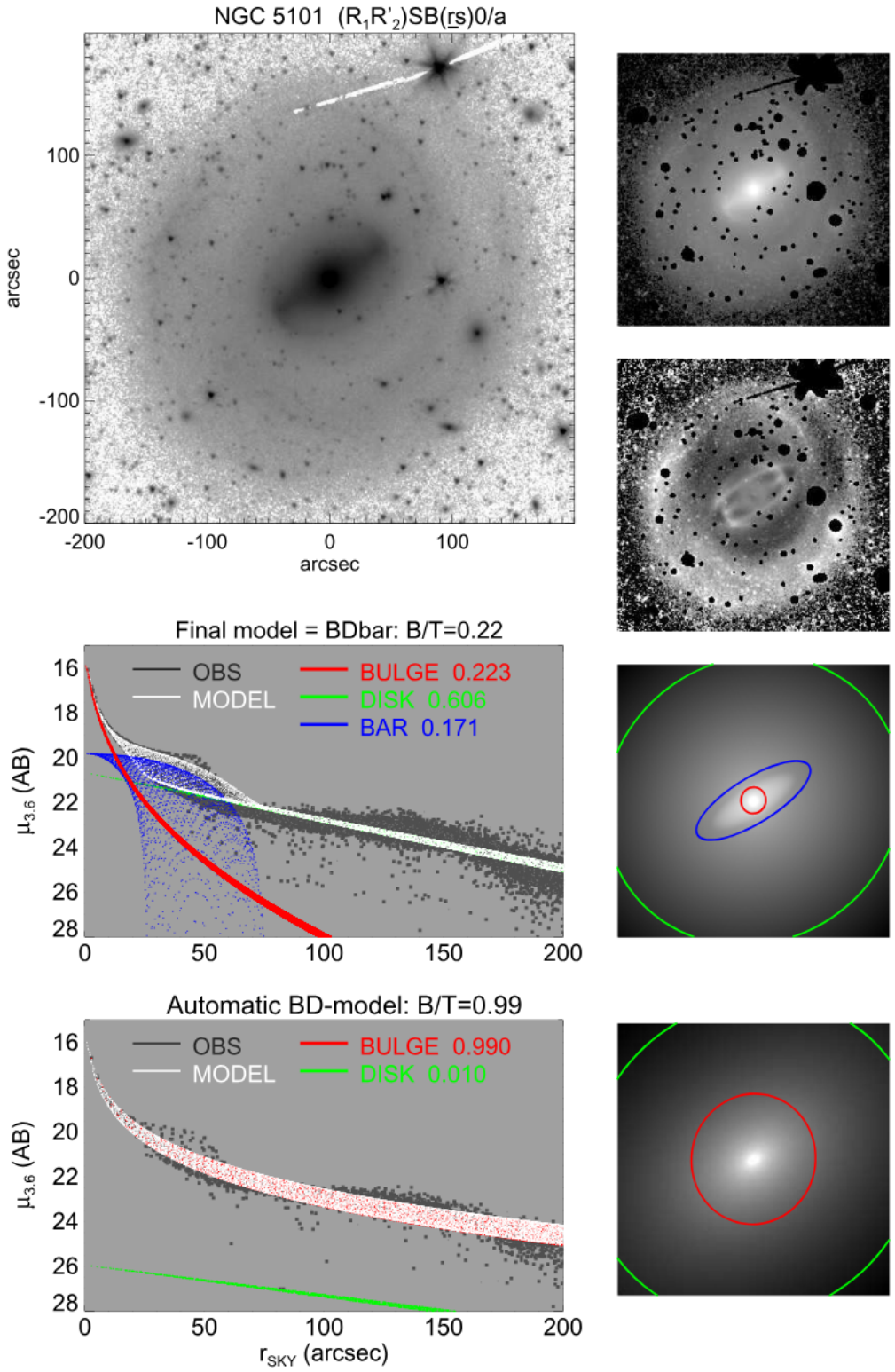

Figure 1.8: Photometric decomposition of a barred galaxy [Fig. 18 from Salo et al., 2015]. The galaxy image is shown in the top left, with the four right panels showing the masked image (top), the model-subtracted residual image (middle), and the model images (bottom two). The bottom left panels show the 2D profiles of the observed and model images for the inclusion and exclusion of the bar model.

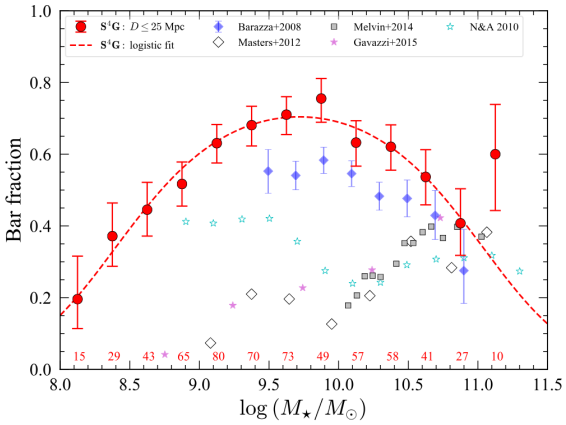

Figure 1.9: The fraction of disc galaxies with bars in the S^{4}G sample as a function of stellar mass [Fig. 5 from Erwin, 2018].

indicates a purely-ellipsoidal shape and $c > 2$ is more boxy.

Bars can vary in size by an order of magnitude, where some nearby bars are < 1 kpc in length (although these are typically referred to as 'nuclear bars', as opposed to the 'normal' bars discussed here), all the way to > 10 kpc, which are extremely strong and dominant features. Gadotti [2011] observed the peak in bar length to be 4.5 kpc for nearby barred galaxies. Extending to higher redshifts, $0.2 \leq z \leq 0.8$, Kim et al. [2021] observed the bar length of over 300 galaxies in the COSMOS survey and measured a mean length of ≈ 4.5 kpc for galaxies $\log(\mathrm{M}_\star/\mathrm{M}_\odot) \leq 10.6$.

Theory suggests that, over time, a bar will grow in length. This evolution is due to the slowing down of the rotational pattern speed of the bar, resulting in the location of resonances extending to greater radii, thus allowing the trapping of stars on elongated orbits to reach these new limits [Athanassoula, 2003]. In the Auriga cosmological simulations, bars that form at $z \leq 1$ form short in length and grow with time, whereas those formed at high-z form very long (with a semi-major axis of about 6 kpc), possibly due to an interaction-driven bar formation, and do not show an evolution in length [Fragkoudi et al., 2025], i.e., they form 'saturated' in length. Alternatively, some cosmological simulations find weak interaction-induced bars at Cosmic Noon [e.g., Bi et al., 2022], which weaken and reform throughout their evolution.

Observations of nearby galaxies have reported that bar lengths evolve, growing over Cosmic time. In a sample of 300 nearby barred galaxies, Gadotti [2011] found

longer and stronger bars in galaxies with a higher bulge-to-total luminosity ratio (indicating more evolved galaxies), suggesting that the bars grow longer and stronger with time. A similar argument was put forward by Erwin [2018], who found that more massive galaxies host longer bars in a sample of nearby barred galaxies from the Spitzer Survey of Stellar Structure in Galaxies [S^4G Sheth et al., 2010]. Recently, with direct measurements of bar ages in nearby galaxies of the TIMER sample [Gadotti et al., 2019], de Sá-Freitas et al. [2025] found that older bars are longer. It should be noted that these observational results are, to date, still consistent with the Auriga results, whereby bar growth depends on bar formation epoch. More explicitly, the oldest bars form around the time of a significant merger with bar lengths > 4 kpc that do not evolve, whereas younger bars appear to form shorter (< 4 kpc), but grow up to twice their formation length.

The Milky Way has properties similar to those of nearby barred galaxies. The length of the bar is ≈ 5 kpc [Bland-Hawthorn and Gerhard, 2016], with an ellipticity of 0.6 [Bovy et al., 2019], and exhibiting an exponential luminosity profile [Wegg et al., 2015].

1.3 Bar-driven evolution

The stellar bar is the primary driver of internal secular evolution in a disc galaxy. The strongly non-axisymmetric structure effectively facilitates the redistribution of angular momentum from the inner to outer disc and out to the halo, thus influencing the morphology [e.g., Athanassoula, 2005, 2003, Di Matteo et al., 2013, Fragkoudi et al., 2018, Lynden-Bell and Kalnajs, 1972, Menéndez-Delmestre et al., 2007, Regan et al., 2006]. The process has a dramatic effect on gas transportation, particularly in the form of inflows towards the central kiloparsec of the galaxy. Hence, it enhances star formation and creates a gas reservoir at the centre of the galaxy. The mechanisms of gas transport at the centre of the galaxy are crucial for understanding the fuelling of the central SMBH and, thus, active galactic nuclei (AGN).

1.3.1 Angular momentum

A rotationally supported disc galaxy simultaneously attempts to minimise its energy whilst conserving angular momentum. To conserve angular momentum, different regions of the galaxy will either lose or gain angular momentum, achieved by transporting angular momentum and mass outward [Lynden-Bell and Kalnajs, 1972]. Thus, stellar systems will simultaneously contract towards the centre and expand their outer regions to greater radii. The shedding of angular momentum is effectively supported by the stellar bar [Athanassoula, 2003]. The bar achieves this by trapping circular orbits of disc stars and transforming them into more elongated orbits, which, in turn, increase the bar's length, making it stronger. As these orbits become more elongated, the bar becomes thinner. This process can happen simultaneously with the bar pattern speed slowing down, thus extending the CR to greater radii and trapping further stars [e.g., Athanassoula, 2003, Athanassoula and Misiriotis, 2002]. The location of angular momentum exchange is at the resonances, in which the ILR expels, and the CR absorbs [Ceverino and Klypin, 2007]. This has been tested in N-body simulations, which show that the disc loses angular momentum and the halo gains it [Athanassoula, 2003].

1.3.2 Gas dynamics

Bars play a major role in transporting gas in the disc, with substantial effects on star formation throughout the galaxy. Gas inflow is promoted by the loss of angular momentum from shocks in gas clouds when they interact with the torques generated by the bar [e.g., Kim et al., 2024]. The bar transports gas from the outer disc, along the bar dust lanes, and deposits the gas within a few kpc of the galaxy centre [Athanassoula, 1992]. Bar-driven gas inflow is supported by observational studies that have measured higher molecular gas content within the first kpc of barred galaxies than in unbarred galaxies. Sheth et al. [2005] confirmed the result of Sakamoto et al. [1999], namely that the central kiloparsec of barred galaxies contains a higher degree of molecular gas concentrations. In simulations, Fragkoudi et al. [2016] observed a consequential reduction in the gas inflow to the central

kiloparsec associated with the growth of a vertical bar component, i.e., the B/P bulge. At the galaxy centre, the gas supports the formation of rotationally supported substructures, i.e., the nuclear disc, rings, and bar. Hence, the innermost region of barred galaxies experiences the compression of gas and enhanced star formation [e.g., Allard et al., 2006, Bittner et al., 2020, Coelho and Gadotti, 2011, de Lorenzo-Cáceres et al., 2012, Gadotti et al., 2020, Knapen et al., 1995, Sanders and Tubbs, 1980].

Whilst star formation is enhanced in some regions of barred galaxies, the bar depletes star formation in other areas. Specifically, within the radial extent of the bar. For a small sample of barred galaxies, Neumann et al. [2020] explored the star formation history across the bar region, and found intermediate-aged stars (2 - 6 Gyrs) to have the most elongated orbits, whilst the oldest stars ($>$ 8 Gyrs) constitute the rounder and thicker part of the bar, and the youngest stars are found along the leading edge of the bar. In a comparative analysis of barred galaxies, Neumann et al. [2019] found a clear divide between star-forming and non-star-forming types that linked to the bar surface-brightness profile, with the flattest bars being actively star-forming. Additionally, it was reported that star formation is 1.75 times stronger on the leading than on the trailing edge of the bar and decreases radially.

Star formation along the bar remains poorly understood; however, some studies find that in violent dynamical environments, shocks and shear along the bar strongly impact star formation [Emsellem et al., 2015, Kim et al., 2024]. Finally, Emsellem et al. [2015] commented on the interplay at the subparsec scale between a galactic bar and the AGN in simulations, and found shear to inhibit star formation in gas-rich regions of the bar. Altogether, the acceleration of star-formation in the innermost regions [e.g., Lin et al., 2017], which consumes the reservoir of gas, in addition to the depletion of star-formation in the disc, means that the bar significantly contributes to the quenching of disc galaxies [e.g., Masters et al., 2011].

1.3.3 Boxy/Peanut structures

While bars are clearly observed in face-on disc galaxies, they are significantly harder to identify in highly inclined systems. However, evidence of their presence comes

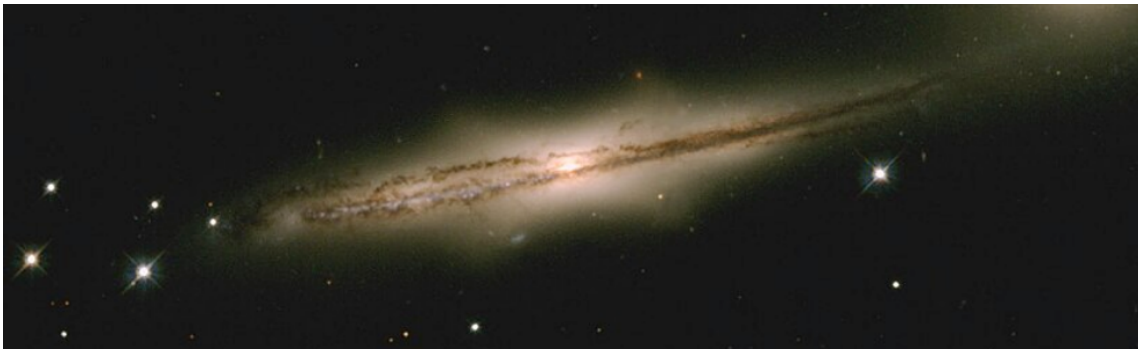

Figure 1.10: Edge-on barred galaxy ESO 597-G036 with a clear boxy/peanut structure, captured by the NASA/ESA Hubble Space Telescope.

from the observation of a vertical stellar component formed by dynamical processes. Once a strong rotating bar forms in a thin disc, the system can undergo a second instability, driven by resonant heating and dynamical instabilities. Orbits are transformed vertically out of the disc plane by the 2:1 resonance, forming a characteristic boxy or peanut-shaped (B/P; otherwise referred to as X-shaped) bulge when viewed edge-on. This vertical thickening is in alignment with the semi-major axis of the bar [e.g., Carles et al., 2016, Combes and Sanders, 1981, Combes et al., 1990, Ishizuki et al., 1990, Kormendy, 1982, Kormendy and Kennicutt, 2004].

In the local Universe, B/Ps are common structures in barred galaxies; using imaging, Erwin and Debattista [2017] found an occurrence of $\approx$ 80 % in Milky Way-like mass galaxies, which declines in lower-mass barred galaxies. These studies are challenged by the fact that B/P structures are visible only over a limited range of viewing angles, and when the semi-major axis is oriented parallel to the line of sight, these structures resemble a 'classical' bulge. Hence, recent studies employ kinematics to identify substructures and find that $\approx$ 67 % of their edge-on disc sample possess a B/P morphology [e.g., Fraser-McKelvie et al., 2025]. The vertical height of the peak in the B/P shape ranges from $\approx$ 0.5 to 1.5 kpc [e.g., Ciambur and Graham, 2016, Ciambur et al., 2021]. The B/P extends from one-quarter to three-quarters of the bar length [Erwin and Debattista, 2017]. Lastly, the Milky Way is also confirmed to have a B/P [e.g., Kent et al., 1991, Ness and Lang, 2016, Wegg and Gerhard, 2013].

1.3.4 Nuclear stellar structures

As discussed thus far, bars are efficient drivers of gas inflow towards the centre of the galaxy. The inflow of gas ceases a few hundred parsec from the centre of the galaxy, and the mechanisms behind this are still debated. Oftentimes described as the primary cause, the region of halted gas inflow is limited by the ILR of the bar potential [Shlosman et al., 1989], corresponding to the x_2 orbital family, which populate nuclear discs and rings. However, studies have proposed that the residual angular momentum in the gas ceases to be inflowing. The gas reservoir creates an environment that fosters the formation and growth of a flattened, rotating stellar system at the centre of a galaxy. Both terms, nuclear disc and nuclear ring, have been introduced, and they are primarily distinguished by their morphological stellar structures. Nuclear rings show a star-forming ring with a void towards the centre, whereas nuclear discs are a continuous stellar structure. An example of a galaxy with a nuclear disc is shown in Figure 1.11. Observations of these nuclear structures in nearby galaxies suggest that the nuclear ring is simply the star-forming outer edge of the nuclear disc [e.g., Bittner et al., 2020]. Gadotti et al. [2020] supported this theory by demonstrating that these nuclear structures have the same kinematic properties; thus, they should be considered equivalent. Despite their morphological differences, it is believed that the same bar-driven mechanisms form these nuclear structures.

The formation of a nuclear disc indicates that bar-driven galaxy evolution has begun, and such structures can form relatively quickly. Simulation and observational studies have shown that the nuclear disc forms $\sim 10^8$ yrs after the bar's formation [e.g., Athanassoula, 1992, Emsellem et al., 2015, Seo et al., 2019]. Recent studies of nearby galaxies have reported on the typical size of a nuclear disc being a few hundred parsecs, and more specifically extending to radii $\sim 13\%$ of their bar lengths [Gadotti et al., 2020]. They are a region of densely accumulated mass and have been measured to have masses of $\sim 10^9 M_\odot$ [de Sá-Freitas et al., 2025], which can form a nearly axisymmetric disc, or be the host to non-axisymmetric nuclear structures, such as a nuclear bar or spiral arms, which form under similar dynamical processes to the main disc. The nuclear disc also exhibits properties similar to those of the main

Figure 1.11: A detailed image of the centre of the barred spiral galaxy NGC 1097 captured by NASA/ESA Hubble Space Telescope with the Wide Field Camera 3 (WFC3) and the Advanced Camera for Surveys (ACS), which shows a nuclear disc.

disc, which is described by an exponential radial intensity profile and is kinematically cold [Gadotti et al., 2020]. The properties of the host galaxy typically influence those of the nuclear disc, so a range of sizes and properties has been discussed in recent works [e.g., Comerón et al., 2010, Erwin, 2004, see also Schultheis et al. [2025] for a review].

The nuclear disc can be observed photometrically or kinematically, and is considered ubiquitous in local barred galaxies; even the Milky Way is known to have a nuclear disc, although this is often referred to as the "Central Molecular Zone" [Henshaw et al., 2023, Morris and Serabyn, 1996]. One of the first studies to highlight a large population of nuclear discs was Gadotti [2009], which performed photometric decompositions of nearly 1000 galaxy images from the Sloan Digital Sky Survey (SDSS), and found that 32% of disc galaxies with bulges were host to a nuclear disc. The first atlas of nuclear discs was compiled in the Atlas of Images of NUclear Rings [AINUR: Comerón et al., 2010], which observed 113 nuclear rings in a variety of galaxy types. In this large sample of nuclear rings, they found $\approx$ 20% to be star-forming in local disc galaxies, and a surprising 19% of nuclear rings were found in unbarred galaxies. However, in several of these peculiar cases, non-axisymmetric features are present, which could facilitate the formation of a nuclear disc. Since

these photometric studies, a kinematic study of nuclear discs was conducted, named as the Time Inference with MUSE in Extragalactic Rings [TIMER: Gadotti et al., 2019], which selected a sample of 21 massive barred galaxies with evident nuclear discs, and observed 19 of these to have rapidly rotating discs.

Inside-out evolution is one of the most convincing scenarios for nuclear disc growth and is proposed by Bittner et al. [2020]. This study utilised the TIMER sample to derive 2D properties that indicate mean stellar ages, metallicities, and [α/Fe] abundances. The study reported that, compared with the bar and main disc, the stellar population in the nuclear disc is younger and more metal-rich. Additionally, within the nuclear disc, a well-defined radial gradient is observed, with age decreasing with radius. The radial gradient is due to the radial migration of the ILR as the pattern speed of the bar slows, and mass is deposited on the nuclear disc edge [e.g., Athanassoula, 1992, Kim and Lee, 2012].

Not only is the nuclear disc an interesting environment for secular galaxy evolution, but it has also recently been used to probe the ages of stellar bars. de Sá-Freitas et al. [2023] introduced a novel technique that used data from the TIMER survey to disentangle the star-formation history of the nuclear disc from that of the main disc. This approach assumes that the nuclear disc forms quickly after bar formation, thereby igniting star formation in the nuclear ring. In de Sá-Freitas et al. [2025], the authors reported bar ages for the entire TIMER sample and found that bar formation occurs throughout Cosmic time, is evident in the early Universe, and is still ongoing in some galaxies today.

In summary, our understanding of nuclear discs has recently expanded with the advent of advanced telescope facilities; however, there remains scope to explore their properties, particularly their role in gas transport and AGN fueling. A nuclear disc is explicit evidence that bar-driven evolution is ongoing in a disc galaxy, and can be a useful tool to probe bar ages. With the advent of JWST and as observational techniques continue to improve, there is scope to study nuclear structures beyond the local Universe.

1.3.5 AGN fuelling

Major galaxy mergers were long considered the primary drivers of the coevolution between SMBHs and their host galaxies. However, recent simulations demonstrate that merger-free black hole growth can be equally significant [e.g., Martin et al., 2018, McAlpine et al., 2020, Smethurst et al., 2024]. In the absence of mergers, another mechanism must channel gas efficiently toward the galactic centre, and stellar bars are a compelling candidate. Although the precise influence of bars on black hole growth remains debated, both theoretical models and observations agree that bars can effectively funnel gas into the inner kiloparsec [e.g., Alonso et al., 2013, 2018, Cisternas et al., 2015, Garland et al., 2023, 2024, Knapen et al., 1995, Silva-Lima et al., 2022], building a reservoir to feed the SMBH and potentially triggering nuclear activity through other processes bringing gas closer to the SMBH [Athanassoula, 2003, Garland et al., 2023]. Although some studies find no strong correlation between bar presence and AGN incidence [e.g., Goulding et al., 2017], others report an enhancement of AGN activity in barred systems, suggesting that bar-driven inflows may play a role under certain conditions [e.g., Knapen et al., 2000]. For a nearby sample of Galaxy Zoo disc galaxies, Garland et al. [2024] determines that the fraction of AGN in strongly barred galaxies is $\approx 32\%$, whilst only 14% in unbarred galaxies. Thus, while bars are not required for AGN fuelling, they appear to enable it.

1.4 Thesis structure

It is well understood that in the local Universe, bars are ubiquitous stellar structures in disc galaxies and that they are the key drivers of internal galaxy evolution; however, the onset of bar formation and their impact in the early stages of a galaxy's evolution have not yet been observed. To date, studies have explored intermediate redshift ranges ($z < 1$), which were believed to provide a relatively complete picture of bar formation and evolution [e.g., Eskridge et al., 2000, Jogee et al., 2004, Masters et al., 2011, Sheth et al., 2008, Simmons et al., 2014]. However, these observations faced several challenges in identifying and quantifying the properties of

a higher-redshift barred galaxy population, including spatial resolution, sensitivity limitations, and band-shifting. The majority of these observational studies used HST imaging; thus, a galaxy at $z = 1$ is probed in the bluest part of the optical spectrum, where dust and star formation obscure the bar's older stellar population. Additionally, the spatial resolution of HST imaging means bars shorter than ≈ 2 kpc are missed, thereby excluding more than 10% of barred galaxies in nearby galaxies [Erwin, 2018]. Alternatively, simulations predict populations of barred galaxies beyond $z = 1$, with some systems displaying properties similar to those in the local Universe [e.g., Fragkoudi et al., 2025, Rosas-Guevara et al., 2022]. To fully understand the onset of bar formation and the significance of bar-driven evolution in young galaxies, observations of these systems are required during the epoch of Cosmic Noon.

For the first time, we can explore this high-redshift regime with the JWST. The imaging instrument, the Near Infrared Camera (NIRCam), addresses the challenges faced by previous studies. With improved sensitivity and a broader wavelength coverage, we can now observe Cosmic Noon galaxies at rest-frame wavelengths from the NIR to the red end of the optical spectrum.

In this thesis, I expand our current understanding of higher-redshift barred galaxies by testing whether bar formation begins at $z = 1$, thereby obtaining, for the first time, a sample of barred galaxies at Cosmic Noon. I seek to evaluate the role of bar-driven evolution in these young galaxies by measuring their structural properties through several analytical techniques, and observing the formation of nuclear structures.

In Chapter 2, I present the first measurements of the bar fraction at a redshift range of $1 \leq z \leq 3$. I describe the methodology used to process galaxy images from the first four JWST Cosmic Evolution Early Release Science Survey (CEERS) pointings, which are present in the HST Cosmic Assembly Near-infrared Deep Extragalactic Legacy Survey (CANDELS) observations. The corresponding HST and JWST disc galaxy samples are obtained from Kartaltepe et al. [2015] and Ferreira et al. [2023]. I optimise the sample to be near-face-on systems, yielding 368 galaxies. Five collaborators perform visual

classifications on the HST and JWST images, categorising barred galaxies. The bar fraction obtained from JWST is twice the bar fraction obtained from HST, and decreases from $\approx 18\%$ for the redshift range $1 \leq z < 2$ to 14% at $2 \leq z \leq 3$. This result shows that bar-driven evolution commences earlier than we previously thought.

In Chapter 3, I present an extension to my study in Chapter 2. Here, I corroborate my previous findings using a significantly larger CEERS sample (by a factor of 2.5) that extends to $z = 4$, and I measure the visually classified bar fraction for shorter-wavelength NIRCam filters, which have improved spatial resolution. Thus, I test whether we can identify a shorter population of high-redshift bars. I find the bar fraction to be independent of wavelength. In total, we identified 70 barred galaxies beyond $z = 1$. I use ellipse-fitting techniques to observe the evolution of the bar length at Cosmic Noon. I show that bars grow in tandem with their discs, for the bar length normalised by disc size does not evolve from the local Universe to Cosmic Noon. Finally, in nearby massive galaxies, a correlation between stellar mass and bar length is observed; however, I find that this correlation is absent at high redshifts.

In Chapter 4, I present the detailed methodology of photometric decomposition on the sample of strongly barred galaxies found in my previous studies. With this rigorous technique, I can measure the structural properties of these barred galaxies, including the Sérsic index, bar length, bar ellipticity, and bar-to-total luminosity ratio. I show that these barred galaxies have properties similar to those of nearby galaxies, suggesting that bar-driven evolution begins shortly after bar formation and proceeds quickly, enabling these younger galaxies to resemble those of more mature systems in the local Universe.

In Chapter 5, I share the compelling discovery of the first nuclear disc beyond the local Universe. One of the most telling signs that effective bar-driven evolution is underway is the formation of nuclear structures, such as the nuclear disc. They are formed by the inflow of gas along the bar, which is halted by orbital resonances. In this study, I perform an in-depth analysis of the NIRCam

F150W and F200W images of the galaxy CEERS 4031 at $z = 1.5$. The techniques included unsharp masking, photometric decomposition, and ellipse fits, which are consistent with evidence for a nuclear disc 1.3 kpc in radius, nuclear spiral arms, and potentially a nuclear bar. From SED fitting, I find that within the nuclear disc region, elevated star formation rates are observed, and the youngest stellar population resides. Star formation is expected as it is a consequence of the bar-driven gas inflow, and the nuclear disc properties observed here are the same as those observed in nearby galaxies. This discovery urges us to consider the role of bars in galaxy evolution only a few billion years after the Big Bang.

In Chapter 6, I summarise the findings of this thesis and share an outlook plan for future work.

CHAPTER 2

A JWST investigation into the bar fraction at redshifts $1 \leq z \leq 3$

In this chapter, I present a paper published in the Monthly Notices of the Royal Astronomical Society [Le Conte et al., 2024] on the evolution of the bar fraction beyond $z = 1$.

The presence of a stellar bar in a disc galaxy indicates that the galaxy hosts in its main part a dynamically settled disc and that bar-driven processes are taking place in shaping its evolution. Studying the cosmic evolution of the bar fraction in disc galaxies is therefore essential to understanding galaxy evolution in general. Previous studies using the HST have found that the bar fraction declines significantly from the local Universe to redshifts near one. Using the first four pointings from the JWST Cosmic Evolution Early Release Science Survey (CEERS) and the initial public observations for the Public Release Imaging for Extragalactic Research (PRIMER), I extend the studies of the bar fraction in disc galaxies to redshifts $1 \leq z \leq 3$, i.e., for the first time beyond redshift two. I only use galaxies that are also present in the Cosmic Assembly Near-IR Deep Extragalactic Legacy Survey (CANDELS) on the Extended Groth Strip (EGS) and Ultra Deep Survey (UDS) HST observations. An optimised sample of 368 close-to-face-on galaxies is visually classified to find the fraction of bars in disc galaxies in two redshift bins: $1 \leq z \leq 2$ and $2 < z \leq 3$. The bar fraction decreases from $\approx 17.8^{+5.1}_{-4.8}$ per cent to $\approx 13.8^{+6.5}_{-5.8}$ per cent (from the lower to the higher redshift bin), but is about twice the bar fraction found using bluer HST filters. These results show that bar-driven evolution may have begun at early cosmic times and that dynamically settled discs are already present at a lookback time of $\sim$ 11 Gyrs.

2.1 Introduction

Barred galaxies are frequent in the local Universe, as discussed in § 1.2.3. Typically, the bar fraction is traced through cosmic time, defined as the number of barred structures identified in a sample of disc galaxies. The bar fraction decreases from $> 60\%$ in the nearby galaxy population to $\sim 10\%$ at $z = 1$. Whereby, studies could not probe bar fractions beyond $z = 1$ as they were limited by spatial resolution and instrument sensitivity. However, the JWST has enabled investigations of the bar fraction at higher redshifts [e.g., Guo et al., 2023]. Imaging from the NIRCam probes the rest-frame NIR emission of galaxies at redshifts up to $z = 3$ and probes the rest-frame optical at redshifts up to $z = 7$; NIR emission traces the older stellar populations, which dominate bar features and are also less affected by dust extinction and recent star formation. In addition, the primary mirror on JWST is over 2.5 times the diameter of the HST primary mirror, meaning that the sensitivity of JWST is significantly better. The improved sensitivity, along with JWST's longer rest-frame wavelengths, makes elongated bar structures more discernible than in their counterparts in HST images [e.g., Huertas-Company et al., 2023]. For this reason, we can now study the bar-driven evolution of galaxies with JWST by searching for the epoch at which stellar barred structures form in disc galaxies.

In this study, I use the first four NIRCam JWST observations from CEERS to track the evolution of the bar fraction at redshifts $z = 1 - 3$. To this aim, collaborators and I visually classify a mass-complete sample of these high-resolution rest-frame NIR images for barred features in disc galaxies.

This chapter is organised as follows: in § 2.2, I describe the NIRCam image-reduction pipeline and my sample selection. Stellar bar identification techniques and my methodology for visual classifications are discussed in § 2.3. In § 2.4, I present the bar fraction for two redshift bins, $z = 1 - 2$ and $z = 2 - 3$. § 2.5 discusses the implications of my findings on when bar-driven evolution commences, and I summarise my results in § 2.6. Throughout this thesis, I assume the latest Planck flat ΛCDM cosmology with $H_0 = 67.36$, $\Omega_m = 0.3153$, and $\Omega_\Lambda = 0.6847$ [Planck Collaboration et al., 2020].

2.2 The parent sample

To define my sample, I use the initial four public NIRCam JWST observations from the Cosmic Evolution Early Release Science Survey (CEERS; PI: Finkelstein, ID=1345, Finkelstein et al. 2023, CEERS1, CEERS2, CEERS3 and CEERS6) taken in June 2022 that overlap with the Cosmic Assembly Near-IR Deep Extragalactic Legacy Survey (CANDELS; Grogin et al. 2011, Koekemoer et al. 2011) on the Extended Groth Strip field (EGS), as well as the initial public observations for the Public Release Imaging for Extragalactic Research (PRIMER; PI: Dunlop, ID=1837, Dunlop et al. 2021), that overlap with the CANDELS Ultra Deep Survey (UDS) Field observations. Together, the data cover $\sim$ 30 arcmin^2 of an area with CANDELS HST overlap.

2.2.1 Data reduction pipeline

We reprocess all uncalibrated lower-level JWST data products using a modified version of the JWST official pipeline. This is similar to the process used in Adams et al. [2023] and exactly the same reductions as used in Ferreira et al. [2023], which can be summarised as follows: (1) We use version 1.6.2 of the pipeline with the Calibration Reference Data System (CRDS) version 0942 which was the most up-to-date version at the time these data products were generated. Use of CRDS 0942 is essential for zero point issues as discussed in Adams et al. [2023]. (2) We apply the 1/f noise correction derived by Chris Willott on the resulting level 2 data of the JWST pipeline.[1] (3) We extract the sky subtraction step from stage 3 of the pipeline and run it independently on each NIRCam frame, allowing for quicker assessment of the background subtraction performance and fine-tuning. (4) We align calibrated imaging for each individual exposure to GAIA using `tweakreg`, part of the DrizzlePac python package.[2] (5) We pixel-match the final mosaics with the use of `astropy reproject`. The final resolution of the drizzled images is 0.03″pixel^{-1}.

Furthermore, an additional step was added for the PRIMER reductions in step

[1] `https://github.com/chriswillott/jwst`
[2] `https://github.com/spacetelescope/drizzlepac`

(2) above due to the presence of a significant stripping pattern artefact at a 45-degree angle in the NIRCam footprint, resembling the diffraction pattern of a bright star outside the field of view of the camera. This issue was resolved by adapting the 1/f noise algorithm: first, rotate the observations by 45 degrees to align the pattern with one of the axes, then subtract the background for each row using its mean. Finally, the adjusted file is rotated back to its original orientation. This drastically reduces the artefact in the final products, although some remain visible in colour composites because the artefact is non-uniform across different NIRCam filters. Galaxy stamps that present these residual artefacts are flagged during subsequent classification as described in § 2.3.3.

Each of the four June CEERS observations was processed into an individual mosaic, while the PRIMER UDS observations were stacked into a single mosaic due to the large overlap.

2.2.2 Sample selection

To produce a selection with robust photometric redshifts and stellar masses, I use the CANDELS-based catalogues from Duncan et al. [2019], which include observations from HST, Spitzer, and ground-based facilities. These redshifts are robustly calibrated from spectroscopic redshifts, with an average outlier fraction of $\frac{|\Delta z|}{1+z_{spec}} \sim 5\%$ (see Duncan et al. 2019 for details).

From these catalogues, I select all sources within the footprints of the CEERS and PRIMER observations outlined previously. All sources with photometric redshifts and stellar masses that are present in both CANDELS and the new JWST observations are selected. Additionally, no magnitude or signal-to-noise cut is applied to mitigate selection bias arising from differences in sensitivity between HST and JWST, preventing JWST bright galaxies from being excluded when they are faint in HST bands. Then, all overlapping sources between $1 \leq z \leq 3$ are selected, resulting in a parent sample of 5218 galaxies present within the combined area of CEERS+PRIMER and 5445 galaxies in the area of CANDELS EGS and UDS fields, including 3559 galaxies with visual Hubble type classifications from Ferreira et al. [2023] at $z > 1.5$. I note that some galaxies fall between the NIRCam detectors;

therefore, although they are included in the HST sample, they cannot be analysed using JWST data.

For each of the CEERS+PRIMER 5218 galaxies in the sample, we produce 30 mas 128×128 pixel cutouts for the JWST filters, namely F356W and F444W. For the 5445 CANDELS galaxies observed with the HST Wide Field Camera 3 (WFC3) F160W filter, we produce 60 mas 64×64 pixel cutouts covering a consistent angular field of view, enabling us to probe the same galaxies in a relatively similar wavelength regime between the two instruments. In this study, I select the F444W JWST filter and compare these galaxies with those observed with the HST WFC3 F160W filter.

2.3 Bar identification

The random orientation of galaxies complicates observational attempts to measure bar lengths. Stellar bars are distinguishable in near-face-on galaxies and become less well defined in high-inclination galaxies. This study aims to determine the fraction of disc galaxies that harbour a bar in an optimised sample of F444W NIRCam and F160W WFC3 images. For my bar identification process, I use visual inspection of galaxy images and radial profiles of position angle and ellipticity.

2.3.1 Sample optimisation

Given the challenges of identifying bars, as noted above, I removed highly inclined, faint, or poorly resolved galaxies from the sample using an automated process. This optimisation process is intended to remove only galaxies that would be visually classified as ambiguous or unclassifiable. To do so, I fit ellipses to the isophotal contours of all galaxies in the parent sample to extract radial profiles of ε and PA [see, e.g., Aguerri et al., 2009, Barazza et al., 2008, 2009, Gadotti et al., 2007]. Figure 2.1 shows, in the left panel, the ellipse fits superposed on the F444W NIRCam image of the galaxy EGS 23205, and in the right panel, radial profiles of the ε and PA of the fitted ellipses. EGS 23205 is an example of a barred galaxy in this study and is observed relatively face-on.

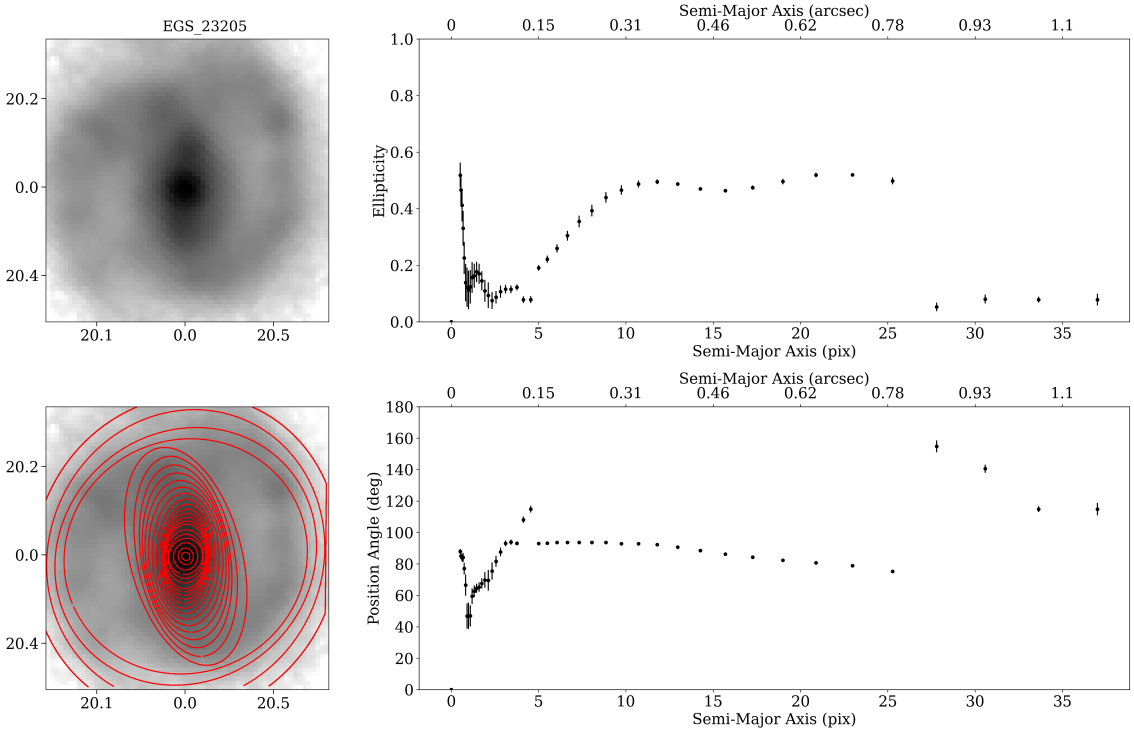

Figure 2.1: Elliptical isophotal fits using the module `photutils.isophote` from Python's astropy package [Bradley et al., 2022] to logarithmic F444W NIRCam images of the galaxy EGS 23205 at redshift $z \sim 2.12$. The left-hand side shows the F444W image, annotated with pixel coordinates (top) and superimposed elliptical isophotal fits (bottom). The right-hand side shows radial profiles of the ellipticity (ε) (upper) and position angle (PA) in degrees (lower) as derived from the ellipse fits.

Before visually classifying galaxies as barred or unbarred, I apply a three-step procedure to obtain my final, optimised galaxy sample containing galaxies in which a bar can be identified robustly: **(1)** ellipse-fitting to NIRCam images without fixing the centre; **(2)** second ellipse-fitting with fixed centres; **(3)** removal of highly inclined galaxies. In the following, I give a detailed explanation of these three steps:

Phase 1 Elliptical isophotes are fitted to F444W NIRCam images of the JWST galaxy sample and analysed using `photutils.isophote` from Python's astropy package [Bradley et al., 2022]. This package uses an iterative method to measure the isophotes [Jedrzejewski, 1987]. The objective in this optimisation phase is to eliminate galaxies that are overly disturbed, extremely poorly resolved, or low-surface-brightness and visually unclassifiable. In general, the algorithm fails to produce any result when applied to these objects. Therefore, at this stage, all galaxies for which successful fits can be obtained are retained, even if the fits do not perfectly align with the galaxy. Approximately 30% of the parent sample had successful ellipse fits in the F444W filter. The remaining $\sim$ 70% of galaxies that failed ellipse fittings are overly disturbed, poorly resolved, and/or low surface brightness systems and were removed from the sample. In addition, in a small number of cases, these were images of point sources that clearly showed the unique JWST point-spread function (PSF) diffraction spikes.

Phase 2 The ellipses fitted in the previous step do not have a specified centre, which may prevent the correct identification of highly inclined galaxies. I thus first fit the inner 10%−40% of the isophotes to the galaxy, and take the average position of the centre of these isophotes as the galaxy centre. The choice for this range of radii ensures that one has enough pixels to compute a statistically robust position of the galaxy centre and simultaneously avoids strongly asymmetric structures, which are often at larger radii. By using isophotes up to 40% of the fitted outer radius, I minimise the effect of a bright, near-central point source on shifting the centre of isophotal fits from the correct galaxy centre. Visually inspecting the fits, I do not see this as a significant issue. It

is also important to note that a bright point source overlapping the galaxy will often render the galaxy visually unclassifiable, thereby removing it from the Phase 1 sample. In addition, a function assesses pixel values within a 10×10 pixel window centred on the new galaxy's central pixel coordinates to ensure that bright foreground stars do not influence the determination of the galactic centre. To improve convergence stability against non-elliptical structures, including stars, `photutils.isophote` clears aberrant points from each isophote with a k-sigma algorithm. I then rerun `photutils.isophote` on F444W NIRCam galaxy images with the specified central positions fixed. With fixed centres, the ellipse fits failed for approximately 26% of the newly optimised sample. I verified that the failed ellipse fits correspond to galaxies with overly irregular or ambiguous morphology. These systems are also removed from the sample. I use the default scheme developed by Jedrzejewski [1987] to determine when fitting stops. By visually inspecting the fits, I verified that the fits only rarely stop before reaching the outskirts of the galaxy.

Phase 3 An inclination limit of $i \leq 60°$ is applied to remove highly inclined galaxies, as it is difficult to identify if a bar is present in these cases. I define the inclination of a galaxy by measuring the ellipticity of the outermost fitted ellipse,

$$\varepsilon = 1 - \frac{b}{a}, \tag{2.1}$$

where b is the semi-minor axis length and a is the semi-major axis length. The inclination is defined as

$$\cos i = \frac{b}{a}. \tag{2.2}$$

Approximately 34% of the galaxies in the F444W filter of the newly optimised sample were seen to be too highly inclined and were removed from the sample. While highly inclined, disturbed, and edge-on galaxies have been removed in this and previous phases of the optimisation, I note that a residual fraction of regular disc galaxies with inclinations greater than 60° still entered the optimised sample despite this final optimisation step, which means my final bar fractions could be slightly underestimated (although, in some cases, a bar

Phase	HST		JWST	
	N_{gal} removed	N_{gal} remain	N_{gal} removed	N_{gal} remain
1	4980	465	3635	1583
2	230	235	416	1167
3	102	133	399	768

Table 2.1: Number of galaxies removed from the sample and the resultant sample size after each optimisation phase. Col. 1: the optimisation phase. Col. 2 and Col. 3 are in the context of HST CANDELS F160W images. Col. 2: the number of galaxies which failed to meet the phase criteria. Col. 3: the sample size after the criteria are applied, with phase 1 being applied to the parent sample. Col. 4 and Col. 5 are the same as Col. 2 and Col. 3, but in the context of JWST CEERS F444W images.

could be seen despite the high inclination). I speculate that a combination of relatively poor spatial resolution and lower outer-surface brightness than that of local galaxies is responsible for the residual highly inclined galaxies remaining in the optimised sample.

I applied this three-step optimisation procedure to my initial large CEERS F444W galaxy sample, ensuring that elliptical isophotes could be fitted to the galaxy image, that an identified galactic centre was present, and that the galaxy was not edge-on. The resultant optimised sample of galaxies suitable for my analysis is 768 CEERS images in the NIRCam F444W filter (hereafter referred to as the optimised JWST sample). Of the optimised galaxy sample, 404 galaxies are between the redshifts $1 \leq z \leq 2$, and 364 galaxies are between the redshifts $2 < z \leq 3$. Before visual classifications, a collaborator (DG) visually verified that all removed objects were indeed poorly resolved, overly faint/irregular, or too inclined. Table 2.1 gives the number of galaxies removed at each phase and the resultant galaxy sample size.

To measure the difference in the bar fraction between JWST and HST, I also applied the three-step optimisation procedure in my HST CANDELS F160W galaxy sample. This reduced my HST CANDELS sample to an optimised sample of 133 galaxies (hereafter referred to as the optimised HST sample). The reduced sensitivity and bluer wavelength range of HST mean that many galaxies appear highly pixelated, making features difficult to discern. Therefore, the ellipse-fitting technique failed for many of these galaxies, greatly reducing the optimised HST sample

size.

2.3.2 Disc identification

Naturally, the bar fraction is the number of barred galaxies divided by the number of disc galaxies, and I therefore need first to compute the latter. The variations in morphology and orientation dependence make disc galaxies challenging to identify visually. Given the different wavelength ranges probed by JWST and HST, I compute the disc fraction in my parent samples to avoid potential bias from my optimisation procedure on the number of disc galaxies, and then extrapolate it to the optimised sample. This is also important because the optimised sample is significantly smaller than the parent sample, and uncertainties thus increase. I obtain the JWST disc fraction from the published visual classifications in Ferreira et al. [2023]. In their study, six independent participants visually classified 3559 CEERS sources in their rest-frame NIR images using the NIRCam filters F277W, F356W, and F444W over the redshift range $z = 1.5 - 3.0$, which contained 1531 discs. The disc fraction found in Ferreira et al. [2023] does not extend to the lower end of the redshift range selected for this thesis. Thus, I assume that the disc fraction between redshifts 1 and 1.5 is the same as between redshifts 1.5 and 2. For the redshift bins $1 \leq z \leq 2$ and $2 < z \leq 3$, the disc fraction of the optimised JWST sample is thus $f_{disc} = 0.49 \pm 0.039$ and $f_{disc} = 0.39 \pm 0.046$, respectively. The systematic error on f_{disc} is the standard error of f_{disc} found by the six participants in Ferreira et al. [2023]. By extrapolating f_{disc} to the optimised JWST sample, the number of disc galaxies $count_{disc} = 196$ and 143 for $1 \leq z \leq 2$ and $2 < z \leq 3$, respectively.

For the HST sample, I use the visual classifications by Kartaltepe et al. [2015] to determine the optimised HST f_{disc}. For the redshift bins $1 \leq z \leq 2$ and $2 < z \leq 3$, the disc fraction of the HST parent sample is $f_{disc} = 0.75$ and $f_{disc} = 0.78$, respectively. It is important to point out that the detailed classification of Kartaltepe et al. [2015] includes disc galaxies in the category 'irregular', which is also further subdivided in categories such as 'spheroid and irregular' to separate disc galaxies that are irregular from both disc galaxies with regular morphology and spheroidal galaxies that are irregular. I thus include in f_{disc} a smaller fraction of galaxies ($\sim 15\%$) noted

as irregulars (but after removing those noted as 'spheroid and irregular') following the classifications of Kartaltepe et al. [2015], strictly. It is important to include these galaxies in f_{disc} because these are disc galaxies despite their disturbed morphology, and their discs can develop bars. The Large Magellanic Cloud is a notable example of an irregular galaxy with a disc that hosts a bar. Furthermore, Kartaltepe et al. [2015] showed that the Sérsic index and colour distributions of their irregularly classified galaxies match those of galaxies classified as discs. And, indeed, some of the barred galaxies I find were classified as irregulars in Kartaltepe et al. [2015, see my Table 2.2]. The systematic error on f_{disc} is the standard error of $f_{disc} = \pm 0.026$ found by comparing the results from the three classifiers in Kartaltepe et al. [2015]. By extrapolating f_{disc} to the optimised HST sample, $count_{disc} = 81$ and 19 for $1 \leq z \leq 2$ and $2 < z \leq 3$, respectively. I note that the HST disc fraction may be a lower limit since Nelson et al. [2023], using JWST, found that massive, dusty edge-on discs could have been missed as HST-dark galaxies. This would lead to an overestimation of the bar fraction using HST data.

Additionally, I visually classified the optimised JWST sample to study the stellar mass distributions of barred and unbarred galaxies in it, as discussed further below. I classified the galaxy as disc-like or non-disc-like based on the F444W NIRCam images and a log-intensity radial profile. In principle, artefacts (discussed in § 2.2.1) could mislead visual classifications, but these PSF effects are clearly distinguishable. The diffraction spikes mostly appeared as a large hexagon over the galaxy image, indicating that the galaxy is not elongated in any particular direction. Therefore, we typically class these as non-discs/unidentifiable. To ensure we were not affected by less prominent artefacts, we checked for effects in the intensity radial profile of each galaxy. Figure 2.2 shows three examples of disc and three non-disc galaxies in rest-frame JWST NIRCam F444W and HST WFC3 F160W filters. Non-disc galaxies can include strong PSF-affected sources, as shown by the central source in the figure. In this classification, the average disc fraction of the optimised JWST sample is $f_{disc} = 0.40 \pm 0.14$ for the full redshift range $1 \leq z \leq 3$ (the quoted uncertainty is the difference in f_{disc} found by a collaborator and me). The disc fraction derived in this study thus agrees with that found by Ferreira et al. [2023],

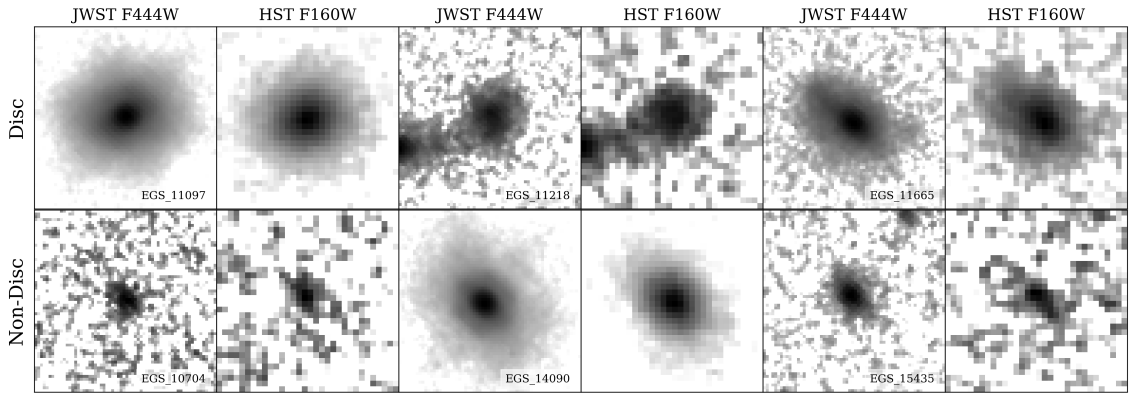

Figure 2.2: Images of three disc (upper) and three non-disc (lower) galaxies. The three exemplars for each classification, with IDs in the lower-right corner of the NIRCam F444W image, are shown in the JWST NIRCam F444W (left) and HST WFC3 F160W (right) images.

which is 0.45 ± 0.034 when I employ their classifications and consider my optimised sample at $1.5 \leq z \leq 3$.

2.3.3 Bar visual classifications

The optimised JWST sample was then visually classified by five collaborators, including myself (ZLC, DG, CdSF, TK and JN). Participants were asked to vote *barred, maybe-barred*, or *unbarred* for the F444W NIRCam images. The votes were tallied, and a galaxy was classified as follows: a galaxy is classified as strongly barred if it obtained at least three out of five votes for barred; a galaxy is classified as weakly barred if it obtained two out of five votes for barred or at least three out of five votes for maybe-barred; a galaxy is classified as unbarred if it did not obtain the vote thresholds. Figure 2.3 is a histogram of the number of barred and maybe-barred votes the participants gave on each galaxy in the optimised JWST sample. The figure does not show the galaxies on which the participants unanimously agreed were unbarred. The figure illustrates the difficulties in identifying bars: 75% of the galaxies shown here fall below the vote threshold and are therefore classified as unbarred.

The visual classification method was then repeated for the optimised JWST sample in the NIRCam F356W filter. The resolution marginally improves at this shorter wavelength, thereby improving the definition of structural features. However,

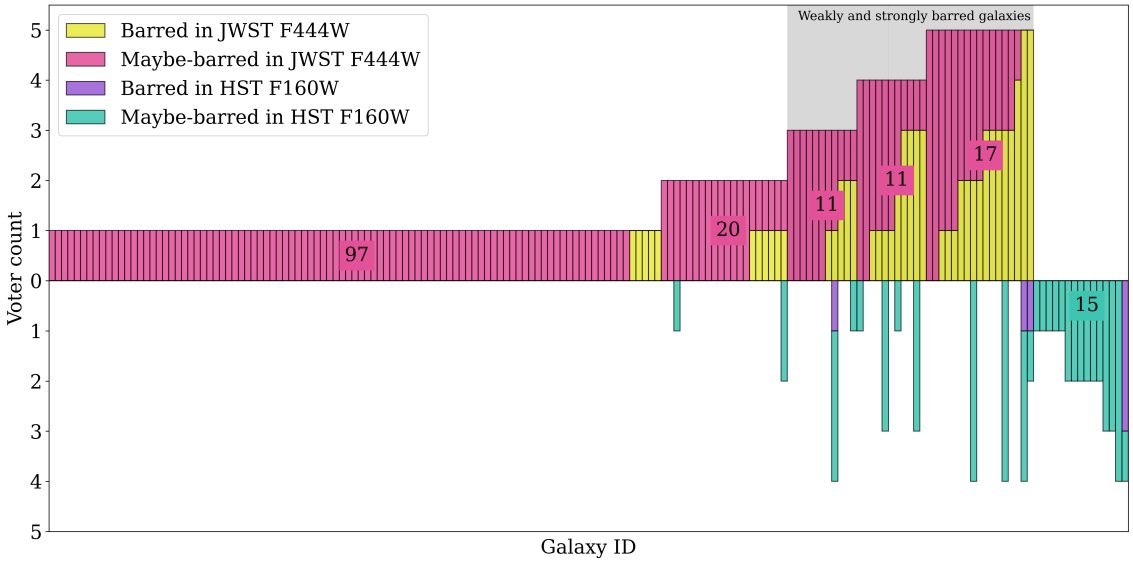

Figure 2.3: Distribution of the total number of barred in yellow (purple) and maybe-barred in pink (green) votes cast by the five participating collaborators to candidate galaxies in the optimised JWST (HST) sample. 171 galaxies received barred or maybe-barred votes in the NIRCam F444W filter, or WFC3 F160W filter from the classifiers, and 597 galaxies received zero votes. The number of galaxies in each voter count category is shown. A grey-shaded area covers galaxies classified as weakly or strongly barred. I exclude galaxies that received zero barred or maybe barred votes from this figure.

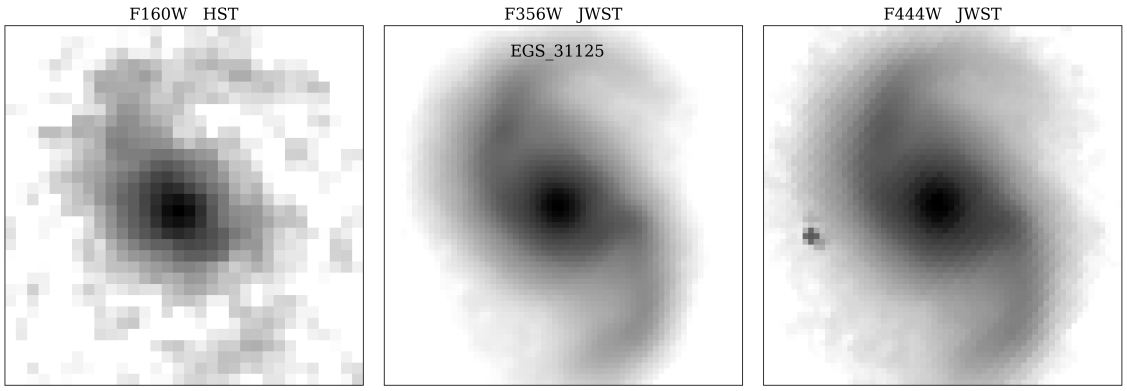

Figure 2.4: The image of galaxy EGS 31125 at redshift $z \simeq 2.06$, visually classified as strongly barred from the JWST NIRCam F444W image, shown in an HST filter and two JWST filters. From left to right: HST WFC3 F160W and JWST NIRCam F356W and F444W. This filter comparison demonstrates how PSF, sensitivity, and wavelength range affect a galaxy image, particularly in the context of bars. The image shows EGS 31125 in rest frame 0.52, 1.16, and 1.45 μm, respectively.

this wavelength is more susceptible to dust extinction and star-formation effects, so the bar-dominated evolved stellar populations may be only moderately traced. The overall bar fraction did not change between the two NIRCam filters, but a few weaker bars became stronger when observed through the F356W filter. Finally, the visual classification method was reapplied to the optimised HST sample. EGS 31125 is shown in Figure 2.4 in the three different filters employed: HST WFC3 F160W, JWST NIRCam F356W, and F444W. EGS 31125 is classified in the F444W filter as strongly barred and unbarred in the F160W filter. This figure clearly shows the impact of improved sensitivity and longer wavelength with JWST on the galaxy at redshift $z \simeq 2.06$ and how distinctive the disc structures become [see also Guo et al., 2023].

On the other hand, 15 galaxies in the HST sample were classified as barred but received no votes when classified using the JWST data. These images were re-inspected, and while these galaxies could indeed be barred, I note that in some cases, JWST PSF effects affect the classification. In other instances, details in the structure of the galaxy are better discerned in the JWST images, rendering the impression of a bar somewhat uncertain. I show examples of these galaxies in Figure 2.5. The figure shows three galaxies in the HST WFC3 F160W filter and two JWST NIRCam filters, F356W and F444W. These galaxies are interesting because

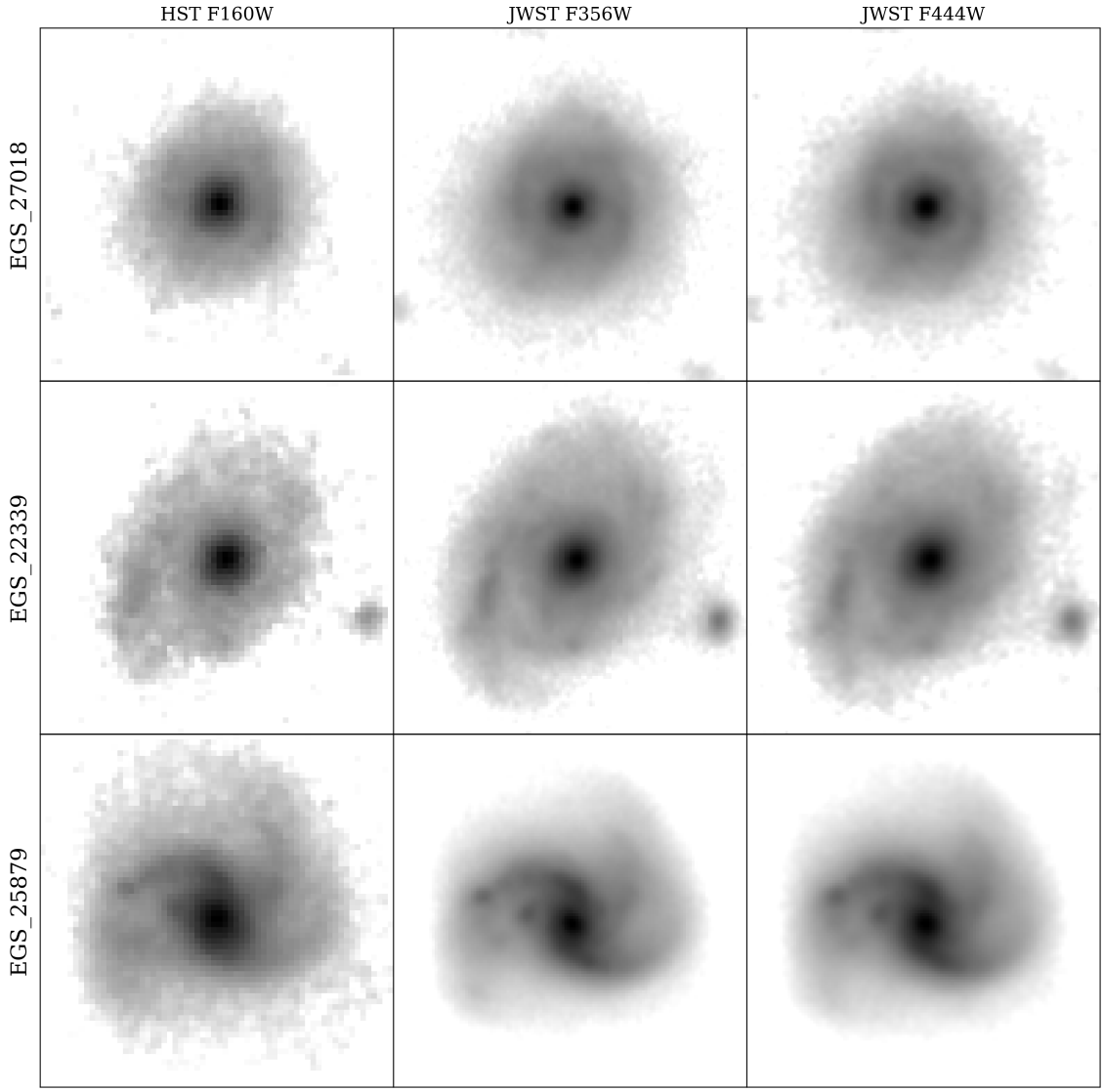

Figure 2.5: Images of the galaxies EGS 27018, EGS 22339 and EGS 25879, which received maybe-barred or barred votes by the classifiers in the HST WFC3 F160W filter, but unbarred votes in the JWST NIRCam F444W filter. The three galaxies are shown in the HST WFC3 F160W (left), JWST NIRCam F356W (middle) and JWST NIRCam F444W (right).

they received a maybe-barred or barred vote in visual classifications of HST WFC3 F160W, but an unbarred vote from all classifiers in JWST NIRCam F444W. A PSF artefact (as described in § 2.2.1) can be identified in the JWST NIRCam images of EGS 27018 but becomes inconspicuous in the HST WFC3 image. EGS 22339 is a disc galaxy with spiral features, which could have misled visual classifications in the HST WFC3 image, but is clearly unbarred in JWST NIRCam images. The only galaxy to receive barred votes in the HST WFC3 filter and unbarred votes in JWST NIRCam filters is EGS 25879, which is due to the blurring of prominent spiral arms in the F160W filter.

2.4 The bar fraction

I aim to determine the fraction of disc galaxies at redshifts $z = 1 - 3$ that host a bar. We visually classified the optimised JWST sample, which met the criteria described in § 2.3.1. The process is repeated for the optimised HST sample to determine whether an increase in the bar fraction is observed with JWST. Galaxies were classified as described in § 2.3.3. Figure 2.6 shows three examples of strongly barred, weakly barred and unbarred galaxies in the JWST NIRCam F444W and HST WFC3 F160W filters. The strongly barred galaxies have distinct stellar structures, while some weakly barred galaxies have less prominent outer discs.

The bar fraction is found for two redshift bins, $1 \leq z \leq 2$ and $2 < z \leq 3$, to observe the evolution of the bar fraction. The redshift was only divided into two bins, as the number of barred galaxies is relatively small. In the optimised JWST sample, 29 galaxies were identified as barred in the lower redshift bin, where eight are strongly barred, and 21 are weakly barred, which decreased to ten barred galaxies in the higher redshift bin, where five are strongly barred, and five are weakly barred. All galaxies classified as barred are shown in the figures 2.7 and 2.8. Figure 2.7 shows the strongly barred galaxies, and Figure 2.8 shows the weakly barred galaxies. The 39 barred galaxies are listed in Table 2.2, along with their photometric redshift and HST visual classifications from Kartaltepe et al. [2015], of which only one galaxy was identified as barred. In the optimised HST sample, nine galaxies were identified

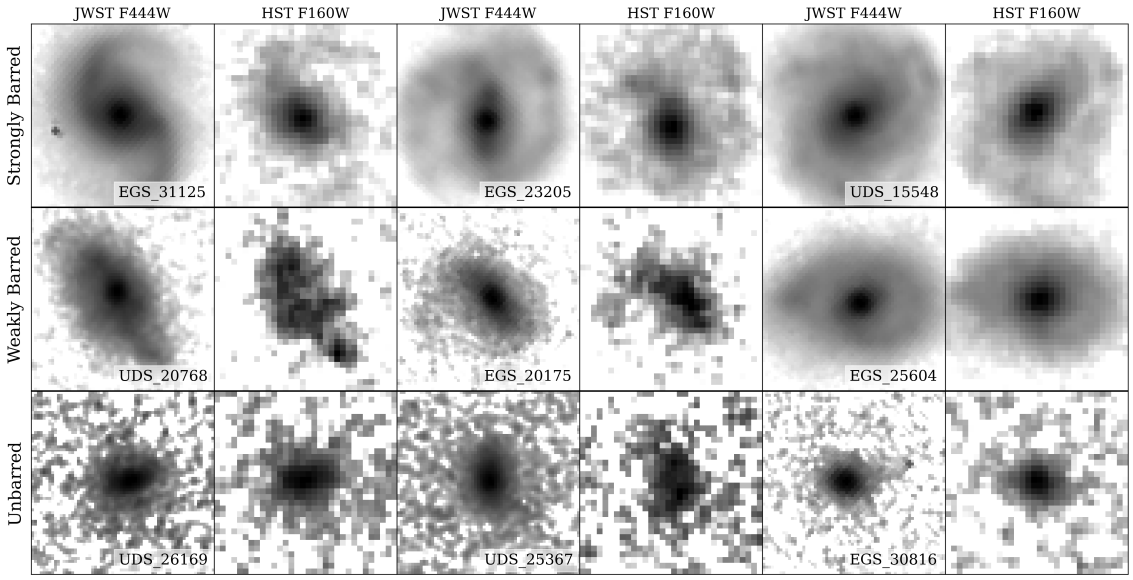

Figure 2.6: Images of three strongly barred (top row), weakly barred (middle row) and unbarred (bottom row) galaxies. The three exemplars for each classification, with IDs in the lower-right corner of the NIRCam F444W image, are shown in the JWST NIRCam F444W (left) and HST WFC3 F160W (right) images.

as weakly or strongly barred in the lower redshift bin, and only one weakly barred galaxy was identified in the higher redshift bin.

It is debated how the bar fraction depends on the stellar mass [e.g., Barazza et al., 2008, Erwin, 2018, Gavazzi et al., 2015, Masters et al., 2011, Melvin et al., 2014, Nair and Abraham, 2010, Sheth et al., 2008]. In Figure 2.9, I show the stellar mass distribution as a function of redshift for all disc galaxies in the optimised sample. The disc galaxies are taken from the disc classification procedure. Still, I verified that qualitatively similar results are found regardless of the classifier. The 95% empirical completeness limit of the sample, as estimated in Duncan et al. [2019], is shown, indicating that most of my sample lies above or near this limit. Interestingly, this figure shows that barred galaxies tend to avoid the least massive galaxies at each redshift, consistent with the results of Sheth et al. [2008]. To calculate the bar fraction in a sample as complete in mass as possible, I use the 95% completeness step function as a mass limit, i.e., I select galaxies above the 95% completeness line. This includes a new computation of the disc fractions as above, but now only for galaxies above the 95% completeness line, which slightly increases the disc fractions for both HST and JWST.

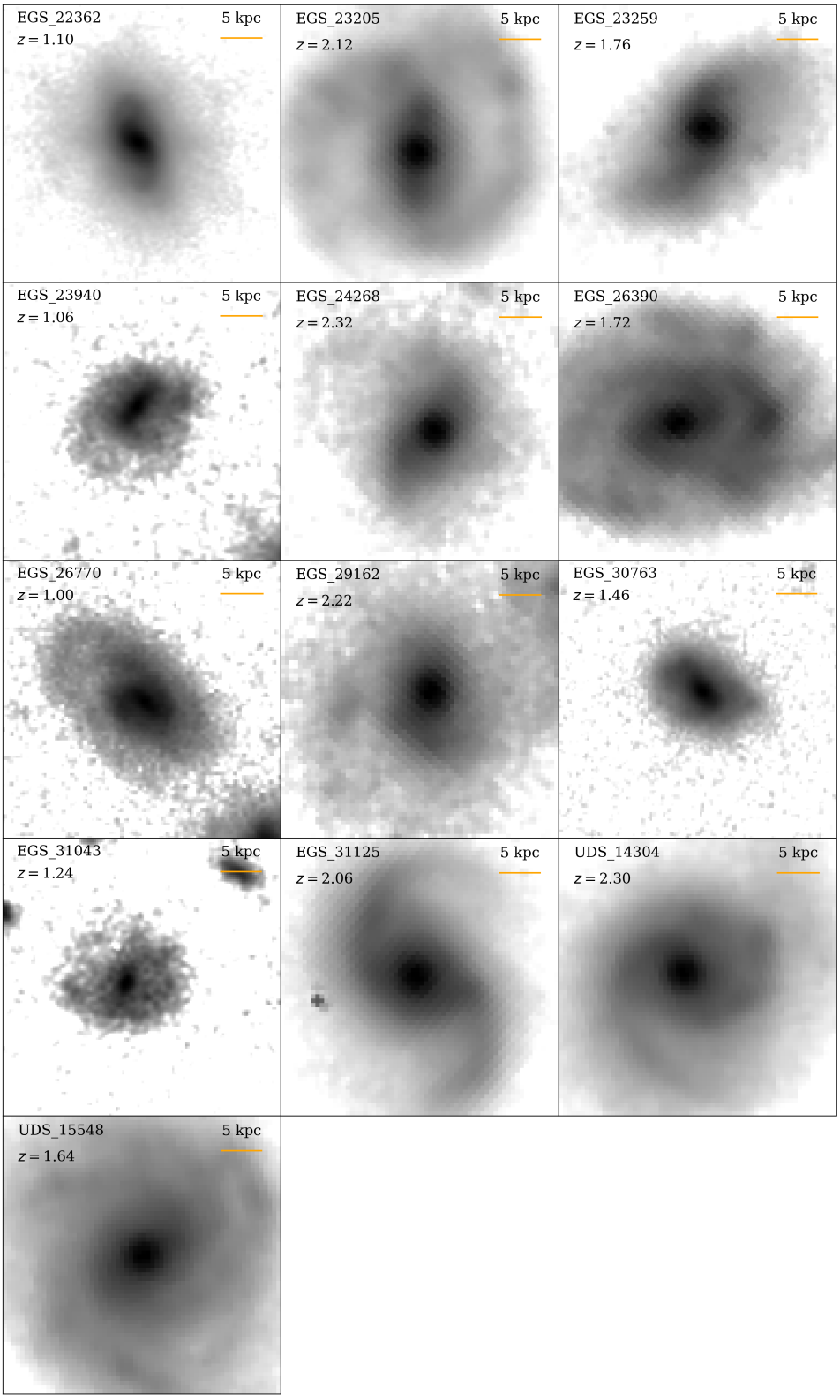

Figure 2.7: Images of strongly barred galaxies using the JWST NIRCam F444W filter between the redshifts $1 \leq z \leq 3$. The redshift of the galaxy is noted in the upper left corner of each image. A 5 kpc scale is shown in the upper-right corner of each image.

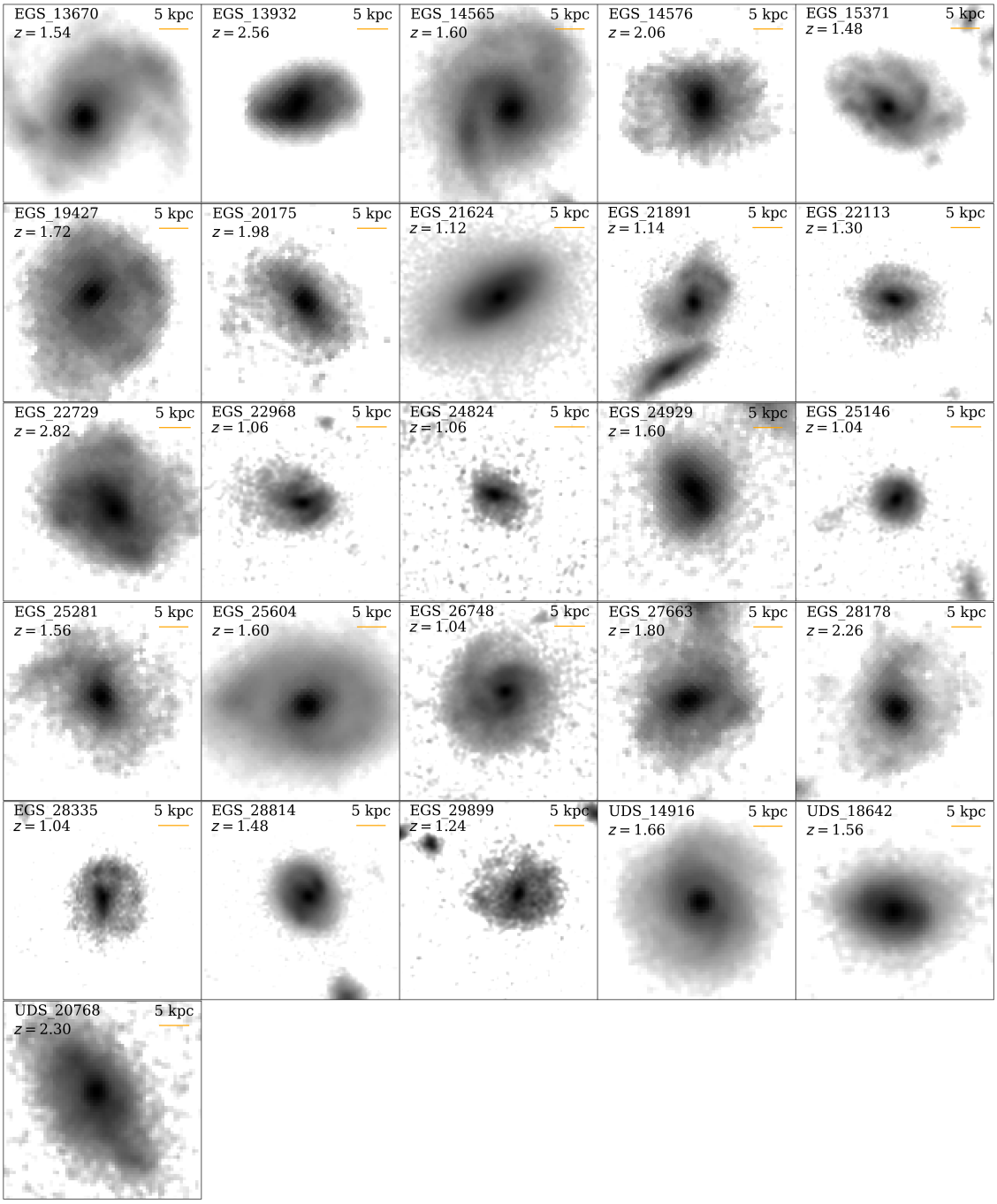

Figure 2.8: Images of weakly barred galaxies using the JWST NIRCam F444W filter between the redshifts $1 \leq z \leq 3$. The redshift of the galaxy is noted in the upper left corner of each image. A 5 kpc scale is shown in the upper-right corner of each image .

Galaxy ID	z	$\log_{10}(M_\star/M_\odot)$	Bar	Class
EGS 13670	1.54	10.63	Weak	Face-on barred disc with spiral arms
EGS 13932	2.56	10.61	Weak	Disc
EGS 14565	1.60	10.24	Weak	Barred disc dominated with spiral arms
EGS 14576	2.06	9.53	Weak	Disc
EGS 15371	1.48	10.67	Weak	Asymmetric disc
EGS 19427	1.72	9.95	Weak	Disc with non-interacting companion
EGS 20175	1.98	9.36	Weak	Disc
EGS 21624	1.12	10.65	Weak	Disc dominated spheroid
EGS 21891	1.14	9.73	Weak	Interacting disc with spiral arms
EGS 22113	1.30	9.75	Weak	Disc
EGS 22362	1.10	10.71	Strong	Spheroidal disc
EGS 22729	2.82	10.23	Weak	Irregular asymmetric disc
EGS 22968	1.06	9.11	Weak	Disc with spiral arms
EGS 23205	2.12	11.20	Strong	Disc
EGS 23259	1.76	10.47	Strong	Interacting asymmetric irregular disc
EGS 23940	1.06	9.70	Strong	Disc with spiral arms and non-interacting companion
EGS 24268	2.32	10.20	Strong	Asymmetric irregular
EGS 24824	1.06	9.03	Weak	Disc
EGS 24929	1.60	9.48	Weak	Asymmetric irregular with non-interacting companion
EGS 25146	1.04	9.27	Weak	Disc with non-interacting companion
EGS 25281	1.56	9.33	Weak	Face-on disc dominated spheroid
EGS 25604	1.60	10.89	Weak	Face-on spheroidal disc
EGS 26390	1.72	10.69	Strong	Face-on asymmetric disc
EGS 26748	1.04	10.08	Weak	Face-on disc
EGS 26770	1.00	9.74	Strong	Interacting face-on disc
EGS 27663	1.80	9.88	Weak	Face-on disc with non-interacting companion
EGS 28178	2.26	10.03	Weak	Face-on asymmetric disc dominated irregular
EGS 28335	1.04	9.33	Weak	Disc with spiral arms
EGS 28814	1.48	10.16	Weak	Asymmetric irregular disc
EGS 29162	2.22	10.04	Strong	Interacting asymmetric irregular
EGS 29899	1.24	8.96	Weak	No classification found
EGS 30763	1.46	10.11	Strong	Asymmetric irregular
EGS 31043	1.24	9.14	Strong	Face-on disc with non-interacting companion
EGS 31125	2.06	11.30	Strong	Face-on disc with spiral arms
UDS 14304	2.30	11.43	Strong	Interacting spheroidal point source
UDS 14916	1.66	10.59	Weak	Face-on disc dominated spheroid
UDS 15548	1.64	11.18	Strong	Edge-on disc with non-interacting companion
UDS 18642	1.56	10.40	Weak	Asymmetric disc
UDS 20768	2.30	10.07	Weak	Disc

Table 2.2: The 39 visually classified strongly and weakly barred galaxies. Col. (1): The ID number is from the original SExtractor catalogue based on the full EGS and UDS mosaic. Col. (2): CANDELS-based catalogue photometric redshifts [Duncan et al., 2019]. Col. (3): CANDELS-based catalogue stellar masses [Duncan et al., 2019]. Col. (4): The classification of bar strength determined from JWST NIRCam images. Col. (5): HST visual classifications from Kartaltepe et al. [2015].

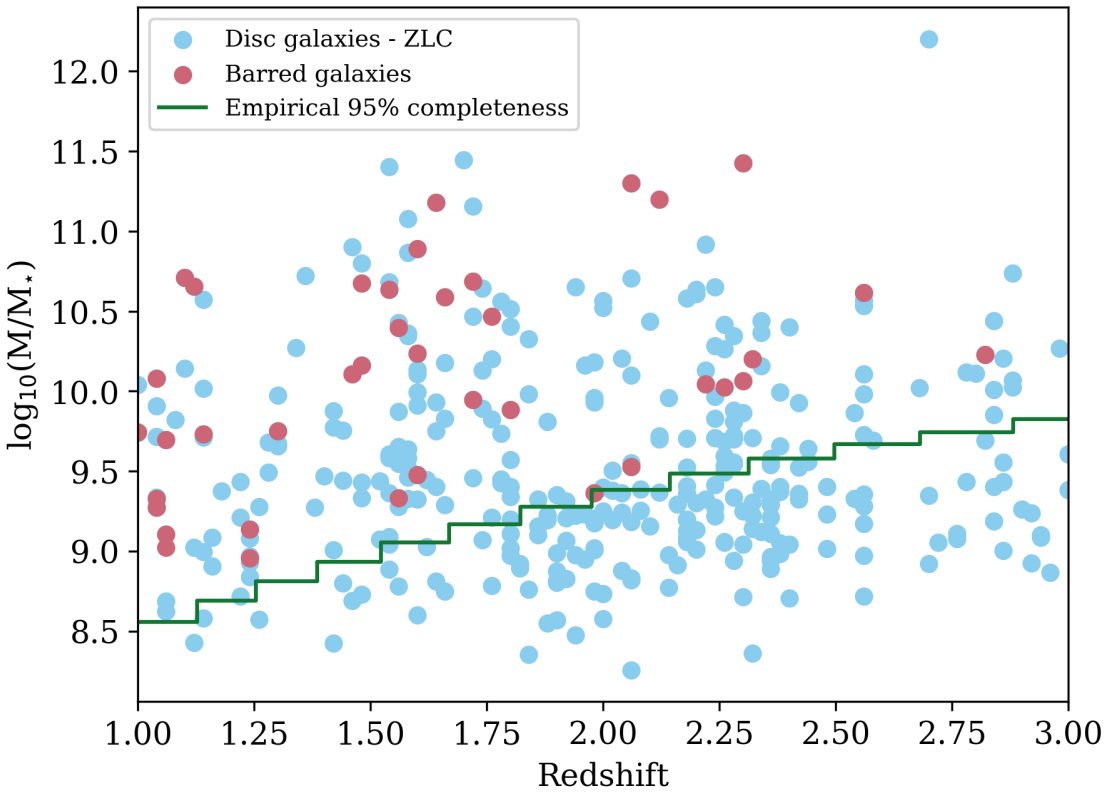

Figure 2.9: Distribution of stellar masses for the sample of disc galaxies as classified by ZLC in JWST CEERS between the redshifts $1 \leq z \leq 3$. Disc galaxies are shown in blue, while the weakly and strongly barred galaxies are in pink. A green step-wise line shows the 95% empirical completeness of the sample [see Figure 8 of Duncan et al., 2019]. The parameter space below this line in this plot corresponds to a completeness fraction of $\approx 85 - 90\%$.

For the redshift ranges $1 \leq z \leq 2$ and $2 < z \leq 3$ the JWST bar fraction is $\approx 17.8^{+5.1}_{-4.8}$ per cent and $\approx 13.8^{+6.5}_{-5.8}$ per cent, and the HST bar fraction is $\approx 11.2^{+4.7}_{-3.8}$ per cent and $\approx 6.0^{+8.4}_{-3.7}$ per cent, respectively. The uncertainties on these bar fractions are the sum in quadrature of the systematic and statistical errors, which are discussed below. For a 95% complete stellar mass sample, the fraction of bars found in disc galaxies in JWST is approximately twice that in HST. Table 2.3 shows the progression of the JWST and HST galaxy sample sizes after the different selection and classification criteria are applied.

Sample Sizes						
Sample	Redshift	$N_{gal,HST}$	$N_{gal,JWST}$	$N_{gal,HST}$ Mass Complete	$N_{gal,JWST}$ Mass Complete	Criteria applied
Parent sample	$1 \leq z \leq 3$	5445	5218	1299	1180	Redshift
Optimised sample	$1 \leq z \leq 3$	133	768	126	368	ellipse fitting, $i \leq 60°$
	$1 \leq z \leq 2$	108	404	105	237	
	$2 < z \leq 3$	25	364	21	131	
Disc sample	$1 \leq z \leq 3$	100	339	98	229	HST discs from Kartaltepe et al. [2015] and JWST discs from Ferreira et al. [2023]
	$1 \leq z \leq 2$	81	196	81	157	
	$2 < z \leq 3$	19	143	17	72	
Weakly Barred	$1 \leq z \leq 3$	9	26	9	25	Visually classified bars
	$1 \leq z \leq 2$	8	21	8	20	
	$2 < z \leq 3$	1	5	1	5	
Strongly Barred	$1 \leq z \leq 3$	1	13	1	13	Visually classified bars
	$1 \leq z \leq 2$	1	8	1	8	
	$2 < z \leq 3$	0	5	0	5	
The Bar Fraction						
Bar Fraction	$1 \leq z \leq 2$	$0.11^{+0.05}_{-0.04}$	$0.15^{+0.05}_{-0.05}$	$0.11^{+0.05}_{-0.04}$	$0.18^{+0.05}_{-0.05}$	$\frac{N_{weakly\_barred}+N_{strongly\_barred}}{N_{disc}}$
	$2 < z \leq 3$	$0.05^{+0.08}_{-0.04}$	$0.07^{+0.07}_{-0.06}$	$0.06^{+0.08}_{-0.04}$	$0.14^{+0.07}_{-0.06}$	

Table 2.3: Sample sizes after selection and classification criteria are applied. Col. (1): the sample label. Col. (2): the redshift range. Col. (3): the number of galaxies after applying the criteria to HST CANDELS F160W images. Col. (4): the number of galaxies after applying the criteria to JWST CEERS F444W images. Col. (5) and (6): the same as col. (3) and (4) but with the 95% mass completeness cut applied to the sample from Duncan et al. [2019]. Col. (7): the criteria applied. The bar fractions derived before and after applying the 95% mass completeness limit are given for the two redshift bins at the bottom of the table. The bar fraction errors are explained in § 2.4.

Figure 2.10 shows the visually classified bar fraction versus redshift and lookback time in the context of other observational work assessing bar fractions using HST. The figure shows that previous results based on HST data indicate a decline in the bar fraction from lower to higher redshifts. While the JWST bar fraction also decreases from the redshift bin $1 \leq z \leq 2$ to the redshift bin $2 < z \leq 3$, the JWST bar fraction in the lower redshift bin is greater than the HST bar fraction in the same redshift bin. A dashed line indicates the redshift range of my visually identified barred galaxies, and a thick solid line indicates the distribution quartiles, i.e. 25%-75%. I identify the highest redshift strongly barred galaxy as EGS 24268 at $z \simeq 2.32$ [also found in Guo et al., 2023] and the highest redshift weakly barred galaxy as EGS 22729 at $z \simeq 2.82$.

The Jeffreys interval [Brown et al., 2001, Gelman et al., 2003] is used to determine the statistical uncertainty in the computed bar fractions. Considering the fraction of a large population with a given attribute (i.e., bars) and neither close to 0 nor 1, the Normal approximation can be assumed to derive uncertainties, but for small sample sizes and extreme population proportion values (e.g., the HST bar fraction at $2 < z \leq 3$), Cameron [2011] convincingly argued for a beta distribution quantile technique over the 'normal approximation' and the Clopper and Pearson [1934] approach, in which the Jeffreys 'non-informative' prior can be used interchangeably with the uniform prior. I adopt this method to estimate the full 68 per cent confidence intervals of the bar fraction in the two redshift bins. The sample used in this study is mass-complete, meaning that I do not account for incomplete sampling in the uncertainty estimates. On the other hand, the more important systematic errors in my analysis arise from the difficulty of defining a galaxy as disc or barred. The fraction of disc galaxies was taken from Kartaltepe et al. [2015, HST disc fraction] and Ferreira et al. [2023, JWST disc fraction]. The standard error of the mean disc fraction reported by the participants in the two independent studies is interpreted as the main systematic error in the bar fractions. Hence, I sum the systematic and statistical uncertainties in quadrature for the bar fractions to obtain the final uncertainties quoted above. The statistical errors for the lower and higher redshift bins are, respectively, $^{+0.041}_{-0.030}$ and $^{+0.083}_{-0.035}$ for HST, and $^{+0.033}_{-0.028}$ and

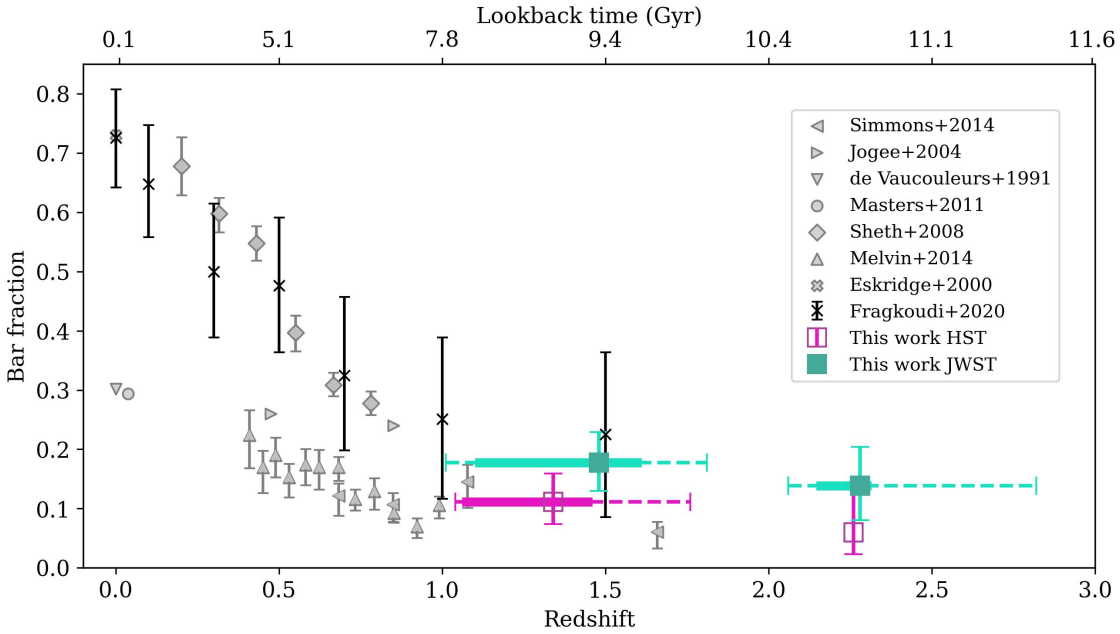

Figure 2.10: Evolution of the fraction of stellar bars in disc galaxies with redshift in the context of other bar assessment work using HST. The fractions of barred disc galaxies found in JWST NIRCam images are shown as green squares, and the fractions of barred disc galaxies found in this study in HST WFC3 images are shown as purple squares. The bar fraction was found for two redshift bins, $1 \leq z \leq 2$ and $2 < z \leq 3$, where the marker indicates the median redshift of the barred galaxies. All of the bar fraction errors in this study indicate the sum in quadrature of the systematic and statistical errors. A dashed line indicates the redshift range of barred galaxies. A thick solid line indicates the redshift range of the quartiles 25%-75% of the barred galaxies distribution. At low redshifts, de Vaucouleurs et al. [1991, down-pointing triangle] and Masters et al. [2011, circle] found strong bars in a third of disc galaxies, while Eskridge et al. [2000, cross] found strong and weak bars in over two-thirds of disc galaxies. Simmons et al. [2014, left-pointing triangles], Sheth et al. [2008, diamonds] and Melvin et al. [2014, up-pointing triangles] found a decreasing trend of the bar fraction for higher redshifts. Jogee et al. [2004, right-pointing triangles] found a minimal decline in the bar fraction at higher redshifts. Finally, the bar fractions, as found in the Auriga cosmological simulations in Fragkoudi et al. [2020, x] are shown in black.

$^{+0.046}_{-0.035}$ for JWST. The systematic errors for the lower and higher redshift bins are, respectively, ± 0.023 and ± 0.011 for HST, and ± 0.039 and ± 0.046 for JWST.

2.5 Discussion

Using NIRCam F444W images, corresponding to NIR rest-frame wavelengths at $1 \leq z \leq 3$, the visually identified fraction of disc galaxies hosting a bar at redshifts $z = 1 - 2$ is ~ 18 per cent, which decreases to ~ 14 per cent at redshifts $z = 2 - 3$. I found the bar fraction obtained from the F444W JWST images to be greater than that obtained using F160W HST images by a factor of about two, as shown in Figure 2.10. The value of the bar fraction at $z = 1 - 2$, derived from HST images, is consistent with the estimate from Simmons et al. [2014, see their Fig. 6] who also use HST data. This raises the question: why do I find more bars in JWST images than in HST images? Considering that the parent sample was chosen to contain sources present in both HST CANDELS and JWST CEERS and that the same bar-detection method was applied to both the JWST F444W and HST F160W images, the considerable difference between the JWST and HST bar fractions at each redshift bin implies that the identification of bars in disc galaxies is dependent on the sensitivity and wavelength range of the instrument; the bar fraction increases at longer wavelengths and with improved sensitivity. Defining the resolution of an instrument as the full-width half maximum (FWHM) of the empirical PSF, the resolution of HST at 1.6 μm is $0.151''$[3] and the resolution of JWST at 4.44 μm is $0.145''$[4], and therefore, both instrumental setups have very similar resolution. Hence, spatial resolution is not a factor here.

Interestingly, the HST bar fractions at the two redshift bins do not change significantly after applying the 95% mass completeness limit, whereas the JWST bar fraction at $2 < z \leq 3$ increases substantially (although within the error bars). This may reflect JWST's ability to detect more low-mass discs at high redshifts than

[3]PSF FWHM taken from the HST user documentation: `https://hst-docs.stsci.edu/wfc3ihb/chapter-7-ir-imaging-with-wfc3/7-6-ir-optical-performance`

[4]PSF FWHM taken from the JWST user documentation: `https://jwst-docs.stsci.edu/jwst-near-infrared-camera/nircam-performance/nircam-point-spread-functions`

HST, but it still does not enable the detection of the presumably shorter bars in low-mass discs, since the spatial resolutions of the HST and JWST images used in this work are comparable.

These results build on previous studies that find that bar-driven internal evolutionary processes in settled disc populations begin at $z \simeq 1$, whereas my new results suggest this occurs at $z \simeq 2$ or later. This study finds that a sizable population of barred galaxies exists at $z \leq 3$, implying that massive disc galaxies can become dynamically settled with prominent bars at a lookback time of ~ 11 Gyrs. The idea that bar-driven galaxy evolution happens in some cases at $z > 2$ is generally consistent with the early bar formation epochs estimated for local galaxies in the Time Inference with MUSE in Extragalactic Rings (TIMER) project [Gadotti et al., 2019]. For NGC 4371, it has been estimated that the bar formation happened at $z \approx 2$ [Gadotti et al., 2015], while for NGC 1433, this happened at $z \approx 1$ [de Sá-Freitas et al., 2023]. Nonetheless, it is important to point out that not necessarily all barred galaxies observed at $2 < z \leq 3$ will remain as a barred disc galaxy down to $z \approx 0$, as the galaxies in the TIMER sample: late violent mergers may destroy the bar, as well as the disc altogether.

In a recent study conducted by Guo et al. [2023], six strongly barred galaxies were identified at $z > 1$ using rest-frame NIR images from the first four pointings of CEERS. The six observed galaxies have a range in redshift from $z \approx 1.1$ to $z \approx 2.3$ [see Guo et al., 2023, Stefanon et al., 2017]. In a cross-check, I find that all barred galaxies identified by Guo et al. were also classified as barred in this study.

Several previous studies have found a decline in the fraction of bars in disc and spiral galaxies with redshift. However, mass and volume limits vary across studies, as do the bar classification methods. Sheth et al. [2008] observe the evolution of the bar fraction at redshifts $0.2 < z < 0.84$ from luminous (brighter than $L_V^\star$) face-on spiral galaxies in the COSMOS 2 deg^2 field. The classification methods used in this study are ellipse fitting and visual inspection, which were cross-checked, yielding an agreement of 85%. Masters et al. [2011] found the bar fraction of a volume-limited visually selected SDSS sample using Galaxy Zoo at redshifts $0.01 < z < 0.06$ and $M_r < -19.38$. Melvin et al. [2014] uses visually selected galaxies via Galaxy Zoo

from COSMOS HST images at redshifts $0.4 \leq z \leq 1.0$ with an applied stellar mass limit of $\log(\mathrm{M}_\star/\mathrm{M}_\odot) \geq 10$. The bar fraction was extended to redshifts $0.5 \leq z \leq 2.0$ in Simmons et al. [2014] through the visually selected CANDELS galaxies via Galaxy Zoo with an absolute $H-$band magnitude limit of $H < 25.5$. Given that their work overlaps with the lower-redshift bin of my study and uses visually identified CANDELS galaxies, I find good agreement with my results. Although many studies have found a decrease in the bar fraction between $z = 0$ and $z = 1$, some have found little or no evolution in the bar fraction. Jogee et al. [2004] identified bars in spiral galaxies using three independent techniques and found the fraction of bars to be $\sim 30 \pm 6$ per cent in COSMOS-ACS galaxies at redshifts $z \sim 0.2 - 0.7$ and $z \sim 0.7 - 1.0$, with completeness cuts of $M_V \leq -19.3$ and -20.6, respectively. Elmegreen et al. [2004] also found a constant bar fraction of $\sim 23 \pm 3$ per cent at redshifts $z \sim 0.0 - 1.0$ in COSMOS-ACS galaxies.

A direct comparison of the results from these studies is difficult, given the different techniques used to identify bars and the different sample selection criteria. In particular, Erwin [2018] showed that in the local Universe the bar fraction depends strongly on galaxy mass, with a peak at $\mathrm{M}_\star \sim 10^{9.7}\mathrm{M}_\odot$, declining towards both higher and lower masses. At redshifts $0.2 \leq z \leq 0.6$ for a mass complete sample of $\mathrm{M} > 10^{10.5}\mathrm{M}_\odot$ galaxies in the COSMOS field, Cameron et al. [2010] found the bar fraction of early-type discs with intermediate stellar masses to be twice that of late-type discs, and is reversed for high stellar masses. In this context, it is important to note that my sample probes the galaxy population with masses above $\approx 10^9\mathrm{M}_\odot$, which, at redshift zero, may reflect the peak in the bar fraction distribution. Considering all barred galaxies I find in my study, their mean stellar mass is $\mathrm{M}_\star \sim 1.2 \times 10^{10}\mathrm{M}_\odot$, with a standard deviation of $\sim 5.8 \times 10^{10}\mathrm{M}_\odot$.

With the different redshift ranges and stellar masses probed, as well as rest-frame wavelength ranges, samples and techniques employed to find bars and disc galaxies in the different studies, it is clear that while Figure 2.10 presents an interesting summary of the findings from different studies, a direct comparison between these studies must account for a number of effects. One could, for example, account for the various mass ranges by assuming a $z = 0$ variation in the bar fraction with mass

and then translate it to samples probed at higher redshifts. However, this exercise would have to assume that such variation is constant with redshift, an assertion that, to the best of my knowledge, has not yet been investigated in sufficient depth. Moreover, the other effects mentioned may be as important, and recipes to account for those are not straightforward to devise.

Using the magnetic-hydrodynamical cosmological simulation TNG50 [Nelson et al., 2019], Rosas-Guevara et al. [2022] found that $M_\star \geq 10^{10} M_\odot$ spiral galaxies with bar formation are present as early as $z = 4$. When an angular resolution limit of twice the HST I-band angular PSF FWHM was applied, the fraction of bars dropped to a tenth of its original value at $z = 2$, reconciling theoretical predictions and observations. The rapid onset of bar formation in massive galaxies at early cosmic times has been predicted in numerical simulations for baryon-dominated systems [see e.g., Algorry et al., 2017, Bland-Hawthorn et al., 2023, Fragkoudi et al., 2021]. In fact, recent studies have identified candidate barred galaxies at redshifts higher than my limit of $z = 3$. Costantin et al. [2023] used HST and JWST images in multiple filters to study a galaxy at $z \simeq 3$ in the mass range of Milky Way progenitors and found evidence of a bar. Going further in wavelength than what is possible with JWST, Tsukui et al. [2023] and Smail et al. [2023] explored the sub-millimetre domain to find dusty, star-forming galaxies at $z > 4$ with morphology indicative of a bar. If these galaxies are confirmed as barred, they provide strong constraints to cosmological simulations.

Some of the previous observational studies discussed above suggest that the decrease in the bar fraction in massive disc galaxies out to $z \sim 1$ could be due to minor merger events that keep the disc dynamically hot. However, depending on the details of the merger/flyby interaction, this could, in fact, tidally induce bar formation [e.g., Berentzen et al., 2003, Peschken and Łokas, 2019].

The decline in the bar fraction in disc galaxies could be explained by the decreasing spatial resolution at higher redshifts. At lower resolution, bar ellipticity decreases, resulting in a rounder, less elongated, more compact bar and making the stellar bar less distinguishable. The perceptibility of a bar could be considerably affected by a clumpy outer disc, a bright central bulge and/or the angular size of

the bar [e.g., Lee et al., 2019]. In the context of my results using JWST, the PSF FWHM for the JWST F444W filter is 0.145″. The median redshift for barred galaxies between $1 \leq z \leq 2$ is $z = 1.48$, corresponding to a mean linear resolution of ≈ 1.26 kpc. As for the redshift bin $2 < z \leq 3$, the median redshift of barred galaxies is $z = 2.28$, corresponding to a mean linear resolution of ≈ 1.22 kpc. Bars smaller in angular size could have been preferentially missed at the high redshifts explored in this study. In a volume-limited SDSS galaxy sample where bars were identified through ellipse fits and Fourier analysis, Aguerri et al. [2009] established that only bars with lengths above 2.5 times the FWHM can be identified. The proposal that the high-redshift bar fraction is systematically underestimated was thoroughly discussed in the context of a mass- and volume-limited S^4G galaxy sample in Erwin [2018], where visual bar length measurements were obtained from Herrera-Endoqui et al. [2015]. Erwin successfully reproduced SDSS bar fraction trends using SDSS observational parameters in simulations on the S^4G galaxy sample and suggested a bar length detection limit of ~ 2 times the FWHM. Applying these detection limits on NIRCam F444W images implies that bars shorter than $\sim 2.5 - 3$ kpc in radius (semi-major axis) are missed in my study.

The resolution limit thus indicates that all bars detected in this study are longer than ≈ 3 kpc. In fact, Erwin [2005] found that the mean bar semi-major axis is 3.3 kpc for early-type disc galaxies and 1.5 kpc for late-type disc galaxies [see also Gadotti, 2011]. Therefore, unless the bar size distribution at high redshifts differs from the local distribution, even with JWST, I am likely missing a sizeable fraction of barred galaxies [see also the discussion in Liang et al., 2023]. In a sample of massive galaxies ($M_\star \geq 10^{10} M_\odot$, $0.02 \leq z \leq 0.07$) studied in Gadotti [2011], there are not many bars that are shorter than 3 kpc (see his Fig. 1) although the author points out that due to resolution limits, he may also miss bars with semi-major axis below $2 - 3$ kpc. However, in Erwin [2005], mass is not presented, so a direct comparison is not straightforward. Erwin [2019], on the other hand, shows that bar length increases with mass for galaxies more massive than $\log (M_\star/M_\odot) \geq 10.1$ for local galaxies, and a substantial fraction of the galaxies in his study has bars shorter than 3 kpc.

Not only absolute bar length but the ratio of bar length to the galaxy size (e.g., disk scale length h, or parameters such as R_{50} or R_{90}) may be more useful to compare at different redshifts, since it has been shown that the galaxy size also evolves [Buitrago et al., 2008, 2014, Trujillo et al., 2007, van der Wel et al., 2014, Whitney et al., 2019, mostly for massive early-type galaxies but also in the case of disk galaxies]. Kim et al. [2021] measured bar length for galaxies at $0.2 \leq z \leq 0.84$ and found that the mean length of the bar is ~ 5 kpc for galaxies with $\log(\mathrm{M}_\star/\mathrm{M}_\odot) \geq 10$ (see their Fig. 2). However, the normalised bar length R_{bar}/h of galaxies at $0.2 \leq z \leq 0.84$ in the study of Kim et al. [2021] is similar to that of local bars in Gadotti [2011]. I postpone a thorough discussion on these aspects to Chapter 3, in which I will also present measurements of the bar length and its evolution at higher redshifts.

It is also interesting to note that the abundance of weakly barred galaxies significantly declines at the higher redshift bin, more so than the abundance of strongly barred galaxies. This suggests the presence of another possible observational bias. While the linear resolution remains similar between $1 \leq z \leq 2$ and $2 \leq z \leq 3$ (as discussed above), cosmological surface brightness dimming is significantly more powerful at the higher redshift bin. This could diminish my ability to see weaker bars, particularly at the higher redshift bin, and this bias could produce a relative drop in the total bar fraction at the higher redshift bin even if the bar fractions in the two redshift bins are in reality comparable.

2.6 Summary and conclusions

Deriving the fraction of stellar bars in disc galaxies at high redshifts is an essential step towards understanding the onset of bar-driven galaxy evolution, which previous studies using rest-frame optical HST images found to occur at $z \sim 1$. However, stellar bars are populated by evolved stars emitting strongly at longer wavelengths, and thus, bars can be more effectively identified in rest-frame NIR images.

In this chapter, I examine the evolution of the bar fraction at redshifts $z = 1 - 3$ in a sample of galaxies observed in both HST CANDELS and JWST CEERS and

PRIMER, and compare the results obtained using rest-frame optical HST images and rest-frame NIR JWST images for galaxies in the same parent sample. I use the longest-wavelength JWST NIRCam F444W filter to trace the underlying stellar mass distribution as best as possible. The initial mass complete parent sample of 1180 galaxies is optimised to produce a sample in which bars can be more robustly identified, in particular by removing galaxies with peculiar morphology and those in close-to-edge-on projections, with an inclination limit of $i \leq 60°$. After optimisation, the parent sample is reduced to 368 galaxies in the JWST F444W filter and 126 galaxies in the HST F160W filter. Five participants visually classified all galaxies in the two optimised samples, searching for bars supported by radial profiles of isophotal ellipticity and position angle.

To observe the evolution of stellar bars in disc galaxies, I used published disc classifications from Ferreira et al. [2023, JWST disc classifications] and Kartaltepe et al. [2015, HST disc classifications]. The fraction of bars in disc galaxies was thus derived for two redshift bins, $1 \leq z \leq 2$ and $2 < z \leq 3$, with robust photometric redshifts and ensuring a mass completeness above 95%. The bar fractions I found in JWST F444W are, respectively, $\approx 17.8^{+5.1}_{-4.8}$ per cent and $\approx 13.8^{+6.5}_{-5.8}$ per cent for the lower and higher redshift bins. In HST F160W, I found the bar fractions to be $\approx 11.2^{+4.7}_{-3.8}$ per cent and $\approx 6.0^{+8.4}_{-3.7}$ per cent for the lower and higher redshift bins, respectively. Notably, at lower redshifts, I identify 20 additional barred galaxies in JWST images that were not identified in HST images, and at higher redshifts, I classify nine additional galaxies as barred. I thus found the bar fraction to be approximately twice as large in JWST F444W as in HST F160W. The rest-frame NIR bar fractions are twice those in the optical, indicating that the detectability of stellar bars depends significantly on the wavelength range and instrument sensitivity.

A decrease in the bar fraction is observed at higher redshifts, but this trend may be due to shorter bars being preferentially missed in this study. I detect a substantial number of barred galaxies at redshifts $z \leq 3$, implying that bar-driven galaxy evolution could commence at least in some galaxies at a lookback time ~ 11 Gyrs, given that some bar-driven processes, such as promoting gas inflow along the bar leading edges, are thought to proceed quickly after bar formation [~ 0.1

Gyrs; see, e.g., Athanassoula, 1992, Baba and Kawata, 2020, Seo et al., 2019]. In fact, Guo et al. [2023] have recently reported the finding of a barred galaxy at $z \approx 2.3$, and other teams have reported candidate barred galaxies beyond redshift three [Amvrosiadis, 2023, Costantin et al., 2023] and even beyond redshift four [Smail et al., 2023, Tsukui et al., 2023]. In this study, the highest-redshift strongly and weakly barred galaxies are found at $z \simeq 2.3$ and $z \simeq 2.8$, respectively.

This study does not extend beyond $z = 3$ to remain in the rest-frame NIR, thereby improving the detection of evolved stellar populations within the bar. Interesting investigations can be conducted into the bar fraction dependence on stellar mass and the evolution of bar length, which are beyond the scope of this chapter but will be explored in Chapter 3. This study used the first four CEERS pointings, and Chapter 3 will present an expanded census of the bar fraction at redshifts $1 \leq z \leq 4$ using the remaining six CEERS pointings.

CHAPTER 3

The evolution of the bar fraction and bar lengths in the last 12 billion years

In this chapter, I present a paper published in the Monthly Notices of the Royal Astronomical Society [Le Conte et al., 2026] on the evolution of the bar fraction and bar length beyond $z = 1$.

I investigate the evolution of the bar fraction and length using an extended JWST NIRCam imaging dataset of galaxies at $1 \leq z \leq 4$. I assess the wavelength dependence of the bar fraction and bar length evolution by selecting a nearly mass-complete CEERS disc sample and performing visual classifications on the short (F200W) and long (F356W+F444W) wavelength channels. A similar bar fraction is observed in both samples, and combining them, I find a decline from $0.16^{+0.03}_{-0.03}$ to $0.07^{+0.03}_{-0.01}$ over the redshift range. No evolution in the F356W+F444W bar length is measured, with a mean of 3.6 kpc. A slight increase of ~ 1 kpc towards $z = 1$ is measured in the F200W sample, with a mean of 2.9 kpc. I find that the correlation between bar length and galaxy mass, for massive galaxies at $z < 1$, is unseen at $z > 1$. By incorporating barred galaxies at $z < 1$, I show that there is a modest increase in the bar length (≈ 2 kpc) towards $z = 0$, but bars longer than ≈ 8 kpc are only found at $z < 1$. I show that bars and discs grow in tandem, because the bar length, normalised by disc size, does not evolve. Not only is a significant population of bars forming beyond $z = 1$, but my results also show that some of these bars are as long and strong as the average bar at $z \approx 0$.

3.1 Introduction

The improved sensitivity and broader wavelength coverage of the JWST have enabled bar-fraction studies to extend to $z \approx 4$. In the previous chapter, I used JWST to explore for the first time the abundance of barred galaxies out to $z = 3$. Chapter 2 identified that the bar fraction observed in JWST NIRCam images is twice that viewed in bluer HST filters of similar resolution, but still, a declining trend was observed in the bar fraction, from $\approx 17.8^{+5.1}_{-4.8}$ per cent at $1 \leq z < 2$ to $\approx 13.8^{+6.5}_{-5.8}$ at $2 \leq z \leq 3$. I showed that, despite similar spatial resolution, the difference was due to NIRCam's higher sensitivity and longer wavelengths, which enabled us to detect twice as many barred galaxies as HST had previously. The longer wavelengths observed with JWST could facilitate these results, as the NIR is a better tracer of the underlying stellar mass distribution of barred galaxies, which are mainly composed of older stellar populations [de Sá-Freitas et al., 2023, Gadotti and de Souza, 2006, Marinova and Jogee, 2007, Sánchez-Blázquez et al., 2011].

This study already indicates that bar-driven internal evolution began ~ 11 Gyrs ago, based on 30 newly classified barred galaxies in the redshift range $1 \leq z \leq 3$. The PSF FWHM limited this study to bars with radii greater than ~ 2.5 kpc, leading us to conclude that my results could still be a lower limit to the bar fraction.

Since my first study, several JWST bar-fraction investigations have supported my finding of a bar fraction twice that of HST [Espejo Salcedo et al., 2025, Géron et al., 2025]. I repeat the results reported by Guo et al. [2025] here, as I frequently compare this Chapter's results with theirs. Guo et al. [2025, hereafter referred to as G25] found a decline in the JWST CEERS bar fraction within the agreement of Chapter 2, across the redshift range $0.5 \leq z \leq 4$ in a mass-limited, $M_\star > 10^{10} M_\odot$ sample. Using ellipse fit techniques, the results showed a decrease in the bar fraction from 28.2 ± 3.6 per cent at $z \sim 0.5$ to 6.4 ± 2.4 per cent at $z \sim 3.5$.

In-depth studies have found bar-driven gas inflow in individual galaxies at high-z [e.g., Huang et al., 2023, 2025, Pastras et al., 2025]. Early-Universe bars are now recognised as long-lived and robust structures that exhibit the same mechanisms as in local-Universe barred galaxies, such as bar-driven gas inflows. The statement

that bar-driven evolution has commenced at $z \approx 3$ is supported not only by these bar fraction studies, but also by in-depth studies of individual barred galaxies at high-z. Several of these studies were discussed in Chapter 1, but I briefly mention them here. The prominent stellar bar at $z \sim 2.5$ found in Huang et al. [2023] and Huang et al. [2025] indicates that bar-driven star formation is present in a gas-rich massive disc galaxy, for which the funnelling of molecular gas is observed towards the galactic centre. Early-Universe bars are now seen to be long-lived and robust structures that exhibit the same mechanisms as in local-Universe barred galaxies, such as bar-driven gas inflows. Active star formation from bar-driven rapid gas inflow at Cosmic Noon is found in a massive gas-rich disc galaxy at $z \sim 1.5$ studied by Pastras et al. [2025].

Several barred galaxies at high redshift have been observed recently with ALMA. A massive barred galaxy was confirmed by Amvrosiadis et al. [2025] at $z = 3.8$, 1.7 Gyr after the Big Bang, in a gas-rich system. Additionally, these young barred galaxies have long bars. In the case of a barred galaxy at $z = 4.4$, Tsukui et al. [2024] measured the bar to be 3.3 kpc long, which is comparable to the bars ranging in length from ~ 1 to 10 kpc in the local Universe [e.g., Erwin, 2005, Gadotti, 2011]. These detailed studies push the boundaries of bar identification and show that some bars form significantly earlier than previously thought.

Theory suggests that over time, a bar will evolve and grow in length, as the rotational pattern speed of the bar slows, extending resonances to greater radii, thus allowing the trapping of stars on elongated orbits to reach these new limits [Athanassoula, 2003]. In this Chapter, I will investigate whether the bar length grows across cosmic time. Hence, I repeatedly compare the results of this chapter with those of two studies at lower redshifts, which I will detail here. Observations at $z \approx 0$ have suggested that bars grow with time. In a sample of 300 nearby barred galaxies, Gadotti [2011, hereafter referred to as G11] found longer and stronger bars in galaxies with a higher bulge-to-total luminosity ratio (indicating more evolved galaxies), suggesting that the bars grow longer and stronger with time. However, in direct observations beyond the nearby Universe, Kim et al. [2021, hereafter referred to as K21] found no evolution between $0.2 < z < 0.8$ and a mean bar length at those

redshifts similar to the mean bar length from G11 at $z \approx 0$. G25 is the only study to have investigated the properties of a sample of barred galaxies beyond $z = 1$ thus far. The average projected bar length reported in G25 increased from ~ 1.7 – 2.5 kpc at $z \sim 2.5$ to ~ 2.6 – 3.8 kpc at $z \sim 0.75$, in the F200W sample, but no evolution was observed in the F444W sample.

In this chapter, I investigate the abundance of barred galaxies and their properties at $z \geq 1$ using JWST NIRCam images (§ 3.2.1) selected by redshift and stellar mass (§ 3.2.2). In contrast to Chapter 2, my parent sample is significantly larger (by nearly a factor of three in sky area), and this study extends to $z = 4$, also exploring wavelength dependencies. The following methodology is applied independently to both short-wavelength (F200W) and long-wavelength (F356W+F444W) NIRCam images. The ellipse-fitting technique is applied to reduce the sample to less inclined, more face-on galaxies (§ 3.3.2). The disc sample is selected by removing point sources through the automated process of fitting the galaxy with a 2D Sérsic model (§ 3.3.3). Subsequently, the visual classifications are determined by five independent participants, of which the final disc and barred galaxy samples are obtained (§ 3.3.3).

These results show strong agreement with the bar fraction from Chapter 2, along with the finding of three barred galaxies at $z \geq 3$ (§ 3.4). I report no strong correlation between the bar fraction and stellar mass(§ 3.5). Using ellipse-fitting techniques, I measure the evolution of bar length and compare the trends for short and long wavelengths (§ 3.5.2). Similarly, the strength of the bar differs between the two filters (§ 3.5.3). I discuss the implications of my findings for when bar-driven evolution commences and for the impact of observed wavelengths in § 3.6, and present my conclusions in § 3.7.

3.2 The sample

To investigate the epoch at which bar-driven secular evolution commences, I use the ten public NIRCam JWST observations from CEERS, combining June 2022 observations (CEERS1, CEERS2, CEERS3 and CEERS6) and January 2023 observations

(CEERS4, CEERS5, CEERS7, CEERS8, CEERS9 and CEERS10), which overlap with 50 per cent of CANDELS on the EGS field. Together, the data cover $\sim$ 88 arcmin^2 of an area with CANDELS HST overlap.

3.2.1 Data reduction pipeline

We reprocessed all raw NIRCam exposures retrieved from the `Mikulski Archive for Space Telescopes (MAST)` with the official JWST pipeline (v1.8.2, CRDS v1084), following the procedures of Ferreira et al. [2023] and Adams et al. [2023] but incorporating several refinements. After Stage 1 calibration and application of the latest post-flight reference files, we remove large-scale "wisp" artefacts with second-generation Space Telescope Science Institute (STScI) templates. Stage 2 processing includes the 1/f-noise correction [Adams et al., 2025], while Stage 3 is split so that sky subtraction—flat, then 2-D with photutils—is tuned on a frame-by-frame basis before the full mosaicking step.

Similarly to what is described in § 2.2.1, background-corrected frames are then combined using the STScI `DrizzlePac` software, anchoring the astrometry to GAIA DR3 via `tweakreg`; each filter is subsequently reprojected onto the F444W grid at $0.03''$ pixel^{-1} to ensure sub-pixel alignment across the dataset. A comprehensive description of the workflow and its validation is given in Adams et al. [2024], Conselice et al. [2024] and Harvey et al. [2025].

3.2.2 Sample selection

For this work, I use the robust photometric redshifts and stellar masses originating from CANDELS-based catalogues [see Duncan et al., 2019, for details]. I do not use JWST-based photometric redshifts, for Conselice et al. [2024] reported essentially no difference in results at $z < 3$.

I select a sample of sources within the CEERS footprint that have photometric redshifts and stellar masses. I limit my sample selection to the high redshift range $1 \leq z \leq 4$. No magnitude or signal-to-noise cut is applied, but rather an empirical 95 per cent mass completeness limit dependent on redshift is adopted from Duncan

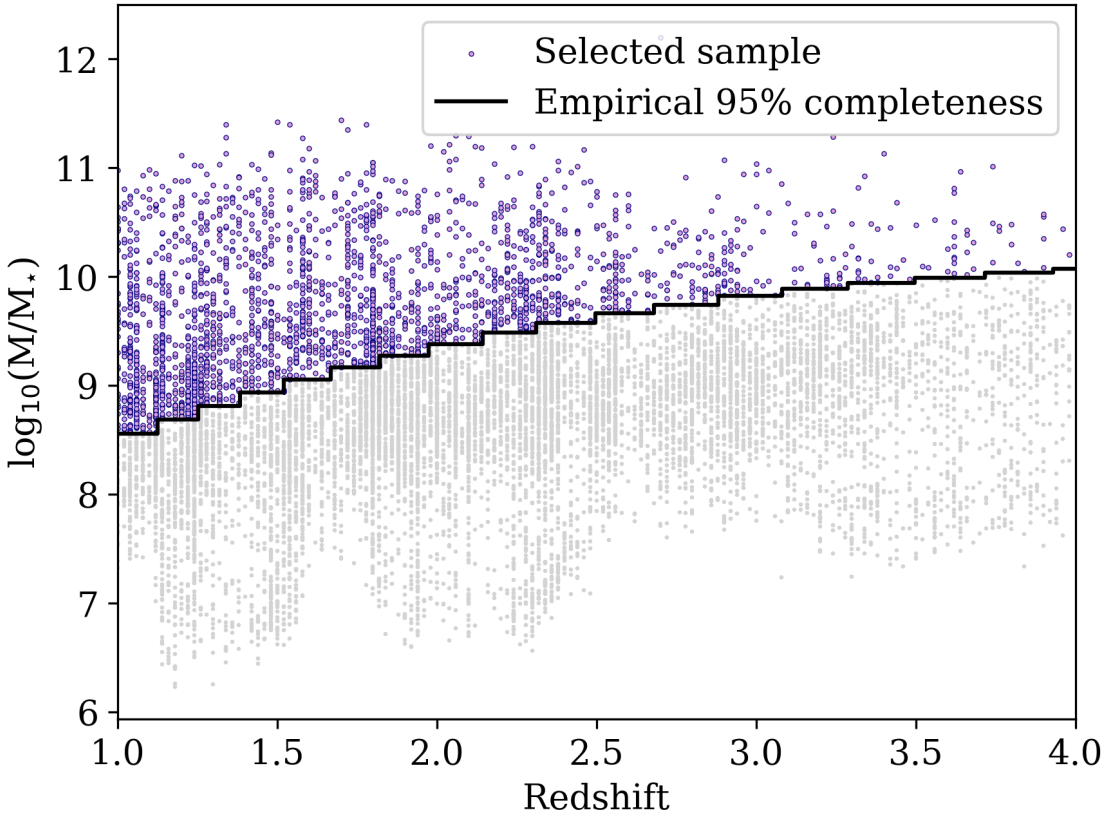

Figure 3.1: Stellar mass-redshift distribution of CEERS galaxies in the redshift range $1 \leq z \leq 4$. I adopt the 95% empirical completeness of Duncan et al. [2019, black step function], originating from CANDELS data. My sample is selected to be those with stellar masses greater than the redshift-dependent stellar mass limit (purple).

et al. [2019, see their Section 3.4.1 for further details]. For full details on how the mass-completeness limit is determined by the flux limits of the HST, Spitzer, and ground-based surveys, I refer the reader to the overall method in Duncan et al. [2019]. My redshift and stellar mass cuts result in a sample of 2438 galaxies selected for this study, for which the stellar mass-redshift distribution is shown in Figure 3.1. For my sample, we produce 128×128-pixel cutouts at 30 mas for the JWST filters F200W, F356W, and F444W (the NIRCam filter selection is discussed in § 3.3.1).

3.3 Methodology

This study aims to observe the onset of bar-driven secular evolution at high$-z$ by measuring the bar fraction and bar properties. The bar fraction, f_{bar}, is defined as

the fraction of disc galaxies which are hosts to a stellar bar:

$$f_{bar} = \frac{N_{bar}}{N_{disc}}, \tag{3.1}$$

where N_{disc} is the observed sample size of disc galaxies and N_{bar} is the number of barred galaxies identified in the disc galaxy sample. Hence, in this work, I seek to identify a sample of disc galaxies and subsequently a sample of barred galaxies.

The parent sample is refined by removing galaxies through a series of procedures. Given that stellar bars are distinguishable in moderately inclined disc galaxies but become challenging to define in highly inclined galaxies, the sample must be reduced to exclude near-edge-on galaxies. For a moderately inclined sample, point sources can be removed by imposing a constraint on the distribution of Sérsic indices. I explore the possibility of using the global Sérsic index to define the disc sample, but find that at high redshifts the Sérsic index is insufficient to distinguish disc from spheroid morphological types. Hence, I perform visual classifications to identify morphological type and bars. I discuss the NIRCam imaging selected for my sample in § 3.3.1, the removal of highly inclined objects through an optimisation routine in § 3.3.2, using the global Sérsic index to remove point sources in § 3.3.3, followed by disc and bar visual classifications in § 3.3.3.

3.3.1 NIRCam imaging

To observe prominent bars in the early Universe, I use the wide, long-wavelength JWST NIRCam filters F356W and F444W to capture the underlying stellar mass distribution of the disc while reducing the effects of dust obscuration and clumpy star formation, which can hamper bar identification. To observe NIRCam images with comparable rest frame wavelengths, the filter F356W is used for galaxies between $1 \leq z < 2$, obtaining a rest-frame wavelength of 1.4μm for the median redshift of the bin $z = 1.5$. Furthermore, F444W is used for galaxies between $2 \leq z \leq 4$; with a rest-frame wavelength of 1.1μm for the median redshift $z = 3$. The NIRCam empirical

PSF FWHM[1] is amplified at longer wavelengths and is 0.116″ and 0.145″ for the filters F356W and F444W, respectively. At the median of the two redshift bins, the corresponding linear resolutions are 1.01 kpc and 1.14 kpc. Regarding bar detection, the minimum identifiable bar length is 2× FWHM [e.g., Erwin, 2005], which for the NIRCam long-wavelength channels is 2.02 kpc and 2.28 kpc, respectively. Hence, I am likely missing bars shorter than $\approx$ 2 kpc in this study when using the long-wavelength filters.

To evaluate the effects of rest-frame wavelength, I also use images of all galaxies across $1 \leq z \leq 4$ in the NIRCam short-wavelength filter F200W. This filter corresponds to a rest-frame wavelength of 0.67μm at $z = 2$ and has a PSF FWHM of 0.066″, resulting in a linear resolution of 0.6 kpc. Hence, the shortest bars identified with these NIRCam images are 1.2 kpc in length. However, at this rest-frame wavelength, dust and star formation effects may hamper the identification of bars. Hence, my methodology is applied independently to NIRCam imaging using the short-wavelength filter F200W and the long-wavelength filters F356W and F444W. Note that in a few cases, galaxies fall between the gaps of the NIRCam detectors; therefore, I could not retrieve images in the F200W and F356W/F444W bands. However, I still include these sources in my sample when available, since the samples are independent from this point onward.

Before proceeding with my sample optimisation, SExtractor is used to mask neighbouring objects [Bertin and Arnouts, 1996]. Figure 3.2 demonstrates the masking process on the example galaxy EGS 1246 in the F444W NIRCam image. This process is particularly important because the sample optimisation procedure depends on the ellipticity of the isophotes tracing the outer disc, which, in this case, has changed significantly due to source masking.

3.3.2 Sample optimisation

Barred galaxies are clearly identifiable in face-on galaxies; however, at higher inclinations, they become increasingly challenging to identify. Thus, to avoid this bias, I

[1]PSF FWHM taken from the JWST user documentation: https://jwst-docs.stsci.edu/jwst-near-infrared-camera/nircam-performance/nircam-point-spread-functions

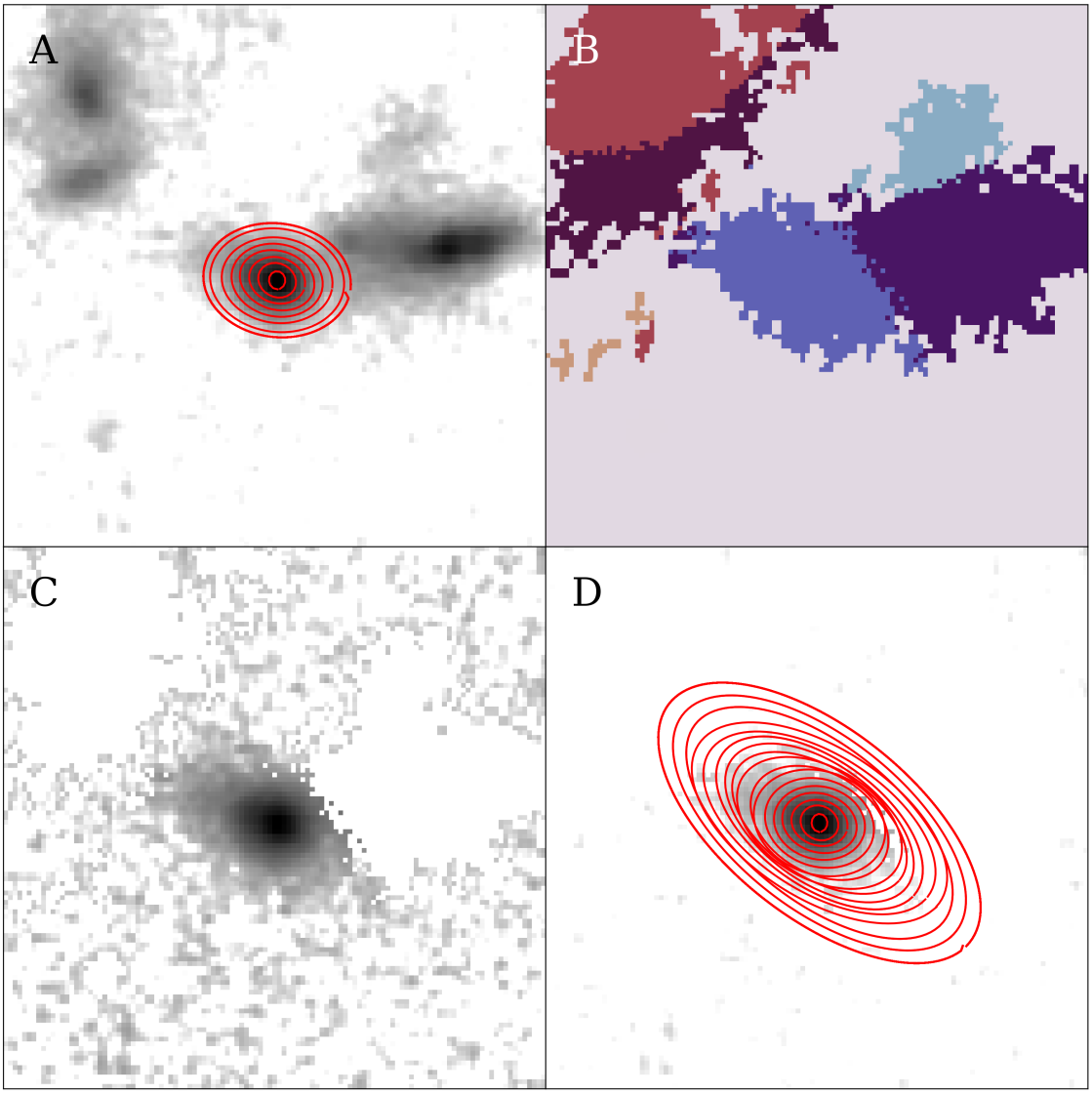

Figure 3.2: Masking of neighbouring sources with SExtractor performed on the example galaxy EGS 1246. Top left - JWST NIRCam F444W image with fitted elliptical isophotes. Top right - SExtractor segmentation map. Bottom left - Resulting image with identified neighbouring sources masked out. Bottom right - Masked image with newly fitted elliptical isophotes. This figure shows the influence of nearby sources on the orientation and elongation of isophotal ellipse fits.

remove highly inclined galaxies with $i > 65°$ from the sample using an optimisation process. A detailed description can be found in § 2.3.1, but the three stages are summarised below. The inclination of a galaxy is measured by fitting elliptical isophotes to the image using `photutils.isophote` from the Python astropy package [Bradley et al., 2022]. An ellipticity limit, corresponding to $i > 65°$, is then applied to the outer isophotes.

Phase 1 The first run of elliptical isophotes fits is performed, with the pixel coordinates of the centre of the galaxy as free parameters. For a given galaxy, fits are performed using a set of initial parameters until the galaxy is successfully fitted, even if the fits do not align perfectly with the galaxy. Approximately 90% and 75% of the parent sample had successful ellipse fits in the F356W+F444W and F200W filters, respectively. The remaining $\sim 10 - 25\%$ of galaxies that failed ellipse fittings are overly disturbed, poorly resolved, and/or low surface brightness systems and are removed from the sample.

Phase 2 `photutils.isophote` selects the central position of a galaxy by assessing a 10×10 window about a specified centre. I specify the centre of each galaxy as the average of the central pixels within the inner 10-40% of the isophotes fitted in phase 1. The lower isophote limit is set to exceed 2×FWHM to avoid bright star-forming regions near the galactic centre, and the upper isophote limit is set to avoid tracing structures toward the outer regions of the galaxy, such as spiral arms, which could lead to a mistaken identification of the galaxy centre.

Isophote fitting is repeated on the sample of galaxies that pass phase 1, with a fixed centre. Phase 2 achieved success rates of 75% and 57% with the F356W+F444W and F200W filters, respectively. Those galaxies that failed, typically those that were overly irregular or ambiguous in morphology, were removed.

Phase 3 I define the inclination of a galaxy in equations 2.1 and 2.2. The success rates for phase 3 were 64% for the F356W+F444W filter and 63% for the F200W filter. Galaxies deemed too highly inclined were removed from the

sample, resulting in overlapping optimised samples of 1073 and 649 galaxies, all of which had successful ellipse fits.

In summary, the optimisation phase aimed to fit elliptical isophotes to the NIRCam images and to measure eccentric outer isophotes with an approximate ellipticity $\varepsilon > 0.5$, implying that the galaxy is highly inclined and therefore removed from my sample. Overall, of the 2438 galaxies in my mass-complete sample, the following were removed at each phase for F356W+F444W: 223 at phase 1, 540 at phase 2, and 597 at phase 3, resulting in an optimised sample of 1073 galaxies. As for F200W: 616 at phase 1, 782 at phase 2 and 386 at phase 3; resulting in an optimised sample of 649 galaxies. The optimisation routine reduced the F200W sample significantly more than the F356W+F444W sample, which I attribute to the short-wavelength filter tracing star formation, which appears clumpy and makes ellipse fitting challenging.

3.3.3 Morphological classification

Classification studies at high redshifts have identified three distinct galaxy types: discs, spheroids, and irregulars. Ormerod et al. [2024] studied the evolution of structural parameters with CEERS galaxies at $0.5 \leq z \leq 8$, to which they found shallower light profiles and diffuse brightness distributions for all morphological types at high-z, when compared to their low-z counterparts. Therefore, uncertainties arise when distinguishing among galaxy types using surface-brightness profiles. Hence, I followed a two-step method to select the disc sample of this study. Firstly, I fit single Sérsic functions to the NIRCam images to obtain structural information, which I then use to select and remove point sources from my sample. I then had five classifiers visually classify and identify the disc and barred galaxies.

Sérsic fits

A 2D elliptical Sérsic profile can model the light distribution in disc galaxies, and the program IMFIT [Erwin, 2015] is designed to fit such functions to astronomical images. The program produces a best-fitting model by minimising the Cash statistic using a differential evolution (DE) algorithm [Storn and Price, 1997], after convolving the

model image with oversampled PSF images created by the Space Telescope PSF (STPSF) package[2]. The stochastic nature of the DE approach is beneficial because it can search large areas of the parameter space whilst being less likely to be trapped in local minima. In addition, this approach does not require initial parameter values, only lower and upper limits, and has been shown to yield the best results compared to iterative, human-supervised fits [Gadotti, 2026].

I fitted a single Sérsic component to all galaxy images, and the best-fitting model parameters that I focus on are ellipticity (ε), Sérsic index (n), and effective radius (r_e). The distributions of these parameters for all galaxies in the optimised samples of F356W+F444W and F200W are shown in Figure 3.3. Across all parameters, the distributions show similar trends between the shorter- and longer-wavelength NIRCam filters. This is to be expected, as for each parameter, the model is convolved with the corresponding PSF, so the single-component model is, to some extent, independent of the observed wavelength. The slight difference in r_e between the two samples is less than 1σ. Hence, the result is statistically insignificant and not explored further. The occurrence of only a few galaxies with $\varepsilon > 0.6$ demonstrates the efficiency of the optimisation process described in § 3.3.2 to remove highly inclined galaxies.

There is a noticeable peak in sources with $\varepsilon \approx 0$, which I attribute mostly to point sources and unresolved sources. To reduce my sample for visual classification, I use the best-fit parameters n and r_e to define a sample of point sources. Point sources have discrete near-circular brightness distributions and are selected by the limits $\varepsilon \leq 0.2$ and $n \leq 1$, selecting 152 and 37 galaxies in F356W+F444W and F200W, respectively. From this selected sample of point sources, my collaborator (DG) and I visually inspected the NIRCam images and light profiles to assess the accuracy of this process and reintroduced galaxies that we had classified as point sources. After this step, the optimised samples comprise 927 and 628 galaxies in F356W+F444W and F200W, respectively, from which the disc sample is selected.

In the local Universe, galaxy morphological types can be separated by their global

[2]https://www.stsci.edu/jwst/science-planning/proposal-planning-toolbox/psf-simulation-tool

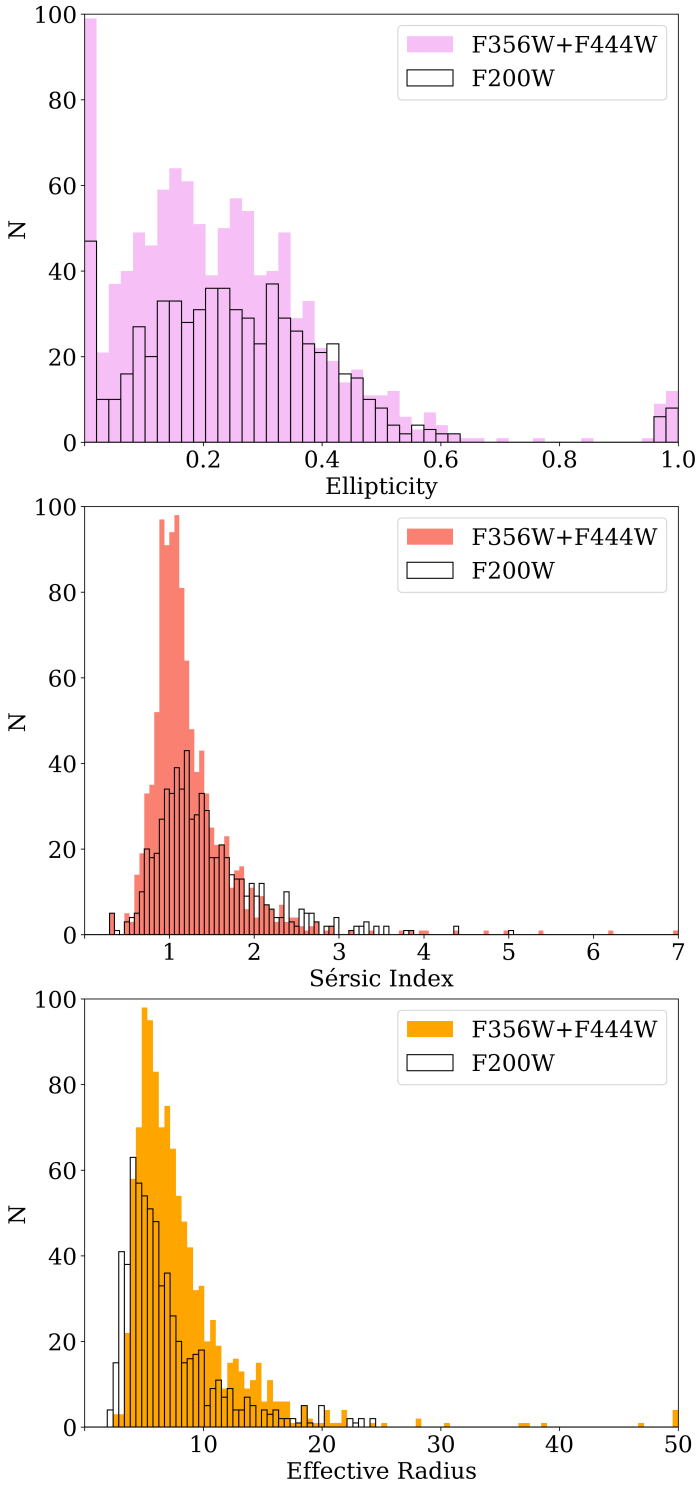

Figure 3.3: Distribution of the best-fit structural parameters from a single 2D Sérsic function fitting using IMFIT, performed on the optimised samples for galaxies between $1 \leq z \leq 4$. Models fit to F356W and F444W NIRCam images are filled distributions, and those as a result of fits to F200W NIRCam images are unfilled distributions with black edges. Left: single Sérsic best-fit ellipticity, ε. Middle: single Sérsic best-fit Sérsic index, n. Right: single Sérsic best-fit effective radius, r_e.

n, with massive ellipticals having high n and a high degree of central concentration, whilst massive discs have a more diffuse central concentration and lower n. Figure 3.3 shows that over 90 per cent of the sample has values of n between 0 and 2. Hence, I decided not to use the Sérsic index as a selection criterion for the disc sample, as the Sérsic index distribution of these high-redshift galaxies is significantly lower than that of ellipticals in the local Universe [see also Ormerod et al., 2024]. Instead, I incorporated disc selection into the visual classification process.

Visual classifications

This study incorporates disc identification into my visual classification method to find barred and unbarred disc galaxies. Five participants (ZLC, DG, CdSF, JN and TK) inspected the NIRCam F356W+F444W and F200W images and intensity radial profiles of each galaxy in the sample of 927 and 628 galaxies, respectively. The visual classification categories were *Barred, Maybe Barred, Unbarred Disc, Spheroid, Other* and *Unresolved*. Each classifier assigned each galaxy to one of these six categories and independently repeated the process for both short- and long-wavelength NIRCam filters. An outline of the categories is as follows:

Barred These galaxies present an ordered outer disc with a prominent elongated central stellar bar. The outer disc may exhibit spiral-arm features or rings.

Maybe Barred Similar in structure to the barred galaxy category, but for deviations from a prominent barred structure. These include rounder, thicker bars and systems with dominant spiral arms that obscure a barred structure.

Unbarred Disc These galaxies show a well-ordered disc, ranging from near circular to somewhat flattened. They have exponential surface-brightness profiles and may contain features such as spiral arms, rings, and centrally concentrated structures, but will be classified into one of the preceding categories if a bar is present.

Spheroid Appearing smooth, round-like and featureless, these systems share the likeness of elliptical galaxies in the local Universe, sometimes with high degrees of central concentration.

Other Some galaxies at high-z appear peculiar and clumpy in nature, and these can often be disguised as interaction or merger systems. If disciness cannot be observed, then the galaxy is assigned to this category.

Unresolved Despite my efforts to remove point sources, a few can be found in my samples and would fall into this category at this stage. Occasionally, a bright central feature in a galaxy caused PSF diffraction spikes to dominate the image, hampering a proper morphological classification.

The ultimate classification of a galaxy is attributed to a consensus vote, in which 3 out of 5 classifiers agree on a category. When a consensus cannot be reached, the source is allocated to the *Unclassified* category. The disc sample is compiled of galaxies attributed to the categories *Unbarred Disc*, *Barred* and *Maybe Barred*, meaning 3 out of 5 votes from one to any combination of all three of these categories would proceed to a disc classification. Examples of unbarred disc classifications include, but are not limited to, galaxies which obtained 3 unbarred disc votes; 2 maybe-barred and 1 unbarred disc vote; 1 barred, 1 maybe-barred and 1 unbarred disc vote. I establish two barred galaxy classifications:

Strongly Barred These are disc galaxies that have prominent elongated stellar bars, and accordingly have achieved above the consensus threshold of 3 out of 5 votes for *Barred*.

Weakly Barred These disc galaxies have rounder and less apparent bars, subsequently achieve the threshold of 3 out of 5 for *Maybe Barred* or by combining *Barred* and *Maybe Barred* votes.

This classification scheme is similar to that in § 2.3.3, for which the process worked well, and my results from Chapter 2 were consistent with subsequent bar-fraction studies. I deemed that the bar fraction should be determined using a similar methodology to identify the disc sample as well as the barred sample. Hence, since the disc sample cannot be established by limits on structural parameters, I have decided to reapply visual classifications to identify barred galaxies at high-z. Morphological analysis of sources at high-z is challenged by the faintness of the targets

Redshift	Sample Size								
	F200W			F356W+F444W			F200W+F356W+F444W		
	SB	WB	UD	SB	WB	UD	SB	WB	UD
$1 \leq z < 2$	15	17	196	11	32	274	23	43	358
$2 \leq z < 3$	2	2	61	5	5	103	5	7	137
$3 \leq z \leq 4$	0	1	14	0	1	14	0	2	25

Table 3.1: The sample sizes for the visually classified samples in F200W, F356W+F444W and F200W+F356W+F444W in three redshift bins. The sample size is presented for strongly barred galaxies (SB), weakly barred (WB) and unbarred disc galaxies (UD).

and their very small angular size. Thus, I include two barred galaxy classifications to provide upper and lower limits to the bar fraction.

The bar fraction is determined as:

$$f_{bar} = \frac{N_{bar}}{N_{disc}} = \frac{N_{SB} + N_{WB}}{N_{UD} + N_{SB} + N_{WB}} \tag{3.2}$$

where N_{SB} is the observed sample size of strongly barred galaxies, N_{WB} is the observed sample size of weakly barred galaxies, and N_{UD} is the observed sample size of unbarred discs. The sample sizes for each redshift are presented in Table 3.1.

Strong agreement between classifiers is considered achieved when the vote threshold is met. Visual classifications from the NIRCam filters F356W+F444W showed high agreement between classifiers in 74 per cent of cases, and were similar for F200W, with 70 per cent of cases in high agreement.

I evaluated the reliability of agreement between the classifiers of this study in categorical assignment using the descriptive statistic Randolph's kappa, κ [Randolph, 2010]. The free-marginal multirater κ measures the nominal agreement between multiple classifiers, employing 1 / number of categories as the proportion of agreement expected by chance. The statistic κ takes values from 1 to -1; values between 1 and 0 indicate agreement better than chance, 0 indicates a level of agreement expected by chance, and values between 0 and -1 indicate agreement worse than chance. Considering all categories in my visual classifications, I obtain a Randolph

κ of 0.30 for F356W+F444W and 0.28 for F200W, indicating agreement beyond chance.

3.4 The bar fraction

This study uses the improved sensitivity and longer wavelengths of JWST to observe the evolution of the bar fraction - the number of barred galaxies in the number of disc galaxies across the redshift range $1 \leq z \leq 4$. I split the redshift range into three bins, and those redshift bins are specified as follows: $1 \leq z < 2$, $2 \leq z < 3$ and $3 \leq z \leq 4$. The disc and barred galaxy samples have been visually classified in the NIRCam filters F356W+F444W and F200W (two independent samples), across the redshift range (F356W for $1 \leq z < 2$, F444W for $2 \leq z \leq 4$ and F200W for $1 \leq z \leq 4$; for further details see § 3.3.1), to assess the impact of rest-frame wavelength and resolution on the bar fraction.

Firstly, a brief comment on the general outcome of the classification scheme. The f_{disc}, based on a 3/5 vote threshold, is found to be 0.48 and 0.43, considering the whole sample in F356W+F444W and F200W, respectively. my results of f_{disc} agree with the visual classifications of Ferreira et al. [2023], with which my parent sample overlapped, which obtained $f_{disc} \approx 0.48$ for the same redshift range. I found a significantly smaller spheroidal population, $f_{spheroid} \approx 0.07$ and $f_{spheroid} \approx 0.06$ for the samples in F356W+F444W and F200W, respectively. This is less than the fraction classified by Ferreira et al. [2023], who found $f_{spheroid} \approx 0.15$. The lower spheroidal fraction found in this study could be due to the additional categories included in my visual classifications, such as *Other* and *Unresolved*.

I consider a combined sample, where I combine the F356W+F444W and F200W disc sample, such that if a disc were to be identified in the short-wavelength filter but not in the long-wavelength filters, it was added to the sample, creating a sample of disc galaxies classified in either short or long wavelength NIRCam filters (hereafter referred to as the combined sample). I consider this combined sample to capture shorter bars missed by the lower resolution of the longer-wavelength filters, whilst observing barred galaxies that might exhibit highly significant star formation and

dust obscuring the bar. The combined sample comprises 520 disc galaxies.

The bar fraction, f_{bar}, is measured in each of the three redshift bins, for the short-, long-wavelength and combined samples. Figure 3.4 shows the evolution of the bar fraction across the 12 Gyr range, comparing the bar fractions observed with JWST in this study to those found in other theoretical and observational work [de Vaucouleurs et al., 1991, Eskridge et al., 2000, Espejo Salcedo et al., 2025, Euclid Collaboration et al., 2025, Fragkoudi et al., 2025, Guo et al., 2025, Géron et al., 2025, Jogee et al., 2004, Masters et al., 2011, Melvin et al., 2014, Sheth et al., 2008, Simmons et al., 2014].

The bar fraction decreases at higher redshifts in both short- and long-wavelength filters. The F356W+F444W sample has bar fractions $f_{bar,long} \approx 0.14, 0.09$ and 0.07 for redshift bins $1 \leq z < 2$, $2 \leq z < 3$ and $3 \leq z \leq 4$. Similarly, the F200W sample has bar fractions $f_{bar,short} \approx 0.14, 0.06$ and 0.07 for the redshift bins $1 \leq z < 2$, $2 \leq z < 3$ and $3 \leq z \leq 4$. The combined sample has a slightly higher bar fraction $f_{bar,comb} \approx 0.16, 0.08$ and 0.07 for the redshift bins $1 \leq z < 2$, $2 \leq z < 3$ and $3 \leq z \leq 4$.

The bar fraction has been investigated at $z < 1$ in *Euclid* Q1 [Euclid Collaboration et al., 2025], finding the largest barred galaxy sample beyond the local Universe. Over 7,700 barred galaxies were identified using `Zoobot` classifications [Walmsley et al., 2025], obtaining a mean bar fraction of 0.2 to 0.4, for $\log_{10}(M_\star/M_\odot) > 10$ galaxies, at $z = 1$ to $z = 0$, respectively. The decreasing trend found in *Euclid*, shown in Figure 3.4, agrees with HST observations and simulations; however, by $z = 1$, the bar fraction is twice that previously measured in HST, and corroborates the conclusions of Chapter 2. The *Euclid* mission has achieved unprecedented spatial resolution for very large surveys, which will be vital for population statistics.

At the two Cosmic Noon bins, $0.8 < z < 1.3$ and $2.0 < z < 2.5$, Espejo Salcedo et al. [2025, hereafter referred to as ES25] obtained the visually classified bar fractions of ≈ 16 per cent and 3 per cent with JWST NIRCam imaging. The Galaxy Zoo CEERS project [Géron et al., 2025, hereafter referred to as GZ CEERS] observed a decreasing bar fraction in a volume-limited sample that ranged from 25 per cent at $0.5 < z < 1.0$ to 3 per cent at $3.0 < z < 4.0$. The decreasing trends reported by

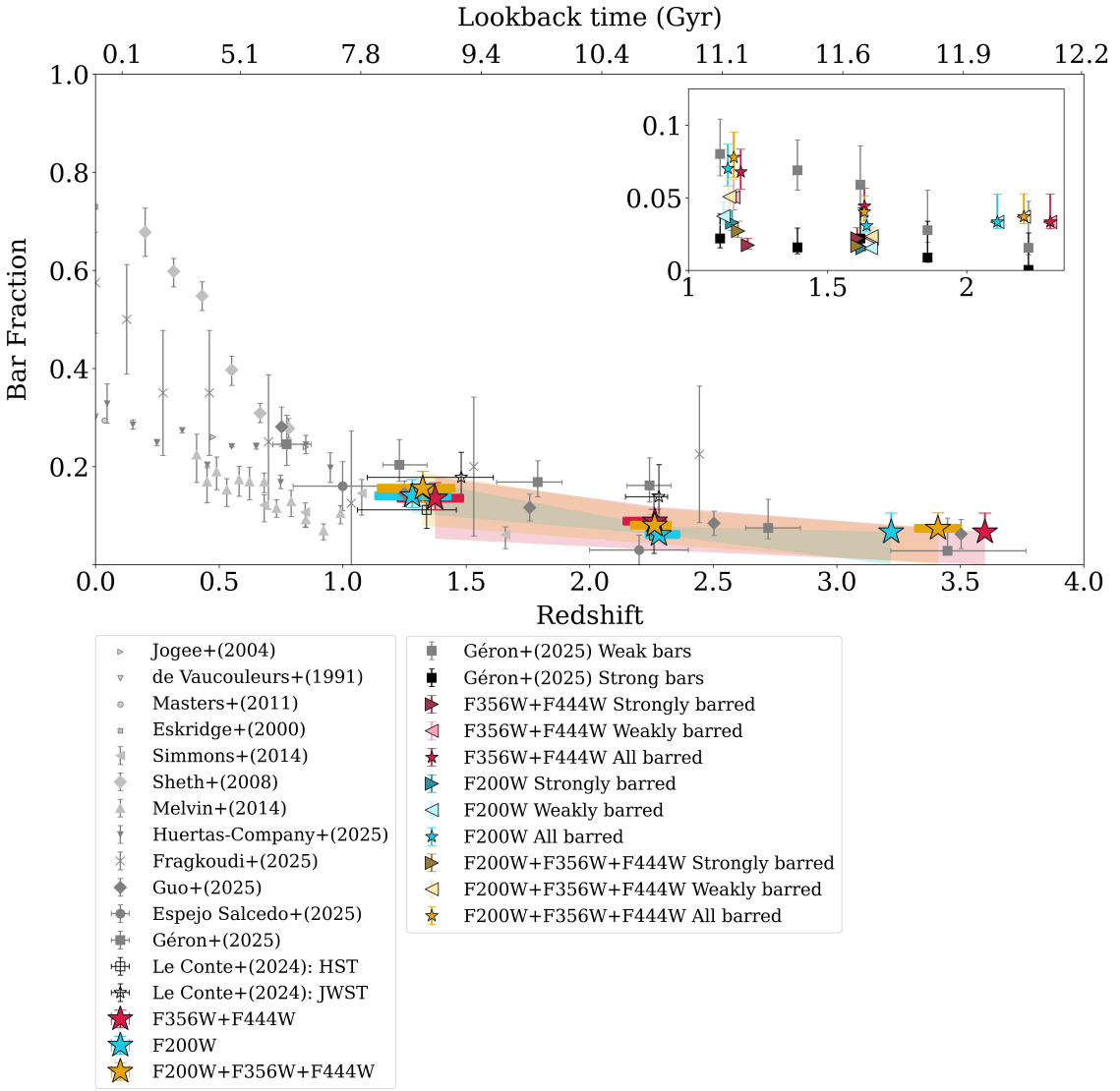

Figure 3.4: Evolution of the bar fraction in disc galaxies. At high-z the bar fraction is found in three redshift bins, $1 \leq z < 2$, $2 \leq z < 3$ and $3 \leq z \leq 4$, using the visual classification of the images from the JWST NIRCam filters F356W+F444W (red stars) and F200W (blue stars) and combining these results to find a total bar fraction (yellow stars). Error bars in f_{bar} are the 1σ bimodal interval, and the shaded area is the upper and lower bounds of the bar fraction (see text for details). Dashed horizontal error bars show the full range in z of the identified bars, while thick horizontal solid lines show the corresponding 25%-75% inter-quartile range. The insert shows the bar fraction for the breakdown of strongly (right-pointing triangle) and weakly (left-pointing triangle) barred galaxies. The results of Chapter 2 are black unfilled squares (HST) and stars (JWST), and in grey are the JWST bar fraction of G25 (diamond), ES25 (circle) and GZ CEERS (square).

Redshift	Bar Fraction								
	F200W			F356W+F444W			F200W+F356W+F444W		
	SB	WB	B	SB	WB	B	SB	WB	B
$1 \leq z < 2$	$0.07^{+0.02}_{-0.01}$	$0.07^{+0.02}_{-0.01}$	$0.14^{+0.03}_{-0.02}$	$0.03^{+0.01}_{-0.01}$	$0.10^{+0.02}_{-0.02}$	$0.14^{+0.03}_{-0.02}$	$0.05^{+0.01}_{-0.01}$	$0.10^{+0.02}_{-0.02}$	$0.16^{+0.03}_{-0.03}$
$2 \leq z < 3$	$0.03^{+0.01}_{-0.01}$	$0.03^{+0.01}_{-0.01}$	$0.06^{+0.02}_{-0.01}$	$0.04^{+0.01}_{-0.01}$	$0.04^{+0.01}_{-0.01}$	$0.09^{+0.02}_{-0.01}$	$0.03^{+0.01}_{-0.01}$	$0.05^{+0.01}_{-0.01}$	$0.08^{+0.02}_{-0.01}$
$3 \leq z \leq 4$	-	$0.07^{+0.04}_{-0.01}$	$0.07^{+0.04}_{-0.01}$	-	$0.07^{+0.04}_{-0.01}$	$0.07^{+0.04}_{-0.01}$	-	$0.07^{+0.03}_{-0.01}$	$0.07^{+0.03}_{-0.01}$

Table 3.2: The bar fraction for the visually classified samples in F200W, F356W+F444W and F200W+F356W+F444W in three redshift bins. The f_{bar} is presented for strongly barred galaxies (SB), weakly barred (WB) and all barred galaxies (B). No strongly barred galaxies were found beyond $z = 3$. The errors shown are the statistical 1σ bimodal intervals (see the text for details).

ES25, G25, and GZ CEERS are consistent with my results within the uncertainties. These JWST studies support the conclusion that the bar fraction is twice that found in HST and that the onset of bar formation occurs earlier than previously thought.

The bar fraction is broken down into its weakly and strongly barred counterparts across the redshift range in the insert of Figure 3.4, compared to the strong and weak bar fractions of GZ CEERS. A lower bar fraction is seen for my strongly barred galaxies, which remains ~ 0.05 across the redshift range $1 \leq z < 3$. At the lowest redshift bin, a higher bar fraction for weakly barred galaxies is found, which decreases towards higher redshifts. This difference between strongly and weakly barred galaxies is also found in GZ CEERS.

As detailed in § 2.4, I use the Jeffreys interval [Brown et al., 2001, Gelman et al., 2003, as argued in Cameron [2011]] to determine the statistical uncertainty on the bar fraction. The sample used in this study is approximately mass-complete, meaning I do not account for incomplete sampling in the uncertainty estimates. The visually classified derived bar fractions, with statistical uncertainties, for the single-band NIRCam images in either F200W, F356W+F444W, or combined can be found in Table 3.2.

Systematic uncertainties arise from difficulties in morphological classification and can be described by the agreement between classifiers. I introduced Randolph κ in § 3.3.3 and state the strong agreement between classifiers in over 70 per cent of cases.

However, since the κ thresholds for agreement better than chance are not universally agreed upon, I present a different method for the upper and lower bounds of the bar fraction. The shaded regions in Figure 3.4 represent the upper and lower bar fractions, obtained from a more lenient and a more restrictive threshold, respectively. The upper f_{bar} is determined by a barred and disc sample with a 2 out of 5 voter threshold, whereas the lower f_{bar} requires a 4 out of 5 consensus threshold. I include these variations on the voting threshold to emphasise the impact of classification definitions and consensus on the results. These upper and lower f_{bar} uncertainties encompass my results in this work and Chapter 2, and also the work of G25 and ES25.

3.5 Bar properties

Thus far, I have responded to the question of when the onset of bar formation occurs by exploring the bar fraction at $1 \leq z \leq 4$. I now wish to analyse these high-z barred galaxies in more detail and to understand how they differ from barred galaxies at $z < 1$ and $z \approx 0$. I explore the mass dependence of the bar fraction in § 3.5.1 and measure the evolution of the bar length in § 3.5.2 and strength in § 3.5.3.

3.5.1 Mass dependence

Observational studies have reported a dependence of the bar fraction on stellar mass from the local to high-redshift Universe [e.g., Erwin, 2018, Sheth et al., 2008]. I extend these investigations to $z \geq 1$ for my 95% empirically complete sample (discussed in § 3.2) between the redshift range $1 \leq z \leq 4$. In Figure 3.5, I show the mean stellar mass across the redshift range for my bars identified in F200W (blue) and F356W+F444W (red), separated into the weakly and strongly barred samples. The adopted completeness limit yields fewer massive galaxies at lower redshifts that host bars, whereas at higher redshifts bars are present in the most massive galaxies. This is, of course, driven by the redshift-dependent completeness limits, as the plot shows that all masses probed within these limits (from 10^9 to 10^{10}M$_\odot$) include barred galaxies. Nevertheless, I find that strongly barred galaxies

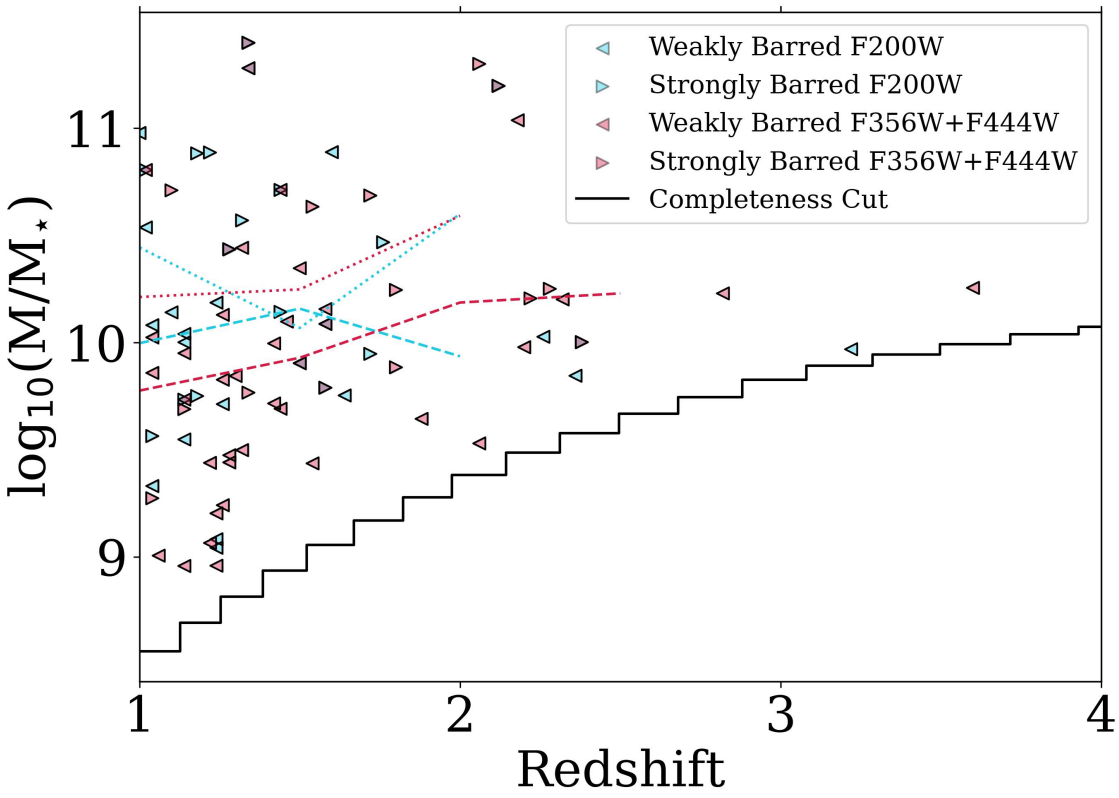

Figure 3.5: Stellar mass - redshift distribution of barred galaxies found by visual classification. For the independent studies using NIRCam filters F200W (blue) and F356W+F444W (red), galaxies are defined as strongly barred (right-pointing triangle, dotted) and weakly barred (left-pointing triangle, dashed). For the strongly and weakly barred galaxies, I show the mean stellar mass across the redshift range as dotted and dashed lines, respectively. The 95% empirical completeness adopted from Duncan et al. [2019] (black step function) sets the lower limit to the stellar mass distribution.

tend to have higher stellar masses across all redshifts. The mean is similar for both wavelength samples, with the spread in stellar masses being slightly greater in the longer wavelength sample.

I show the bar fraction dependence on stellar mass in Figure 3.6 for the two JWST samples. A low f_{bar} – about 0.1 or less – is seen in $\log(M_\star/M_\odot) \leq 10$. In F200W, a steady increase in the bar fraction with mass is observed for both weak and strong bars, rising to $f_{bar} \approx 0.2$ at $\log(M_\star/M_\odot) \approx 10.75$. At the highest stellar masses, $\log(M_\star/M_\odot) \approx 11.25$, f_{bar} peaks, with $f_{bar} > 0.2$ for the short wavelength, and with $f_{bar} > 0.5$ for the long wavelengths, but it is worth noting that this stellar mass bin is less statistically significant compared to the others, as it contains a small sample of only eight disc galaxies. Nevertheless, this trend of increasing bar fraction for higher galaxy masses agrees with the results using HST from Sheth et al. [2008], for galaxies at $0.37 < z < 0.84$ (see their Figure 3) and Melvin et al. [2014], for galaxies at $0.4 < z < 1.0$ (their Figure 5).

3.5.2 The bar length

Another open question I aim to address is at what length bars form and whether the bar length evolves over cosmic time. For the remainder of this study, I measure and analyse the lengths of my high-z barred galaxy sample at short and long NIRCam wavelengths to address these questions and test the impact of rest-frame wavelength on the observed evolution of bar length.

Visual and automated bar-fitting techniques are used to measure bar lengths, but in the local Universe, barred-galaxy studies have found that automated bar identification techniques, such as isophotal and Fourier analysis, are favourable for large samples. At higher redshifts, I find that automated processes remain challenging despite JWST's improved sensitivity. Ellipse fitting to star-forming massive galaxies at cosmic noon, and thus to clumpy and irregular systems, is used in this study, but it is challenging given the number of initial free parameters and requires tailoring for each galaxy to avoid spurious bar-length measurements. Consequently, I identify the barred galaxy sample through visual classification but use ellipse-fitting techniques to quantify bar properties. I emphasise that adjustments to the initial

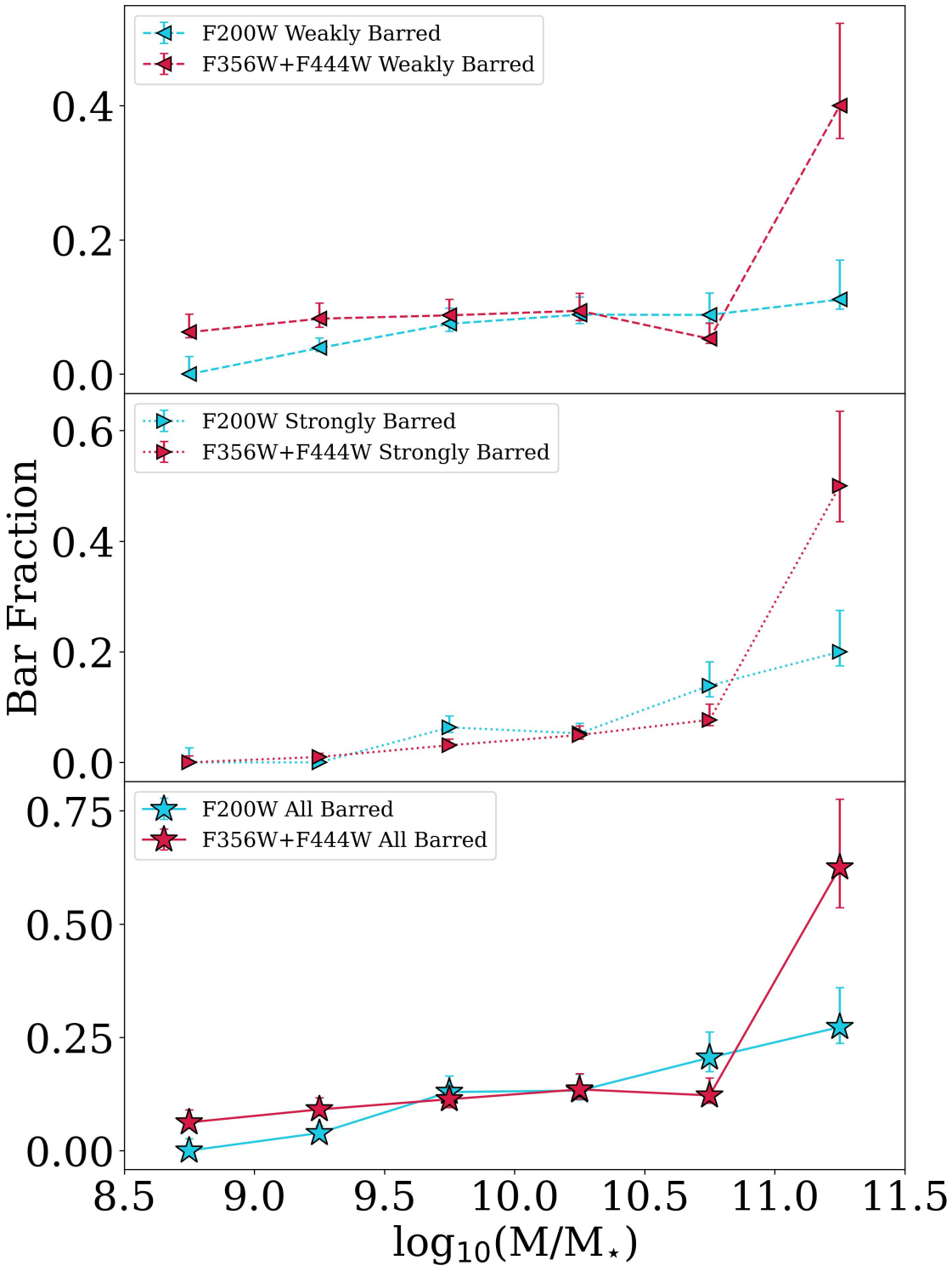

Figure 3.6: The fraction of bars in disc galaxies for a given stellar mass in the range $8.5 \leq \log(M_\star/M_\odot) \leq 11.5$. I show results for the NIRCam filters F200W (blue) and F356W+F444W (red). Three different samples are shown: weakly barred (top panel), strongly barred (middle panel), and the sum of both weakly and strongly barred galaxies (bottom panel). Error bars in f_{bar} show the 1σ bimodal interval.

parameters are made on a case-by-case basis and involve visual inspection of each galaxy's fitting. In some cases, this also involved adjusting the fitting parameters until a satisfactory fit was obtained, namely, one in which the fitted ellipses outlining the bar agree with my visual assessment.

To perform this structural analysis, the strongly and weakly barred galaxies from the visual classification are fitted by elliptical isophotes using `photutils.isophote` (for further details, see § 3.3.2) with fixed central coordinates obtained from the initial ellipse fits. The stellar bar can be traced by ellipse fits, which remain at a constant position angle, PA (with a change in PA, $\Delta\text{PA} \leq 10^{\circ}$) and a gradual increase in ellipticity, ε, towards the end of the bar. The end of the bar is the point at which the position angle changes by more than 10 degrees ($\Delta\text{PA} > 10^{\circ}$) and the ellipticity peaks (with $\varepsilon_{peak} > 0.2$). See Figure 2.1 for an example of the ellipse fit radial profiles discussed here. Some studies have found that the end of the bar can also be parameterised as a minimum in ellipticity, following the peak. Still, I found that this feature was not observed across all barred-galaxy ellipticity radial profiles. Hence, in this study, the bar length, L_{bar}, is defined as the average of the bar lengths at ΔPA and ε_{peak}, i.e., L_{bar} is effectively the semi-major axis of the bar.

The measured projected L_{bar} from ellipse fits is checked and adjusted through visual inspection of the radial profiles, and, when necessary, parameter thresholds are applied. Theoretical work shows that bars form in rotationally supported, cold stellar discs; hence, I assume that these high-z disc galaxies are dynamically settled and vertically thin. This assumption is vital as it enables us to deproject the measured L_{bar}, and is a reasonable assumption at least towards the ends of the bar, where it matters most. I thus derive the deprojected semi-major axis, semi-minor axis, ε, and PA of the observed projected ellipse at the end of the bar [for full derivation details, see Appendix A of Gadotti et al., 2007]. To carry out this deprojection procedure, I require the inclination of the galaxy, the position angle of the line of nodes and the position angle of the bar, all of which are derived through the ellipse fits.

I emphasise that this study of high-z barred galaxies has focused on the derived deprojected bar lengths. The deprojection technique, described in § 3.5.2, is depen-

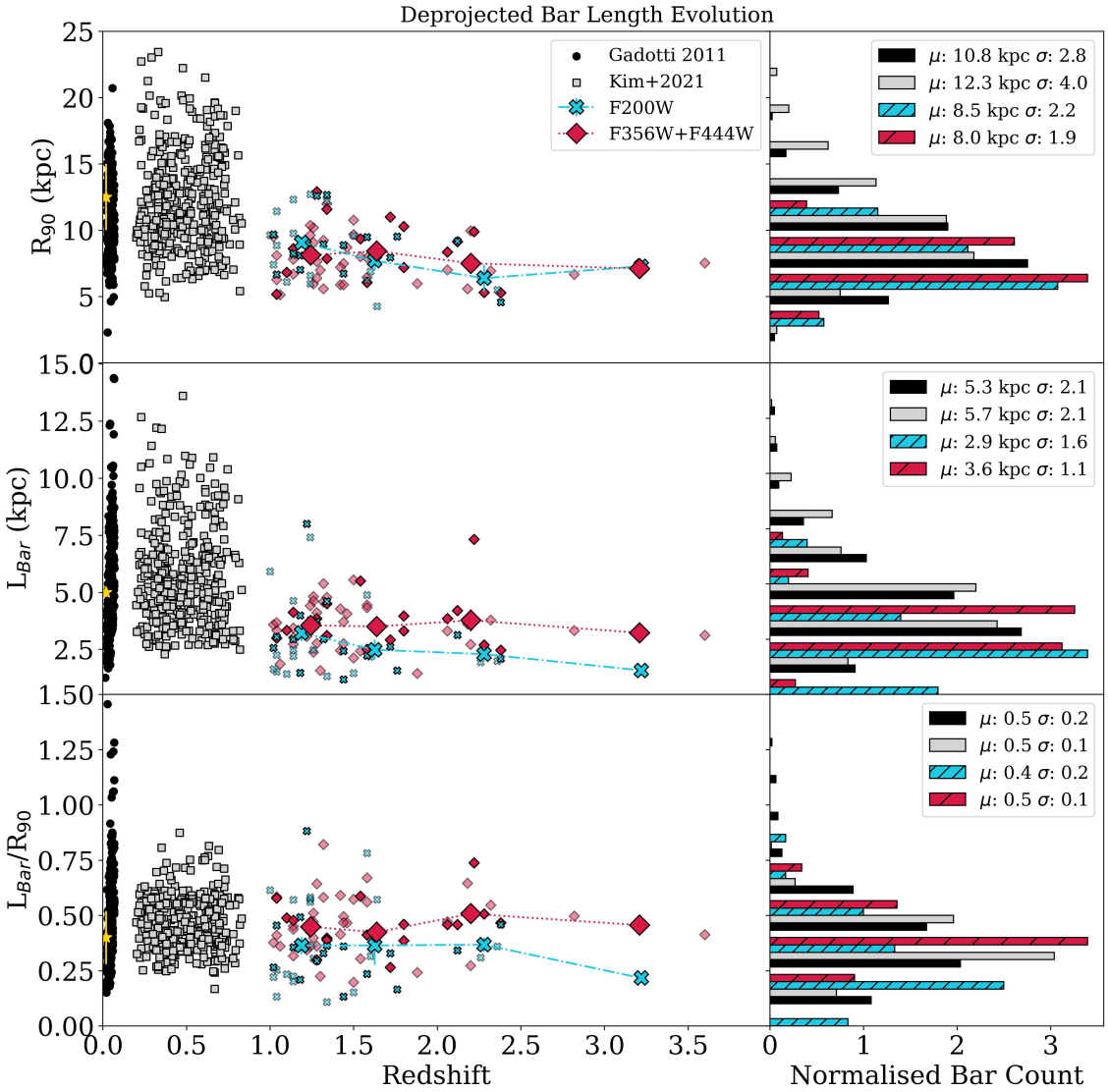

Figure 3.7: The evolution of the bar length over $0 \leq z \leq 4$. The left panels show lengths measured in this work from JWST NIRCam filters F200W (blue crosses) and F356W+F444W (red diamonds) for bars found in galaxies between the redshift range $1 \leq z \leq 4$, with their normalised distribution (see text for details) shown on the right panels. Weakly barred galaxies are shown as fainter markers, and strongly barred galaxies are brighter. The first row shows the distribution of R_{90}, whilst the second row is the deprojected L_{bar} and the third row is the normalised L_{bar}, L_{bar}/R_{90}. The high redshift sample is compared against a sample of SDSS $i-$band barred galaxies at $z \approx 0$ [G11, black circles], the Milky Way [with measurements from Bland-Hawthorn and Gerhard, 2016, yellow star], and a sample of barred galaxies at $0.2 < z \leq 0.835$ using F814W images from the COSMOS survey [K21, grey squares]. The mean, μ, and standard deviation, σ, for each parameter in each sample are shown in the right panel.

dent on the inclination of the galaxy, which is derived from the isophotal contours of the disc. This measurement of bar length is critical for making comparisons with lower-redshift studies that have near-face-on galaxy samples. The deprojected L_{bar} distribution for barred galaxies identified in short and long NIRCam wavelength filters is shown in the second row of Figure 3.7.

On average, shorter bars are measured in F200W, with a mean $L_{bar} \approx 2.9$ kpc, than in F356W+F444W, with mean $L_{bar} \approx 3.6$ kpc, but in both samples, the average L_{bar} has minimal variation across the redshift range, with the F200W values of L_{bar} increasing slightly towards lower redshifts. Additionally, the distributions of the two JWST samples overlap greatly, as can be seen in the right panel of Figure 3.7. In Figure 3.7, the bar count is normalised by dividing the count by the number of observations times the bin width to form a probability density. Bars as short as ~ 1 kpc are measured in F200W, but bars as long as ~ 8 kpc are found in both barred samples, showing that long bars are already present in $z \geq 1$.

The bar-length comparison across wavelengths is discussed for the entire barred-galaxy sample. However, I distinguish between strongly and weakly barred galaxies by making the markers in Figure 3.7 brighter and fainter, respectively. For the longer wavelength sample, there is no difference in the mean of the weakly and strongly bar lengths, which are 3.5 kpc and 3.8 kpc, respectively. Furthermore, the shorter-wavelength sample shows the same results, with the mean bar length for weakly barred galaxies being 2.8 kpc and 3.0 kpc for strongly barred galaxies.

To understand the origin of this minimal L_{bar} evolution in F200W and no evolution in F356W+F444W, I normalise L_{bar} by galaxy size and assess the evolution of both R_{90} and the ratio L_{bar}/R_{90}. I use the value of R_{90} as a proxy for galaxy size, where R_{90} is the distance from the centre of the galaxy that contains 90% of the total light in a given NIRCam filter. The first row of Figure 3.7 shows the evolution of R_{90} for the barred galaxy samples, along with their distribution on the right panel. The measured values of R_{90} cannot be disentangled for the two JWST samples across the redshift range. A slight increase towards lower redshifts is observed in F200W, whilst F356W+F444W remains approximately constant. To assess if the bar grows with disc size, or if the bar grows at rates greater than the growth of

the disc, I observe the evolution of the bar length normalised by disc size, L_{bar}/R_{90}, in the bottom row of Figure 3.7. Within the redshift range $1 \leq z < 2.5$, there is no evolution observed in either barred sample, and the shorter wavelength filter is marginally shorter than the longer wavelength filters. This result indicates that the increase in L_{bar} in F200W is accompanied by an increase in disc size.

This high redshift sample is compared to a sample of barred galaxies from SDSS at $z \approx 0$ [G11. See also Neumann et al., 2024, for more bar length measurements at $z \sim 0$]. The volume-limited, near-face-on, massive galaxy sample ($0.02 \leq z \leq 0.07$, $b/a \geq 0.9$, $> 10^{10}\mathrm{M}_{\odot}$) is fit for a bulge, disc and bar in $i-$band images, to determine a sample of 291 barred galaxies. The SDSS PSF FWHM at $z \approx 0.05$ results in a spatial resolution of ≈ 1.5 kpc, meaning the resolution of the SDSS sample is comparable to the longer NIRCam wavelength filter, at $z \sim 2$. The mean $L_{bar} \approx 5.3$ kpc is slightly longer than that measured for the JWST sample; however, the distribution strongly overlaps with that of the JWST sample. Similarly, the values of R_{90} at $z \approx 0$ are ~ 2 kpc greater than the high-z sample, but the entire distributions overlap. The normalised bar length is found to be the same at $z \approx 0$ and $z \geq 1$, with the distributions peaking at $L_{bar}/R_{90} = 0.5$. That is, longer bars are found in larger discs in SDSS, as in the JWST samples, resulting in a constant ratio.

The Milky Way stellar mass, disc size and bar length are indicated in Figure 3.7, and taken from Bland-Hawthorn and Gerhard [2016]. The Milky Way has features comparable to those of the local barred galaxy population.

I bridge the gap between $z \approx 0$ and $z > 1$, using a sample of 379 barred galaxies identified in the F814W images from the COSMOS survey at $0.2 < z \leq 0.835$ with $10.0 \leq \log(\mathrm{M}_{\star}/\mathrm{M}_{\odot}) \leq 11.4$ [K21]. Ellipse fits are used to measure L_{bar}, and the physical resolution of COSMOS is ≈ 0.6 kpc at $z \approx 0.5$, making it comparable to the PSF FWHM of F200W in JWST NIRCam at $z \approx 2$. The COSMOS sample has the longest mean L_{bar} (5.7 kpc) and a broader distribution. Bars with $L_{bar} < 2$ kpc have not been identified in this sample, possibly due to the selection of more massive galaxies than my high-z sample, namely a mass cut such that $\log(\mathrm{M}_{\star}/\mathrm{M}_{\odot}) \geq 10$. This observation is supported by the association that the most massive galaxies host the longest structures in the local Universe [e.g., Díaz-García et al., 2016, Erwin,

2019]. However, it should be noted that the $z \approx 0$ SDSS sample of G11 has the same mass cut but does not show a similar dearth of bars with $L_{bar} < 2$ kpc. Many long bars, greater than 6 kpc, are found across the redshift range of G11, K21, and such bars are present but not abundant beyond $z = 1$. The disc size of this intermediate sample is shifted towards the larger end, but exhibits stronger overlap with the high-z sample than the bar length does. However, the normalised bar length achieves the same ratio as $z = 0$ and $z \geq 1$, which means that the bar length scales with the size of the disc.

Surprisingly, while I see an increase of ≈ 2 kpc in the mean values of L_{bar} from $z > 1$ to $z \approx 0$, there is significant overlap in all distributions. Additionally, when the bar length is normalised by the disc size, I find that its value, L_{bar}/R_{90}, remains approximately constant on average from $z = 4$ to $z = 0$. In this context, it is also interesting to note that bars as long as $4 - 6$ kpc are already abundant at $z > 1$, and this corresponds to the mean bar length at $z \sim 0$ [G11]. However, I observe a population of bars with lengths of $8 - 12$ kpc at $z < 1$ that is not seen at higher redshifts. The lack of long bars is due to the smaller size of high-z disc galaxies.

For completeness, I share the evolution of the projected bar length from $1 \leq z \leq 4$ in Figure 3.8, in the NIRCam filters F200W and F356W+F444W. No significant differences are found.

The population of long bars with $L_{bar} > 8$ kpc at low and intermediate redshifts, found in G11 and K21, respectively, suggests that in some galaxies a period of pronounced bar growth commences after the formation of high-z bars, which are measured in this study to be < 8 kpc (and more typically less than < 6 kpc). To assess the validity that bars with $L_{bar} > 8$ kpc do not exist at Cosmic Noon, and that a period of growth occurs, I consider volume effects. The area of SDSS (3324 deg^2) and COSMOS (2 deg^2) are significantly larger than in CEERS; hence, long bars in my sample could be missed due to their rarity and the smaller volume of CEERS (88 arcmin^2). The co-moving volumes of the samples from G11 and K21 are larger than the co-moving volume of CEERS between $1 \leq z \leq 4$ by a factor of ~ 11 and ~ 12, respectively. However, in nearby disc galaxies, 37 very long bars were observed, whilst 58 were found at intermediate redshifts. This means that one

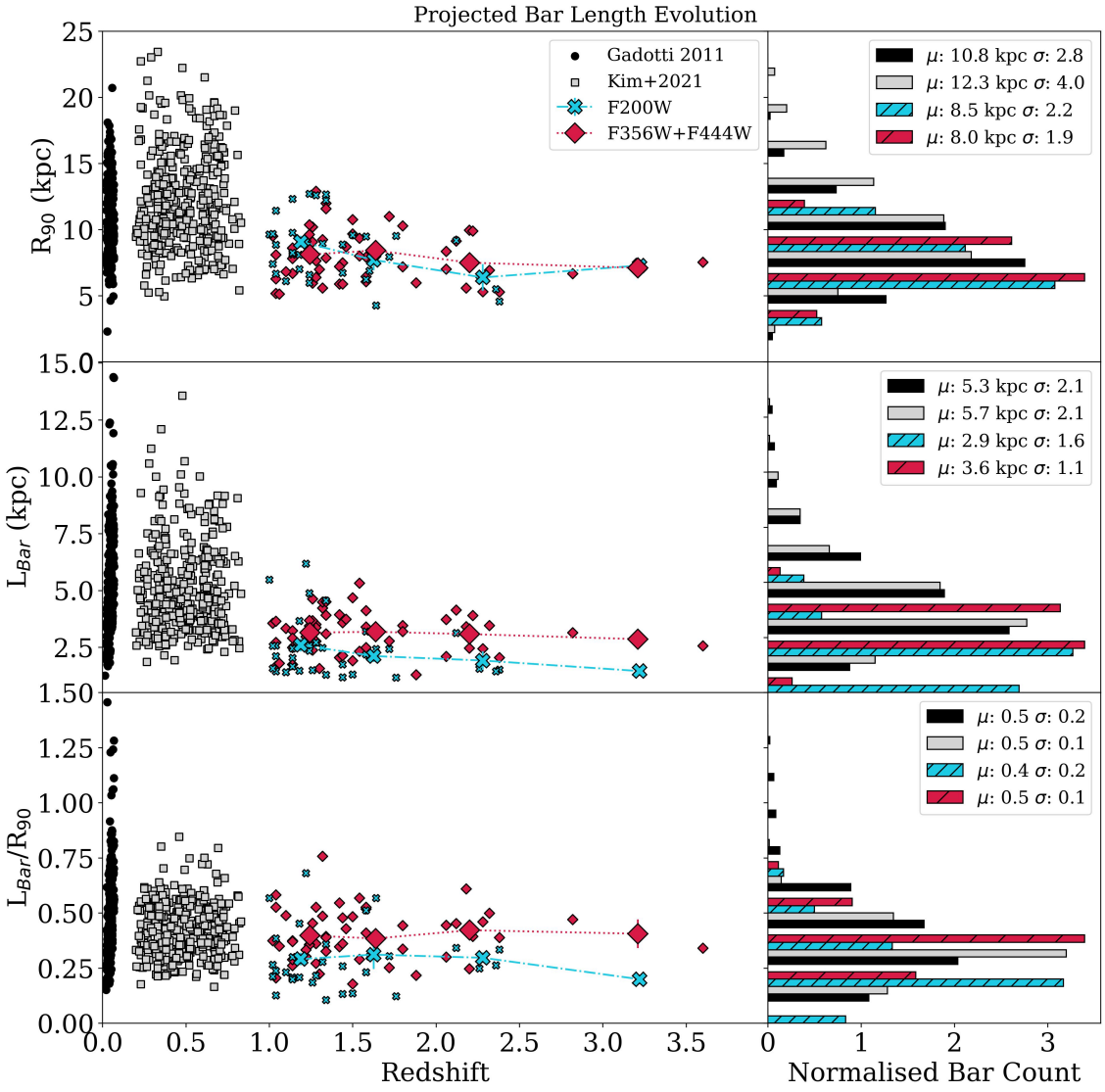

Figure 3.8: The evolution of the bar length over $0 \leq z \leq 4$. The left panels show lengths measured in this work from JWST NIRCam filters F200W (blue) and F356W+F444W (red) for bars found in galaxies between the redshift range $1 \leq z \leq 4$, with their normalised distribution shown on the right panels. The first row shows the distribution of R_{90}, whilst the second row is the projected L_{bar} and the third row is the normalised L_{bar}, L_{bar}/R_{90}. The high redshift sample is compared against the projected values from a sample of SDSS $i-$band barred galaxies at $z \approx 0$ [G11, black] and a sample of barred galaxies at $0.2 < z \leq 0.835$ using F814W images from the COSMOS survey [K21, grey]. The mean, μ, and standard deviation, σ, for each parameter in each sample are shown in the right panel.

bar with $L_{bar} > 8$ kpc is observed per $251,824$ Mpc^3 and $178,274$ Mpc^3 for the two samples, respectively. Since the co-moving volume of this study is $884,085$ Mpc^3, approximately 4 and 5 long bars should be identified if the occurrence follows G11 and K21, respectively. Therefore, the lack of long bars at high-z is not determined to be due to volume effects, but rather could indicate a period of bar growth.

3.5.3 The bar ellipticity

Various techniques and definitions are used to determine a bar's strength. These include, but are not limited to, the axis ratio; the ratio of the fluxes inside and outside of the bar (i.e., the bar contrast); the ratio of the $m = 2$ and $m = 0$ Fourier components. Many of these methods require deprojecting and decomposing the galaxy image; however, bar and central component modelling is beyond the scope of this chapter. Therefore, in this study, the bar's strength is parameterised as the projected ellipticity of the ellipse at L_{bar}. Nevertheless, I note that measuring the bar ellipticity, ε_{bar}, in high-redshift galaxies can be severely affected by unresolved bright central sources, the prominence of the central component, and PSF and resolution effects, as I show below. Here, I present an initial assessment of the bar ellipticity at high redshifts and briefly compare short- and long-wavelength filters. Additionally, the previously described deprojection technique is not used, as it can spuriously broaden the bar if the bar's position angle is aligned with the line of nodes.

The distribution of ε_{bar} is shown in Figure 3.9 for short and long JWST NIRCam wavelengths and is compared to the SDSS barred galaxy sample at $z \approx 0$. The bar count is normalised as in Figure 3.7. The ellipse-fitting technique is shown to underestimate the ellipticity by 20 per cent in Gadotti [2008]; hence, I derive the corrected ε_{bar} as $\varepsilon_{bar} \times 1.2$. The mean $\varepsilon_{bar} \approx 0.4$ for the sample of barred galaxies in F356W+F444W, but for F200W, there is a greater proportion of elongated bars; however, the entire F200W sample also results in a mean $\varepsilon_{bar} \approx 0.4$. These high redshift bars thus appear significantly rounder than the near face-on (disc axial ratio $b/a \geq 0.9$) bars observed at $z \approx 0$, for which the mean $\varepsilon_{bar} \approx 0.6$. I speculate that the barred galaxies in F356W+F444W may appear rounder due to lower resolution than in F200W. Overall, the bars in the high-z sample are rounder than those in

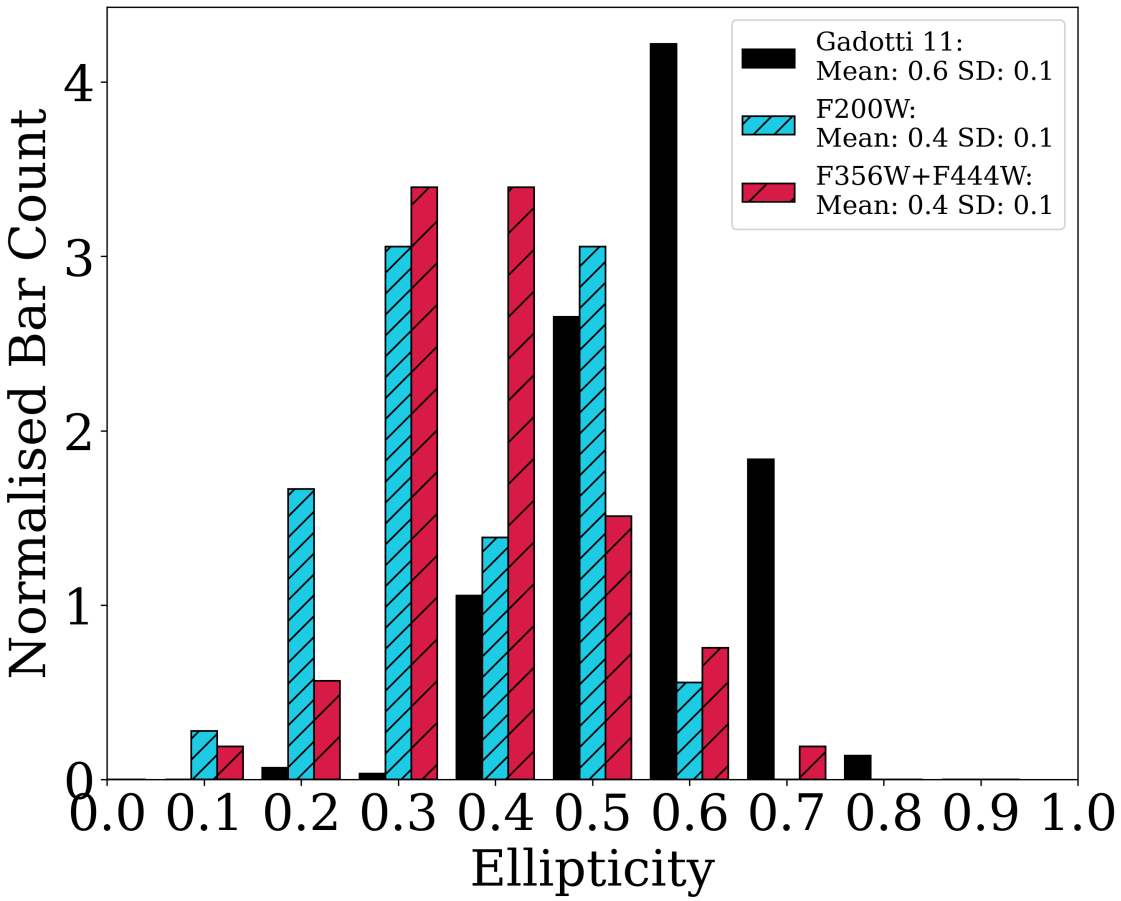

Figure 3.9: Distribution of the projected bar ellipticity for JWST NIRCam filters F200W (double hatched) and F356W+F444W (hatched) for bars found in galaxies in the redshift range $1 \leq z \leq 4$. The high redshift sample is compared against a sample of SDSS barred galaxies at $z \approx 0$ [G11, solid black]. The mean ellipticity and standard deviation are given for each sample.

the $z \approx 0$ sample; however, I cannot rule out the possibility that unresolved bright galactic centres and the broadening of central structures by the PSF may artificially make bars appear rounder.

3.6 Discussion

In this study, I report on the evolution of the bar fraction over the redshift range $1 \leq z \leq 4$. I identified a significant population of high-redshift barred galaxies with the bar fraction decreasing from $f_{bar} \approx 0.16^{+0.03}_{-0.03}$ at $1 \leq z < 2$ to $0.08^{+0.02}_{-0.01}$ at $2 \leq z < 3$ and $0.07^{+0.03}_{-0.01}$ at $3 \leq z \leq 4$. I also measured the evolution of the absolute value of the deprojected bar length from $z = 4$ to $z = 0$, finding shorter bars in the F200W filter and little to no evolution in both samples. Subsequently, I measured the normalised bar length relative to disc size and found no evolution from the local to the high-redshift Universe.

Identifying barred galaxies at high redshift poses several challenges, particularly due to spatial-resolution limitations and cosmological surface-brightness dimming. It should be noted that observational studies spanning $z = 0 - 4$ used to map the evolutionary path of barred galaxies employ different rest-frame wavelengths, which can affect the derived structural parameters. The sample analysed in G11 is based on rest-frame optical data, in the SDSS i-band. However, K21 measured bar lengths using F814W, which corresponds to the rest-frame $g-$ and r-bands in the corresponding redshift range. In this study, I use a combination of filters that probe a broader wavelength range: rest-frame $g-$ to $i-$bands using the F200W filter, and rest-frame $i-$band to NIR ($\sim 1.6\mu m$, H-band equivalent) using the F356W+F444W filters. Below, I discuss my main findings, particularly regarding the co-evolution of discs and bars.

3.6.1 Capturing short bars with the F200W filter

How confident can I be that I have identified the entire barred galaxy population? The simulation-based work of Liang et al. [2024, hereafter referred to as L24] suggested that the bar fraction would be significantly greater, $f_{bar} > 40$ per cent for

$z < 3$, when using the shorter wavelength channels of NIRCam for improved spatial resolution. This motivated a repeat of the study with both the F200W and F356W+F444W filters. I discussed the limitations of using the long wavelength filter, F444W, in § 2.5 as bars shorter than $\sim 2-3$ kpc were missed from the sample, since the PSF FWHM is 0.145″; hence, in this study, I aimed to test if I could capture the shorter bars by performing visual classification on F200W as well, with its improved PSF FWHM of 0.07″.

Surprisingly, I found no difference in the bar fraction between the two samples (i.e., with the F200W and F356W+F444W filters), despite obtaining different barred galaxy populations. I suggest that the similar result in the bar fraction is due to the shorter-wavelength filter being subject to dust and star-formation obscuration, whilst the longer-wavelength images trace the underlying older stellar population of the bar more accurately. Thus, I combined the two samples to capture both the shorter bars observed in F200W and those observed only in F356W+F444W, which are obscured at shorter wavelengths. This combined sample agrees within the uncertainties with the independent bar fractions of this study and with the few other studies on the high-z bar fraction [ES25, G25, GZ CEERS].

Simulations predict that bars are strengthened and grow with time [e.g., Algorry et al., 2017, Athanassoula, 2003]. In the context of missing shorter bars, this would suggest that toward the highest redshift end, it becomes more difficult to identify young bars, as their size could be below the detection threshold [Erwin, 2005]. In my efforts to mitigate biases, I still observe a decreasing bar fraction trend; however, it is less steep than previously reported by HST investigations. Nevertheless, I acknowledge that this bar fraction could still be a lower limit due to redshift effects, including reduced physical spatial resolution, surface-brightness dimming, and possibly enhanced gas/dust content and star formation at high redshifts.

Attempting to disentangle the true length of the bars, I compared the bars in F200W with those of F356W+F444W. Systematically, the bars are shorter in F200W than in F356W+F444W images. The simulation work from L24 commented on the robustness of barred studies at high-z, and showed that the PA is unchanged by resolution effects and that the bar size is minimally affected under the condition

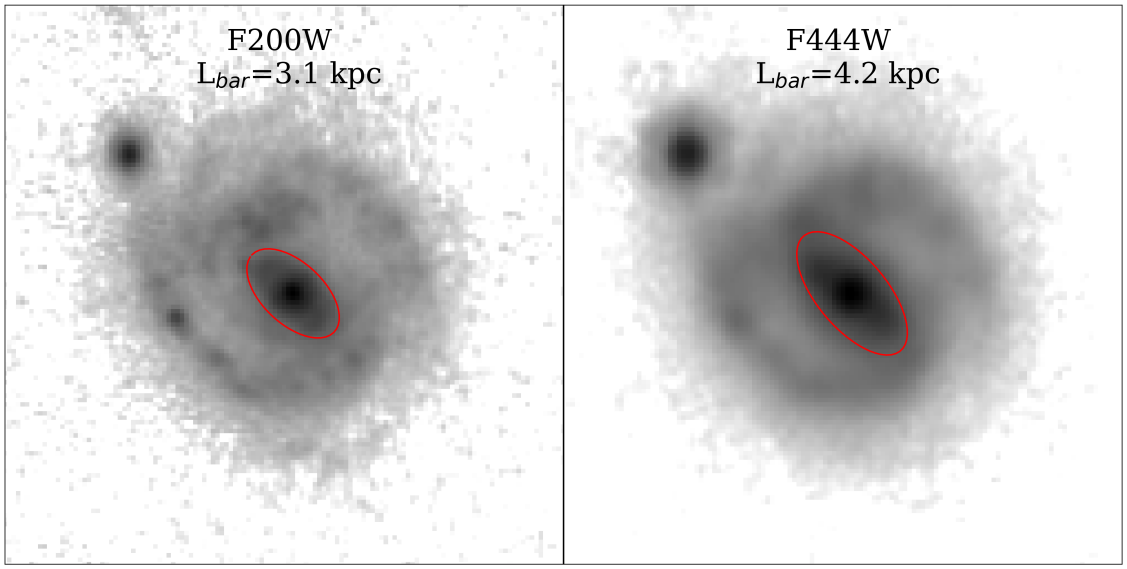

Figure 3.10: Single-band images of the example galaxy EGS 23205 in the NIRCam filters F200W (left) and F444W (right) at $z \approx 2.1$. The deprojected bar length is specified, and the bar is represented by a red ellipse. This galaxy is chosen to illustrate how bars are measured to be shorter in the short wavelength channels of NIRCam than in the long wavelength channels. The rest-frame wavelength is $\sim 0.645\mu m$ and $1.4\mu m$ for the two wavelengths, respectively.

that $L_{bar} > 2\times$ FWHM.

Considering the mean L_{bar} measured in F200W images is 2.9 kpc, the bias-corrected bar length $L_{corr} = 2.93$ kpc [For further details see § 3.6.5, or Equation 4 of L24]. Hence, considering resolution effects, the short-wavelength bars remain systematically shorter than those obtained with longer-wavelength filters.

For galaxies identified as barred in both the short and long wavelength filters of NIRCam, I measure the ratio of bar length, $\frac{L_{bar,F356W+F444W}}{L_{bar,F200W}}$. I find that the bars in F356W+F444W are 1.4 times as long as those in F200W.

To understand the phenomenon behind this result, I show the example galaxy EGS 23205 in Figure 3.10 in both filters. In this case, the bar is clearly shorter in the shorter-wavelength image. I speculate on the origin of this observation; this galaxy is at $z \approx 2.1$, meaning that the corresponding rest-frame wavelength for F200W is ~ 6450Å.

It is known that bars are more apparent in the NIR than in visible wavelengths [e.g., Marinova and Jogee, 2007]. Hence, the ends of the bar in EGS 23205 are fainter/obscured in F200W due to the bar dust lanes crossing the bar-spiral arm

boundary. Therefore, the fact that I find that on average bars tend to be shorter in F200W as compared to F356W+F444W seems to be due to two effects: first, because of the effect just mentioned at the bar-spiral arm boundary, but also, second, because the better spatial resolution in F200W allows us to see some short bars that are not detected in F444W.

In contrast, bars were found to be 9 per cent longer in B-band observations than at $3.6\mu m$ in 16 nearby S^{4}G galaxies in Menéndez-Delmestre et al. [2024]. On the other hand, an increase in bar length and ellipticity at bluer wavelengths was not observed in the study by Gonçalves et al. [2025], which analysed 50 barred galaxies in the TNG50 simulations. However, when considering only star-forming galaxies, the wavelength dependence becomes prominent. The authors argue that the older stars populating the bar form shorter, rounder bars, whilst younger stars extend to greater radii, thereby increasing bar length and ellipticity. This contrasts with my results, where bars are *shorter* at shorter wavelengths. However, it is not clear whether the effects of dust absorption and scattering are comparable across these studies and those of this chapter. In addition, the aforementioned studies have employed much broader wavelength ranges than I do here. Furthermore, it should be noted that star-forming spiral arms become more apparent at bluer wavelengths, which can bias bar-length measurements based on ellipse fits to trace bars as longer structures, artificially extending beyond the boundary between the spiral arms and the stellar bar. In this study, I have carefully inspected my ellipse fits individually and taken appropriate action to counter this effect (see § 3.5.2).

3.6.2 Bar length-stellar mass relation

I showed that strongly barred galaxies are most commonly found in the most massive galaxies in § 3.5.1 in my nearly mass-complete sample of high-z galaxies. To explore further the mass dependence of these high-z barred galaxies, I show the bar length versus the galaxy mass in Figure 3.11.

In the local Universe, the well-known association between bar size and stellar mass was observed in S^{4}G galaxies by Díaz-García et al. [2016]. Erwin [2019] reported on a correlation between bar length and galaxy mass, which is nearly flat for

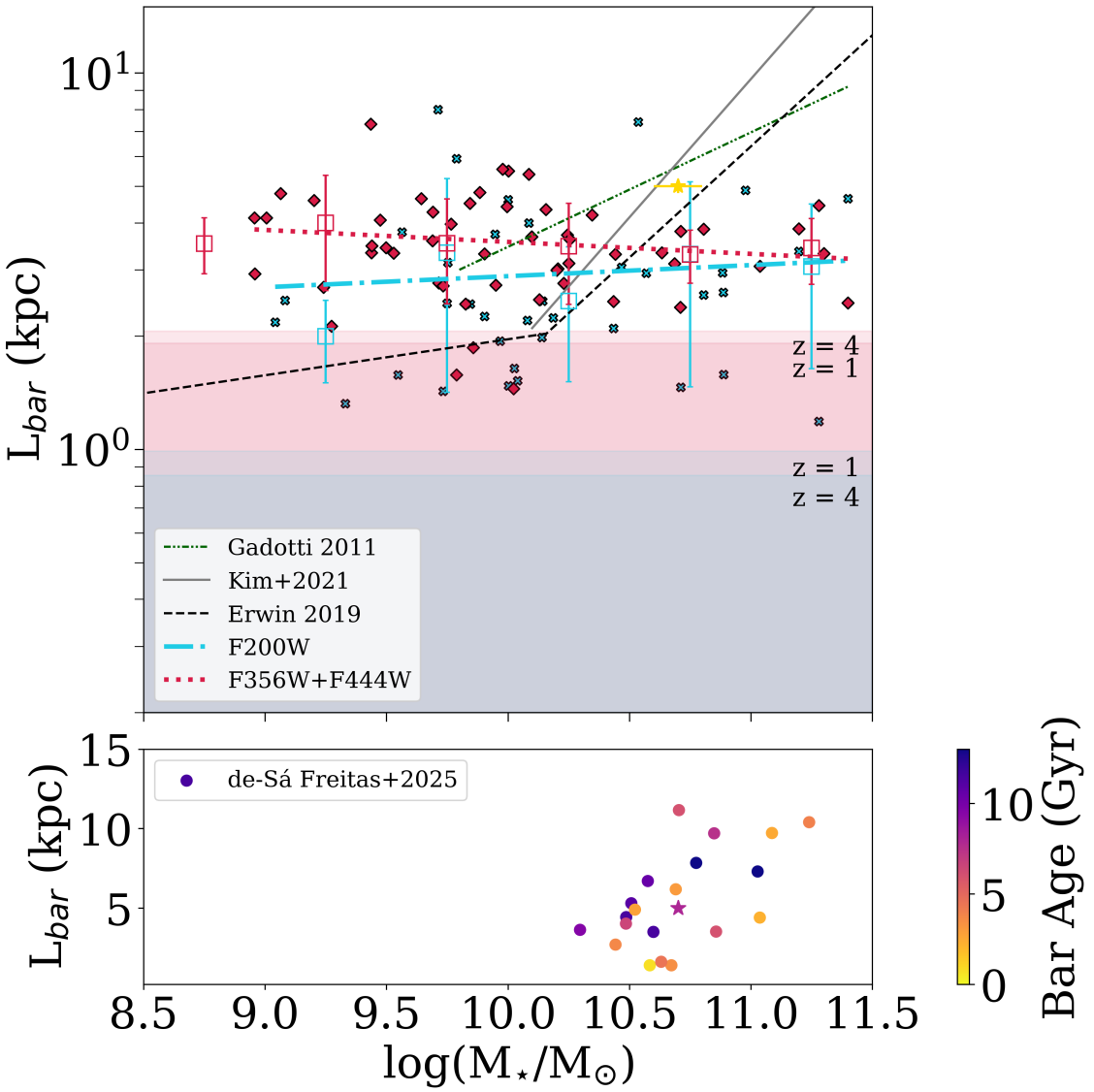

Figure 3.11: Bar length versus stellar mass for JWST NIRCam barred galaxies at $1 \leq z \leq 4$. The two JWST samples in F200W (crosses) and F356W+F444W (diamonds) with ordinary least squares fits (dash-dotted and dotted, respectively); binned mean L_{bar} as boxes and standard deviation as error bars. The star indicates the Milky Way [see results in Bland-Hawthorn and Gerhard, 2016, Wylie et al., 2022]. The green dashed-dotted line is the ordinary least-squares fit to nearby SDSS barred galaxies from G11. The grey solid line is the ordinary least squares bisector fit to barred galaxies between $0.2 \leq z \leq 0.8$ from K21. The black dashed line shows the locally weighted regression fit for nearby S^4G spiral galaxies from Erwin [2019]. The red and blue shaded regions show $2 \times$ FWHM for the lower and upper redshift boundaries of the F356W+F444W and F200W samples, respectively. The bottom panel shows the bar-length stellar mass relation for local galaxies, with bar ages estimated.

$\log(M_\star/M_\odot \leq 10)$ and becomes steep for greater masses; hence, the most massive disc galaxies are host to the largest structures (see his Fig. 1). The Milky Way resides on this relation, with the Galactic stellar mass and bar length taken from Bland-Hawthorn and Gerhard [2016] and the bar age from Wylie et al. [2022].

The sample does not show a steep relation for $\log(M_\star/M_\odot \geq 10)$, as I measure shorter bars in the most massive galaxies at high redshifts than in their local counterparts. Using an ordinary least-squares fit, I find that the galaxies in the F200W sample follow $\log(R_{bar}) = 0.20 \times \log(M_\star/M_\odot) + 0.91$, and that the galaxies in the F356W+F444W sample follow $\log(R_{bar}) = -0.26 \times \log(M_\star/M_\odot) + 6.15$. The improved PSF FWHM of the F200W sample implies that I should observe shorter bars in less massive galaxies; however, my observations lie above the linear relation.

I also report on the fit to nearby SDSS galaxies in G11, which follow the S^{4}G trend, albeit with a shallower slope. Additionally, the intermediate redshift, $\log(M_\star/M_\odot) \geq 10$ barred galaxy sample from K21 scales to L_{bar} with a slightly steeper linear fit than to the S^{4}G sample.

I show the steeper relation of K21 in Figure 3.11, which is derived from their entire sample with a redshift range of $0.2 < z < 0.8$. However, the authors reported that the relation depends on the redshift. Hence, considering only galaxies at $z \geq 0.5$, the steepness of the relation decreases; see their Fig. 2d. I report that the relation is flat for $z > 1$; hence, between $0.5 < z < 1.5$, I suggest that the relation evolves. Based on the deviation between the high and low-z relations at $> 10^{10} M_\odot$, the greatest growth would occur in the most massive galaxies.

In fact, in the inset of Figure 3.11, I show the bar length as a function of galaxy mass for the sample of local galaxies for which bar ages were estimated in de Sá-Freitas et al. [2025]. These initial results indicate that older bars lie within the upper envelope of the locally observed relation, which is generally consistent with this conjecture.

However, further studies with larger samples are required to make definitive statements. Toward the less-massive end, the JWST samples lie above the flatter relation. I speculate that these galaxies are progenitors of the more massive galaxies in the local Universe; hence, they would grow in mass and shift towards the steeper

linear relation at $z = 0$. These results suggest that the bars at $z > 1$ are forming long, through mechanisms independent of their stellar mass, such as mergers. The lack of a trend is supported by the perspective of simulations on bar length evolution, namely the finding of merger-induced long bars in Fragkoudi et al. [2025, see § 3.6.4 for further discussions].

3.6.3 The "downsizing" scenario

In Figure 3.5, the mean stellar mass for strongly barred galaxies is greater than that of weakly barred galaxies, identified in either short or long wavelength images across the redshift range. Furthermore, the strongly barred fraction in disc galaxies surpasses the weakly barred fraction toward the most massive end of Figure 3.6, altogether suggesting that the first bars formed in the most massive galaxies. These results are consistent with the proposed model for "downsizing" in bar formation, in which the lowest-mass galaxies could be the most dynamically hot due to the greater effects of star formation, accretion, and interactions. Hence, the most massive disc population has the greatest ability to withstand these interactions and remain dynamically cold [Sheth et al., 2012], thus being subject to bar instabilities.

On the other hand, de Sá-Freitas et al. [2025] found no correlation between the bar age and the total present-day stellar mass of galaxies in the TIMER sample of nearby galaxies, which contrasts with the downsizing scenario. The possibility of reconciling these seemingly opposing results concerns the effects of the environment. If interactions form bars that grow stronger faster than bars that form with no help from interactions [e.g., Łokas et al., 2016], then, by considering that the most massive galaxies tend to reside in denser environments, the most massive galaxies would form stronger bars even without downsizing effects. Testing this possibility with a quantitative measurement of the environmental density for the galaxies in my sample of barred galaxies would thus be of major importance, but is beyond the scope of this chapter.

3.6.4 Co-evolution of the bar and disc

Prior to JWST, measuring bar lengths beyond $z = 1$ was limited, and my understanding of how bar length evolves was informed by simulations. Athanassoula [2003] reported that the bar length should evolve, in coordination with the slowing down of the pattern speed of the bar, causing the co-rotation radius to expand to greater radii, hence increasing the growth potential for the bar.

In this study, one sees that there is a slight increase in both bar length and disc size from $z = 4$ to $z = 1$, which corresponds to a period of approximately 4 Gyr, but then at the transition between $z \approx 1.5$ and $z \approx 0.5$ (which also corresponds to about 4 Gyr) there is a sharp increase in both parameters, which remain approximately constant (on average) all the way to $z \approx 0$.

These results show that bars at $z > 1$ have lengths between 1 kpc and 8 kpc, with a mean $L_{bar} = 2.9 - 3.6$ kpc, depending on the observed wavelength. Across the redshift range $0 \leq z \leq 4$, I observe no evolution in the normalised bar length. I observe some evolution in the mean absolute bar length (2 kpc on average) and the appearance of very long bars (i.e., with $L_{bar} > 8$ kpc; see Figure 3.7). In addition, while bar length correlates with galaxy mass for bars at $z < 1$, I find that this is not the case beyond $z = 1$ (see Figure 3.11). These results do not necessarily imply that individual galaxies do not evolve; rather, they indicate that the overall population exhibits little average evolution. The current sample of bars at $z > 1$ is not large enough to test the dependencies predicted by simulations, but such studies would be important follow-ups.

The bars identified in this study are at different evolutionary stages, even within the same redshift bin; thus, the mean values of the properties provide a broad representation of the ages and stages of bar evolution. In simulations, the formation time of the bar, as well as the mechanisms under which the bar forms, are known, and it has been seen that the evolutionary rate of the bar depends on the environment and host galaxy properties [see, e.g., Athanassoula and Misiriotis, 2002, Fragkoudi et al., 2025, Łokas et al., 2016].

Remarkably, the bar length normalised by disc size from the local to the high redshift Universe is constant at $L_{bar}/R_{90} \approx 0.5$ (see Figure 3.7). This result indicates

that the growth of a bar scales with the disc size. In other words, both bars and discs grow from high redshifts to $z \sim 0$, but do so at a similar rate.

In the Auriga suite of magneto-hydrodynamical cosmological zoom-in simulations [Grand et al., 2017], Fragkoudi et al. [2025] reported on the evolution of 39 Milky-Way-like barred galaxies. Through significant merging events at $z > 1.5$, bars form with lengths that remain at $4 < L_{bar} < 7$ kpc. However, bars that form at later epochs are shorter due to disc instabilities and evolve in length. My results are consistent with these findings, as I see both some evolution of the mean bar length towards $z < 1$, as well as bars at $z > 1$ that are already as long as the mean bar length at $z \sim 0$, namely ~ 5 kpc, and even some bars at $z > 1$ with lengths up to 8 kpc.

3.6.5 Bar ellipticity correction

The parameter most affected by low-resolution images is the bar ellipticity [L24]. In § 3.5.3, I share the results that the average ε_{bar} in JWST bars is significantly less than that reported at $z = 0$. These values correspond to projected measurements, as deprojecting the bar can systematically yield lower ε_{bar} (i.e., rounder bars) when the bar is aligned with the galaxy line of nodes.

L24 showed the impact of resolution levels, defined as $n = L_{bar}/\mathrm{FWHM}$, on the mean fractional difference ($\overline{\Delta\varepsilon/\varepsilon}$) between true and observed bar ellipticities for simulated data (see their Fig. 10). I can use $\overline{\Delta\varepsilon/\varepsilon}$ to obtain the bias-corrected bar ellipticity, following Equation 4 in L24.

The mean resolution level for the F200W sample is $n = 5.1$, and the standard deviation is 2.8. Hence, the mean n corresponds to the value $\overline{\Delta\varepsilon/\varepsilon} = -0.10$. Thus, for the average F200W bar ellipticity, $\varepsilon_{bar} = 0.4$, the bias-corrected average bar ellipticity becomes $\varepsilon_{corr} = 0.48$. Figure 3.12 shows the shift from rounder observed bar ellipticities in the F200W sample, which are significantly rounder than the SDSS sample at $z = 0$, to more elongated structures when corrected for resolution effect biases.

I do not repeat this bias correction in the JWST F356W+F444W sample, as the resolution corrections derived from simulated data are produced from images in the

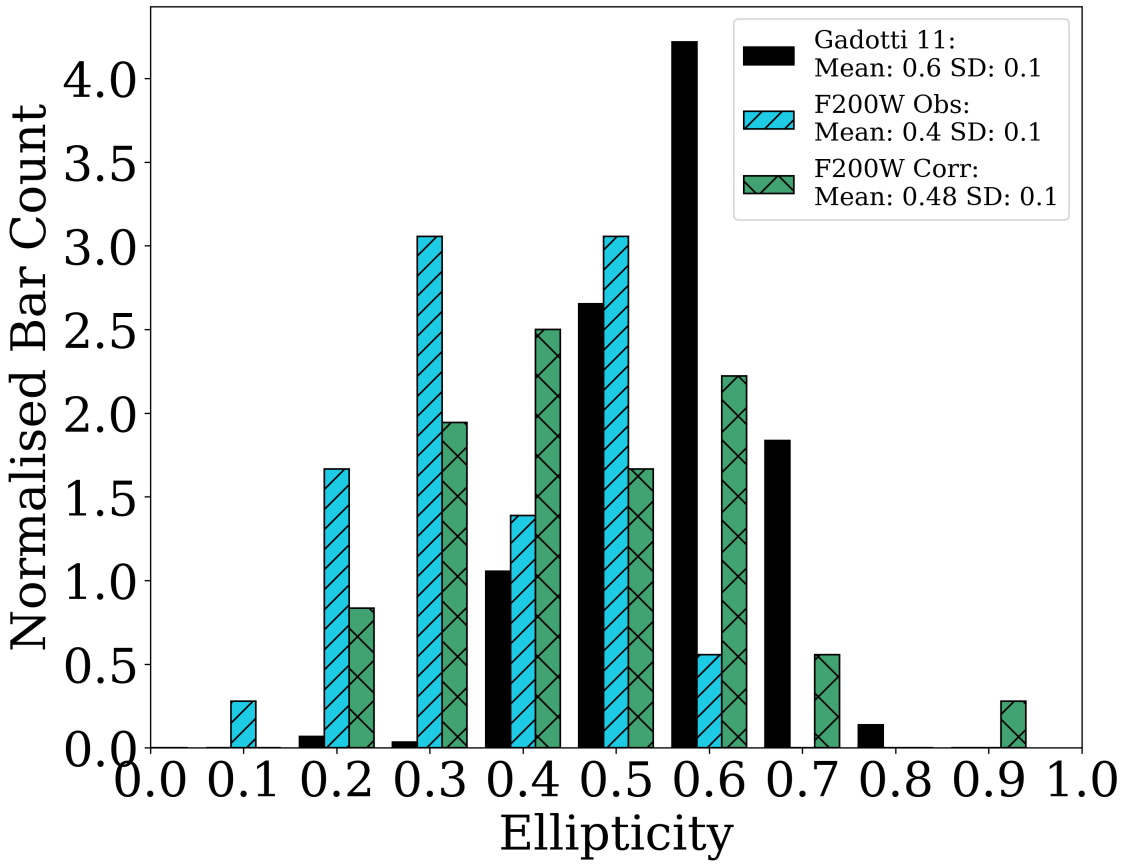

Figure 3.12: Distribution of the projected bar ellipticity for the JWST NIRCam filter F200W (double hatched) and corrected for resolution effects (cross hatched) for bars found in galaxies in the redshift range $1 \leq z \leq 4$. Bias-corrected bar ellipticities are derived from L24 (their Equation 4). The high redshift sample is compared against a sample of SDSS barred galaxies at $z \approx 0$ G11 (solid black). The mean ellipticity and standard deviation are given for each sample.

F200W filter in L24, but I caution that the correction would most likely be greater, as the PSF FWHM worsens towards longer wavelengths in NIRCam. This implies that the barred structures observed at high-z are often rounder and broader due to resolution effects, but could, in reality, resemble the well-defined, elongated bars in nearby disc galaxies.

3.7 Summary and conclusions

I observed that bar-driven secular internal evolution began earlier than previously thought, only 2 billion years after the Big Bang. This was made possible by the JWST NIRCam's improved sensitivity and longer wavelengths. Several studies of

barred galaxy abundance have observed that the bar fraction declines towards higher redshifts; however, it is twice that previously measured in HST studies [ES25, G25, GZ CEERS]. To date, only G25 have explored the evolution of the bar length for a barred galaxy sample at $z > 1$. Hence, I measure the bar fraction and bar-length evolution in a sample three times the size of the initial sample in Chapter 2.

This study uses NIRCam imaging of all 10 CEERS pointings and selects a 95% empirically complete sample of 2438 galaxies in the redshift range $1 \leq z \leq 4$. To assess the wavelength dependence of the bar fraction and properties, I applied the methodology to two independent samples in different NIRCam wavelength filters: with the filters F356W+F444W I observe the older stellar population in the bar; the filter F200W has an improved PSF FWHM, to capture bars shorter than $\sim 2-3$ kpc, which may go undetected in the F356W or F444W images.

Neighbouring sources are removed using SExtractor. The samples are then optimised using ellipse fits to remove highly inclined systems, after which the samples comprise 1073 and 649 galaxies in the F356W+F444W and F200W filters, respectively. IMFIT is used to fit 2D Sérsic models to the images, and through parameter limits, 152 and 37 point sources are removed from the F356W+F444W and F200W samples, respectively. The disc and barred galaxy samples are obtained by visual classifications from five participants, and a bar fraction is derived for the F200W and F356W+F444W samples. Using the ΔPA and ε_{peak} values from the ellipse fits, I derive the deprojected bar lengths for the barred galaxy samples at Cosmic Noon.

A similar bar fraction is observed for both samples, and by combining the two samples I find a declining trend in the bar fraction: $0.16^{+0.03}_{-0.03}$ at $1 \leq z < 2$; $0.08^{+0.02}_{-0.01}$ at $2 \leq z < 3$; $0.07^{+0.03}_{-0.01}$ at $3 \leq z \leq 4$. These results are consistent with my previous work and other recent bar fraction investigations, suggesting that dynamically cold, rotationally supported massive discs (and therefore bar-unstable) are present at Cosmic Noon. Nonetheless, at least a fraction of these observed bars could have formed via interactions triggering the bar instability in otherwise stable discs.

The lowest bar fraction ($< 10\%$) is seen for galaxies with $\log(M_\star/M_\odot) \leq 10$, which then raises to about 20% for galaxies with $\log(M_\star/M_\odot) \approx 10.75$ and above. These results suggest that the first bars formed in the most massive galaxies, con-

sistent with the "downsizing" model of bar formation. However, I discuss how interactions can trigger stronger bars in more massive galaxies without leading to downsizing.

Systematically shorter bars in the short-wavelength channel are observed due to the higher spatial resolution, but I suggest that dust obscuration may also contribute to this result. Interestingly, I find that the correlation between bar length and galaxy mass for galaxies more massive than $10^{10}\mathrm{M}_{\odot}$ observed at $z < 1$ is not seen at $z > 1$.

No evolution in the bar length is measured in the long-wavelength NIRCam images in the range $1 \leq z \leq 4$, with a mean of 3.6 kpc, but a slight increase of about 1 kpc from $z = 4$ to $z = 1$ is measured in the short-wavelength images, which have a mean of 2.9 kpc. By adding samples of barred galaxies studied with images from HST (at $0.2 < z < 0.8$) and SDSS (at $z \approx 0$), from K21 and G11, respectively, I find that the absolute value of bar length increases by about 2 kpc on average from $z = 4$ to $z = 0$. However, there is significant overlap in the distributions of bar lengths at all redshifts. In addition, I show that bars and discs grow in tandem, for the bar length normalised by disc size, L_{bar}/R_{90}, does not evolve from $z = 4$ to $z = 0$.

Finally, I show that some bars at $z > 1$ are already as long and as strong as the average bar at $z \approx 0$. On the other hand, I find that the long bars (with $L_{bar} > 8$ kpc) found at $z < 1$ are not seen beyond $z = 1$. Altogether, my results show that, as a population, bars grow only moderately longer from $z > 1$ to $z < 1$, with long bars already present at $z > 1$, but that some bars have undergone significant growth during the same period.

CHAPTER 4

Structural properties of barred galaxies at $z \geq 1$

In this chapter, I present a study that builds on previous chapters and uses robust analytical techniques to measure the structural properties of barred galaxies at Cosmic Noon.

Stellar bars are common structures in the local Universe, and become less frequent as we look back to earlier epochs. However, with the improved capabilities of JWST, studies have revealed a significant population of high-redshift barred galaxies, at $z \geq 1$. The bar is a key driver of internal galaxy evolution, and a system's evolutionary progress can be probed through its structural properties. To derive the structural properties of barred galaxies in the early Universe, I photometrically decompose 27 strongly barred galaxies at $z \geq 1$, imaged with JWST CEERS in F200W, F356W, or F444W. I fit three components to the images: a disc (an exponential function), a bar (a generalised Sérsic function), and a central component (a Sérsic function). I find that the high-redshift population of barred galaxies has structural properties similar to those of nearby galaxies, specifically a peak bar-to-total luminosity of 0.1, an ellipticity of 0.6, and a bar length of 3 kpc. I also find that bars in passive galaxies contribute more luminosity to their host galaxies, are rounder, and have flatter light profiles than those in star-forming galaxies. In this study, I have confirmed that well-established, evolved stellar bars exist at Cosmic Noon, suggesting that their formation must be rapid to produce bars similar to those in nearby galaxies. This work highlights the need to re-evaluate the mechanisms at play in bar formation and disc settling in the early Universe and suggests that important aspects of bar-driven evolution are not secular.

4.1 Introduction

In the previous two chapters, I have established a significant population of barred galaxies at Cosmic Noon. Chapter 3 reported on the length and ellipticity of these barred galaxies, finding that minimal evolution occurred at $z > 1$; however, a population of long bars (> 8 kpc) is missing at these high redshifts. Previously, I derived the bar's structural properties via ellipse fitting; however, this technique has limitations, as the ellipsoidal shape is inherently rounder. Thus, I use the robust image-analysis technique of 2D photometric decomposition to derive the structural properties of this barred-galaxy population at high redshifts, with the aim of deciphering how these bars evolve across cosmic time.

This chapter is ordered as follows: I briefly summarise the barred galaxy sample in § 4.2, describe the image preparation and procedures of photometric decomposition in § 4.3, present the structural properties of the disc § 4.4.1, bar § 4.4.2, and central component § 4.4.3, before discussing challenges of high redshift studies and how these results impact the commonly used term 'secular' in § 4.5, and finally share my conclusions in § 4.6.

4.2 Data and sample selection

In this chapter, I build on the analysis of the strongly barred galaxies identified in Chapter 3. Hence, in this study, I select JWST CEERS NIRCam images in the filter in which a strongly barred galaxy was identified. The filters used in Chapter 3 were selected to test the wavelength dependence of the bar fraction by conducting two independent visual classifications, one in the short-wavelength channel of NIRCam with the F200W filter, and one in the long-wavelength channel of NIRCam with the F356W filter for galaxies at redshifts $z < 2$, and the F444W filter for galaxies at $z \geq 2$. Therefore, in this study, I have selected 16 galaxies in the F200W filter, 11 in the F356W filter, and six in the F444W filter. Of these, six galaxies are classified as strongly barred in both the short- and long-wavelength filters, meaning I have a sample size of 27 strongly barred galaxies. The strongly barred galaxy sample is shown in Figures 4.1 and 4.2 for all of the NIRCam filters used in this study.

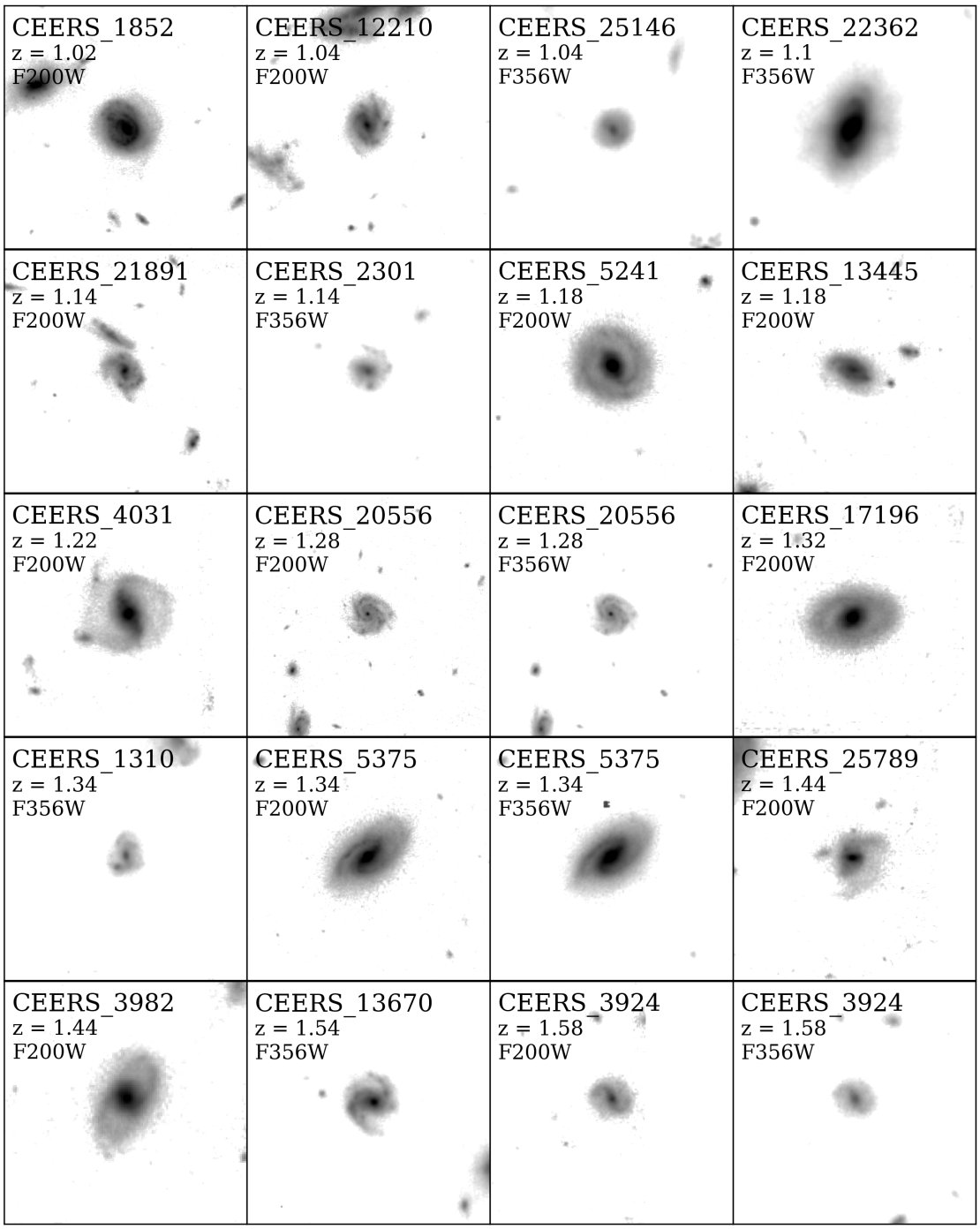

Figure 4.1: JWST NIRCam images of 27 strongly barred galaxies identified in one or more of the filters F200W, F356W, and F444W in the redshift range $1 \leq z \leq 4$. The CEERS ID, redshift, and NIRCam filter of the galaxy are noted in the top left corner of each image.

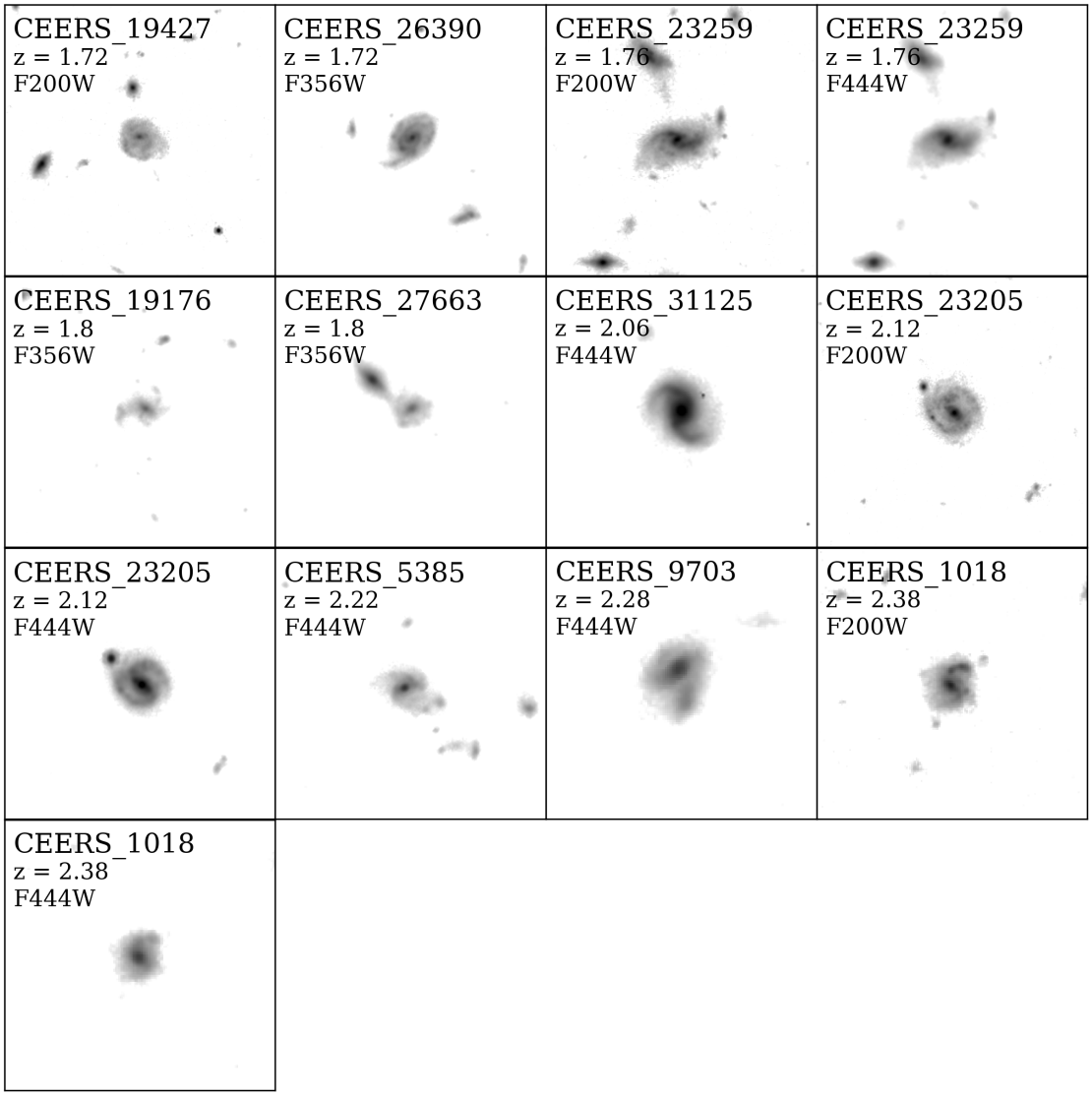

Figure 4.2: A continuation of Figure 4.1.

The NIRCam exposures we retrieved from the `Mikulski Archive for Space Telescopes (MAST)` and reprocessed with the official JWST pipeline (v1.8.2, CRDS v1084), following the procedures of Ferreira et al. [2023] and Adams et al. [2023] but incorporating several refinements which are summarised in § 3.2.1. To ensure sub-pixel alignment across the dataset, each filter is reprojected onto the F444W grid at a pixel scale of $0.03''\text{pixel}^{-1}$. A comprehensive description of the workflow and its validation is given in Adams et al. [2024], Conselice et al. [2024], Harvey et al. [2025]. We thus produce 30 mas 128×128 pixel cutouts from the NIRCam data.

In this study, I use the photometric redshifts and stellar masses from Duncan et al. [2019]. In alignment with Chapter 3, the galaxy sample lies in the redshift range $1 \leq z \leq 4$.

By using both the short- and long-wavelength channels of NIRCam, I trace different stellar components in these galaxies. For example, a galaxy at $z = 2$ imaged in F200W will have a rest-frame wavelength of 0.67μm, residing in the R-band, whereas the same galaxy imaged in the F356W or F444W filter will be at a rest-frame wavelength of 1.19μm and 1.48μm respectively, and correspond to the NIR. Additionally, the short-wavelength channel has a lower NIRCam empirical PSF FWHM[1], resulting in improved spatial resolution. The F200W PSF FWHM is $0.066''$; corresponding to a linear resolution of 0.567 kpc for $z = 2$. The PSF FWHM degrades for longer-wavelength filters; hence, the F356W and F444W PSF FWHM are $0.116''$ and $0.145''$, corresponding to a linear resolution of 0.996 kpc and 1.245 kpc, respectively.

4.3 Photometric decomposition

The properties of stellar structures contain information about the galaxy's evolutionary history and the mechanisms that drive it. In this thesis, I focus on the impact of bar-driven evolution in young galaxies at Cosmic Noon. Bar-driven evo-

[1]JWST user documentation: https://jwst-docs.stsci.edu/jwst-near-infrared-camera/nircam-performance/nircam-point-spread-functions

lution is traceable by the growth of the stellar bar component, with regard to its strength and length, and the formation of central components, such as bulges, which all relate to the properties of the host galaxy. A powerful technique for deriving a galaxy's structural properties is two-dimensional photometric decomposition.

Photometric decomposition is a robust analytical technique that identifies, separates, and quantifies the surface-brightness contributions of individual structural components in 2D images. Structural properties are derived from fitting multi-component models to the surface-brightness distribution. In this study, I use the program IMFIT v1.8 [Erwin, 2015] to perform photometric decompositions on 33 NIRCam images in the filters F200W, F356W, and F444W on a population of 27 strongly barred galaxies at $z \geq 1$.

I fit all images with three components: (i) a disc, (ii) a bar, and (iii) a central component. As described in § 3.3.2, the sample has been selected to avoid overly inclined galaxies ($i < 65°$), and I do not perform deprojection of the images. The individual components are combined to form a model image, which is matched to the original image by adjusting the parameters of the 2D mathematical function via χ^2 minimisation. I select the differential evolution (DE) minimisation routine, which I describe in § 4.3.2, and provide details on NIRCam image preparation in § 4.3.1. I describe the radial light/mass profiles of the three components below.

Disc components are described by an exponential function. The disc exponential function is built by the extrapolation of concentric and homologous ellipses, defined by position angle $\mathrm{PA_d}$ and ellipticity ε_d, in the form of:

$$\varepsilon = 1 - \frac{b}{a}, \tag{4.1}$$

where b is the length of the minor axis and a is the length of the major axis of the ellipse. Thus, the intensity of a given ellipse is such that:

$$I_d(r) = I_0 \exp(-r/h) \tag{4.2}$$

whereby r is the distance from the centre along the semi-major axis of the ellipse, I_0 is the central intensity of the disc, and h is the scale length of the

disc.

Bar components are described by a generalised Sérsic function. Meaning, the concentric and homologous ellipses are in fact generalised ellipses. Specifically, a bar is described by the Lamé curve [Lamé, 1818], an ellipse with more than two foci, and appears as a rounded rectangle. The generalised ellipse of a bar with position angle $\mathrm{PA_b}$ and ellipticity ε_b is described as:

$$\left(\frac{|x|}{a}\right)^{c_0+2} + \left(\frac{|y|}{b}\right)^{c_0+2} = 1 \tag{4.3}$$

where $|x|$ and $|y|$ are the distances from the ellipse centre, whereby the ellipse is centred at the origin, and the ellipse semi-major axis is along the x-axis. The boxiness of bars is parameterised by c_b, where $c_b < 2$ indicates a discy bar and $c_b > 2$ indicates a boxy bar; $c_b = 2$ is a regular ellipse. IMFIT measures the deviation from a regular ellipse c_0, where $c_b = c_0 + 2$. The intensity for a given generalised ellipse is defined as:

$$I_b(r) = I_e \exp\left(-b_n\left[\left(\frac{r}{r_e}\right)^{1/n} - 1\right]\right), \tag{4.4}$$

where I_e is the intensity at the effective radius r_e, n_b is the Sérsic index, and b_n is a parameter that is a fixed function of n. I use this model to obtain the effective radius of the bar ($R_{e,b}$) and the Sérsic index (n_b), and, in conjunction with the disc and central component models, to define the bar-to-total luminosity ratio (Bar/T).

Central component is a generic term to describe the unknown physical nature of the excess central brightness contribution, and does not inform us on whether this contribution originates from a classical bulge, a B/P, a rotationally supported nuclear disc, or other physical candidates, such as nuclear star clusters or even AGN.

I parameterise this central mass concentration with a Sérsic function, and preemptively classify the physical nature of the component with the Sérsic index, n_c. Such that, $n_c > 2$ describes a classical bulge, i.e., a pressure-

supported spheroid, while $n_c < 2$ typically describes a rotationally supported disc, thus indicating a nuclear disc [Fisher and Drory, 2008]. However, further analysis is required to determine the true physical nature of this component, which would benefit from direct measurements of stellar kinematics, though such measurements are challenging at high redshifts.

The central component is also described by concentric and homologous ellipses, as in equation 4.1, with position angle $\mathrm{PA_c}$ and ellipticity ε_c. The intensity, $I_c(r)$, for a given ellipse is defined as in equation 4.3, where the Sérsic index is denoted as n_c, the effective radius of the central component is $(R_{e,c})$, and the central component-to-total luminosity ratio is (C/T).

Collectively, I fit 18 free parameters to each NIRCam image, incorporating all three structural components. I subtract the combined models from the original NIRCam image to create a residual image that can be assessed visually for unmodelled stellar structures, such as spiral arms and nuclear stellar structures.

4.3.1 Image preparation

I prepare the NIRCam images for IMFIT through a series of steps. Firstly, I use SExtractor to create masks of neighbouring sources, background objects, and foreground stars that IMFIT rejects and are not incorporated into the component models. Additionally, I convert the NIRCam pixel units from MJy/sr to DN/s by dividing each image by the `FLUXCONV` constant specified in the image header.

The model components are described in the IMFIT configuration file. I edit the configuration file to have the corresponding gain, readout noise, subtracted background, and exposure time for a given NIRCam filter. Additionally, in the configuration file, I specify the centre of a galaxy as the derived central coordinates from the ellipse-fitting routine described in § 3.3.2. The central coordinate is constrained to lie between ±2 pixels of the specified value. This central coordinate is used by IMFIT to fit structural components centred on it.

The model image is convolved with a PSF image to better match the original NIRCam images. I fed IMFIT with simulated NIRCam PSF images generated by

STPSF package [Perrin et al., 2014]. I selected a region of ±20 pixels centred on the galaxy to convolve with an oversampled PSF (oversample = 4), so that the bright central regions, where a more accurate PSF convolution is desirable, receive a higher-resolution convolution.

4.3.2 Differential evolution

The IMFIT program can optimise model fits via three different algorithms. Firstly, the Levenberg-Marquardt (LM) algorithm is a commonly used optimisation algorithm in astronomy; for example, it is employed in GALFIT. This method is favourable because it often converges faster than first-order methods, thanks to the Gauss-Newton algorithm; however, when interpolating with iterative gradient descent, the LM algorithm can be trapped in local minima. Alternatively, the Nelder-Mead (NM) simplex algorithm is less likely to be trapped in local minima but is slower. It is a direct-search method that iteratively transforms in the χ^2 landscape through reflection, expansion, and contraction. These two algorithms require careful selection of the initial parameter values for the functions used to fit the images. To prevent getting trapped in local minima, the process may be repeated, with the initial values adjusted after inspecting the resulting model fits. However, this can be a tedious and biased technique within the complex parameter space that characterises galaxy photometric decompositions.

Two other algorithms are available in IMFIT: the Markov Chain Monte Carlo (MCMC) and Differential Evolution (DE) algorithms. These unsupervised methods benefit from global optimisation, making them less likely to be trapped in local minima of the χ^2 landscape; however, this comes at the cost of significantly slower computation. On a sample of nearby barred galaxies, Gadotti [2026] tested the unsupervised DE and MCMC method against the supervised NM method and determined that the fits are in excellent agreement. In addition, these galaxies were identified as having nuclear discs based on stellar kinematics, and the central component fits from the unsupervised routines produced models with stellar parameters consistent with nuclear discs. Hence, in this study, I use the DE algorithm [Storn and Price, 1997] to minimise the fit statistic and identify the best-fit model. Since

this method is based on global optimisation, the algorithm does not require an initial guess for the function parameters; instead, it requires upper and lower bounds, which I specify based on an inspection of the NIRCam images.

4.4 Structural properties

Bars are ubiquitous in nearby disc galaxies and are key drivers of internal galaxy evolution. Studies of these nearby systems find that the properties of the stellar bar depend on those of the host galaxy. However, in the early universe, disc galaxies exhibited a range of properties, including higher star formation rates, smaller sizes, and greater dynamical heat from recent mergers and interactions. These conditions have led studies to conclude that bar formation begins at $z < 1$; however, Chapters 2 and 3 show that it occurs earlier than previously thought. Additionally, the latter measures the evolution of bar length. Hence, this chapter uses different image analysis techniques to determine whether these bars differ from those in the local Universe by measuring the stellar properties of the disc and bar. This will also provide insight into the significance of bar-driven evolution in young galaxies.

To derive the stellar structural properties of high-redshift barred galaxies, I have performed photometric decompositions of NIRCam images using three-component fits. These components consist of the disc, the bar, and the central component. I show the three separate components, combined model, and residual image of unmodelled stellar structures for the example galaxy CEERS 3924 in Figure 4.3. The residual image has a compressed surface-brightness range to highlight unmodelled structures, with dark regions indicating emission and light regions indicating no emission. This galaxy is a near-face-on disc at redshift $z = 1.58$ with two prominent spiral arms extending from the central bar. A fit of the three components is achieved, and the residual image shows significant light deficits on either side of the bar, known as the 'Dark Gaps', which can be used to probe the bar strength. Additionally, an absence of light along the edge of the bar is seen in the lower arm, which may be the stellar bar dust lane.

Three-component fits are conducted for all 33 NIRCam images, and the best fit

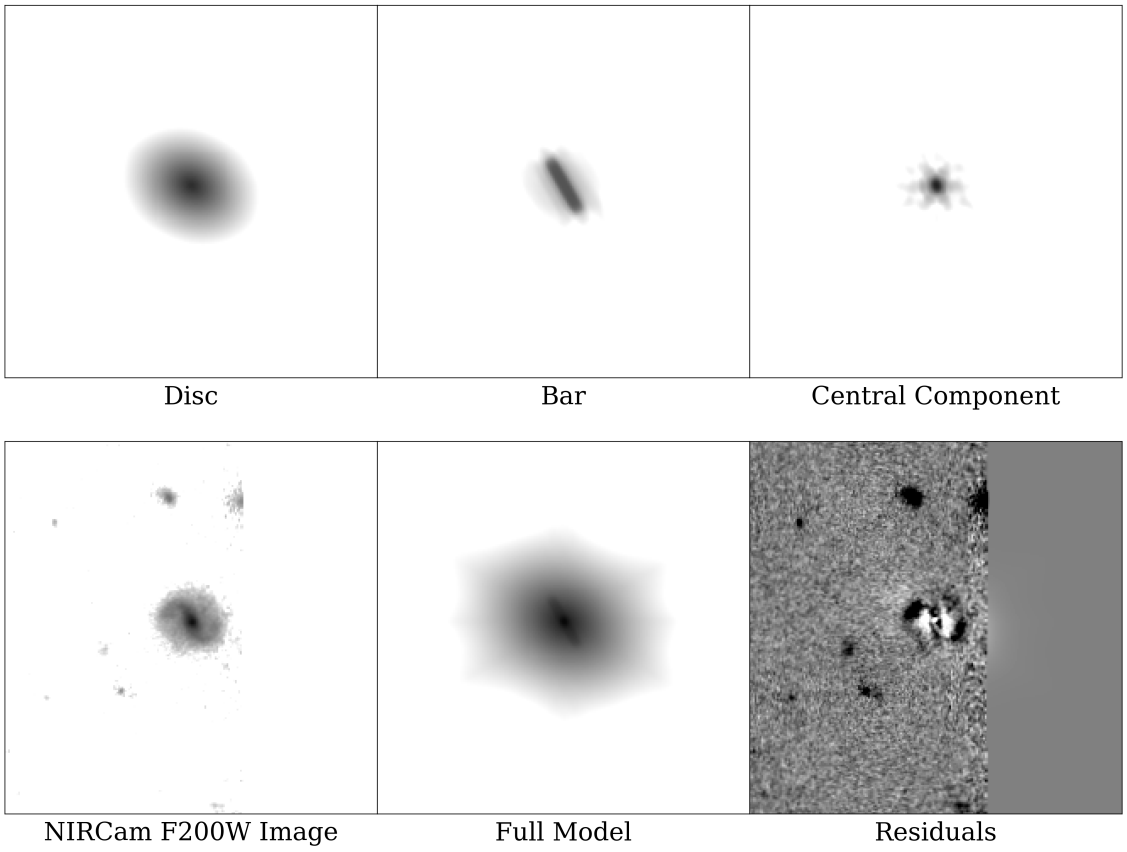

Figure 4.3: Photometric decomposition of galaxy CEERS 3924 at $z = 1.58$ in the JWST NIRCam filter F200W. The top row shows the three components fitted to the image: the disc (exponential function), the bar (generalised Sérsic function), and the central component (Sérsic function). The bottom row shows the original image, the combined model image to be matched to it, and the full-model residuals, obtained by subtracting the combined model image from the original.

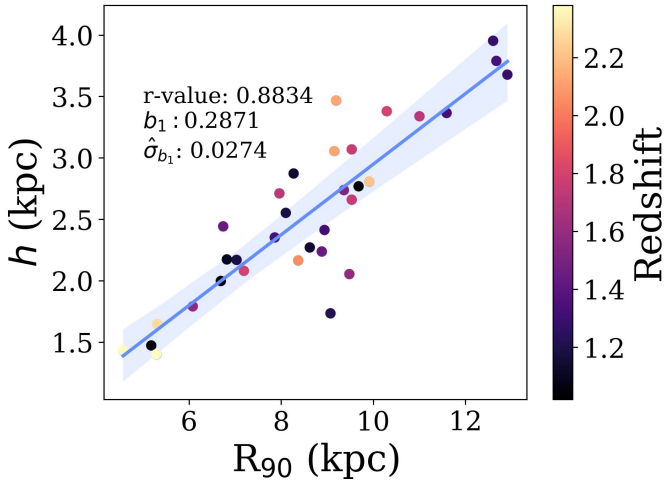

Figure 4.4: Disc scale length, h, and disc size, R_{90}, relation for strongly barred galaxies at $z > 1$. The Pearson's correlation coefficient, the slope, b_1, and standard error on the slope, $\hat{\sigma}_{b_1}$, are given in the top left corner for the least-squares regression with a 3σ error, shown as a shaded region.

function parameters are given in Table 4.1. I report on the stellar properties of the disc in § 4.4.1, the bar properties in § 4.4.2, and the central component in § 4.4.3.

4.4.1 The disc galaxies that host bars

Firstly, as discussed in § 3.5.1, I do not find that this high-redshift sample of barred galaxies peaks at $M_\star \approx 10^{10} M_\odot$, as seen in nearby galaxies. Instead, I observe a strongly barred disc galaxy sample that has a broad range in stellar mass, $9.2 < \log(M_\star/M_\odot) < 11.4$. In general, the highest redshift galaxies have the smallest discs, and this can be measured by either the disc scale length, h, or the radius at which 90% of the total light of the galaxy is contained within, R_{90} (also referred to as the Pretrosian-90 radius). The h value is derived from the exponential function fit to the galaxy disc during image decomposition, and R_{90} is obtained from MORFOMETRYKA [Ferreira et al., 2023]. Figure 4.2 shows the correlation between h and R_{90}, for which I find the ratio to be $h/R_{90} = 0.29 \pm 0.03$, and the relation has a Pearson's correlation coefficient of 0.88. Although these two measures of disc size provide similar insights into structural properties, it is necessary to report both to provide a complete picture of the properties that favour bar formation and to enable direct comparisons with other studies.

CEERS ID	z	$\log(M_\star/M_\odot)$	Filter	PA_b	ε_b	C_b	n_b	Bar/T	$R_{e,b}$ (kpc)	L_b (kpc)	R_{90} (kpc)
1852	1.02	10.80	F200W	28.91	0.78	2.00	2.00	0.04	3.00	1.86	9.68
12210	1.04	9.56	F200W	21.34	0.90	5.00	0.61	0.07	8.58	5.35	6.69
25146	1.04	9.27	F356W	42.13	0.50	4.00	0.22	0.15	8.00	4.99	5.18
22362	1.10	10.71	F356W	131.56	0.44	2.30	0.53	0.28	5.07	3.20	6.82
21891	1.14	9.73	F200W	160.37	0.57	5.00	0.24	0.06	3.98	2.53	8.27
2301	1.14	9.69	F356W	60.00	0.62	4.91	0.62	0.11	7.98	5.07	8.62
5241	1.18	10.88	F200W	31.06	0.60	2.00	0.00	0.14	8.00	5.11	8.10
13445	1.18	9.75	F200W	86.12	0.80	2.10	0.10	0.17	6.00	3.83	7.03
4031	1.22	10.89	F200W	20.67	0.73	3.50	0.65	0.33	15.00	9.62	9.07
20556	1.28	10.44	F200W	44.90	0.90	2.10	0.50	0.01	5.00	3.23	12.60
20556	1.28	10.44	F356W	44.89	0.90	2.10	0.50	0.01	5.00	3.23	12.91
17196	1.32	10.57	F200W	150.72	0.30	2.10	0.88	0.23	2.81	1.82	8.94
1310	1.34	9.77	F356W	191.22	0.50	2.00	0.10	0.03	2.95	1.91	7.86
5375	1.34	11.40	F200W	133.62	0.76	3.42	0.36	0.10	9.86	6.39	12.67
5375	1.34	11.40	F356W	136.07	0.73	3.53	0.33	0.12	11.04	7.15	11.59
25789	1.44	10.14	F200W	87.82	0.62	4.00	0.57	0.18	3.70	2.41	8.88
3982	1.44	10.71	F200W	49.19	0.34	4.66	0.42	0.29	5.22	3.40	6.74
13670	1.54	10.63	F356W	80.00	0.52	3.37	1.00	0.10	3.89	2.54	9.36
3924	1.58	9.79	F200W	29.77	0.81	4.91	0.11	0.08	10.71	6.99	9.48
3924	1.58	9.79	F356W	30.77	0.80	5.00	0.18	0.07	11.04	7.20	6.08
19427	1.72	9.95	F200W	88.32	0.66	2.11	0.11	0.02	2.16	1.41	7.96
26390	1.72	10.69	F356W	115.00	0.90	2.00	3.00	0.00	4.00	2.61	11.00
23259	1.76	10.47	F200W	185.00	0.36	3.00	0.50	0.06	3.44	2.24	9.53
23259	1.76	10.47	F444W	165.34	0.60	2.00	0.08	0.04	3.00	1.95	9.53
19176	1.80	10.25	F356W	70.73	0.57	7.00	0.75	0.23	12.00	7.80	10.29
27663	1.80	9.88	F356W	122.40	0.68	4.00	0.95	0.08	5.00	3.25	7.19
31125	2.06	11.30	F444W	140.00	0.58	4.00	0.10	0.06	9.05	5.80	8.37
23205	2.12	11.20	F200W	46.41	0.70	2.35	0.77	0.15	8.61	5.50	9.19
23205	2.12	11.20	F444W	47.08	0.69	4.00	0.68	0.14	10.00	6.39	9.15
5385	2.22	10.21	F444W	123.29	0.72	5.00	0.35	0.10	11.19	7.10	9.91
9703	2.28	10.25	F444W	118.40	0.70	3.00	0.31	0.12	8.60	5.43	5.31
1018	2.38	10.00	F200W	45.00	0.66	5.00	0.96	0.18	6.18	3.87	4.57
1018	2.38	10.00	F444W	41.84	0.60	4.00	0.50	0.09	5.30	3.32	5.29

Table 4.1: Structural properties of strongly barred galaxies at $z \geq 1$ derived from photometric decomposition. Col. 1: galaxy ID number from the CEERS catalogue; Col. 2: redshift; Col. 3: stellar mass [Duncan et al., 2019]; Col. 4: NIRCam filter used in image decompositions; Col. 5: bar position angle; Col. 6: bar ellipticity; Col. 7: bar boxiness; Col. 8: bar Sérsic index; Col. 9: bar-to-total luminosity ratio; Col. 10: bar effective radius; Col. 11: bar length; Col. 12: galaxy Petrosian-90 radius [Ferreira et al., 2023].

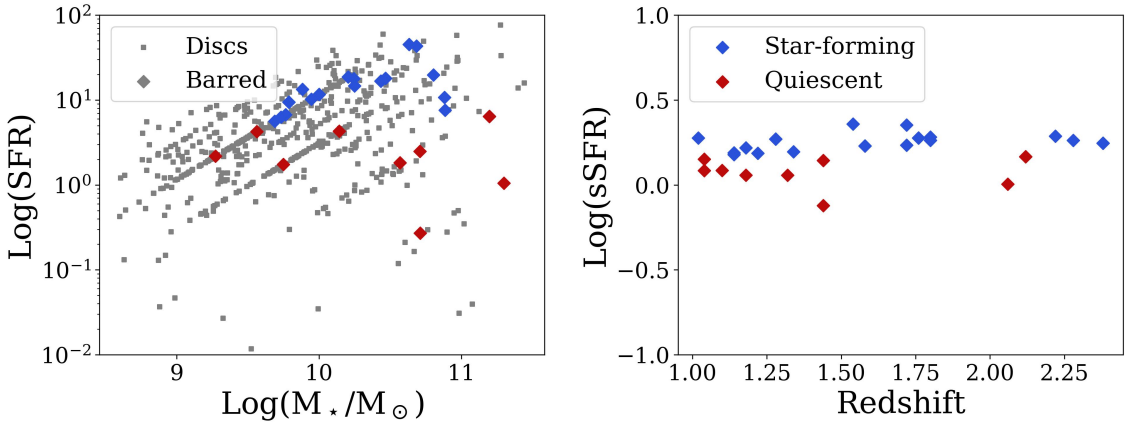

Figure 4.5: The specific star formation rate (sSFR) of disc galaxies at $z > 1$. The left panel shows the star formation rate (SFR) per stellar mass for disc galaxies (squares), used to determine the sSFR threshold for the given redshift bins. The right panel shows the sSFR of the strongly barred galaxies (diamonds) across the redshift range. Those with sSFR values above the threshold are star-forming, and those below are quiescent.

For the redshift range of this study, Ormerod et al. [2024] reported that galaxies become smaller at higher redshifts and that their stellar light profiles flatten. It was found that more passive galaxies at redshifts $z < 3$ have steeply concentrated stellar light profiles and that star formation typically occurs in disc galaxies. To understand the role of the bar in star formation, I categorise galaxies as passive or star-forming based on their specific Star Formation Rate (sSFR), with those above (below) the mean sSFR of all disc galaxies for a given redshift bin classified as star-forming (quiescent). I calculate the sSFR for this galaxy sample using stellar masses and star formation rates from Duncan et al. [2019]. Figure 4.5 shows the SFR-stellar mass relation for the optimised and visually classified disc sample in Chapter 3. I use the disc sample rather than the strongly barred galaxy sample to achieve a larger sample size per redshift bin, and the redshift bins are spaced at 0.5 intervals. Figure 4.5 shows the evolution of the sSFR for the strongly barred galaxy sample. I find a larger population of star-forming barred galaxies beyond $z = 1.5$, which could be due to recently formed bars being at early stages of bar-driven evolution. Two quiescent barred galaxies beyond $z = 2$ are seen, which could possibly be caused by rapid bar-driven evolution or by gas stripping from galaxy interactions.

4.4.2 Structural properties of bars

To fully understand the role of bars in the evolution of young galaxies and, consequently, the impact of bar-driven evolution, it is necessary to have a detailed description of their properties throughout cosmic time. In this study, the bar properties are derived from fitting a generalised Sérsic function, with initial upper and lower parameter limits estimated by visual inspection of the NIRCam images. A thorough depiction of the structural properties of bars at Cosmic Noon is given in Figure 4.6. This figure shows the normalised distributions of six structural properties. These distributions are normalised by dividing the count by the product of the number of observations and the bin width, yielding a probability density.

At first glance, it is obvious that the structural properties of bars at high redshifts are similar to those of bars in nearby galaxies and those at intermediate redshifts. The studies that I have selected to compare this high-redshift sample to are the bar properties of nearly 300 nearby barred galaxies, derived from photometric decompositions of SDSS images [Gadotti, 2011]. Additionally, for several parameters, I compare their distributions with those of over 300 intermediate-redshift ($0.2 < z < 0.8$) galaxies in the HST COSMOS field, also derived from image decompositions [Kim et al., 2021].

Several key results are shown in this figure. Firstly, I find a mean Bar/T of 0.1, meaning that at $z > 1$, bars on average contain $\approx 10\%$ of the total light within the galaxy. In a few galaxies, this contribution can reach up to 0.3, and the distribution is consistent with that of the lower-redshift samples. This result shows that during bar-driven evolution, the bar's light contribution probably increases rapidly after bar formation, then remains constant. A Sérsic index of $n_b = 0.6$ shows that many of these high-redshift bars have closer to Gaussian profiles ($n_b = 0.5$) than exponential profiles ($n_b = 1$). Therefore, these bars have a shallower central core than nearby bars, which have an average of $n_b = 0.7$. I derive a broad range of bar boxiness values, with a standard deviation of 1.3, indicating that many bars are well fit by a pure ellipse ($C_0 = 0$). This value increases to $C_0 = 3$ for nearby galaxies, which could be from the strengthening of bars throughout galaxy evolution and the formation of a boxy-peanut. Gadotti [2011] derived a mean boxiness value of 2.7; my results

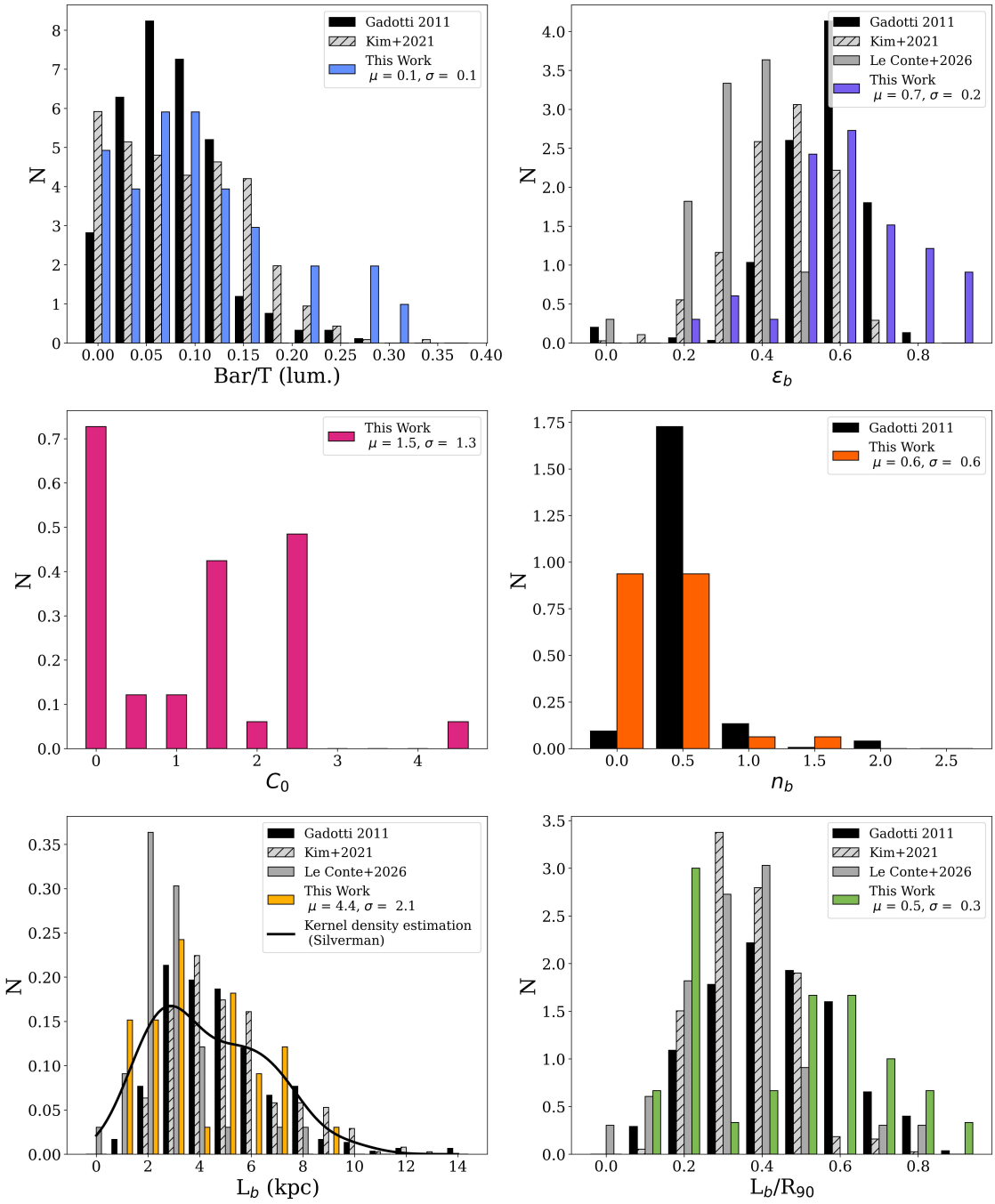

Figure 4.6: Stellar properties of the fitted bar model from photometric decompositions of high redshift barred galaxies with JWST NIRCam. From top left to bottom right: Bar-to-Total luminosity ratio, bar ellipticity (ε_b), bar boxiness (C_0), bar Sérsic index (n_b), bar length (L_b), and normalised bar length by R_{90} (L_b/R_{90}). I show the mean, μ, and standard deviation, σ, of the distributions. I compare these bar properties to those of a nearby barred galaxy sample in SDSS [Gadotti, 2011, solid black], an intermediate redshift sample in COSMOS [Kim et al., 2021, hashed grey], and the results of Chapter 3 derived from ellipse fitting [Le Conte et al., 2026, solid grey]. A kernel density estimate, using the Silverman test [Silverman, 1986], of the bar-length probability density function is shown as a black curve.

agree with those for nearby galaxies, as bars are more frequently boxy than discy, as indicated by my values of $C_0 > 0$.

In this study, I find a pronounced peak in ellipticity for the high-redshift bar sample, with $\varepsilon_b = 0.7$. This is marginally higher than the nearby galaxy sample, which finds $\varepsilon_b = 0.6$ using photometric decompositions. Additionally, my result exceeds that of the intermediate sample, which peaks at $\varepsilon_b = 0.5$; however, this study uses ellipse-fitting techniques, as described in § 2.3.1. Similarly, this study finds a peak ellipticity 1.74 times higher than that derived from ellipse fits for the same sample (see § 3.5.3 for the results using ellipse fits).

Figure 4.7 shows the ellipticity derived via ellipse-fitting or photometric decompositions for each galaxy in this high-redshift sample. I find that photometric decomposition consistently yields higher ellipticity values for all galaxies, regardless of the observing filter. Specifically, I fit a linear least-squares regression and estimate a slope of 0.35 ± 0.11; however, only a moderate correlation is observed, as indicated by a Pearson's correlation coefficient of 0.51. The systematic decrease in ellipticity observed with ellipse-fitting techniques is because the isophotes mapping the bar are, in fact, rounder than the bar itself due to PSF effects and, if present, a central component, and thus the ellipse is rounder. Additionally, these contours cannot differentiate the central contribution from the bar, which broadens the centre of the ellipse. Since decomposition methods account for the surface brightness contributions from the PSF, disc, and central component, this technique provides a better estimate of the bar ellipticity. Similar studies in the local Universe show that the difference in ellipticity between ellipse-fitting and 2D fits is in fact 20 per cent [e.g., Gadotti, 2008, 2011]. The underlying cause of the difference in ellipticity is supported by Marinova et al. [2009], which found higher ellipticity in bars in disc-only systems than in galaxies with a disc and a bulge.

Lastly, in Figure 4.6, I report on the bar length for this sample at $z > 1$. I obtain the effective radius, $R_{e,b}$, of the bar from the image decompositions. This analysis is based on projected images; I haven't taken the galaxy's inclination into account, as discussed in Chapter 3. The deprojection of the image as a whole is beyond the scope of this study, and I do not obtain a proxy for the bar's semi-major axis from

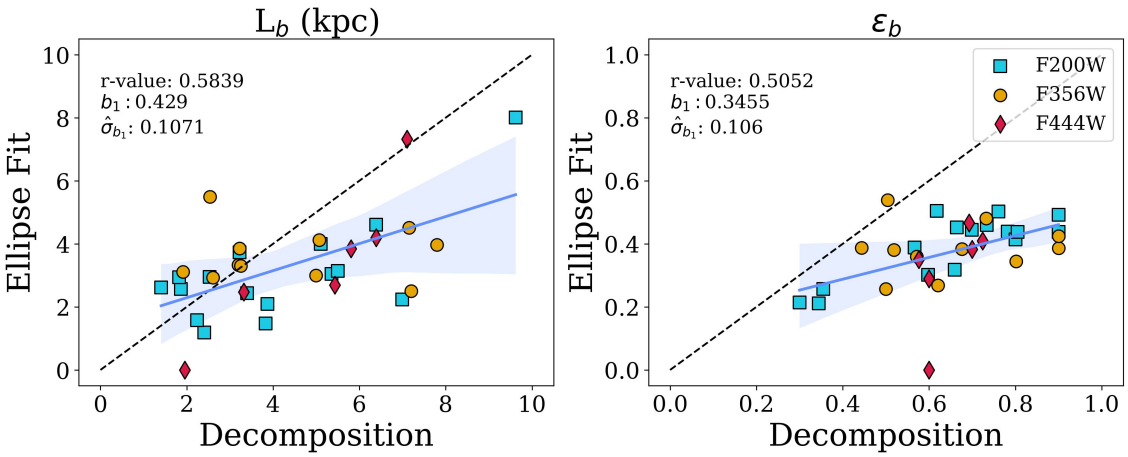

Figure 4.7: Structural properties of bars derived by ellipse fitting techniques versus photometric decomposition, for barred galaxies at $z \geq 1$ in the NIRCam filters F200W (squares), F356W (circles), and F444W (diamonds). Left panel is the derived bar length, L_b, and the right panel is the bar ellipticity, ε_b. A 1:1 relation is shown as a black dashed line. The Pearson's correlation coefficient, the slope, b_1, and standard error on the slope, $\hat{\sigma}_{b_1}$, are given in the top left corner for the least-squares regression with a 3σ error, shown as a shaded region.

the generalised Sérsic function. Thus, here, I present the results of the projected bar length. For consistency, I compare the results of this study to the projected bar lengths derived by ellipse fits in § 3.5.2. However, it must be noted that the bar lengths reported in Gadotti [2011] were of nearly face-on galaxies, and Kim et al. [2021] used deprojected images. Hence, in a few of the high-redshift cases, the bar lengths could increase.

Gadotti [2011] reported on the difference between the bar length, L_b, and the effective radius, $R_{e,b}$, from image decompositions and identified that the two measurements differ by a factor of 2.5. The L_b in their study corresponds to the measurement of the minimum ellipticity following the peak ellipticity of the bar ellipticity radial profile. Hence, these measurements may be slightly larger than those of similar nearby barred galaxies that follow different rules. Since, in this study, I derive the structural properties of the bar from a generalised Sérsic function, I obtain the best-fit $R_{e,b}$ but not L_b. Thus, I correct for the bar length using the correction factor reported in the nearby galaxy sample.

The mean bar length for this high redshift sample is $L_b = 4.4$ kpc with a broad standard deviation of 2.1 kpc. The high-z distribution is consistent with lower

redshift studies and observes a similar peak in bar length at ≈ 3. A few long bars ($L_b > 6$ kpc) are identified; however, none are above 10 kpc, as is seen in the lower redshift studies.

The results of Chapter 3 found that the bar length marginally evolves over the redshift range for the barred galaxies imaged in F200W; however, when normalised by R_{90}, a constant ratio was measured for all samples from the local Universe, out to high redshifts. Here, using photometric decomposition to derive these parameters, I observe the same trend. The mean normalised bar length is $L_b/R_{90} = 0.5$, which is the same as in the other studies we compare this sample to. A not-so-common result seen in nearby galaxies is that galaxies reside at the high end of this normalised bar length ratio, with values of $L_b/R_{90} > 0.6$. Here, I identify several of these systems. This could arise from surface-brightness dimming, which is particularly prominent in this redshift range; thus, a fainter disc would yield smaller values of R_{90}.

In the bar length distribution, a bimodal feature is amplified by the normalised density of the bins. Thus, I test for a bimodal distribution by applying the Silverman test [Silverman, 1986] to estimate the bandwidth of the probability density function, shown in Figure 4.6 as a black curve. Only one maximum is identified; hence, I cannot infer that this distribution is bimodal. However, a known weakness of the implementation here is that a simplified version of an estimator proposed by Silverman is used, and thus, the function is smoothed. If the bimodal feature is accepted, it is challenging to determine its cause due to the small sample size. The origin could be the different NIRCam wavelengths used, or it could indicate that two different bar-formation mechanisms are at work: interactions or mergers producing long bars and disc instabilities producing shorter bars. Nevertheless, results across the full redshift range from nearby galaxies to Cosmic Noon show that bars grow in tandem with their discs. Since long bars are found at Cosmic Noon, this study corroborates the idea that bar formation can occur in the early Universe and that a period of rapid growth must occur in these galaxies for their bars to be so well established.

I have not reported uncertainties for these photometrically decomposed structural parameters, as this is non-trivial and the DE algorithm does not provide gra-

dients for the fitting landscape. Thus, I discuss the uncertainties reported in Kim et al. [2014], which used the program BUDDA [de Souza et al., 2004, Gadotti, 2008] for photometric decomposition. The code produces 1σ *statistical* errors on each structural parameter, whereby the minimised χ^2 is iterated until a variation of 1σ is achieved, while all other parameters are fixed. For the structural parameters of the bar, the authors reported an error of 8%, corresponding to $\sigma = 0.008$ for my mean value of Bar/T = 0.1; 5% on the bar ellipticity, corresponding to 0.035 for $\varepsilon = 0.7$; 24% on the bar Sérsic index, corresponding to 0.144 for $n_b = 0.6$; 17% on the bar effective radius, corresponding to 0.748 for $L_b = 4.4$ kpc; 10% on the disc scale length, thus corresponding to 0.135 for $L_b/R_{90} = 0.5$.

A comparison of the bar length derived from ellipse fits and image decomposition is shown in Figure 4.7. The image decomposition method doesn't always measure longer bar lengths than the ellipse-fit method; however, in most cases, it does. This is indicated by a linear least-squares regression slope of 0.43 ± 0.11, with only a moderate correlation (Pearson's r = 0.58). Additionally, this is observed irrespective of the NIRCam filter. The longer wavelengths in the image decompositions may be due to my assumption that the $R_{e,b}$-L_b correction factor for nearby galaxies is equivalent at high redshifts. The ellipse-fit derived bar length was obtained by taking the average of radii where the ellipticity peaks and the position angle changes by more than ten degrees. To repeat, Gadotti [2011] noted that his corrected L_b corresponds to the minimum ellipticity, following the peak bar ellipticity, and thus derives a slightly longer bar length.

To understand how the models respond to the different stellar populations traced by the NIRCam filters, I compare image decomposition results for galaxies identified as strongly barred in both the short- and long-wavelength channels. Figure 4.8 shows the same bar structural properties as Figure 4.6 but of six galaxies derived for the short- and long-NIRCam wavelength channels. Overall, the algorithm consistently identifies a similar best fit; however, there are a few features worth noting. Slightly higher values of Bar/T and n_b are obtained for the F200W NIRCam images, as estimated by the linear least-squares regression slopes of 0.6 ± 0.2 and 0.5 ± 0.3, respectively. This shows that bluer wavelengths, which trace star

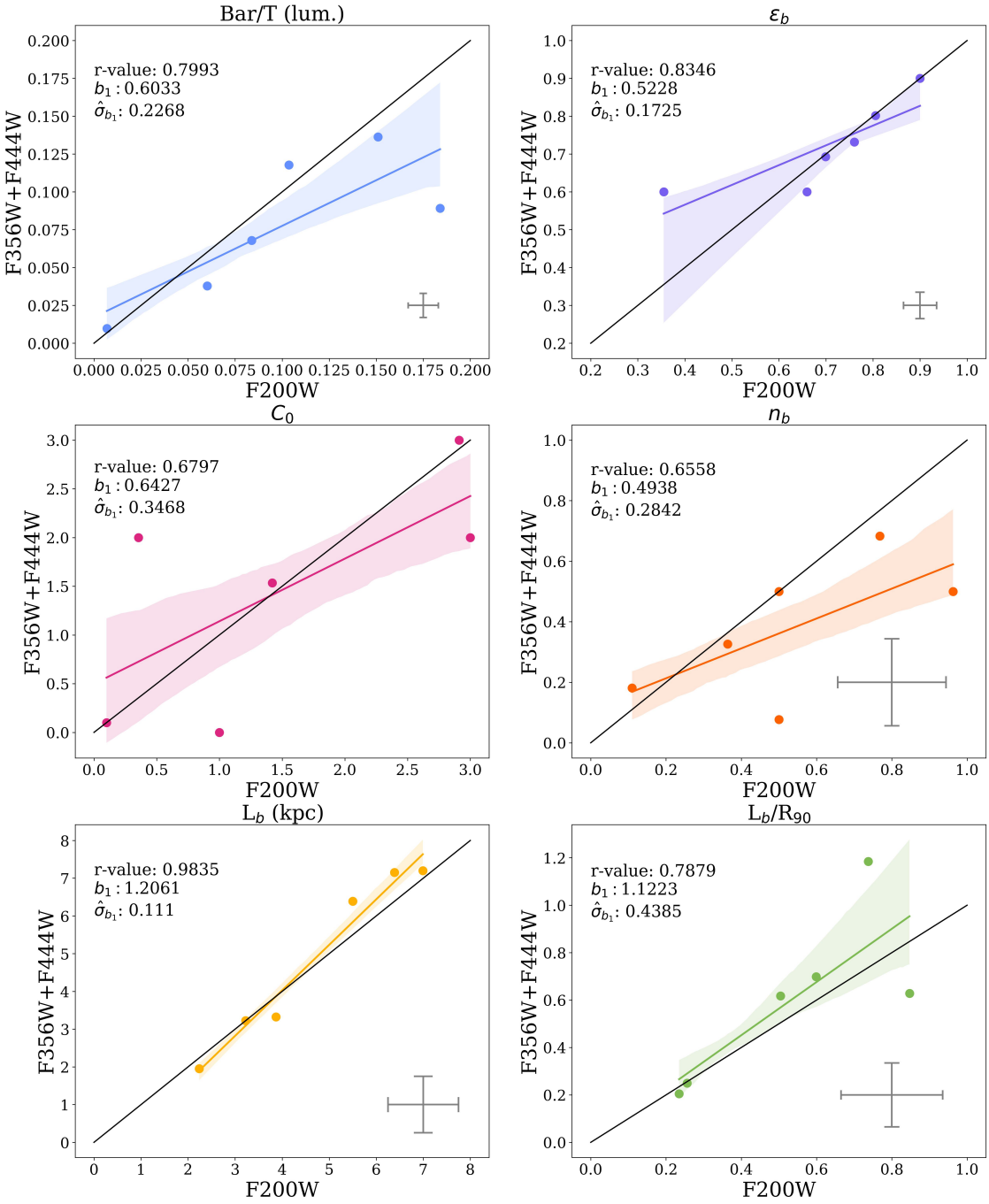

Figure 4.8: Stellar bar properties derived for the same galaxies in the JWST NIRCam filters F200W and F356W+F444W. From top left to bottom right: Bar-to-Total luminosity ratio, bar ellipticity (ε_b), bar boxiness (C_0), bar Sérsic index (n_b), bar length (L_b), and normalised bar length by R_{90} (L_b/R_{90}). The Pearson's correlation coefficient, the slope, b_1, and standard error on the slope, $\hat{\sigma}_{b_1}$, are given in the top left corner for the least-squares regression with a 3σ error, shown as a shaded region. In the lower-right corners of each figure, error bars show the 1σ uncertainty on the mean, which adopts the *statistical* percentage errors reported in Kim et al. [2014].

formation and younger stellar populations but are also more susceptible to dust obscuration, produce brighter (i.e., higher Bar/T) and more centrally concentrated bars (i.e., higher n_b). Similar ellipticity, bar length, and normalised bar length values are obtained across the different NIRCam filters. This contradicts the results of Chapter 3, in which I find that bars in F200W images are ≈ 1 kpc shorter than in the F356W+F444W sample. Finally, the boxiness values obtained can vary widely, making them notoriously difficult to measure and exacerbating this in the high-redshift sample. The inconsistency could be due to the fitting of other stellar structures, such as spiral arms, or to improved spatial resolution in F200W, which may make the ends of the bar more defined; however, further investigation of this result is beyond the scope of this study.

To test the role of bar-driven evolution in these young disc galaxies, I examine the distributions of bar structural properties in star-forming and quiescent galaxies in Figure 4.9. The bars residing in star-forming discs tend to have smaller contributions to the overall luminosity of the galaxy, with an average Bar/T = 0.1. This is most likely due to star formation in the outer disc, which significantly contributes to the surface brightness. Whereas quiescent galaxies will have dimmer outer discs, meaning the bar has a higher contribution to the overall luminosity.

I find the most elliptical bars to occur in star-forming galaxies, which peaks at $\varepsilon_b = 0.6$, and the roundest bars in quiescent galaxies. More elliptical bars may result from star formation at the end of the bar, a feature observed in nearby galaxies that makes the bar more elliptical [e.g., Géron et al., 2024, Reynaud and Downes, 1998, Verley et al., 2007]. Additionally, during a bar's lifetime, a vertical buckling instability may set in, weakening the bar [e.g., Combes et al., 1990, Ghosh et al., 2024, Merritt and Sellwood, 1994]. This might explain why I observe rounder bars in quiescent systems. By contrast, Elmegreen and Elmegreen [1985] argued that more elliptical and longer bars are present in early-type spiral galaxies, as theoretically these bars are comprised of more elongated stellar orbits that extend to the corotation radius. Whereas, a late-type spiral may only have stellar bar orbits that extend to the ILR.

Star-forming galaxies have bars with profiles closer to exponential ($n_b = 0.6$) than

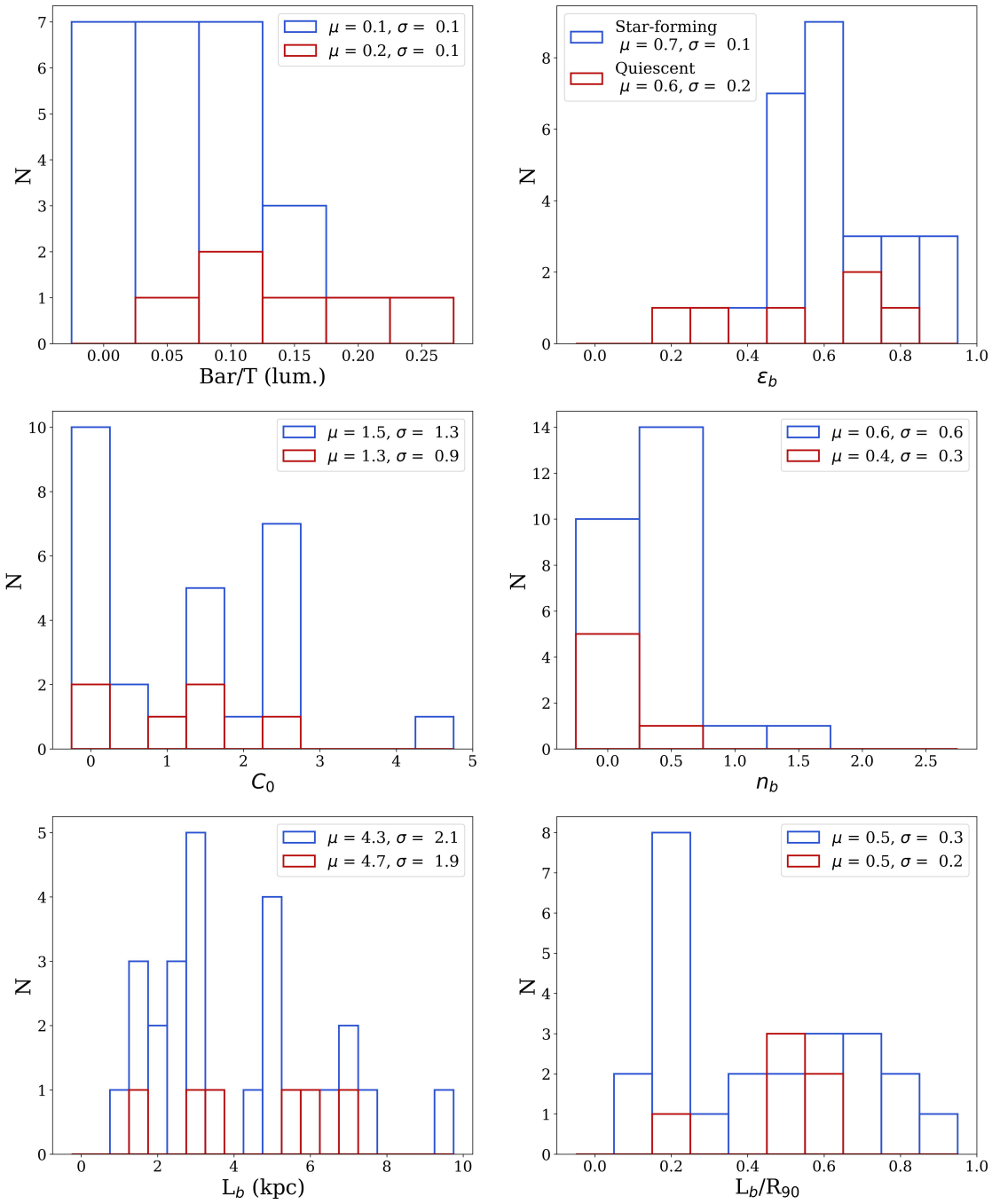

Figure 4.9: Stellar properties of the bar in star-forming (blue) and quiescent (red) strongly barred galaxies. From top left to bottom right: Bar-to-Total luminosity ratio, bar ellipticity (ε_b), bar boxiness (C_0), bar Sérsic index (n_b), bar length (L_b), and normalised bar length by R_{90} (L_b/R_{90}). I show the mean, μ, and standard deviation, σ, for the two samples.

quiescent galaxies ($n_b = 0.4$). This shows that bars are not strongly concentrated at the centres of quiescent systems and demonstrates that, in galaxies with heightened star formation, the bar drives gas inflow, which ignites star formation at its centre. This correlation was observed by Elmegreen and Elmegreen [1985], who reported that early Hubble-type spiral galaxies have flat intensity profiles for the stellar bar, whereas late Hubble types have exponential intensity profiles.

I observe similar C_0, L_b, and L_b/R_{90} distributions for the two galaxy samples. Despite observing several features in these bar properties, these results must be interpreted with caution, as the galaxy sample sizes are too small to be statistically significant.

4.4.3 Central component contribution

The final component in the NIRCam image fit is the central component, which is necessary to correctly fit the bar and can also provide insight into the physical properties of the central structure. The central component is fitted with a Sérsic function; thus, I use the Sérsic index to classify it as a structural candidate. Such that a Sérsic index of $n_c < 0.5$ indicates a point source, $0.5 \leq n_c < 2$ suggests a nuclear disc, and $n_c \geq 2$ is a classical bulge. Classifying these structures with certainty would require kinematic information, which is beyond the scope of this study. From the 33 image decompositions, I classify 20 as point sources ($n_c < 0.5$), 10 as nuclear discs, and 3 as classical bulges. This distribution of classifications is interesting, since classical bulges are thought to form through galaxy mergers, which are considered frequent at these redshifts. Nuclear discs form via bar-driven evolution; thus, their presence indicates that these systems have evolved quickly to reach this level of maturity.

Figure 4.10 shows the evolution of the stellar mass, L_b, ε_b, and Bar/T for the strongly barred galaxies categorised by their central component classification. Firstly, all central component classification types are observed across the redshift range, with classical bulges found at $z < 2$ and point sources in the highest-redshift galaxies. Additionally, I do not observe a central type-stellar mass dependence. Gadotti [2011] found bars with classical bulges to be longer than those with nuclear

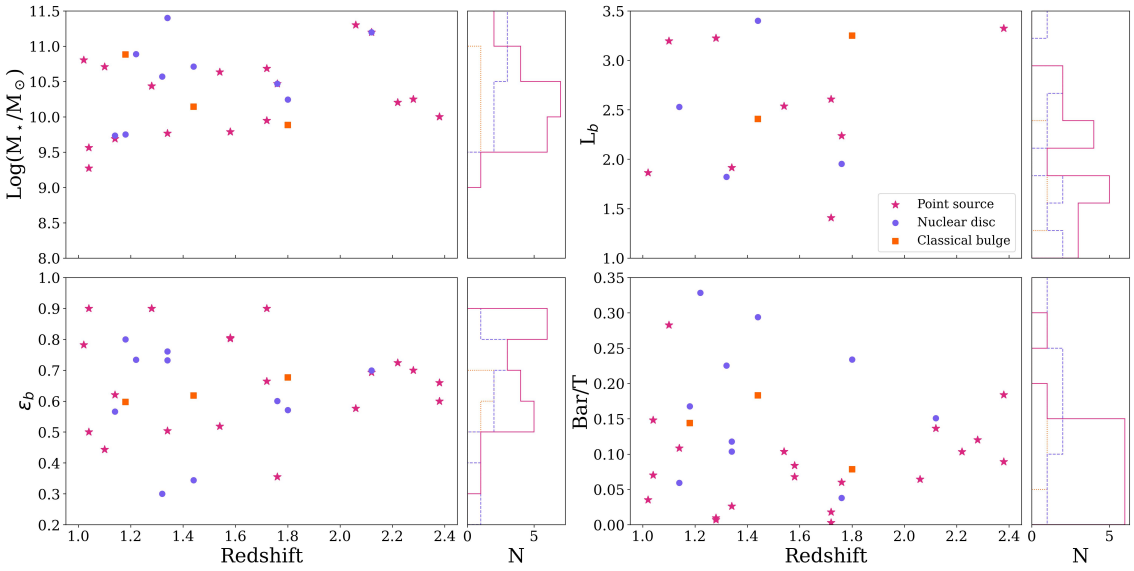

Figure 4.10: Redshift distributions of bar structural properties for the central component candidates: point sources ($n_c < 0.5$, stars, solid line), nuclear discs ($0.5 \leq n_c < 2$, circles, dashed line), and classical bulges ($n_c \geq 2$, squares, dotted line). From top left to bottom right, the distributions of: stellar mass, bar length (L_b), bar ellipticity (ε_b), and bar-to-total luminosity (Bar/T). The parameter distribution is shown to the right of each figure.

discs. By contrast, in this study, I find that classical bulges reside in barred galaxies with a mean $L_b \approx 3.6$ with a standard deviation of 1.1, whereas nuclear discs reside in barred galaxies with a mean $L_b \approx 5$ with a standard deviation of 2.6. I do not observe a dependence on bar ellipticity; however, I find nuclear discs in bars with the highest Bar/T values, with a mean of Bar/T ≈ 0.17 and standard deviation 0.09, and classical bulges with a mean of Bar/T ≈ 0.14 and standard deviation of 0.04. I cannot determine whether these values are robust because the Sérsic index of the central component is difficult to measure due to limited resolution. Whereby, the central component size will be similar to that of 2×FWHM for those observed in the longest wavelength filter, F444W.

4.5 Discussion

The results of this chapter have built on and revealed novel observational facts about the structural properties of high-redshift barred galaxies. The primary result, that the structural properties (including ellipticity, bar length, and luminosity contri-

bution) of bars at $z \geq 1$ are of similar values to those of nearby barred galaxies, implies that in these cases, bar formation and evolution must occur quickly. These well-established structures in young galaxies grow in tandem with their host discs, as evidenced by a constant normalised bar length across the redshift range. This leads us to rethink the framework for galaxy formation and evolution, since bar-driven evolution begins in settled, rotationally supported discs much earlier than previously thought, despite the Universe's turbulent nature at Cosmic Noon.

To derive these structural properties, I used photometric decomposition to model and fit the disc, bar, and central component. I find that for galaxies classified as strongly barred in both the short and long NIRCam wavelength channels, image decomposition yields good agreement in best-fit parameters across the observed wavelengths. Compared with ellipse-fitting methods, I measure higher ellipticities and longer bar lengths because the commonly used method traces rounder ellipses than the bars themselves. I discuss the challenges of applying these techniques to high-redshift systems in § 4.5.1.

Another major result is that star-forming galaxies exhibit slightly different bar structural properties from those of passive galaxies. The bars in star-forming galaxies tend to have lower luminosities, be more elliptical, and have steeper central concentrations. Below, I discuss how dark gaps could be used as a proxy for bar strength in § 4.5.2, and how the results of this study compare to those of simulations in § 4.5.3, and lastly, how the terminology of secular evolution is no longer compatible with the results of high redshift studies in § 4.5.4.

4.5.1 Challenges at high-z

Until now, bar studies have been limited to redshifts $z < 1$, since the bar was unresolvable in really young galaxies. However, the application of visual classification and ellipse-fitting techniques has made investigations into high-redshift barred galaxies possible with JWST's improved sensitivity. Even though we have an evident occurrence of bars in young disc galaxies, how robustly can their properties be measured, and what are the limitations of imaging techniques for structural properties?

In Chapter 3, I selected a visually classified barred galaxy sample in the short-

and long-wavelength channels of NIRCam. Out of the 27 unique galaxies classified as strongly barred, only six were identified as strongly barred in both wavelength channels. This small fraction suggests that shorter bars identified in F200W were missed in F356W+F444W, as even JWST experiences resolution effects, which hinder bar identification. A limitation of this study is the small number of barred galaxies, which is further reduced when using redshift bins. This limitation stems from the sample selection criteria and the use of visual classification. Future studies that use automated techniques will be more efficient at analysing larger datasets, and a more relaxed selection criterion will include lower-mass galaxies at the highest redshifts (although these bars will be shorter since bar length correlates with disc size and galaxy mass). Visual inspection of the NIRCam images shows that all filters are affected by the PSF, particularly by rounding the central structures, thereby broadening the bar. This is a major limitation of using ellipse fits to measure the evolution of bar structural properties.

Employing image decompositions circumvents the effects of PSF, since the model is convolved with the PSF, thereby yielding more accurate measures of structural properties. To test for biases introduced in higher redshift studies, Gadotti [2008] artificially redshifted images of 12 nearby barred galaxies to $z = 0.05$ (achieving a comparable spatial resolution to S^{4}G images), and verified that most parameters, including Bar/T and h, could be reliably estimated in these higher redshifted images. Subsequently, Gadotti [2011], using the same methodology as in his previous work, verified that the structural properties n_b, $\mathrm{L_b}$, ε_b, and C_0 can be reliably obtained from lower-resolution images. However, the boxiness of the bar remains difficult to measure in lower-resolution images, and its ellipticity decreases accordingly. Similar results are observed in this work. By comparing the properties obtained from F200W images to F356W+F444W images, Figure 4.8 shows that similar values are achieved for all properties, other than boxiness.

A recent study tested photometric decomposition techniques on images of redshifted S^{4}G barred galaxies [Gadotti, 2026]. This sample was selected to have kinematically confirmed nuclear discs. The work focused on the photometric decomposition's ability to reliably measure the Sérsic index of the central component and

found that unsupervised DE produces large scatter and yielded systematically larger values of n_c (see their Fig. 11). Hence, this study, alongside other investigations [Fisher and Drory, 2016, Gadotti, 2009, Kormendy, 2016], question the accuracy of the practice of defining the central stellar component into classical bulge, and nuclear disc using only the Sérsic index, and caution against using just this parameter. Instead, a combination of signatures would be required to define the central component, such as kinematic observations to unveil dynamical features, the presence of unmodelled nuclear substructures in residual images, and the existence or absence of star formation. For these young galaxies, $z \geq 1$, only the Sérsic index is readily available, and follow-up observations would be required to obtain well-resolved kinematics on galaxy centres.

A novel result from this study is the relationship between structural properties and sSFR. However, a limitation of the comparison is the definition of star-forming and passive galaxies, which uses the average sSFR of a given redshift bin. As a result, the threshold varies across redshift bins. Additionally, we note that the bins are selected in increments of $z = 0.5$; however, alternative bin sizes could have been chosen based on a constant population size or cosmic time. I attempted to mitigate biases by averaging the sSFRs of all disc galaxies, thereby substantially increasing the sample size. Furthermore, this holds more information about how the barred galaxies behave compared to the norm for unbarred galaxies. Finally, I chose not to use a constant sSFR threshold across the entire redshift range because the highest-redshift bin would predominantly contain passive galaxies, rendering a comparison impossible.

4.5.2 Dark gaps as a proxy for bar strength

At lower redshifts, a commonly used parameter to measure the evolutionary stage of a barred galaxy is the bar strength. The bar strength can be defined by the amplitude of the $m = 2$ Fourier moment in nearby observational studies [e.g., Aguerri et al., 2000] and in simulations [e.g., Ghosh et al., 2024]. However, Fourier analysis is challenging at high redshifts because it requires high S/N in the outer regions of the galaxy, and, for these distant systems, surface-brightness dimming typically

makes them faint. Additionally, the technique requires deprojecting galaxy images, which is challenging due to the clumpiness of galaxies in the early Universe, and resolution limits can lead to overestimation of vertical disc thickness and clump sizes. Likewise, the bar ellipticity derived from ellipse fits has been used to define bar strength, but we have discussed throughout this work how ellipticity can be biased by the technique and definitions selected.

Rather, the strength of the bar can be defined by the magnitude of the light deficit perpendicular to the bar's semi-major axis, known as the 'dark gap' [Buta, 2017, Gadotti and de Souza, 2003, Kim et al., 2016]. It is observed that as the bar evolves, stars are trapped into elongated orbits by the bar, thus the radially bright light profile along the bar major axis enhances, magnifying the light deficit on either side of the bar, and simulations show that dark gaps and the stellar bar grow in tandem [e.g., Ghosh and Di Matteo, 2024]. The extent of the dark gap correlates with the bar's speed, indicating the evolutionary stage of the barred galaxy. I.e., Kim et al. [2025] found slower bars to have shorter dark gaps, whilst faster bars have larger extents. However, Merrow et al. [2026] showed that bar pattern speed doesn't necessarily indicate a galaxy's evolutionary stage, since they found baryon-dominated galaxies can in fact 'speed up'; contradicting the occurrence of bar slow-down from dynamical friction. In this study, I haven't defined the bar strength; however, the dark gap feature may be used in high-redshift studies to quantify bar strength in young galaxies.

In my sample of strongly barred galaxies, I find several pronounced dark gaps; however, I will focus on only one example here. In Figure 4.11, I show the prominent dark gaps in the galaxy CEERS 5241 at $z = 1.18$. The dark gap features are enhanced in the residual image of the photometric decomposition method, shown as white space on either side of the bar. Previous works are inconclusive about the physical origin of the dark gaps, with some theoretical studies showing depopulated L_4 and L_5 Lagrangian points associated with the CR [Buta, 2017, Salo et al., 1999, Schwarz, 1981]. While other studies find the dark gaps to be more closely associated with the inner ultraharmonic resonance [Aguerri et al., 2023, Krishnarao et al., 2022], and finally Ghosh et al. [2024] found the dark gaps do not correlate with any of these

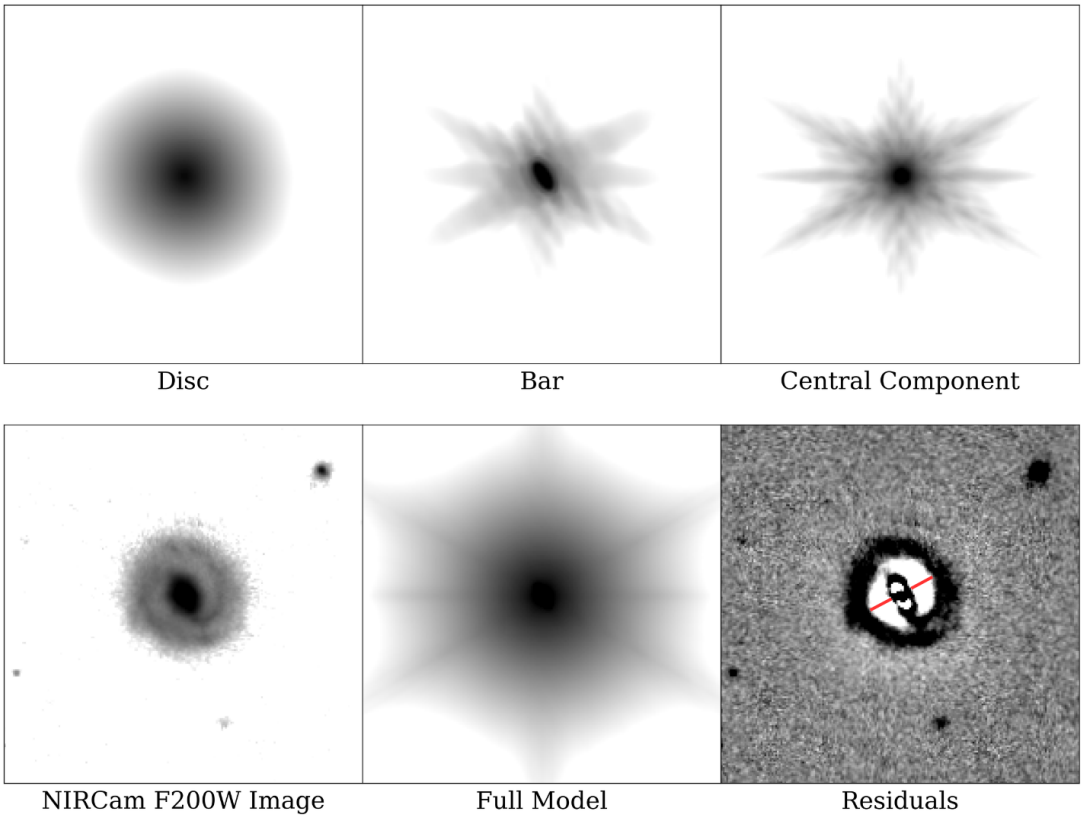

Figure 4.11: Photometric decomposition of galaxy CEERS 5241 at $z = 1.18$ in the JWST NIRCam filter F200W. The top row shows the three components fitted to the image: the disc (exponential function), the bar (generalised Sérsic function), and the central component (Sérsic function). The bottom row shows the original image, the combined model image to be matched to it, and the full-model residuals, obtained by subtracting the combined model image from the original. Red lines show the extent of the dark gap in the residual image.

significant resonances.

Since prominent dark gaps are found at Cosmic Noon, future observational studies should examine their locations and determine their physical origins in relation to bar dynamics. Chattopadhyay (2026; sub.) measures the extent and strength of the dark gaps for the strongly barred galaxies discussed in this chapter. Across the redshift range $0 < z < 4$, the extent of dark gaps remains remarkably constant, with a moderate increase in extent from the highest redshifts to $z = 1$ by $\approx 30\%$, which remains constant at $R_{DG}/R_{90} \approx 0.3$, until $z < 0.05$ where the extent decreases. The strength of the dark gaps is lowest in high-redshift galaxies, indicating that their discs are brighter. This study finds that the dark gaps, created by the sweeping bar, are prominent but less distinct than those seen at intermediate redshifts. This

means that, despite long, well-established bars present in the early Universe, indicating that bar formation occurs rapidly, bar-driven evolution will continue during this epoch and develop the dark gaps.

4.5.3 Cosmic Noon bars in simulations

With observational studies of barred galaxies becoming possible at Cosmic Noon, it is necessary to assess the similarity between these real bars and those produced in simulations. Using IllustrisTNG simulations, Łokas [2025] found four small satellite merger-induced barred galaxies at high redshifts, $z > 3$. These bars form with lengths on the order of 3 kpc and have similar properties to observed high-redshift barred galaxies. The work of Gonçalves et al. [2025] tested the wavelength dependence of bar properties in TNG50. They measure a bar length of $\sim$ 4 kpc when considering only the young stars ($\leq$ 2 Gyrs) in a galaxy, and an ellipticity of 0.6, which decreases by over half when considering only the old stars ($\geq$ 8 Gyrs, see their Fig. 17).

I have derived bar lengths ranging from 1 to 9 kpc, with a peak at 3 kpc. The bar lengths measured in simulations are consistent with this peak, although the longest bar population remains underrepresented. However, I observe an interesting bimodal feature in the bar length distribution. The origin of this feature may be due to the bar's formation mechanism or to subsequent evolutionary processes; however, determining the true origin is challenging. Alternatively, simulations could provide some possible explanations. In the Auriga simulations, Fragkoudi et al. [2025] identified several barred galaxies with bar lengths $>$ 4 kpc, with the majority of long bars forming over 6 Gyrs ago. The weakening of bars has also been explored in the Auriga simulations by López et al. [2025], who studied the B/P fraction in barred galaxies. In these simulations, the vertical buckling instability of the bar occurs $\sim$ 1.1 and 1.6 Gyr after bar formation, and subsequently the bar strength weakens. Despite these few scenarios, observations still conflict with simulations; thus, a revision of young bar formation in simulations is required.

4.5.4 Rethinking bar-driven secular evolution

The theory that bar-driven evolution is secular has been well established and has been frequently used in the context of disc galaxy evolution [Kormendy and Kennicutt, 2004]. Most of the work supported the view that the early Universe was a violent, chaotic period, dominated by mergers and hierarchical clustering [Toomre, 1977]. At a significantly later epoch, slow evolutionary processes dominate the evolutionary track of galaxies, persisting on timescales much longer than the dynamical timescale.

One of these dominating evolutionary processes is bar-driven evolution. The description of bar-driven secular evolution was reinforced by HST studies, which claimed the onset of bar formation at $z \approx 1$ [Simmons et al., 2014]. Additionally, the work of Buta et al. [2010] advocated that secular evolution is bar-driven, based on their observations of weaker bars in S0-type galaxies with higher-mass bulges, suggesting that bars continue to drive galaxy evolution and to grow bulges in gas-depleted galaxies. However, in this study, I have demonstrated that the barred galaxies discovered at Cosmic Noon are indeed mature systems with long, strong bars. Hence, the bar-formation mechanisms that occur in this epoch must form rapidly. Additionally, in order for these bars to have structural properties similar to those in the local Universe, bar-driven evolution must occur over shorter timescales. Thus, whilst the secondary evolutionary phase of galaxies (post the initial violent merging phase) occurs over the longest timescales, the descriptor 'secular evolution' is misleading, as bar-driven processes, at least within the bar radius, can be rapid at Cosmic Noon.

4.6 Summary and conclusions

In this chapter, I have performed 2D photometric fits to visually identified strongly barred galaxies at $z \geq 1$. The sample from JWST CEERS was selected to be a mass-complete disc sample of near-face-on strongly barred galaxies, in either the F200W NIRCam filter or the F356W+F444W. This study focuses on 27 barred galaxies, of which 16 were observed in the F200W filter, 11 in the F356W filter,

and 6 in the F444W filter. Of these, six galaxies are classified as strongly barred in both the short- and long-wavelength filters. The images are fitted with a combined disc (exponential function), bar (generalised Sérsic function), and central component (Sérsic function) model, which is then convolved with the PSF to produce a residual image of unmodelled stellar structures. I employ the differential evolution algorithm to minimise the fit statistic and identify the best-fit model of each image. I obtained structural properties of each component from the fitted functions.

The main findings are as follows:

(i) In general, high-redshift barred galaxies exhibit similar properties to those in the local Universe. They have a peak bar-to-total luminosity ratio of Bar/T = 0.1, peak bar ellipticity of $\varepsilon_b = 0.6$ and peak bar length of $L_b = 3$ kpc. The normalised bar length is observed to be constant across the redshift range, implying that bars grow in tandem with their discs.

(ii) Higher redshift bars have shallower concentrated light profiles, since their Sérsic index is $n_b = 0.6$.

(iii) The 2D photometrically derived structural bar properties (ellipticity and length) have greater values than those derived from ellipse fits. This is due to the photometric decomposition technique incorporating the PSF and central components into the models, both of which are rounding effects in ellipse fits.

(iv) I verify that the property values derived are robust for these high redshift galaxies, since similar values are obtained irrespective of the wavelength (in which shorter wavelengths have improved spatial resolution).

(v) Bars in passive disc galaxies tend to contribute to the overall galaxy luminosity more than those in star-forming systems. As a result, they are also rounder bars with flatter light profiles. A potential explanation for this result is that bars in passive systems are more evolved and weakened by buckling instabilities.

(vi) The observation in nearby galaxies that classical bulges tend to be in galaxies with higher values of Bar/T and ones with longer bars, is not seen here; in fact,

I find the opposite. It is unclear whether this trend is real or due to challenges in defining central stellar structures at high redshifts, where the Sérsic index cannot be determined robustly.

Overall, this study presents barred galaxies in the early Universe as well-established, evolved structures that must have undergone rapid bar formation and early bar evolution to produce long bars with properties similar to those observed in nearby galaxies. This work provides insight into the role of bar-driven evolution in young galaxies and underscores the need to re-evaluate the theory of early disc settling and the onset of bar formation.

CHAPTER 5

A nuclear disc at Cosmic Noon: evidence of early bar-driven galaxy evolution

In this chapter, I present a paper submitted to the Letters of the Monthly Notices of the Royal Astronomical Society [Le Conte et al., 2026] on the discovery of a nuclear disc at Cosmic Noon.

Recent studies have revealed that bars can form as early as a few billion years after the Big Bang, already displaying similar characteristics of evolved bars in the Local Universe. Bars redistribute angular momentum throughout the galaxy, regulating star formation and AGN activity and forming new stellar structures, such as nuclear discs. However, the effects of bar-driven evolution on young galaxies are not yet known, as no evidence of bar-built stellar structures has ever been found beyond $z = 1$, until now. In this work, I present evidence for a bar-built, star-forming nuclear disc already present at redshift $z = 1.5$. This is the first evidence of a bar-built stellar structure at Cosmic Noon. I find that this nuclear disc is actively forming stars and is comparable in size to some nuclear discs in nearby galaxies. This evidence solidifies the emerging picture in which bars are fundamental not only in the late evolution of galaxies but also in their early stages. It challenges the current paradigm by urging a revision of my picture of galaxy evolution beyond redshift one to include new considerations of the role of bars as early as a few billion years after the Big Bang.

5.1 Introduction

During the image analysis of Chapter 4, a unique and interesting galaxy was revealed. Thus, in this chapter, I conduct a follow-up study of this galaxy, using several image analysis techniques to accumulate evidence for a nuclear disc at Cosmic Noon.

In this Chapter, I present detailed structural analyses of JWST images of a barred galaxy at a spectroscopic redshift of $z = 1.5$ and provide evidence for a nuclear disc. This is the most distant nuclear disc to date. In the next section, I present the data and analyses performed, while in § 5.3 I present the results, which are discussed in § 5.4. Section 5.5 summarises my main conclusions.

5.2 Data analysis

5.2.1 Data

For this study, I use JWST CEERS observations, including imaging from the NIRCam filters (F115W, F150W, F200W, F277W, F356W, F410M, and F444W) and spectra from the Near Infrared Spectrograph (NIRSpec) with medium resolution, $R \sim 1,000$, and gratings (G140M, G235M, and G395M). The NIRCam exposures I retrieved from the `Mikulski Archive for Space Telescopes (MAST)` and reprocessed with the official JWST pipeline (v1.8.2, CRDS v1084), following the procedures of Ferreira et al. [2023] and Adams et al. [2023] but incorporating several refinements which are summarised in § 4.2. To ensure sub-pixel alignment across the dataset, each filter is reprojected onto the F444W grid at a resolution of $0.03''$ pixel^{-1}. A comprehensive description of the workflow and its validation is given in Adams et al. [2024], Conselice et al. [2024], Harvey et al. [2025]. We thus produce 30 mas 128×128 pixel cutouts from the NIRCam data.

The reduced spectra for the galaxy were obtained from the DAWN JWST Archive[1] (DJA). A consistent redshift of $z = 1.461$ was identified across all 3 spectra (G140M,

[1] https://dawn-cph.github.io/dja/

G235M, G395M) using the `msaexp` redshift fitting tool (which the DJA uses). The spectra cover the nuclear bar, but analysing the spectra is beyond the scope of this chapter, since spectra of the main bar or disc are not available. In this study, I use the NIRCam empirical PSF FWHM[2]. The F115W PSF FWHM is 0.040″; corresponding to a linear resolution of 0.347 kpc for $z = 1.461$. The PSF FWHM degrades for longer-wavelength filters; hence, the F444W PSF FWHM is 0.145″, with a linear resolution of 1.259 kpc. The image analysis of this chapter is primarily conducted in the F150W and F200W filters, with PSF FWHMs of 0.050″ and 0.066″, corresponding to linear resolutions of 0.434 and 0.573 kpc, respectively.

5.2.2 Unsharp masking

Bright components at the centre of galaxies can make it difficult to identify finer substructures, such as the nuclear disc. The change in light between the nuclear disc and the stellar bar or main disc can be enhanced by the effective technique of unsharp masking [e.g., Malin, 1977], which removes light associated with large structures in the galaxy. I generate unsharp masked images by first convolving the NIRCam image with a circular Gaussian kernel with $\sigma = 4.4$ pixels, corresponding to 0.132″. The kernel size was chosen to be greater than 2× FWHM and the radius of a possible nuclear disc. The original NIRCam image is then divided by the convolved image to reveal small structures in the galaxy.

5.2.3 Photometric decompositions

A powerful technique for deriving the structural properties of a galaxy is to perform a two-dimensional photometric decomposition, which I perform here using IMFIT v1.8 [Erwin, 2015]. I proceed with my image preparation and IMFIT configuration, as described in § 4.3.

I fit all NIRCam images with three components: the disc, bar, and central component. Collectively, I fit 18 free parameters. See § 4.3 for a detailed description of

[2]JWST user documentation: https://jwst-docs.stsci.edu/jwst-near-infrared-camera/nircam-performance/nircam-point-spread-functions

the central component fit.

5.2.4 Isophotal analysis

Structures in galaxies can also be traced with contours of equal intensity, i.e., isophotes. The structures deduced from isophotal contours can be parameterised with ellipse fitting. For example, an indication of a barred nuclear disc within a barred galaxy is a double peak in the radial profile of the ellipticity of the isophotes [see Erwin, 2004]. See the ellipse fitting routine described in Chapter 3 for details about this technique.

I obtain the parameters of the fitted ellipses as a function of radius, and I am most interested in the radial profiles of the isophotal ellipticity. I thus focus on identifying the semi-major axis of any major, isolated ellipticity peaks.

5.2.5 SED fitting

We perform resolved SED fitting using the Bayesian SED fitting tool BAGPIPES [e.g., Carnall et al., 2018] via the EXPANSE package [e.g., Harvey et al., 2025] in order to produce resolved measurements of the stellar mass and star formation rate surface densities in the central component, bar, and disc of the galaxy. The SED fitting model is constructed as follows: we fix the redshift to the known spectroscopic redshift, with the flexible non-parametric 'continuity' star formation history (SFH) of Leja et al. [2019]. To model dust attenuation, we use a single-component dust law [Calzetti et al., 2000], with a uniform prior of $0 \leq A_V \leq 5$. We utilise a BPASS [Stanway and Eldridge, 2018] SPS model, with a Kroupa [2001] initial mass function (IMF), allowing for nebular emission from star-forming regions using CLOUDY post-processing with a uniform prior on the logarithm of the ionisation parameter $\log U$ between -4 and -1. We allow a broad log-uniform prior on stellar metallicity, between 10^{-3} and $2.5 Z_{\odot}$.

The resolved SED fitting process broadly follows Harvey et al. [2025]; in short, we convolve all NIRCam cutouts to the measured PSF for the F444W filter using an empirical PSF model, then perform Voronoi binning on the F277W cutout using

VORBIN [Cappellari and Copin, 2012] to ensure a per-bin SNR > 10 in every fitted region. This SNR is sufficient for simple measurements of the 4000Å break (D4000), but in the central regions, which are the focus of this study, it is largely exceeded. We mask a small number of bins very close to the detector edge in the long wavelength filters, which are noise-dominated. We fit each bin independently using BAGPIPES as described above using MultiNest nested sampling [e.g., Feroz et al., 2009]. We probe the strength of the D4000 by also using HST ACS/WFC F606W ($\sim 0.6\mu$m) and F814W ($\sim 0.8\mu$m). We thus produce maps of the star formation rate (SFR) density, stellar mass density, and the strength of the 4000Å break (D4000), corresponding to the 50th percentile of the posterior distribution for each bin and parameter.

5.3 Results

Armed with the analysis tools described above, I studied the structural properties of a subset of barred galaxies at $z > 1$ from the work presented in Chapter 3. The study identified more than 70 barred galaxies via visual classification, and the analysis techniques described here were used to measure their bar properties in Chapter 4. In the course of these analyses, I have found one galaxy (CEERS 4031) with evidence of a nuclear disc.

I thus report here the discovery of the first nuclear disc observed beyond $z = 1$ and having an age of only 4.5 billion years after the Big Bang. The $\log_{10}(M_\star) = 10.75 \pm 0.05$ $M_\odot$ galaxy was categorised as a strongly barred galaxy in my study of the bar fraction, which used visual classification and ellipse fits to identify a high-redshift sample of barred galaxies and measure their properties. This galaxy already stood out in that analysis, as I measured a long bar with a projected length (semi-major axis) of $L_{bar} = 5.33 \pm 0.08$ kpc in a near-face-on spiral disc. However, we note that given the low inclination of the galaxy, the true, deprojected length is not substantially different, although it will naturally be slightly larger.

Figure 5.1 shows the galaxy in seven NIRCam filters, where a central structure is already discernible; in particular, an elongated structure is seen in the bluest filters (which have better spatial resolution). The NIRCam filter wavelength range spans

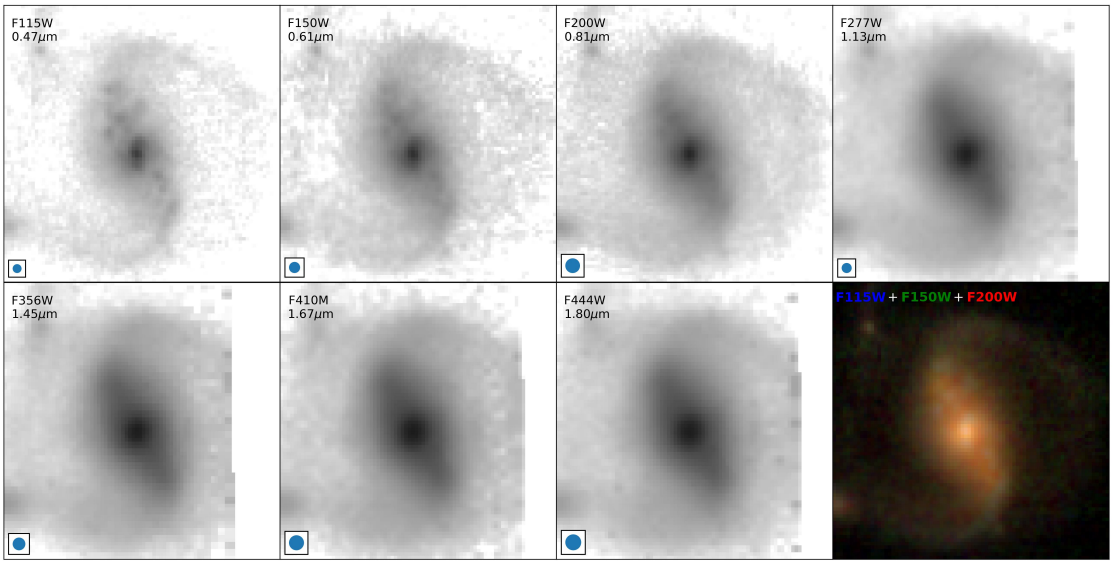

Figure 5.1: The galaxy images from seven NIRCam filters, annotated in the top-left corner of each image with the filter name and rest-frame wavelength for a redshift of $z = 1.461$. A circle depicting 2×FWHM of the PSF is shown in the lower-left corner of each image. The lower-right panel is an RGB image obtained from the filters F115W, F150W and F200W.

from 1.15μm to 4.44μm, corresponding to a rest-frame wavelength of 0.47μm to 1.80μm for this galaxy at $z = 1.461$. The RGB image constructed from the shorter-wavelength channel reveals that the ends of the elongated central stellar structure are bluer, indicating younger stellar populations and enhanced star formation.

Using three of the techniques described in detail in § 5.2, encompassing structure-enhancement and model-dependent approaches, I reveal the nature of the nuclear structure. These techniques are: unsharp masking, which enhances high spatial frequency substructures; 2D photometric decomposition, which involves the fitting of a three-component model composed of a disc, bar, and a central component representing the main stellar structures of the galaxy; and isophotal ellipse fitting to the isoluminance contours of the image, allowing one to obtain a radial ellipticity profile of the galaxy and its inner components. The photometric decomposition can also be used to produce residual images, often revealing substructures.

The results from the analyses of the NIRCam filters F150W and F200W are shown in Figure 5.2. These two filters were chosen for their optimal balance between high spatial resolution and not being too 'blue', where the main bar becomes too

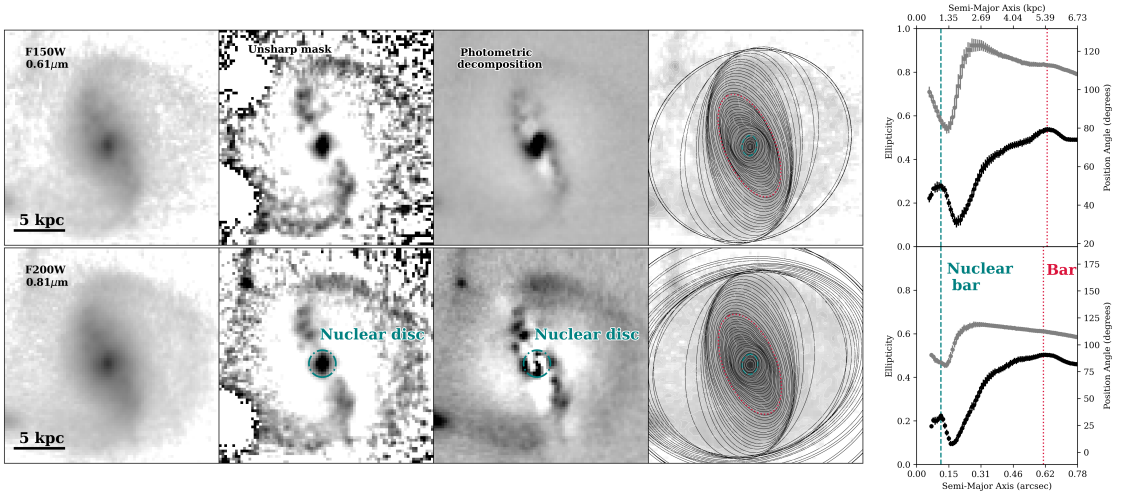

Figure 5.2: Image analysis of the galaxy in the F150W (top row) and F200W (bottom row) NIRCam filters. From left to right: NIRCam image; unsharp masked image; IMFIT residual image for a multi-component fit; isophotal ellipse fitting of the NIRCam image; ellipticity (black) and position angle (grey) radial profile from ellipse fitting, showing the peak in ellipticity of the nuclear bar in the nuclear disc as a dashed line and of the main bar as a dotted line. The nuclear disc size, measured from visual inspection of the images, is indicated by a dot-dashed circle in the unsharp-masked and residual images.

clumpy and a fit cannot be obtained. An elongated structure exhibiting a pair of symmetric 'wings' resembling spiral arms $\approx$ 1.3 kpc in radius, is enhanced in the unsharp-marked images. These images reveal a distinctive light deficit between the bar and this central stellar structure. The light deficit is important because it indicates a physical separation between the central stellar structure and the bar, and thus is not simply a continuation of the bar towards the centre.

The stellar substructure is further highlighted in the residuals of the multi-component fit to the image. For the NIRCam filters F150W and F200W, I subtract the optimised model from the original image, which now clearly reveals a spiral structure. Again, the nuclear spiral structure consists of two winding arms that extend to $\approx$ 1.3 kpc. In F200W, the 2D decompositions indicate a central component with an effective radius, $R_e \approx 0.5$ kpc, and with a Sérsic index, $n = 0.8$. In F150W, I measure an effective radius, $R_e \approx 0.4$ kpc, and a Sérsic index, $n = 0.5$, although note that slight differences between filters may reflect the different dominant stellar populations in each filter. The near-exponential radial profile of the central component strongly suggests that it is indeed a nuclear disc hosting nuclear spiral arms,

much like nearby counterparts such as NGC 1097 and NGC 4314 [see Erwin and Sparke, 2003, Gadotti, 2026, Gadotti et al., 2019].

The uncertainties in parameters derived from photometric decomposition are non-trivial; however, studies have investigated the extent of these errors. Kim et al. [2014] discussed the variation in structural properties when changing the sky background by 1σ, and found that an increased sky background increased the Bar/T and ND/T by $\sim 8\%$, and the same happened in the reverse (see their Sec. 3.2). A variation in the sky value affects the bar and central component effective radius, R_e, by less than 3%. Furthermore, the author derived *statistical* errors[3] of $< 10\%$ for the nuclear disc effective radius, 17% for the bar effective radius, with ellipticities ranging from 5% to 15% for these two components, 13% for the central component Sérsic index, and 24% for the bar Sérsic index. Thus, the 1σ error corresponds to $\sigma = 0.11$ for $n = 0.843$ and $\sigma = 52.5$ for $R_e = 525$. The recent work of Gadotti [2026] conducted nuclear disc structural analysis on the TIMER sample [Gadotti et al., 2019] and reported that nuclear disc Sérsic indexes range from ≈ 0.5 to ≈ 2, peaking at ≈ 1.5. Additionally, the study found the nuclear disc size spans from 200 pc to 900 pc, peaking at 500 pc. I find this nuclear disc at Cosmic Noon to be similar to, if not larger than, those observed in nearby galaxies.

In addition, the elongated central structure from which the nuclear spiral arms emerge, readily seen in the NIRCam images taken with the bluest filters, suggests that the nuclear disc also hosts a nuclear bar. An indication of a barred nuclear disc within a nearby barred galaxy is shown as a double peak in the radial ellipticity profile derived from ellipse fits, since the two bars produce independent ellipticity peaks. Indeed, I do observe this behaviour in the NIRCam F150W and F200W filters. The peak of the nuclear bar ellipticity, $\varepsilon_{\mathrm{F150W}} = 0.28 \pm 0.02$ and $\varepsilon_{\mathrm{F200W}} = 0.22 \pm 0.01$, occurs at the same radii in both filters. Thus, corresponding to the peak in ellipticity, the nuclear bar has a length of 1050 pc, and the radial profile is derived with a step size of 78 pc; hence, the nuclear bar size is $L_{NB} = 1050 \pm 78$

[3]Kim et al. [2014] derives *statistical* errors from BUDDA [de Souza et al., 2004, Gadotti, 2008] which gives robust 1σ uncertainties on each structural parameter. Whereby, the program finds the global χ^2 minimum, and in keeping all other parameters fixed, iterates until the χ^2 values equate to a variation in 1σ.

Property	Value	Unit
RA	214.937795	°
DEC	52.826470	°
Redshift (z)	1.461	
Stellar mass ($\log_{10}(M_\star/M_\odot)$)[a]	10.75 ± 0.05	
Bar length (L_{bar})[b]	5.33 ± 0.08	kpc
Bar ellipticity (ε_{bar})[b]	0.50 ± 0.01	
Nuclear bar size ($L_{\rm NB}$)[b]	1050 ± 78	pc
Nuclear disc size ($R_{\rm ND}$)[c]	1300	pc
Nuclear disc effective radius (R_e)[d]	525 ± 52.5	pc
Nuclear disc Sérsic index (n)[d]	0.843 ± 0.11	
Disc-total luminosity ratio (D/T)[d]	0.50 ± 0.08	
Bar-total luminosity ratio (Bar/T)[d]	0.33 ± 0.03	
Nuclear disc-total luminosity ratio (ND/T)[d]	0.17 ± 0.01	

Table 5.1: Main properties of CEERS-4031.

[a] Photometric.
[b] From ellipse fits in F200W.
[c] From visual inspection of the unsharp-masked images and decomposition residuals in F200W. Both measurements agree on the quoted value.
[d] From the photometric decomposition in F200W.

pc. The shorter wavelength F150W filter indicates a slightly higher ellipticity for the nuclear bar and main bar than in the F200W filter. Such an effect has also been seen in local barred galaxies [e.g., Menéndez-Delmestre et al., 2024]. The PA is not exactly constant in the NSD/NB region but shows a minor variation of about 10 degrees. It is unlikely that this is caused by the nuclear spiral arms because the isophotes corresponding to the latter are quite round, as the galaxy is close to face-on, and so their PA is ill-defined, and their ellipticity is low. The nuclear disc itself is slightly larger than the nuclear bar, as seen often in nearby galaxies. In the two approaches that I have conducted, the measurements agree that the nuclear disc size is approximately 1.3 kpc. I list the structural properties of the nuclear disc derived from my analyses along with the host galaxy properties in Table 5.1.

In local galaxies, the outer parts of nuclear discs are often regions of heightened star formation and younger stellar populations, because gas is driven by the bar towards the centre [see also Huang et al., 2025]. To examine whether the area I have identified as the nuclear disc exhibits this characteristic, we perform resolved Spectral Energy Distribution (SED) fitting and produce property maps, shown in Figure

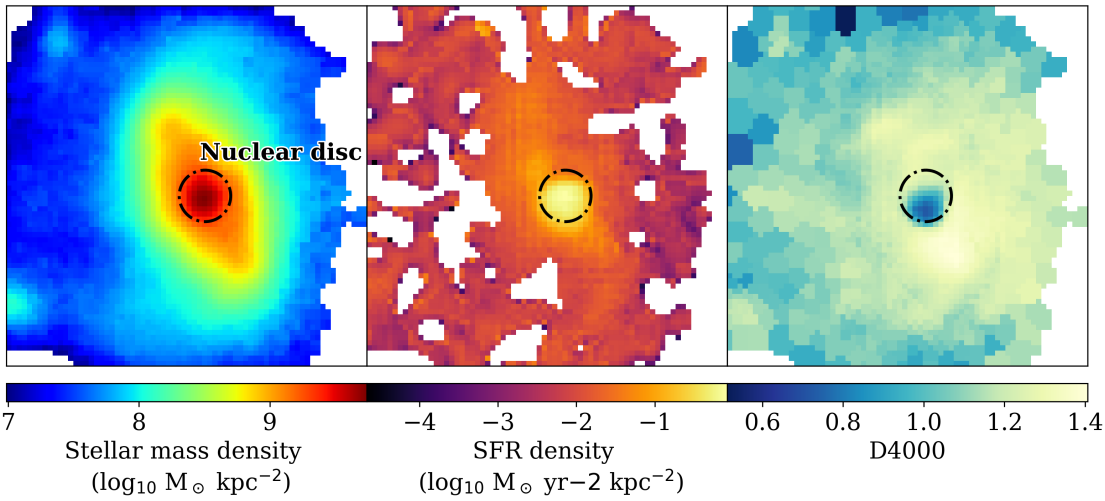

Figure 5.3: Resolved property maps from NIRCam SED fitting. Left to right: stellar mass density, SFR density, and the strength of the 4000Å break.

5.3, which reveal a high SFR density within $R_{\rm ND} = 1.3$. Additionally, we find very low D4000 values within R_{ND}, indicating younger star-forming populations. This enhanced star formation in the nuclear disc qualitatively agrees with the observed bluer ends of the nuclear bar and nuclear spiral arms in the RGB image in Figure 5.1. Altogether, I find that the nuclear structure in this galaxy shares properties with that of star-forming nuclear discs in the local Universe.

5.4 Discussion

I claim in this study that efficient bar-driven galaxy evolution has commenced by Cosmic Noon, resulting in the formation of a large nuclear disc. The size of the nuclear disc correlates with the length of the bar in nearby galaxies [e.g., Gadotti et al., 2020, Seo et al., 2019]. As the bar drives gas inwards, the nuclear disc is believed to grow inside-out [e.g., Kim and Lee, 2012], since the gas halts at successively larger radii, inducing bursts of star formation always more pronounced at the edge of the nuclear disc [e.g., Bittner et al., 2020]. In this study, I discover a large nuclear disc, $R_{\rm ND} \approx 1$ kpc and a long bar ≈ 5 kpc, which sits above the nuclear disc size to bar length relation in Gadotti et al. [2020]. Shlosman et al. [1989] define the co-evolution of the nuclear disc and bar to be limited by the Inner Lindblad Resonance (ILR) at $0.1R_{bar}$. Here, I find a greater radius at $0.2R_{bar}$, suggesting that the

nuclear disc has grown significantly and rapidly. Rapid substructure growth could be facilitated by the higher baryonic gas fractions observed at $z \approx 1.5$ [see Fig. 8 in **?**], which corresponds to $f_{\rm gas} \approx 0.4$ for the redshift and size of this galaxy. Gas is expected to play a significant role in the formation and evolution of barred galaxies, yet studies differ on the extent of its effects. Cosmological simulations find that, for strongly barred and unbarred galaxies, gas fractions are lower in the former [Algorry et al., 2017, **?**], whilst Seo et al. [2019] reported that cold stellar discs with large gas fractions formed bars earlier and more strongly, whereas high gas fractions in warm discs delayed bar formation. On the other hand, **?** shows that bar formation is more delayed in gas-rich discs than in gas-poor discs.

The recent study of Huang et al. [2025] observed that extreme processes were at play in a massive barred galaxy (4.5×10^{11}M$_\odot$) at $z = 2.467$. Through kinematic analysis, the authors found the galaxy to have a gas mass inflow rate of 579M$_\odot$yr^{-1}. By comparison, this is more than an order of magnitude higher than the rates of 0.01 to 50M$_\odot$yr^{-1} found for barred galaxies in the local Universe [Haan et al., 2009]. Hence, is the bar-driven evolution of CEERS-4031 as extreme as the processes reported in Huang et al. [2025]? I make several assumptions to calculate the gas mass inflow rate of CEERS-4031, namely that the ND/T luminosity ratio is equivalent to the ND/T stellar mass ratio. Furthermore, I assume that the nuclear disc forms instantaneously after bar formation. Using the stellar mass and ND/T ratio given in Table 5.1, I estimate the bar formation time given the gas inflow rate measured for local galaxies. For the most extreme and mean molecular gas inflow rates observed in Haan et al. [2009], 22.96 and 8.148M$_\odot$yr^{-1} (see their Table 9), I derive the formation times 0.42 and 1.17 Gyrs before the observation of this galaxy, corresponding to bar formation at the redshifts $z \approx 1.5$ to 1.7. Galaxies at Cosmic Noon are likely to be more gas-rich; thus, the more extreme gas inflow rates of locally barred galaxies would be more representative of this high-redshift galaxy. Alternatively, I calculate the bar formation time to be only 1.65×10^7yrs before the observation of this galaxy, assuming the inflow rate from Huang et al. [2025]. This would require processes that rapidly form a nuclear disc, since some simulation studies find that nuclear discs form $\sim 10^8$ yrs after bar formation [e.g., Athanassoula, 1992, Emsellem et al., 2015,

Seo et al., 2019]. Thus, it is unlikely that CEERS-4031 exhibits the same extreme dynamical processes as those of some other high-redshift galaxies. Altogether, these results suggest that the large gas fraction in CEERS-4031 has not influenced the formation and evolution of the bar, which is in line with the theoretical work of Fragkoudi et al. [2025].

A novel approach to age dating the bar of nearby disc galaxies is developed in de Sá-Freitas et al. [2023, 2025], where the authors predicted that both bars and nuclear discs might be present since $z \sim 4$. The method assumed that the nuclear disc forms quickly after the bar, so differences in the star-formation histories of the nuclear and main discs reflect the bar's age. To date, nuclear discs have been found only in nearby galaxies, and the assumption that nuclear discs form relatively quickly after the stellar bar has been supported by simulations. The discovery of a nuclear disc in a high-redshift galaxy provides evidence that nuclear discs can form at early epochs, particularly during the epoch of bar formation. To understand the star formation history of this galaxy and disentangle the age of the bar, I would require NIRSpec IFU data.

Nuclear structures larger than ~ 600 pc at $z \approx 1.6$ are resolvable with the NIRCam F200W filter, which is remarkably better than other space-based instruments [see table C1 of **?**]. CEERS-4031 has an extremely large nuclear disc with nuclear spiral arms and a nuclear bar, all of which are resolvable with NIRCam photometry. However, nuclear discs < 0.8 kpc in size would be missed. In a study of nearby nuclear discs, Gadotti [2026] reports that the distribution of R_e ranges from 200 to 900 pc. In my study, the derived $R_e \approx 500$ pc agrees with the peak of the nearby galaxy distribution. As expected, the visually measured nuclear disc size is systematically larger than R_e. My result is supported by the theoretical work of Kim and Lee [2012], which finds nuclear spiral arms in nuclear discs of type x_2 and $R_{\rm ND} > 0.6$ kpc. In the local Universe, up to $\approx 50\%$ of the galaxies with stellar mass $\log_{10}(M_\star) > 10.5\,{\rm M}_\odot$ (which corresponds to the galaxy in this study) host a nuclear bar [e.g., Erwin, 2024]. Population statistics will improve our understanding of the environments which promote bar-driven evolution and unveil the role of nuclear discs in AGN fuelling during the peak of cosmic AGN activity. However, such studies will

only reflect the properties of the largest nuclear discs due to the aforementioned resolution effects. The MICADO instrument at the Extremely Large Telescope will be able to resolve most, if not all, nuclear discs at all redshifts [**?**].

My discovery of a nuclear disc at Cosmic Noon provides evidence that we need to reevaluate the use of the term 'secular' in the context of bar-driven evolution. Whilst some aspects of bar-driven evolution may be secular, other processes within the bar radius may be considered to be rapid, especially regarding gas inflow and the building of nuclear structures. Furthermore, I measure the nuclear disc size to be on the larger end of the size distribution in nearby galaxies, indicating that gas has been efficiently transported and accumulated in the central region.

5.5 Conclusions

I discovered the most distant nuclear disc within a barred galaxy to date at $z = 1.461$, providing unequivocal evidence for bar-driven galaxy evolution in the early universe. The nuclear disc has a radius of $R_{\rm ND} \approx 1$ kpc, hosts a nuclear bar and nuclear spiral arms, and exhibits a near-exponential radial profile, thus being consistent with nuclear discs in nearby galaxies. Within the nuclear disc region, I observe heightened star formation and younger stellar populations, indicating bar-driven gas inflow. This nuclear disc thus exhibits all the hallmark signatures of bar-driven evolution in nearby galaxies and provides evidence for the rapid maturation of galaxy discs and bars at Cosmic Noon.

CHAPTER 6

Conclusions and outlook

In this thesis, I present the research conducted during my 3.5-year doctoral study at Durham University. To date, the onset of bar formation and the bar-driven evolution in young galaxies remain poorly understood. Through four investigations, I sought to test whether bars are present in disc galaxies at Cosmic Noon and, if so, how they differ from barred galaxies in the local Universe. Thus, I present the first comprehensive study of high-redshift barred galaxies using JWST NIRCam images in the CEERS survey.

This work was conducted by performing image analysis on several selected filters from the short- and long-wavelength channels of NIRCam. The CEERS sample overlaps with the HST EGS field, enabling a direct comparison. A nearly mass-complete galaxy sample at the redshift range $1 \leq z \leq 4$ was selected, and optimised to select near face-on galaxies. The disc and barred galaxy samples, spanning a range of NIRCam filters, were obtained via visual classification by five participants. With the resultant barred galaxy sample, encompassing the two categories, strongly and weakly barred, I traced the evolution of their incidence and structural properties to evaluate how bars form and evolve in young galaxies.

Taken together, the results of this thesis remarkably build a coherent picture in which bar formation can occur as early as a few billion years after the Big Bang, and bar-driven galaxy evolution in the early Universe is a rapid process capable of forming nuclear substructures.

In the following sections, I summarise the main results of each chapter and highlight how these findings build on our understanding of galaxy formation and bar-driven evolution. I conclude this thesis by outlining future avenues for investigation to develop a comprehensive picture of barred galaxy evolution.

Chapter 2: The JWST bar fraction

I conducted the first investigation into the fraction of bars in disc galaxies beyond $z = 2$. I found that the visually classified barred galaxy sample from JWST NIRCam images was twice that from HST WFC3 images, indicating that the bar fraction may be limited by instrument sensitivity and observing wavelength. Nonetheless, in JWST I still observe a decreasing bar frequency with increasing redshift, specifically from $\approx 17.8^{+5.1}_{-4.8}$ per cent at $z \approx 1.5$, to $\approx 13.8^{+6.5}_{-5.8}$ per cent at $z \approx 2.5$. This study shows that the onset of bar formation is much earlier than previous studies indicated.

Chapter 3: Evolution of the bar length

In the work presented in Chapter 2, I obtained a small sample of high-redshift barred galaxies; however, in this chapter, I expanded on this work by using a larger parent sample and extending it to higher redshifts. Specifically, I used a galaxy sample that was significantly larger by a factor of ~ 2.5, for the redshift range $1 \leq z \leq 4$. I obtained NIRCam images of the entire galaxy sample in the F200W, F356W, and F444W filters and repeated the same methodology of sample selection, optimisation, and visual inspection on the different wavelength samples.

Through this process, I corroborated the bar fraction results in Chapter 2, proving that the onset of bar formation occurs earlier than studies previously thought (see above). I found the same bar fraction across all redshift bins ($1 \leq z < 2$, $2 \leq z < 3$, and $3 \leq z < 4$), irrespective of the observed wavelength (i.e., the F200W

and F356W+F444W samples). In total, I identified more than 70 galaxies, including both weakly and strongly barred galaxies.

Using this larger sample of barred galaxies, I trace the evolution of bar length and ellipticity derived from ellipse fitting, comparing it with samples of nearby and intermediate-redshift barred galaxies. I found the bar lengths measured in longer-wavelength filters to be constant across the redshift range ($1 \leq z \leq 4$), with a mean of 3.6 kpc. Alternatively, in the shorter-wavelength filters, I observed a slight increase of 1 kpc in the bar length. At these high redshifts, I do not identify a population of very long bars with $L_{bar} > 6$ kpc, which are observed in samples at low and intermediate redshifts [Gadotti, 2011, Kim et al., 2021]. I did not observe a correlation between bar length and stellar mass, which is also found at low and intermediate redshifts. Finally, I showed that the bar grows in tandem with the outer disc by normalising the bar length by disc size, and measured a fraction of 0.5 from $z = 0$ to $z = 4$. Thus, this chapter identified a large population of long bars beyond $z = 1$, showing that bars could mature fast in such cases.

Chapter 4: Bar properties at Cosmic Noon

Given that previous chapters identified a large population of long, conspicuous barred galaxies beyond $z = 1$, this Chapter seeks to further our understanding of how the structural properties of bars in the early Universe differ from those in local galaxies. I conducted 2D photometric decompositions of the sample of strongly barred galaxies identified in Chapter 3. Using this state-of-the-art technique, I fitted three components (the disc, the bar and a central component) to the images, which were optimised by differential evolution.

I determined that these high-redshift bars are similar to those at intermediate and low redshifts, as their distributions of bar length, bar-to-total luminosity, ellipticity, and Sérsic index overlap strongly with those of nearby galaxies. Additionally, I derived the specific star formation rate of the sample and found that bars in passive galaxies contribute more luminosity to their host galaxies, are rounder, and have flatter light profiles than those in star-forming galaxies.

Chapter 5: A nuclear disc at $z \approx 1.5$

I identify the first evidence of a nuclear disc in a barred galaxy beyond the local Universe. This discovery was made via the 2D photometric decompositions conducted in Chapter 4, where residual images highlighted a clear nuclear spiral structure in the galaxy CEERS 4031. Thus, I applied image analysis techniques, including unsharp masking, 2D decompositions, and ellipse fitting, to reveal the nuclear structure. I obtained the Sérsic index of the nuclear structure to be $n \approx 0.8$, which is close to exponential; thus, the structure is determined to be a nuclear disc. I measured the nuclear disc radial size to be ≈ 1 kpc and identified evidence of a nuclear bar and spiral arms. The presence of a large nuclear disc with nuclear substructures demonstrates that bar-driven evolution is rapid at Cosmic Noon.

6.1 Future investigations

The work presented in this thesis has substantially revised the picture of secular galaxy evolution and raises a number of new, unanswered questions. Below, I discuss several future investigations that would benefit from the high-redshift JWST/CEERS barred-galaxy sample presented in this thesis and that would advance our understanding of bar-driven evolution in young galaxies.

6.1.1 The radio signatures of barred galaxies

Following my doctoral studies, I will commence a short-term postdoctoral position during which I will focus on the radio signatures of barred galaxies. The high-redshift barred galaxy sample, which I have analysed thoroughly in this thesis, has been identified from the JWST CEERS survey. Radio imaging of these galaxies is now available with the LOFAR Two-metre Sky Survey [LoTSS; Shimwell et al., 2017], which has imaged the entire Northern sky (overlapping with CEERS) at 120-168 MHz. This transformative survey achieves a $5''$ resolution, corresponding to a linear resolution of ≈ 43 kpc at Cosmic Noon. I will measure radio emission from these high-redshift barred galaxies and determine whether it originates from AGN or star formation. With a high sensitivity of 100 μJy/beam, I will be able to

distinguish between the origins of the radio source. Thus, I will test if a correlation exists between the barred galaxy properties and the presence of an AGN or star formation.

6.1.2 The slowing down of barred galaxies

A critical aspect of understanding bar-driven evolution lies in studying the stellar kinematics of barred galaxies, as these motions reveal the underlying gravitational forces that shape galactic structure. The bar pattern speed (Ω_p), which is the angular velocity of the bar, serves as a key diagnostic of secular evolution. It governs the locations of dynamical resonances within the disc and encodes the interaction between the bar and the dark matter halo through dynamical friction.

Cosmological simulations generally predict that bars slow down over time due to angular momentum transfer to the halo and dynamical friction from the dark matter halo, leading to predominantly slow bars [Fragkoudi et al., 2021]. In contrast, observations of nearby galaxies indicate that many bars remain fast [Aguerri et al., 2015], leading to the so-called "fast bar tension". This discrepancy suggests that local barred galaxies may host baryon-dominated central regions, potentially challenging predictions from ΛCDM cosmology. Géron et al. [2023] reported, for a sample of 200 galaxies in MaNGA, that Ω_p could be dependent on stellar mass, where more massive galaxies tend to be faster.

These tensions highlight the need to extend bar-kinematic studies beyond the local Universe. A measurement of Ω_p at high redshifts will, for the first time, test whether the bars were already slowing down in the early stages of disc evolution, thus providing crucial constraints on the timeline and efficiency of bar-driven secular processes.

The Tremaine-Weinberg method is the main technique for measuring Ω_p [Tremaine and Weinberg, 1984]. For my sample of high-redshift barred galaxies identified in JWST/NIRCam, one could use JWST/NIRSpec IFS observations to extract stellar kinematics and thus line-of-sight velocity distributions. The feasibility of this method was explored by Roshan et al. [2025], who reported that an $S/N \simeq 5$ per pixel is sufficient for reliable kinematic measurements, and the technique performed

adequately. The bar length, bar position angle, and galaxy inclination were measured in Chapter 3 and could be used here to infer whether these bars are rotating faster or slower than those in the local Universe. Additionally, the study could test the stellar mass dependence of Ω_p at Cosmic Noon. These results have the potential to constrain galaxy formation models and the effects of dark matter halos on stellar dynamics.

6.1.3 Bar-driven quenching and star formation

Roughly half of nearby barred galaxies exhibit ongoing star formation along their bars, while the remainder show little to none. Despite the presence of cold molecular gas flowing radially along the bar toward the galaxy centre, the local conditions within the bar often appear to be devoid of star formation. Simulations suggest that enhanced shear and turbulence within these fast-flowing gas streams may suppress star-formation efficiency. Yet, the role of star-forming bars within this framework, and how the bar's dynamical state relates to the broader properties of its host galaxy, remains poorly understood.

Recent studies of nearby systems reveal a complex picture. Fraser-McKelvie et al. [2020] found that star-forming bars are more common in low-mass galaxies. Neumann et al. [2019] reported a clear dichotomy between the star-forming and quiescent bars, suggesting a rapid quenching process. When comparing SFRs with the available cold gas content, Maeda et al. [2023] found systematically lower star formation efficiencies (SFE) in bars relative to their surrounding discs, whereas Díaz-García et al. [2021] showed that the SFE in massive barred galaxies does not differ significantly from that of unbarred systems. Clearly, bars have a strong effect on the star formation within a galaxy, and Querejeta et al. [2021] showed the bar diversity in 74 nearby PHANGS galaxies, demonstrating that bars are not always regions devoid of gas and star formation.

In a more global context, studies aim to reveal the bars' influence on a broader scale by measuring star formation across the galaxy. A star formation desert in the inner regions of barred galaxies forms due to the inward transfer of gas, leading to inside-out quenching. George et al. [2019] found 10% of their barred galaxy

population is star-forming, whereas 54% was quenched. However, a contradictory finding is that they find no correlation between bar length and galaxies' offset from the main sequence. Recent observational studies have also supported the inside-out quenching scenario [Scaloni et al., 2024].

The occurrence of star-forming bars in the local Universe remains unexplained. Probing these processes at earlier cosmic epochs will provide vital insight into how bars regulate star formation and quenching over time. Bar-driven mechanisms remain largely unexplored at high redshift, and measuring the star formation rates (SFRs) of barred galaxies at these epochs is crucial for understanding the onset of secular evolution. Investigating star formation activity in young, high-redshift barred galaxies will therefore shed light on the physical conditions that regulate it in dynamically evolving environments.

Future studies could use JWST/NIRSpec data to measure Hα and Hβ, which occur at 2 μm and 1.5 μm at $z = 2$, to trace the SFR distributions of my barred galaxy sample at Cosmic Noon. This could explore the use of spatially resolved SFR maps to assess whether SF is heightened in the central regions of barred galaxies and whether the outer disc appears quenched. Furthermore, this study will contribute to our understanding of SF histories in nearby galaxies and to galaxy assembly.

6.1.4 The bars' role in fuelling AGN

Major galaxy mergers were long considered the primary drivers of the co-evolution between SMBHs and their host galaxies. However, recent observations demonstrate that merger-free black hole growth can be equally significant. In the absence of mergers, another mechanism must channel gas efficiently toward the galactic centre, and stellar bars are a compelling candidate.

Although the precise influence of bars on black hole growth remains debated, both theoretical models and observations agree that bars can effectively funnel gas into the inner kiloparsec, building a reservoir to feed the SMBH and potentially triggering nuclear activity through other processes bringing gas closer to the SMBH [Athanassoula, 2003]. Although some studies find no strong correlation between bar presence and AGN incidence [e.g., Cisternas et al., 2015, Goulding et al., 2017,

Zee et al., 2023], others report an enhancement of AGN activity in barred systems, suggesting that bar-driven inflows may play a role under certain conditions [e.g., Garland et al., 2023, 2024, Knapen et al., 2000, La Marca et al., 2026, Silva-Lima et al., 2022].

At Cosmic Noon ($z \approx 2$), where the global AGN fraction peaks, this question becomes particularly pertinent. This epoch offers an ideal window for quantifying the AGN fraction in high-redshift barred galaxies and disentangling the relative contributions of bar- and merger-driven black hole fueling.

It would be interesting to investigate the occurrence of AGN within my sample of disc galaxies, including unbarred, weakly barred, and strongly barred galaxies, to determine whether AGN activity correlates with bar strength or host properties. This could test whether star formation rates are elevated in AGN-hosting galaxies, probing potential feedback processes and their connection to early bar-driven secular evolution.

X-ray detection is a widely used indicator of AGN; therefore, a study could use Chandra AEGIS-X Deep archival data to estimate the incidence of AGN at $z \geq 1$ [Davis et al., 2007]. Alternatively, the Mid-Infrared Instrument (MIRI) Extended Groth Strip (EGS) Galaxy and Active Galactic Nucleus (MEGA) survey covers $\sim 69\%$ of NIRCam CEERS imaging [Backhaus et al., 2025]. Meaning, a high proportion of my disc galaxy sample, and subsequently barred galaxy sample, is included. By extending IR SED coverage, MEGA can detect more obscured and low-luminosity AGN by identifying PAH features. If bars efficiently fuel AGN at Cosmic Noon, we expect an elevated AGN fraction in strongly barred galaxies relative to the unbarred disc sample. Furthermore, by considering the environment density, it is possible to distinguish between black hole-galaxy co-evolution driven by stellar bars and that driven by mergers.

Bibliography

R. G. Abraham, M. R. Merrifield, R. S. Ellis, N. R. Tanvir, and J. Brinchmann. The evolution of barred spiral galaxies in the Hubble Deep Fields North and South. *MNRAS*, 308(2):569–576, Sept. 1999. doi: 10.1046/j.1365-8711.1999.02766.x. 1.2.3, 1.2.3

S. Abraham, A. K. Aniyan, A. K. Kembhavi, N. S. Philip, and K. Vaghmare. Detection of bars in galaxies using a deep convolutional neural network. *MNRAS*, 477(1):894–903, June 2018. doi: 10.1093/mnras/sty627. 1.2.3

N. J. Adams, C. J. Conselice, L. Ferreira, D. Austin, J. A. A. Trussler, I. Juodžbalis, S. M. Wilkins, J. Caruana, P. Dayal, A. Verma, and A. P. Vijayan. Discovery and properties of ultra-high redshift galaxies (9 ¡ z ¡ 12) in the JWST ERO SMACS 0723 Field. *MNRAS*, 518(3):4755–4766, Jan. 2023. doi: 10.1093/mnras/stac3347. 2.2.1, 3.2.1, 4.2, 5.2.1

N. J. Adams, C. J. Conselice, D. Austin, T. Harvey, L. Ferreira, J. Trussler, I. Juodžbalis, Q. Li, R. Windhorst, S. H. Cohen, R. A. Jansen, J. Summers, S. Tompkins, S. P. Driver, A. Robotham, J. C. J. D'Silva, H. Yan, D. Coe, B. Frye, N. A. Grogin, A. M. Koekemoer, M. A. Marshall, N. Pirzkal, R. E. Ryan, W. P. Maksym, M. J. Rutkowski, C. N. A. Willmer, H. B. Hammel, M. Nonino, R. Bhatawdekar, S. M. Wilkins, L. D. Bradley, T. Broadhurst, C. Cheng, H. Dole, N. P. Hathi, and A. Zitrin. EPOCHS. II. The Ultraviolet Luminosity Function from 7.5 ¡ z ¡ 13.5 Using 180 arcmin^2 of Deep, Blank Fields from the PEARLS Survey and Public JWST Data. *ApJ*, 965(2):169, Apr. 2024. doi: 10.3847/1538-4357/ad2a7b. 3.2.1, 4.2, 5.2.1

N. J. Adams, G. Ferrami, L. Westcott, T. Harvey, V. Estrada-Carpenter, C. J. Conselice, D. Austin, J. S. B. Wyithe, C. M. Goolsby, Q. Li, V. Rusakov, R. A. Windhorst, S. H. Cohen, R. A. Jansen, J. Summers, R. O'Brein, A. M. Koekemoer, S. P. Driver, B. Frye, N. P. Hathi, D. Coe, N. A. Grogin, M. A. Marshall, N. Pirzkal, R. E. Ryan, Jr., C. N. A. Willmer, H. Yan, B. W. Holwerda, P. S. Kamieneski,

T. Broadhurst, W. P. Maksym, P. Saikia, and J. D. Gelfand. JWSTs PEARLS: NIRCam imaging and NIRISS spectroscopy of a $z = 3.6$ star-forming galaxy lensed into a near-Einstein Ring by a $z = 1.258$ massive elliptical galaxy. *arXiv e-prints*, art. arXiv:2504.03571, Apr. 2025. doi: 10.48550/arXiv.2504.03571. 3.2.1

J. A. L. Aguerri, A. M. Varela, M. Prieto, and C. Muñoz-Tuñón. Optical Surface Photometry of a Sample of Disk Galaxies. I. Observations and Data Reduction. *AJ*, 119(4):1638–1644, Apr. 2000. doi: 10.1086/301281. 4.5.2

J. A. L. Aguerri, J. Méndez-Abreu, and E. M. Corsini. The population of barred galaxies in the local universe. I. Detection and characterisation of bars. *A&A*, 495 (2):491–504, Feb. 2009. doi: 10.1051/0004-6361:200810931. 1.2, 1.6, 2.3.1, 2.5

J. A. L. Aguerri, J. Méndez-Abreu, J. Falcón-Barroso, A. Amorin, J. Barrera-Ballesteros, R. Cid Fernandes, R. García-Benito, B. García-Lorenzo, R. M. González Delgado, B. Husemann, V. Kalinova, M. Lyubenova, R. A. Marino, I. Márquez, D. Mast, E. Pérez, S. F. Sánchez, G. van de Ven, C. J. Walcher, N. Backsmann, C. Cortijo-Ferrero, J. Bland-Hawthorn, A. del Olmo, J. Iglesias-Páramo, I. Pérez, P. Sánchez-Blázquez, L. Wisotzki, and B. Ziegler. Bar pattern speeds in CALIFA galaxies. I. Fast bars across the Hubble sequence. *A&A*, 576: A102, Apr. 2015. doi: 10.1051/0004-6361/201423383. 6.1.2

J. A. L. Aguerri, E. D'Onghia, V. Cuomo, and L. Morelli. Evolution of dark gaps in barred galaxies. *A&A*, 670:A123, Feb. 2023. doi: 10.1051/0004-6361/202244344. 1.2.4, 4.5.2

D. G. Algorry, J. F. Navarro, M. G. Abadi, L. V. Sales, R. G. Bower, R. A. Crain, C. Dalla Vecchia, C. S. Frenk, M. Schaller, J. Schaye, and T. Theuns. Barred galaxies in the EAGLE cosmological hydrodynamical simulation. *MNRAS*, 469(1): 1054–1064, July 2017. doi: 10.1093/mnras/stx1008. 2.5, 3.6.1, 5.4

E. L. Allard, J. H. Knapen, R. F. Peletier, and M. Sarzi. The star formation history and evolution of the circumnuclear region of M100. *MNRAS*, 371(3):1087–1105, Sept. 2006. doi: 10.1111/j.1365-2966.2006.10751.x. 1.3.2

M. S. Alonso, G. Coldwell, and D. G. Lambas. Effect of bars in AGN host galaxies and black hole activity. *A&A*, 549:A141, Jan. 2013. doi: 10.1051/0004-6361/2012 20117. 1.3.5

S. Alonso, G. Coldwell, F. Duplancic, V. Mesa, and D. G. Lambas. The impact of bars and interactions on optically selected AGNs in spiral galaxies. *A&A*, 618: A149, Oct. 2018. doi: 10.1051/0004-6361/201832796. 1.3.5

A. Amvrosiadis. A multi-wavelengths view of the ISM for two dusty star-forming galaxies at z~4. In *EAS2023, European Astronomical Society Annual Meeting*, page 1695, July 2023. 2.6

A. Amvrosiadis, S. Lange, J. W. Nightingale, Q. He, C. S. Frenk, K. A. Oman, I. Smail, A. M. Swinbank, F. Fragkoudi, D. A. Gadotti, S. Cole, E. Borsato, A. Robertson, R. Massey, X. Cao, and R. Li. The onset of bar formation

in a massive galaxy at z ~3.8. *MNRAS*, 537(2):1163–1181, Feb. 2025. doi: 10.1093/mnras/staf048. 3.1

E. Athanassoula. The existence and shapes of dust lanes in galactic bars. *MNRAS*, 259:345–364, Nov. 1992. doi: 10.1093/mnras/259.2.345. 1.2, 1.3.2, 1.3.4, 2.6, 5.4

E. Athanassoula. Bar-Halo Interaction and Bar Growth. *ApJ*, 569(2):L83–L86, Apr. 2002. doi: 10.1086/340784. 1.2.1

E. Athanassoula. What determines the strength and the slowdown rate of bars? *MNRAS*, 341(4):1179–1198, June 2003. doi: 10.1046/j.1365-8711.2003.06473.x. 1.2.4, 1.3.1, 3.1, 3.6.1, 3.6.4

E. Athanassoula. Dynamical Evolution of Barred Galaxies. *Celestial Mechanics and Dynamical Astronomy*, 91(1-2):9–31, Jan. 2005. doi: 10.1007/s10569-004-4947-7. 1.3

E. Athanassoula and A. Misiriotis. Morphology, photometry and kinematics of N -body bars - I. Three models with different halo central concentrations. *MNRAS*, 330(1):35–52, Feb. 2002. doi: 10.1046/j.1365-8711.2002.05028.x. 1.3.1, 3.6.4

E. Athanassoula, S. Morin, H. Wozniak, D. Puy, M. J. Pierce, J. Lombard, and A. Bosma. The shape of bars in early-type barred galaxies. *MNRAS*, 245:130, July 1990. 1.2, 1.2.3

E. Athanassoula, S. A. Rodionov, N. Peschken, and J. C. Lambert. Forming Disk Galaxies in Wet Major Mergers. I. Three Fiducial Examples. *ApJ*, 821(2):90, Apr. 2016. doi: 10.3847/0004-637X/821/2/90. 1.2.3

L. Athanassoula. *Angular Momentum Redistribution and the Evolution and Morphology of Bars*, pages 313–326. Springer Berlin Heidelberg, Berlin, Heidelberg, 2003. ISBN 978-3-540-45040-5. doi: 10.1007/978-3-540-45040-5_26. URL https://doi.org/10.1007/978-3-540-45040-5_26. 1.3, 1.3.1, 1.3.5, 6.1.4

J. Baba and D. Kawata. Age dating the Galactic bar with the nuclear stellar disc. *MNRAS*, 492(3):4500–4511, Mar. 2020. doi: 10.1093/mnras/staa140. 2.6

B. E. Backhaus, A. Kirkpatrick, G. Yang, G. Troiani, K. Hamblin, J. S. Kartaltepe, D. D. Kocevski, A. M. Koekemoer, E. Lambrides, C. Papovich, and K. Ronayne. Mega mass assembly with jwst: The miri egs galaxy and active galactic nucleus survey. *The Astronomical Journal*, 170(6):300, nov 2025. doi: 10.3847/1538-3881/ae0cc4. URL https://doi.org/10.3847/1538-3881/ae0cc4. 6.1.4

F. D. Barazza, S. Jogee, and I. Marinova. Bars in Disk-dominated and Bulge-dominated Galaxies at z ~0: New Insights from ~3600 SDSS Galaxies. *ApJ*, 675 (2):1194–1212, Mar. 2008. doi: 10.1086/526510. 2.3.1, 2.4

F. D. Barazza, P. Jablonka, V. Desai, S. Jogee, A. Aragón-Salamanca, G. De Lucia, R. P. Saglia, C. Halliday, B. M. Poggianti, J. J. Dalcanton, G. Rudnick, B. Milvang-Jensen, S. Noll, L. Simard, D. I. Clowe, R. Pelló, S. D. M. White,

and D. Zaritsky. Frequency and properties of bars in cluster and field galaxies at intermediate redshifts. *A&A*, 497(3):713–728, Apr. 2009. doi: 10.1051/0004-6361/200810352. 2.3.1

I. Berentzen, E. Athanassoula, C. H. Heller, and K. J. Fricke. Numerical simulations of interacting gas-rich barred galaxies: vertical impact of small companions. *MNRAS*, 341(1):343–360, May 2003. doi: 10.1046/j.1365-8711.2003.06417.x. 2.5

I. Berentzen, E. Athanassoula, C. H. Heller, and K. J. Fricke. The regeneration of stellar bars by tidal interactions: numerical simulations of fly-by encounters. *MNRAS*, 347(1):220–236, Jan. 2004. doi: 10.1111/j.1365-2966.2004.07198.x. 1.2.1

E. Bertin and S. Arnouts. SExtractor: Software for source extraction. *A&AS*, 117: 393–404, June 1996. doi: 10.1051/aas:1996164. 3.3.1

D. Bi, I. Shlosman, and E. Romano-Díaz. Modeling Evolution of Galactic Bars at Cosmic Dawn. *ApJ*, 934(1):52, July 2022. doi: 10.3847/1538-4357/ac779b. 1.2.4

J. Binney, O. E. Gerhard, A. A. Stark, J. Bally, and K. I. Uchida. Understanding the kinematics of Galactic Centre gas. *MNRAS*, 252:210, Sept. 1991. doi: 10.1093/mnras/252.2.210. 1.1

A. Bittner, P. Sánchez-Blázquez, D. A. Gadotti, J. Neumann, F. Fragkoudi, P. Coelho, A. de Lorenzo-Cáceres, J. Falcón-Barroso, T. Kim, R. Leaman, I. Martín-Navarro, J. Méndez-Abreu, I. Pérez, M. Querejeta, M. K. Seidel, and G. van de Ven. Inside-out formation of nuclear discs and the absence of old central spheroids in barred galaxies of the TIMER survey. *A&A*, 643:A65, Nov. 2020. doi: 10.1051/0004-6361/202038450. 1.3.2, 1.3.4, 1.3.4, 5.4

J. Bland-Hawthorn and O. Gerhard. The galaxy in context: Structural, kinematic, and integrated properties. *Annual Review of Astronomy and Astrophysics*, 54(1): 529–596, Sept. 2016. ISSN 1545-4282. doi: 10.1146/annurev-astro-081915-023441. URL `http://dx.doi.org/10.1146/annurev-astro-081915-023441`. 1.2.4, 3.7, 3.5.2, 3.11, 3.6.2

J. Bland-Hawthorn, T. Tepper-Garcia, O. Agertz, and K. Freeman. The Rapid Onset of Stellar Bars in the Baryon-dominated Centers of Disk Galaxies. *ApJ*, 947 (2):80, Apr. 2023. doi: 10.3847/1538-4357/acc469. 2.5

J. Bovy, H. W. Leung, J. A. S. Hunt, J. T. Mackereth, D. A. García-Hernández, and A. Roman-Lopes. Life in the fast lane: a direct view of the dynamics, formation, and evolution of the Milky Way's bar. *MNRAS*, 490(4):4740–4747, Dec. 2019. doi: 10.1093/mnras/stz2891. 1.2.4

L. Bradley, B. Sipőcz, T. Robitaille, E. Tollerud, Z. Vinícius, C. Deil, K. Barbary, T. J. Wilson, I. Busko, A. Donath, H. M. Günther, M. Cara, P. L. Lim, S. Meßlinger, S. Conseil, A. Bostroem, M. Droettboom, E. M. Bray, L. A. Bratholm, G. Barentsen, M. Craig, S. Rathi, S. Pascual, G. Perren, I. Y. Georgiev, M. de Val-Borro, W. Kerzendorf, Y. P. Bach, B. Quint, and H. Souchereau. astropy/photutils: 1.5.0, July 2022. URL `https://doi.org/10.5281/zenodo.6825092`. 2.1, 2.3.1, 3.3.2

L. D. Brown, T. T. Cai, and A. DasGupta. Interval Estimation for a Binomial Proportion. *Statistical Science*, 16(2):101 – 133, 2001. doi: 10.1214/ss/1009213286. URL `https://doi.org/10.1214/ss/1009213286`. 2.4, 3.4

F. Buitrago, I. Trujillo, C. J. Conselice, R. J. Bouwens, M. Dickinson, and H. Yan. Size Evolution of the Most Massive Galaxies at 1.7 ¡ z ¡ 3 from GOODS NICMOS Survey Imaging. *ApJ*, 687(2):L61, Nov. 2008. doi: 10.1086/592836. 2.5

F. Buitrago, C. J. Conselice, B. Epinat, A. G. Bedregal, R. Grützbauch, and B. J. Weiner. SINFONI/VLT 3D spectroscopy of massive galaxies: evidence of rotational support at z $\sim$ 1.4. *MNRAS*, 439(2):1494–1521, Apr. 2014. doi: 10.1093/mnras/stu034. 2.5

R. Buta, A. J. Alpert, M. L. Cobb, D. A. Crocker, and G. B. Purcell. An Optical, Near-Infrared, and Kinematic Study of Four Early-Type Resonance Ring Galaxies. *AJ*, 116(3):1142–1162, Sept. 1998. doi: 10.1086/300494. 1.2.3

R. Buta, E. Laurikainen, H. Salo, and J. H. Knapen. Decreased Frequency of Strong Bars in S0 Galaxies: Evidence for Secular Evolution? *ApJ*, 721(1):259–266, Sept. 2010. doi: 10.1088/0004-637X/721/1/259. 4.5.4

R. J. Buta. Galactic rings revisited. II. Dark gaps and the locations of resonances in early-to-intermediate-type disc galaxies. *MNRAS*, 470(4):3819–3849, Oct. 2017. doi: 10.1093/mnras/stx1392. 4.5.2

R. J. Buta, K. Sheth, E. Athanassoula, A. Bosma, J. H. Knapen, E. Laurikainen, H. Salo, D. Elmegreen, L. C. Ho, D. Zaritsky, H. Courtois, J. L. Hinz, J.-C. Muñoz-Mateos, T. Kim, M. W. Regan, D. A. Gadotti, A. Gil de Paz, J. Laine, K. Menéndez-Delmestre, S. Comerón, S. Erroz Ferrer, M. Seibert, T. Mizusawa, B. Holwerda, and B. F. Madore. A Classical Morphological Analysis of Galaxies in the Spitzer Survey of Stellar Structure in Galaxies (S4G). *ApJS*, 217(2):32, Apr. 2015. doi: 10.1088/0067-0049/217/2/32. 1.2, 1.2.3, 1.2.3

D. Calzetti, L. Armus, R. C. Bohlin, A. L. Kinney, J. Koornneef, and T. Storchi-Bergmann. The Dust Content and Opacity of Actively Star-forming Galaxies. *ApJ*, 533(2):682–695, Apr. 2000. doi: 10.1086/308692. 5.2.5

E. Cameron. On the Estimation of Confidence Intervals for Binomial Population Proportions in Astronomy: The Simplicity and Superiority of the Bayesian Approach. *Publ. Astron. Soc. Australia*, 28(2):128–139, June 2011. doi: 10.1071/AS10046. 2.4, 3.4

E. Cameron, C. M. Carollo, P. Oesch, M. C. Aller, T. Bschorr, P. Cerulo, H. Aussel, P. Capak, E. Le Floc'h, O. Ilbert, J. P. Kneib, A. Koekemoer, A. Leauthaud, S. J. Lilly, R. Massey, H. J. McCracken, J. Rhodes, M. Salvato, D. B. Sanders, N. Scoville, K. Sheth, Y. Taniguchi, and D. Thompson. Bars in early- and late-type discs in COSMOS. *MNRAS*, 409(1):346–354, Nov. 2010. doi: 10.1111/j.1365-2966.2010.17314.x. 2.5

M. Cappellari and Y. Copin. Vorbin: Voronoi binning method. *Astrophysics Source Code Library*, pages ascl–1211, 2012. 5.2.5

C. Carles, H. Martel, S. L. Ellison, and D. Kawata. The mass dependence of star formation histories in barred spiral galaxies. *MNRAS*, 463(1):1074–1087, Nov. 2016. doi: 10.1093/mnras/stw2056. 1.3.3

A. Carnall, R. McLure, J. Dunlop, and R. Davé. Inferring the star formation histories of massive quiescent galaxies with bagpipes: evidence for multiple quenching mechanisms. *Monthly Notices of the Royal Astronomical Society*, 480(4):4379–4401, 2018. 5.2.5

M. K. Cavanagh and K. Bekki. Bars formed in galaxy merging and their classification with deep learning. *A&A*, 641:A77, Sept. 2020. doi: 10.1051/0004-6361/202037963. 1.2.1

B. Cervantes Sodi. Stellar, Gas, and Dark Matter Content of Barred Galaxies. *ApJ*, 835(1):80, Jan. 2017. doi: 10.3847/1538-4357/835/1/80. 1.2.4

D. Ceverino and A. Klypin. Resonances in barred galaxies. *MNRAS*, 379(3):1155–1168, Aug. 2007. doi: 10.1111/j.1365-2966.2007.12001.x. 1.4, 1.3.1

T.-Y. Cheng, C. J. Conselice, A. Aragón-Salamanca, M. Aguena, S. Allam, F. Andrade-Oliveira, J. Annis, A. F. L. Bluck, D. Brooks, D. L. Burke, M. Carrasco Kind, J. Carretero, A. Choi, M. Costanzi, L. N. da Costa, M. E. S. Pereira, J. De Vicente, H. T. Diehl, A. Drlica-Wagner, K. Eckert, S. Everett, A. E. Evrard, I. Ferrero, P. Fosalba, J. Frieman, J. García-Bellido, D. W. Gerdes, T. Giannantonio, D. Gruen, R. A. Gruendl, J. Gschwend, G. Gutierrez, S. R. Hinton, D. L. Hollowood, K. Honscheid, D. J. James, E. Krause, K. Kuehn, N. Kuropatkin, O. Lahav, M. A. G. Maia, M. March, F. Menanteau, R. Miquel, R. Morgan, F. Paz-Chinchón, A. Pieres, A. A. Plazas Malagón, A. Roodman, E. Sanchez, V. Scarpine, S. Serrano, I. Sevilla-Noarbe, M. Smith, M. Soares-Santos, E. Suchyta, M. E. C. Swanson, G. Tarle, D. Thomas, and C. To. Galaxy morphological classification catalogue of the Dark Energy Survey Year 3 data with convolutional neural networks. *MNRAS*, 507(3):4425–4444, Nov. 2021. doi: 10.1093/mnras/stab2142. 1.2.3

E. Cheung, E. Athanassoula, K. L. Masters, R. C. Nichol, A. Bosma, E. F. Bell, S. M. Faber, D. C. Koo, C. Lintott, T. Melvin, K. Schawinski, R. A. Skibba, and K. W. Willett. Galaxy Zoo: Observing Secular Evolution through Bars. *ApJ*, 779 (2):162, Dec. 2013. doi: 10.1088/0004-637X/779/2/162. 1.2.3

B. C. Ciambur and A. W. Graham. Quantifying the (X/peanut)-shaped structure in edge-on disc galaxies: length, strength, and nested peanuts. *MNRAS*, 459(2): 1276–1292, June 2016. doi: 10.1093/mnras/stw759. 1.3.3

B. C. Ciambur, F. Fragkoudi, S. Khoperskov, P. Di Matteo, and F. Combes. Double X/Peanut structures in barred galaxies - insights from an N-body simulation. *MNRAS*, 503(2):2203–2214, May 2021. doi: 10.1093/mnras/staa3814. 1.3.3

M. Cisternas, K. Sheth, M. Salvato, J. H. Knapen, F. Civano, and P. Santini. The Role of Bars in AGN Fueling in Disk Galaxies Over the Last Seven Billion Years. *ApJ*, 802(2):137, Apr. 2015. doi: 10.1088/0004-637X/802/2/137. 1.3.5, 6.1.4

C. J. Clopper and E. S. Pearson. The use of confidence or fiducial limits illustrated in the case of the binomial. *Biometrika*, 26(4):404–413, 1934. ISSN 00063444. URL `http://www.jstor.org/stable/2331986`. 2.4

P. Coelho and D. A. Gadotti. Bars Rejuvenating Bulges? Evidence from Stellar Population Analysis. *ApJ*, 743(1):L13, Dec. 2011. doi: 10.1088/2041-8205/743/1/L13. 1.3.2

A. Collier and A.-M. Madigan. The Coupling of Galactic Dark Matter Halos with Stellar Bars. *ApJ*, 915(1):23, July 2021. doi: 10.3847/1538-4357/ac004d. 1.2.1

F. Combes and R. H. Sanders. Formation and properties of persisting stellar bars. *A&A*, 96:164–173, Mar. 1981. 1.3.3

F. Combes, F. Debbasch, D. Friedli, and D. Pfenniger. Box and peanut shapes generated by stellar bars. *A&A*, 233:82, July 1990. 1.3.3, 4.4.2

S. Comerón, J. H. Knapen, J. E. Beckman, E. Laurikainen, H. Salo, I. Martínez-Valpuesta, and R. J. Buta. AINUR: Atlas of Images of NUclear Rings. *MNRAS*, 402(4):2462–2490, Mar. 2010. doi: 10.1111/j.1365-2966.2009.16057.x. 1.3.4

C. J. Conselice, N. Adams, T. Harvey, D. Austin, L. Ferreira, K. Ormerod, Q. Duan, J. Trussler, Q. Li, I. Juodzbalis, L. Westcott, H. Harris, L. T. C. Seeyave, A. F. L. Bluck, R. A. Windhorst, R. Bhatawdekar, D. Coe, S. H. Cohen, C. Cheng, S. P. Driver, B. Frye, L. J. Furtak, N. A. Grogin, N. P. Hathi, B. W. Holwerda, R. A. Jansen, A. M. Koekemoer, M. A. Marshall, M. Nonino, A. Robotham, J. Summers, S. M. Wilkins, C. N. A. Willmer, H. Yan, and A. Zitrin. Epochs i. the discovery and star forming properties of galaxies in the epoch of reionization at $6.5 < z < 18$ with pearls and public jwst data, 2024. URL `https://arxiv.org/abs/2407.14973`. 3.2.1

C. J. Conselice, J. T. F. Basham, D. O. Bettaney, L. Ferreira, N. Adams, T. Harvey, K. Ormerod, J. Caruana, A. F. L. Bluck, Q. Li, W. J. Roper, J. Trussler, D. Irodotou, and D. Austin. EPOCHS Paper V. The dependence of galaxy formation on galaxy structure at z ¡ 7 from JWST observations. *MNRAS*, 531(4):4857–4875, July 2024. doi: 10.1093/mnras/stae1180. 3.2.2, 4.2, 5.2.1

G. Contopoulos and T. Papayannopoulos. Orbits in weak and strong bars. *A&A*, 92(1-2):33–46, Dec. 1980. 1.4, 1.2.2

L. Costantin, P. G. Pérez-González, Y. Guo, C. Buttitta, S. Jogee, M. B. Bagley, G. Barro, J. S. Kartaltepe, A. M. Koekemoer, C. Cabello, E. M. Corsini, J. Méndez-Abreu, A. de la Vega, K. G. Iyer, L. Bisigello, Y. Cheng, L. Morelli, P. Arrabal Haro, F. Buitrago, M. C. Cooper, A. Dekel, M. Dickinson, S. L. Finkelstein, M. Giavalisco, B. W. Holwerda, M. Huertas-Company, R. A. Lucas, C. Papovich, N. Pirzkal, L.-M. Seillé, J. Vega-Ferrero, S. Wuyts, and L. Y. A. Yung. A Milky Way-like

barred spiral galaxy at a redshift of 3. *Nature*, 623(7987):499–501, Nov. 2023. doi: 10.1038/s41586-023-06636-x. 2.5, 2.6

H. D. Curtis. Descriptions of 762 Nebulae and Clusters Photographed with the Crossley Reflector. *Publications of Lick Observatory*, 13:9–42, Jan. 1918. 1.1

M. Davis, P. Guhathakurta, N. P. Konidaris, J. A. Newman, M. L. N. Ashby, A. D. Biggs, P. Barmby, K. Bundy, S. C. Chapman, A. L. Coil, C. J. Conselice, M. C. Cooper, D. J. Croton, P. R. M. Eisenhardt, R. S. Ellis, S. M. Faber, T. Fang, G. G. Fazio, A. Georgakakis, B. F. Gerke, W. M. Goss, S. Gwyn, J. Harker, A. M. Hopkins, J.-S. Huang, R. J. Ivison, S. A. Kassin, E. N. Kirby, A. M. Koekemoer, D. C. Koo, E. S. Laird, E. Le Floc'h, L. Lin, J. M. Lotz, P. J. Marshall, D. C. Martin, A. J. Metevier, L. A. Moustakas, K. Nandra, K. G. Noeske, C. Papovich, A. C. Phillips, R. M. Rich, G. H. Rieke, D. Rigopoulou, S. Salim, D. Schiminovich, L. Simard, I. Smail, T. A. Small, B. J. Weiner, C. N. A. Willmer, S. P. Willner, G. Wilson, E. L. Wright, and R. Yan. The All-Wavelength Extended Groth Strip International Survey (AEGIS) Data Sets. *ApJ*, 660(1):L1–L6, May 2007. doi: 10.1086/517931. 6.1.4

A. de Lorenzo-Cáceres, A. Vazdekis, J. A. L. Aguerri, E. M. Corsini, and V. P. Debattista. Constraining the formation of inner bars: photometry, kinematics and stellar populations in NGC 357. *MNRAS*, 420(2):1092–1106, Feb. 2012. doi: 10.1111/j.1365-2966.2011.20100.x. 1.3.2

C. de Sá-Freitas, F. Fragkoudi, D. A. Gadotti, J. Falcón-Barroso, A. Bittner, P. Sánchez-Blázquez, G. van de Ven, R. Bieri, L. Coccato, P. Coelho, K. Fahrion, G. Gonçalves, T. Kim, A. de Lorenzo-Cáceres, M. Martig, I. Martín-Navarro, J. Mendez-Abreu, J. Neumann, and M. Querejeta. A new method for age-dating the formation of bars in disc galaxies. The TIMER view on NGC1433's old bar and the inside-out growth of its nuclear disc. *A&A*, 671:A8, Mar. 2023. doi: 10.1051/0004-6361/202244667. 1.3.4, 2.5, 3.1, 5.4

C. de Sá-Freitas, D. A. Gadotti, F. Fragkoudi, P. Coelho, A. de Lorenzo-Cáceres, J. Falcón-Barroso, P. Sánchez-Blázquez, T. Kim, J. Mendez-Abreu, J. Neumann, M. Querejeta, and G. van de Ven. Bar ages derived for the first time in nearby galaxies: Insights on secular evolution from the TIMER sample. *arXiv e-prints*, art. arXiv:2503.20864, Mar. 2025. doi: 10.48550/arXiv.2503.20864. 1.2.4, 1.3.4, 3.6.2, 3.6.3, 5.4

R. E. de Souza, D. A. Gadotti, and S. dos Anjos. BUDDA: A New Two-dimensional Bulge/Disk Decomposition Code for Detailed Structural Analysis of Galaxies. *ApJS*, 153(2):411–427, Aug. 2004. doi: 10.1086/421554. 1.2.4, 4.4.2, 3

G. de Vaucouleurs, A. de Vaucouleurs, J. Corwin, Herold G., R. J. Buta, G. Paturel, and P. Fouque. *Third Reference Catalogue of Bright Galaxies*. Springer-Verlag, 1991. 1.2.3, 1.2.3, 2.10, 3.4

G. H. de Vaucouleurs. *The Spiral Structure of Our Galaxy*. Reidel, 1970. 1.1

G. H. de Vaucouleurs, A. de Vaucouleurs, and H. Shapley. *Reference catalogue of bright galaxies*. University of Texas Press, 1964. 1.1

P. Di Matteo, M. Haywood, F. Combes, B. Semelin, and O. N. Snaith. Signatures of radial migration in barred galaxies: Azimuthal variations in the metallicity distribution of old stars. *A&A*, 553:A102, May 2013. doi: 10.1051/0004-6361/201220539. 1.3

S. Díaz-García, H. Salo, E. Laurikainen, and M. Herrera-Endoqui. Characterization of galactic bars from 3.6 μm S^{4}G imaging. *A&A*, 587:A160, Mar. 2016. doi: 10.1051/0004-6361/201526161. 3.5.2, 3.6.2

S. Díaz-García, U. Lisenfeld, I. Pérez, A. Zurita, S. Verley, F. Combes, D. Espada, S. Leon, V. Martínez-Badenes, J. Sabater, and L. Verdes-Montenegro. Molecular gas and star formation within 12 strong galactic bars observed with IRAM-30 m. *A&A*, 654:A135, Oct. 2021. doi: 10.1051/0004-6361/202140674. 6.1.3

K. Duncan, C. J. Conselice, C. Mundy, E. Bell, J. Donley, A. Galametz, Y. Guo, N. A. Grogin, N. Hathi, J. Kartaltepe, D. Kocevski, A. M. Koekemoer, P. G. Pérez-González, K. B. Mantha, G. F. Snyder, and M. Stefanon. Observational Constraints on the Merger History of Galaxies since z $\approx$ 6: Probabilistic Galaxy Pair Counts in the CANDELS Fields. *ApJ*, 876(2):110, May 2019. doi: 10.3847/1538-4357/ab148a. 2.2.2, 2.4, 2.2, 2.9, 2.3, 3.2.2, 3.1, 3.5, 4.2, 4.1, 4.4.1

J. S. Dunlop, R. G. Abraham, M. L. N. Ashby, M. Bagley, P. N. Best, A. Bongiorno, R. Bouwens, R. A. A. Bowler, G. Brammer, M. Bremer, A. Calabro', A. Carnall, M. Castellano, M. Cirasuolo, C. Conselice, F. Cullen, R. Dave, P. Dayal, A. Dekel, M. Dickinson, K. J. Duncan, D. Elbaz, R. S. Ellis, H. C. Ferguson, A. Ferrara, S. L. Finkelstein, A. Fontana, S. Furlanetto, J. P. U. Fynbo, S. Gallerani, J. P. Gardner, M. Giavalisco, A. Grazian, N. Grogin, Y. Harikane, P. F. Hopkins, O. Ilbert, G. D. Illingworth, S. Juneau, I. Jung, J. Kartaltepe, S. Kassin, O. B. Kauffmann, S. Khochfar, A. Kirkpatrick, D. D. Kocevski, A. M. Koekemoer, I. Labbe, N. Laporte, R. L. Larson, R. A. Lucas, D. K. Magee, C. Mason, H. J. McCracken, D. McLeod, R. McLure, E. Merlin, A. Mesinger, B. Milvang-Jensen, J. A. Newman, P. Oesch, M. Ouchi, C. Pacifici, C. Papovich, J. Peacock, M. Peeples, L. Pentericci, P. G. Perez-Gonzalez, N. Pirzkal, A. Pope, J. P. Pye, N. A. Reddy, B. Robertson, M. Salvato, P. Santini, D. Schaerer, A. E. Shapley, R. Simons, R. Smit, B. D. Smith, G. Snyder, R. S. Somerville, E. R. Stanway, M. Stefanon, L. Tasca, T. Tikkanen, L. Tresse, J. R. Trump, K. E. Whitaker, S. M. Wilkins, G. Wright, J. S. B. Wyithe, P. van Dokkum, and P. van der Werf. PRIMER: Public Release IMaging for Extragalactic Research. JWST Proposal. Cycle 1, ID. #1837, Mar. 2021. 2.2

G. Efstathiou, G. Lake, and J. Negroponte. The stability and masses of disc galaxies. *MNRAS*, 199:1069–1088, June 1982. doi: 10.1093/mnras/199.4.1069. 1.2.1

B. G. Elmegreen and D. M. Elmegreen. Properties of barred spiral galaxies. *ApJ*, 288:438–455, Jan. 1985. doi: 10.1086/162810. 1.2.4, 4.4.2

B. G. Elmegreen, D. M. Elmegreen, and A. C. Hirst. A Constant Bar Fraction out to Redshift z ~1 in the Advanced Camera for Surveys Field of the Tadpole Galaxy. *ApJ*, 612(1):191–201, Sept. 2004. doi: 10.1086/422407. 1.2.3, 1.2.3, 1.2.3, 2.5

E. Emsellem, F. Renaud, F. Bournaud, B. Elmegreen, F. Combes, and J. M. Gabor. The interplay between a galactic bar and a supermassive black hole: nuclear fuelling in a subparsec resolution galaxy simulation. *MNRAS*, 446(3):2468–2482, Jan. 2015. doi: 10.1093/mnras/stu2209. 1.3.2, 1.3.4, 5.4

P. Erwin. Double-barred galaxies. I. A catalog of barred galaxies with stellar secondary bars and inner disks. *A&A*, 415:941–957, Mar. 2004. doi: 10.1051/0004-6361:20034408. 1.3.4, 5.2.4

P. Erwin. How large are the bars in barred galaxies? *MNRAS*, 364(1):283–302, Nov. 2005. doi: 10.1111/j.1365-2966.2005.09560.x. 2.5, 3.1, 3.3.1, 3.6.1

P. Erwin. IMFIT: A Fast, Flexible New Program for Astronomical Image Fitting. *ApJ*, 799(2):226, Feb. 2015. doi: 10.1088/0004-637X/799/2/226. 1.2.4, 3.3.3, 4.3, 5.2.3

P. Erwin. The dependence of bar frequency on galaxy mass, colour, and gas content - and angular resolution - in the local universe. *MNRAS*, 474(4):5372–5392, Mar. 2018. doi: 10.1093/mnras/stx3117. 1.2.4, 1.9, 1.2.4, 1.4, 2.4, 2.5, 3.5.1

P. Erwin. What determines the sizes of bars in spiral galaxies? *MNRAS*, 489(3):3553–3564, Nov. 2019. doi: 10.1093/mnras/stz2363. 2.5, 3.5.2, 3.6.2, 3.11

P. Erwin. The frequency and sizes of inner bars and nuclear rings in barred galaxies and their dependence on galaxy properties. *MNRAS*, 528(2):3613–3628, Feb. 2024. doi: 10.1093/mnras/stad3944. 5.4

P. Erwin and V. P. Debattista. The frequency and stellar-mass dependence of boxy/peanut-shaped bulges in barred galaxies. *MNRAS*, 468(2):2058–2080, June 2017. doi: 10.1093/mnras/stx620. 1.3.3

P. Erwin and L. S. Sparke. An Imaging Survey of Early-Type Barred Galaxies. *ApJS*, 146(2):299–352, June 2003. doi: 10.1086/367885. 5.3

P. Erwin, V. P. Debattista, and S. R. Anderson. The profiles of bars in spiral galaxies. *MNRAS*, 524(2):3166–3183, Sept. 2023. doi: 10.1093/mnras/stad1972. 1.2.4, 1.7

P. B. Eskridge, J. A. Frogel, R. W. Pogge, A. C. Quillen, R. L. Davies, D. L. DePoy, M. L. Houdashelt, L. E. Kuchinski, S. V. Ramírez, K. Sellgren, D. M. Terndrup, and G. P. Tiede. The Frequency of Barred Spiral Galaxies in the Near-Infrared. *AJ*, 119(2):536–544, Feb. 2000. doi: 10.1086/301203. 1.2, 1.2.3, 1.2.3, 1.4, 2.10, 3.4

J. M. Espejo Salcedo, S. Pastras, J. Vácha, C. Pulsoni, R. Genzel, N. M. Förster Schreiber, J.-B. Jolly, C. Barfety, J. Chen, G. Tozzi, D. Liu, L. Lee, S. Wuyts, L. Tacconi, R. Davies, H. Übler, D. Lutz, E. Wisnioski, J. Shangguan, M. Lee,

S. H. Price, F. Eisenhauer, A. Renzini, A. Nestor Shachar, and R. Herrera-Camus. Galaxy Morphologies at Cosmic Noon with JWST : A Foundation for Exploring Gas Transport with Bars and Spiral Arms. *arXiv e-prints*, art. arXiv:2503.21738, Mar. 2025. doi: 10.48550/arXiv.2503.21738. 1.2, 1.2.3, 3.1, 3.4, 3.4, 3.4, 3.6.1, 3.7

Euclid Collaboration, M. Huertas-Company, M. Walmsley, M. Siudek, P. Iglesias-Navarro, J. H. Knapen, S. Serjeant, H. J. Dickinson, L. Fortson, I. Garland, T. Géron, W. Keel, S. Kruk, C. J. Lintott, K. Mantha, K. Masters, D. O'Ryan, J. J. Popp, H. Roberts, C. Scarlata, J. S. Makechemu, B. Simmons, R. J. Smethurst, A. Spindler, M. Baes, E. M. Corsini, H. Domínguez Sánchez, E. Duran-Camacho, H. Fu, J. Junais, J. Mendez-Abreu, A. Nersesian, F. Shankar, M. N. Le, J. Vega-Ferrero, L. Wang, N. Aghanim, B. Altieri, A. Amara, S. Andreon, N. Auricchio, C. Baccigalupi, M. Baldi, A. Balestra, S. Bardelli, A. Basset, P. Battaglia, F. Bernardeau, A. Biviano, A. Bonchi, E. Branchini, M. Brescia, J. Brinchmann, S. Camera, V. Capobianco, C. Carbone, J. Carretero, S. Casas, M. Castellano, G. Castignani, S. Cavuoti, K. C. Chambers, A. Cimatti, C. Colodro-Conde, G. Congedo, C. J. Conselice, L. Conversi, Y. Copin, F. Courbin, H. M. Courtois, M. Cropper, A. Da Silva, H. Degaudenzi, G. De Lucia, A. M. Di Giorgio, C. Dolding, H. Dole, F. Dubath, C. A. J. Duncan, X. Dupac, S. Dusini, A. Ealet, S. Escoffier, M. Fabricius, M. Farina, R. Farinelli, F. Faustini, S. Ferriol, F. Finelli, S. Fotopoulou, M. Frailis, S. Galeotta, K. George, W. Gillard, B. Gillis, C. Giocoli, J. Gracia-Carpio, A. Grazian, F. Grupp, S. Gwyn, S. V. H. Haugan, H. Hoekstra, W. Holmes, I. M. Hook, F. Hormuth, A. Hornstrup, P. Hudelot, K. Jahnke, M. Jhabvala, E. Keihänen, S. Kermiche, B. Kubik, K. Kuijken, M. Kümmel, M. Kunz, H. Kurki-Suonio, Q. Le Boulc'h, A. M. C. Le Brun, D. Le Mignant, S. Ligori, P. B. Lilje, V. Lindholm, I. Lloro, D. Maino, E. Maiorano, O. Mansutti, S. Marcin, O. Marggraf, M. Martinelli, N. Martinet, F. Marulli, R. Massey, H. J. McCracken, E. Medinaceli, M. Melchior, Y. Mellier, M. Meneghetti, E. Merlin, G. Meylan, A. Mora, M. Moresco, L. Moscardini, C. Neissner, R. C. Nichol, S. M. Niemi, J. W. Nightingale, C. Padilla, S. Paltani, F. Pasian, K. Pedersen, W. J. Percival, V. Pettorino, S. Pires, G. Polenta, M. Poncet, L. A. Popa, L. Pozzetti, F. Raison, A. Renzi, J. Rhodes, G. Riccio, E. Romelli, M. Roncarelli, R. Saglia, Z. Sakr, D. Sapone, B. Sartoris, M. Schirmer, P. Schneider, M. Scodeggio, A. Secroun, G. Seidel, M. Seiffert, S. Serrano, P. Simon, C. Sirignano, G. Sirri, L. Stanco, J. Steinwagner, P. Tallada-Crespí, A. N. Taylor, I. Tereno, S. Toft, R. Toledo-Moreo, F. Torradeflot, I. Tutusaus, L. Valenziano, J. Valiviita, T. Vassallo, G. Verdoes Kleijn, Y. Wang, J. Weller, A. Zacchei, G. Zamorani, F. M. Zerbi, I. A. Zinchenko, E. Zucca, V. Allevato, M. Ballardini, and M. Bolzonella. Euclid Quick Data Release (Q1), A first look at the fraction of bars in massive galaxies at $z < 1$. *arXiv e-prints*, art. arXiv:2503.15311, Mar. 2025. doi: 10.48550/arXiv.2503.15311. 3.4, 3.4

F. Feroz, M. Hobson, and M. Bridges. Multinest: an efficient and robust bayesian inference tool for cosmology and particle physics. *Monthly Notices of the Royal Astronomical Society*, 398(4):1601–1614, 2009. 5.2.5

L. Ferreira, C. J. Conselice, E. Sazonova, F. Ferrari, J. Caruana, C.-B. Tohill, G. Lucatelli, N. Adams, D. Irodotou, M. A. Marshall, W. J. Roper, C. C. Lovell,

A. Verma, D. Austin, J. Trussler, and S. M. Wilkins. The JWST Hubble Sequence: The Rest-frame Optical Evolution of Galaxy Structure at 1.5 ¡ z ¡ 6.5. *ApJ*, 955 (2):94, Oct. 2023. doi: 10.3847/1538-4357/acec76. 1.4, 2.2.1, 2.2.2, 2.3.2, **??**, 2.4, 2.6, 3.2.1, 3.4, 4.2, 4.4.1, 4.1, 5.2.1

S. L. Finkelstein, M. B. Bagley, H. C. Ferguson, S. M. Wilkins, J. S. Kartaltepe, C. Papovich, L. Y. A. Yung, P. A. Haro, P. Behroozi, M. Dickinson, D. D. Kocevski, A. M. Koekemoer, R. L. Larson, A. Le Bail, A. M. Morales, P. G. Pérez-González, D. Burgarella, R. Davé, M. Hirschmann, R. S. Somerville, S. Wuyts, V. Bromm, C. M. Casey, A. Fontana, S. Fujimoto, J. P. Gardner, M. Giavalisco, A. Grazian, N. A. Grogin, N. P. Hathi, T. A. Hutchison, S. W. Jha, S. Jogee, L. J. Kewley, A. Kirkpatrick, A. S. Long, J. M. Lotz, L. Pentericci, J. D. R. Pierel, N. Pirzkal, S. Ravindranath, R. E. Ryan, J. R. Trump, G. Yang, R. Bhatawdekar, L. Bisigello, V. Buat, A. Calabrò, M. Castellano, N. J. Cleri, M. C. Cooper, D. Croton, E. Daddi, A. Dekel, D. Elbaz, M. Franco, E. Gawiser, B. W. Holwerda, M. Huertas-Company, A. E. Jaskot, G. C. K. Leung, R. A. Lucas, B. Mobasher, V. Pandya, S. Tacchella, B. J. Weiner, and J. A. Zavala. CEERS Key Paper. I. An Early Look into the First 500 Myr of Galaxy Formation with JWST. *ApJ*, 946(1):L13, Mar. 2023. doi: 10.3847/2041-8213/acade4. 2.2

D. B. Fisher and N. Drory. The Structure of Classical Bulges and Pseudobulges: the Link Between Pseudobulges and SÉRSIC Index. *AJ*, 136(2):773–839, Aug. 2008. doi: 10.1088/0004-6256/136/2/773. 4.3

D. B. Fisher and N. Drory. An Observational Guide to Identifying Pseudobulges and Classical Bulges in Disc Galaxies. In E. Laurikainen, R. Peletier, and D. Gadotti, editors, *Galactic Bulges*, volume 418 of *Astrophysics and Space Science Library*, page 41, Jan. 2016. doi: 10.1007/978-3-319-19378-6_3. 4.5.1

F. Fragkoudi, E. Athanassoula, and A. Bosma. A close look at secular evolution: boxy/peanut bulges reduce gas inflow to the central kiloparsec. *MNRAS*, 462(1): L41–L45, Oct. 2016. doi: 10.1093/mnrasl/slw120. 1.3.2

F. Fragkoudi, P. Di Matteo, M. Haywood, M. Schultheis, S. Khoperskov, A. Gómez, and F. Combes. The disc origin of the Milky Way bulge. Dissecting the chemo-morphological relations using N-body simulations and APOGEE. *A&A*, 616:A180, Sept. 2018. doi: 10.1051/0004-6361/201732509. 1.3

F. Fragkoudi, R. J. J. Grand, R. Pakmor, G. Blázquez-Calero, I. Gargiulo, F. Gomez, F. Marinacci, A. Monachesi, M. K. Ness, I. Perez, P. Tissera, and S. D. M. White. Chemodynamics of barred galaxies in cosmological simulations: On the Milky Way's quiescent merger history and in-situ bulge. *MNRAS*, 494(4): 5936–5960, June 2020. doi: 10.1093/mnras/staa1104. 1.2.3, 2.10

F. Fragkoudi, R. J. J. Grand, R. Pakmor, V. Springel, S. D. M. White, F. Marinacci, F. A. Gomez, and J. F. Navarro. Revisiting the tension between fast bars and the ΛCDM paradigm. *A&A*, 650:L16, June 2021. doi: 10.1051/0004-6361/202140320. 2.5, 6.1.2

F. Fragkoudi, R. J. J. Grand, R. Pakmor, F. Gómez, F. Marinacci, and V. Springel. Bar formation and evolution in the cosmological context: inputs from the Auriga simulations. *MNRAS*, 538(3):1587–1608, Apr. 2025. doi: 10.1093/mnras/staf389. 1.2, 1.2.1, 1.2.4, 1.4, 3.4, 3.6.2, 3.6.4, 4.5.3, 5.4

A. Fraser-McKelvie, A. Aragón-Salamanca, M. Merrifield, K. Masters, P. Nair, E. Emsellem, K. Kraljic, D. Krishnarao, B. H. Andrews, N. Drory, and J. Neumann. SDSS-IV MaNGA: spatially resolved star formation in barred galaxies. *MNRAS*, 495(4):4158–4169, July 2020. doi: 10.1093/mnras/staa1416. 6.1.3

A. Fraser-McKelvie, J. van de Sande, D. A. Gadotti, E. Emsellem, T. Brown, D. B. Fisher, M. Martig, M. Bureau, O. Gerhard, A. J. Battisti, J. Bland-Hawthorn, A. Boecker, B. Catinella, F. Combes, L. Cortese, S. M. Croom, T. A. Davis, J. Falcón-Barroso, F. Fragkoudi, K. C. Freeman, M. R. Hayden, R. McDermid, B. Mazzilli Ciraulo, J. T. Mendel, F. Pinna, A. Poci, T. H. Rutherford, C. de Sá-Freitas, L. A. Silva-Lima, L. M. Valenzuela, G. van de Ven, Z. Wang, and A. B. Watts. The GECKOS survey: Identifying kinematic sub-structures in edge-on galaxies. *A&A*, 700:A237, Aug. 2025. doi: 10.1051/0004-6361/202452891. 1.3.3

M. Frosst, D. Obreschkow, A. Ludlow, and A. Fraser-McKelvie. Origins and lifetimes of secular and tidal bars in simulated disc galaxies. *arXiv e-prints*, art. arXiv:2508.14626, Aug. 2025. doi: 10.48550/arXiv.2508.14626. 1.2.1

M. S. Fujii, J. Bédorf, J. Baba, and S. Portegies Zwart. The dynamics of stellar discs in live dark-matter haloes. *MNRAS*, 477(2):1451–1471, June 2018. doi: 10.1093/mnras/sty711. 1.2.1

D. A. Gadotti. Image decomposition of barred galaxies and AGN hosts. *MNRAS*, 384(1):420–439, Feb. 2008. doi: 10.1111/j.1365-2966.2007.12723.x. 1.2.4, 3.5.3, 4.4.2, 4.4.2, 4.5.1, 3

D. A. Gadotti. Structural properties of pseudo-bulges, classical bulges and elliptical galaxies: a Sloan Digital Sky Survey perspective. *MNRAS*, 393(4):1531–1552, Mar. 2009. doi: 10.1111/j.1365-2966.2008.14257.x. 1.3.4, 4.5.1

D. A. Gadotti. Secular evolution and structural properties of stellar bars in galaxies. *MNRAS*, 415(4):3308–3318, Aug. 2011. doi: 10.1111/j.1365-2966.2011.18945.x. 1.2.4, 1.2.4, 2.5, 3.1, 3.7, 3.5.2, 3.5.2, 3.8, 3.9, 3.6, 3.11, 3.6.2, 3.12, 3.7, 4.4.2, 4.6, 4.4.2, 4.4.3, 4.5.1, 6

D. A. Gadotti. Robust galaxy image decompositions with differential evolution optimization and the problem of classical bulges in and beyond the nearby Universe. *MNRAS*, 545(4):staf2072, Feb. 2026. doi: 10.1093/mnras/staf2072. 3.3.3, 4.3.2, 4.5.1, 5.3, 5.4

D. A. Gadotti and R. E. de Souza. NGC 4608 and NGC 5701: Barred Galaxies without Disks? *ApJ*, 583(2):L75–L78, Feb. 2003. doi: 10.1086/368159. 4.5.2

D. A. Gadotti and R. E. de Souza. On the Lengths, Colors, and Ages of 18 Face-on Bars. *ApJS*, 163(2):270–281, Apr. 2006. doi: 10.1086/500175. 3.1

D. A. Gadotti, E. Athanassoula, L. Carrasco, A. Bosma, R. E. de Souza, and E. Recillas. Near-infrared surface photometry of a sample of barred galaxies. *MNRAS*, 381(3):943–961, Nov. 2007. doi: 10.1111/j.1365-2966.2007.12295.x. 2.3.1, 3.5.2

D. A. Gadotti, M. K. Seidel, P. Sánchez-Blázquez, J. Falcón-Barroso, B. Husemann, P. Coelho, and I. Pérez. MUSE tells the story of NGC 4371: The dawning of secular evolution. *A&A*, 584:A90, Dec. 2015. doi: 10.1051/0004-6361/201526677. 1.2, 2.5

D. A. Gadotti, P. Sánchez-Blázquez, J. Falcón-Barroso, B. Husemann, M. K. Seidel, I. Pérez, A. de Lorenzo-Cáceres, I. Martinez-Valpuesta, F. Fragkoudi, G. Leung, G. van de Ven, R. Leaman, P. Coelho, M. Martig, T. Kim, J. Neumann, and M. Querejeta. Time Inference with MUSE in Extragalactic Rings (TIMER): properties of the survey and high-level data products. *MNRAS*, 482(1):506–529, Jan. 2019. doi: 10.1093/mnras/sty2666. 1.2.4, 1.3.4, 2.5, 5.3

D. A. Gadotti, A. Bittner, J. Falcón-Barroso, J. Méndez-Abreu, T. Kim, F. Fragkoudi, A. de Lorenzo-Cáceres, R. Leaman, J. Neumann, M. Querejeta, P. Sánchez-Blázquez, M. Martig, I. Martín-Navarro, I. Pérez, M. K. Seidel, and G. van de Ven. Kinematic signatures of nuclear discs and bar-driven secular evolution in nearby galaxies of the MUSE TIMER project. *A&A*, 643:A14, Nov. 2020. doi: 10.1051/0004-6361/202038448. 1.3.2, 1.3.4, 1.3.4, 5.4

I. L. Garland, M. J. Fahey, B. D. Simmons, R. J. Smethurst, C. J. Lintott, J. Shanahan, M. S. Silcock, J. Smith, W. C. Keel, A. Coil, T. Géron, S. Kruk, K. L. Masters, D. O'Ryan, M. R. Thorne, and K. Wiersema. The most luminous, merger-free AGNs show only marginal correlation with bar presence. *MNRAS*, 522(1):211–225, June 2023. doi: 10.1093/mnras/stad966. 1.3.5, 6.1.4

I. L. Garland, M. Walmsley, M. S. Silcock, L. M. Potts, J. Smith, B. D. Simmons, C. J. Lintott, R. J. Smethurst, J. M. Dawson, W. C. Keel, S. Kruk, K. B. Mantha, K. L. Masters, D. O'Ryan, J. J. Popp, and M. R. Thorne. Galaxy Zoo DESI: large-scale bars as a secular mechanism for triggering AGNs. *MNRAS*, 532(2): 2320–2330, Aug. 2024. doi: 10.1093/mnras/stae1620. 1.3.5, 6.1.4

G. Gavazzi, G. Consolandi, M. Dotti, R. Fanali, M. Fossati, M. Fumagalli, E. Viscardi, G. Savorgnan, A. Boselli, L. Gutiérrez, H. Hernández Toledo, R. Giovanelli, and M. P. Haynes. Hα3: an Hα imaging survey of HI selected galaxies from ALFALFA. VI. The role of bars in quenching star formation from z = 3 to the present epoch. *A&A*, 580:A116, Aug. 2015. doi: 10.1051/0004-6361/201425351. 1.2.4, 2.4

A. Gelman, J. Carlin, H. Stern, and D. Rubin. *Bayesian Data Analysis (2nd ed.)*. Chapman and Hall/CRC, 2003. 2.4, 3.4

K. George, S. Subramanian, and K. T. Paul. Significance of bar quenching in the global quenching of star formation. *A&A*, 628:A24, Aug. 2019. doi: 10.1051/0004-6361/201935207. 6.1.3

M. Gerin, F. Combes, and E. Athanassoula. The influence of galaxy interactions on stellar bars. *A&A*, 230:37–54, Apr. 1990. 1.2.1

T. Géron, R. J. Smethurst, C. Lintott, S. Kruk, K. L. Masters, B. Simmons, K. B. Mantha, M. Walmsley, L. Garma-Oehmichen, N. Drory, and R. R. Lane. Galaxy Zoo: kinematics of strongly and weakly barred galaxies. *MNRAS*, 521(2):1775–1793, May 2023. doi: 10.1093/mnras/stad501. 6.1.2

T. Géron, R. J. Smethurst, C. Lintott, K. L. Masters, I. L. Garland, P. Mengistu, D. O'Ryan, and B. D. Simmons. The Effects of Bar Strength and Kinematics on Galaxy Evolution: Slow Strong Bars Affect Their Hosts the Most. *ApJ*, 973(2):129, Oct. 2024. doi: 10.3847/1538-4357/ad66b7. 4.4.2

S. Ghosh and P. Di Matteo. Looking for a needle in a haystack: Measuring the length of a stellar bar. *A&A*, 683:A100, Mar. 2024. doi: 10.1051/0004-6361/202347763. 1.2.4, 4.5.2

S. Ghosh, F. Fragkoudi, P. Di Matteo, and K. Saha. Bars and boxy/peanut bulges in thin and thick discs. III. Boxy/peanut bulge formation and evolution in the presence of thick discs. *A&A*, 683:A196, Mar. 2024. doi: 10.1051/0004-6361/202347831. 4.4.2, 4.5.2

G. F. Gonçalves, R. E. G. Machado, K. Menéndez-Delmestre, and T. Bueno-Dalpiaz. Bar properties as a function of wavelength in TNG50: analysis of mock images. *MNRAS*, 542(4):3154–1380, Aug. 2025. doi: 10.1093/mnras/staf1384. 3.6.1, 4.5.3

A. D. Goulding, E. Matthaey, J. E. Greene, R. C. Hickox, D. M. Alexander, W. R. Forman, C. Jones, B. D. Lehmer, S. Griffis, S. Kanek, and M. Oulmakki. Galaxy-scale Bars in Late-type Sloan Digital Sky Survey Galaxies Do Not Influence the Average Accretion Rates of Supermassive Black Holes. *ApJ*, 843(2):135, July 2017. doi: 10.3847/1538-4357/aa755b. 1.3.5, 6.1.4

R. J. J. Grand, F. A. Gómez, F. Marinacci, R. Pakmor, V. Springel, D. J. R. Campbell, C. S. Frenk, A. Jenkins, and S. D. M. White. The Auriga Project: the properties and formation mechanisms of disc galaxies across cosmic time. *MNRAS*, 467(1):179–207, May 2017. doi: 10.1093/mnras/stx071. 3.6.4

N. A. Grogin, D. D. Kocevski, S. M. Faber, H. C. Ferguson, A. M. Koekemoer, A. G. Riess, V. Acquaviva, D. M. Alexander, O. Almaini, M. L. N. Ashby, M. Barden, E. F. Bell, F. Bournaud, T. M. Brown, K. I. Caputi, S. Casertano, P. Cassata, M. Castellano, P. Challis, R.-R. Chary, E. Cheung, M. Cirasuolo, C. J. Conselice, A. Roshan Cooray, D. J. Croton, E. Daddi, T. Dahlen, R. Davé, D. F. de Mello, A. Dekel, M. Dickinson, T. Dolch, J. L. Donley, J. S. Dunlop, A. A. Dutton, D. Elbaz, G. G. Fazio, A. V. Filippenko, S. L. Finkelstein, A. Fontana, J. P. Gardner, P. M. Garnavich, E. Gawiser, M. Giavalisco, A. Grazian, Y. Guo, N. P. Hathi, B. Häussler, P. F. Hopkins, J.-S. Huang, K.-H. Huang, S. W. Jha, J. S. Kartaltepe, R. P. Kirshner, D. C. Koo, K. Lai, K.-S. Lee, W. Li, J. M. Lotz, R. A. Lucas, P. Madau, P. J. McCarthy, E. J. McGrath, D. H. McIntosh, R. J. McLure, B. Mobasher, L. A. Moustakas, M. Mozena, K. Nandra, J. A. Newman, S.-M. Niemi, K. G. Noeske, C. J. Papovich, L. Pentericci, A. Pope, J. R. Primack, A. Rajan, S. Ravindranath, N. A. Reddy, A. Renzini, H.-W. Rix, A. R. Robaina, S. A.

Rodney, D. J. Rosario, P. Rosati, S. Salimbeni, C. Scarlata, B. Siana, L. Simard, J. Smidt, R. S. Somerville, H. Spinrad, A. N. Straughn, L.-G. Strolger, O. Telford, H. I. Teplitz, J. R. Trump, A. van der Wel, C. Villforth, R. H. Wechsler, B. J. Weiner, T. Wiklind, V. Wild, G. Wilson, S. Wuyts, H.-J. Yan, and M. S. Yun. CANDELS: The Cosmic Assembly Near-infrared Deep Extragalactic Legacy Survey. *ApJS*, 197(2):35, Dec. 2011. doi: 10.1088/0067-0049/197/2/35. 2.2

Y. Guo, S. Jogee, S. L. Finkelstein, Z. Chen, E. Wise, M. B. Bagley, G. Barro, S. Wuyts, D. D. Kocevski, J. S. Kartaltepe, E. J. McGrath, H. C. Ferguson, B. Mobasher, M. Giavalisco, R. A. Lucas, J. A. Zavala, J. M. Lotz, N. A. Grogin, M. Huertas-Company, J. Vega-Ferrero, N. P. Hathi, P. Arrabal Haro, M. Dickinson, A. M. Koekemoer, C. Papovich, N. Pirzkal, L. Y. A. Yung, B. E. Backhaus, E. F. Bell, A. Calabrò, N. J. Cleri, R. T. Coogan, M. C. Cooper, L. Costantin, D. Croton, K. Davis, A. Dekel, M. Franco, J. P. Gardner, B. W. Holwerda, T. A. Hutchison, V. Pandya, P. G. Pérez-González, S. Ravindranath, C. Rose, J. R. Trump, A. de la Vega, and W. Wang. First Look at z ¿ 1 Bars in the Rest-frame Near-infrared with JWST Early CEERS Imaging. *ApJ*, 945(1):L10, Mar. 2023. doi: 10.3847/2041-8213/acacfb. 1.2, 1.2.3, 1.2.3, 2.1, 2.3.3, 2.4, 2.5, 2.6

Y. Guo, S. Jogee, E. Wise, K. Pritchett, E. J. McGrath, S. L. Finkelstein, K. G. Iyer, P. Arrabal Haro, M. B. Bagley, M. Dickinson, J. S. Kartaltepe, A. M. Koekemoer, C. Papovich, N. Pirzkal, L. Y. A. Yung, B. E. Backhaus, E. F. Bell, R. Bhatawdekar, Y. Cheng, L. Costantin, A. de la Vega, M. Giavalisco, N. P. Hathi, B. W. Holwerda, P. Kurczynski, R. A. Lucas, B. Mobasher, P. G. Pérez-González, and F. Pacucci. The Abundance and Properties of Barred Galaxies out to z $\sim$ 4 Using JWST CEERS Data. *ApJ*, 985(2):181, June 2025. doi: 10.3847/1538-4357/adc8a7. 1.2, 1.2.3, 1.2.3, 3.1, 3.4, 3.4, 3.4, 3.6.1, 3.7

T. Géron, R. J. Smethurst, H. Dickinson, L. F. Fortson, I. L. Garland, S. Kruk, C. Lintott, J. S. Makechemu, K. B. Mantha, K. L. Masters, D. O'Ryan, H. Roberts, B. D. Simmons, M. Walmsley, A. Calabrò, R. Chiba, L. Costantin, M. R. Drout, F. Fragkoudi, Y. Guo, B. W. Holwerda, S. Jogee, A. M. Koekemoer, R. A. Lucas, and F. Pacucci. Galaxy zoo ceers: Bar fractions up to z 4.0, 2025. URL `https://arxiv.org/abs/2505.01421`. 1.2, 1.2.3, 3.1, 3.4, 3.4, 3.6.1, 3.7

S. Haan, E. Schinnerer, E. Emsellem, S. García-Burillo, F. Combes, C. G. Mundell, and H.-W. Rix. Dynamical Evolution of AGN Host Galaxies—Gas In/Out-Flow Rates in Seven NUGA Galaxies. *ApJ*, 692(2):1623–1661, Feb. 2009. doi: 10.1088/0004-637X/692/2/1623. 5.4

T. Harvey, C. J. Conselice, N. J. Adams, D. Austin, I. Juodžbalis, J. Trussler, Q. Li, K. Ormerod, L. Ferreira, C. C. Lovell, Q. Duan, L. Westcott, H. Harris, R. Bhatawdekar, D. Coe, S. H. Cohen, J. Caruana, C. Cheng, S. P. Driver, B. Frye, L. J. Furtak, N. A. Grogin, N. P. Hathi, B. W. Holwerda, R. A. Jansen, A. M. Koekemoer, M. A. Marshall, M. Nonino, A. P. Vijayan, S. M. Wilkins, R. Windhorst, C. N. A. Willmer, H. Yan, and A. Zitrin. EPOCHS. IV. SED Modeling Assumptions and Their Impact on the Stellar Mass Function at 6.5 $\leq$ z $\leq$ 13.5 Using PEARLS and Public JWST Observations. *ApJ*, 978(1):89, Jan. 2025. doi: 10.3847/1538-4357/ad8c29. 3.2.1, 4.2, 5.2.1

T. Harvey, C. J. Conselice, N. J. Adams, D. Austin, Q. Li, V. Rusakov, L. Westcott, C. M. Goolsby, C. C. Lovell, R. K. Cochrane, et al. Behind the spotlight: a systematic assessment of outshining using nircam medium bands in the jades origins field. *Monthly Notices of the Royal Astronomical Society*, 542(4):2998–3027, 2025. 5.2.5

J. D. Henshaw, A. T. Barnes, C. Battersby, A. Ginsburg, M. C. Sormani, and D. L. Walker. Star Formation in the Central Molecular Zone of the Milky Way. In S. Inutsuka, Y. Aikawa, T. Muto, K. Tomida, and M. Tamura, editors, *Protostars and Planets VII*, volume 534 of *Astronomical Society of the Pacific Conference Series*, page 83, July 2023. doi: 10.48550/arXiv.2203.11223. 1.3.4

M. Herrera-Endoqui, S. Díaz-García, E. Laurikainen, and H. Salo. Catalogue of the morphological features in the Spitzer Survey of Stellar Structure in Galaxies (S^4G). *A&A*, 582:A86, Oct. 2015. doi: 10.1051/0004-6361/201526047. 2.5

W. Herschel. Xviii. catalogue of 500 new neb nebulous stars, planetary nebula:, and clusters of stars; with remarks on the construction of the heavens. *Philosophical Transactions of the Royal Society of London*, 92:477–528, 12 1802. ISSN 0261-0523. doi: 10.1098/rstl.1802.0021. URL `https://doi.org/10.1098/rstl.1802.0021`. 1.1

F. Hohl. Numerical Experiments with a Disk of Stars. *ApJ*, 168:343, Sept. 1971. doi: 10.1086/151091. 1.2.1

S. Huang, R. Kawabe, K. Kohno, T. Saito, S. Mizukoshi, D. Iono, T. Michiyama, Y. Tamura, C. C. Hayward, and H. Umehata. J0107a: A Barred Spiral Dusty Star-forming Galaxy at z = 2.467. *ApJ*, 958(2):L26, Dec. 2023. doi: 10.3847/2041-8213/acff63. 3.1

S. Huang, R. Kawabe, H. Umehata, K. Kohno, Y. Tamura, and T. Saito. Large gas inflow driven by a matured galactic bar in the early Universe. *Nature*, 641(8064): 861–865, May 2025. doi: 10.1038/s41586-025-08914-2. 3.1, 5.3, 5.4

E. P. Hubble. *Realm of the Nebulae*. Yale University Press, 1936. 1.1, 1.1

M. Huertas-Company, K. G. Iyer, E. Angeloudi, M. B. Bagley, S. L. Finkelstein, J. Kartaltepe, R. Sarmiento, J. Vega-Ferrero, P. Arrabal Haro, P. Behroozi, F. Buitrago, Y. Cheng, L. Costantin, A. Dekel, M. Dickinson, D. Elbaz, N. A. Grogin, N. P. Hathi, B. W. Holwerda, A. M. Koekemoer, R. A. Lucas, C. Papovich, P. G. Pérez-González, N. Pirzkal, L.-M. Seillé, A. de la Vega, S. Wuyts, G. Yang, and L. Y. A. Yung. Galaxy Morphology from $z \sim 6$ through the eyes of JWST. *arXiv e-prints*, art. arXiv:2305.02478, May 2023. doi: 10.48550/arXiv.2305.02478. 2.1

S. Ishizuki, R. Kawabe, M. Ishiguro, S. K. Okumura, and K.-I. Morita. A molecular gas bar fuelling starburst activity in galaxy IC342. *Nature*, 344(6263):224–226, Mar. 1990. doi: 10.1038/344224a0. 1.3.3

R. I. Jedrzejewski. CCD surface photometry of elliptical galaxies - I. Observations, reduction and results. *MNRAS*, 226:747–768, June 1987. doi: 10.1093/mnras/226.4.747. 2.3.1

S. Jogee, F. D. Barazza, H.-W. Rix, I. Shlosman, M. Barden, C. Wolf, J. Davies, I. Heyer, S. V. W. Beckwith, E. F. Bell, A. Borch, J. A. R. Caldwell, C. J. Conselice, T. Dahlen, B. Häussler, C. Heymans, K. Jahnke, J. H. Knapen, S. Laine, G. M. Lubell, B. Mobasher, D. H. McIntosh, K. Meisenheimer, C. Y. Peng, S. Ravindranath, S. F. Sanchez, R. S. Somerville, and L. Wisotzki. Bar Evolution over the Last 8 Billion Years: A Constant Fraction of Strong Bars in the GEMS Survey. *ApJ*, 615(2):L105–L108, Nov. 2004. doi: 10.1086/426138. 1.2, 1.2.3, 1.2.3, 1.4, 2.10, 2.5, 3.4

H. M. Johnson. Is the Galaxy a barred spiral? *AJ*, 62:19, Feb. 1957. doi: 10.1086/107441. 1.1

J. S. Kartaltepe, M. Mozena, D. Kocevski, D. H. McIntosh, J. Lotz, E. F. Bell, S. Faber, H. Ferguson, D. Koo, R. Bassett, M. Bernyk, K. Blancato, F. Bournaud, P. Cassata, M. Castellano, E. Cheung, C. J. Conselice, D. Croton, T. Dahlen, D. F. de Mello, L. DeGroot, J. Donley, J. Guedes, N. Grogin, N. Hathi, M. Hilton, B. Hollon, A. Koekemoer, N. Liu, R. A. Lucas, M. Martig, E. McGrath, C. McPartland, B. Mobasher, A. Morlock, E. O'Leary, M. Peth, J. Pforr, A. Pillepich, D. Rosario, E. Soto, A. Straughn, O. Telford, B. Sunnquist, J. Trump, B. Weiner, S. Wuyts, H. Inami, S. Kassin, C. Lani, G. B. Poole, and Z. Rizer. CANDELS Visual Classifications: Scheme, Data Release, and First Results. *ApJS*, 221(1):11, Nov. 2015. doi: 10.1088/0067-0049/221/1/11. 1.4, 2.3.2, 2.4, 2.2, **??**, 2.4, 2.6

S. M. Kent, T. M. Dame, and G. Fazio. Galactic Structure from the Spacelab Infrared Telescope. II. Luminosity Models of the Milky Way. *ApJ*, 378:131, Sept. 1991. doi: 10.1086/170413. 1.3.3

S. S. Kim and A. Lee. Simulations of Nuclear Star-Forming Rings: A Case of the Milky Way. In *Journal of Physics Conference Series*, volume 372 of *Journal of Physics Conference Series*, page 012049. IOP, July 2012. doi: 10.1088/1742-6596/372/1/012049. 1.3.4, 5.4

T. Kim, D. A. Gadotti, K. Sheth, E. Athanassoula, A. Bosma, M. G. Lee, B. F. Madore, B. Elmegreen, J. H. Knapen, D. Zaritsky, L. C. Ho, S. Comerón, B. Holwerda, J. L. Hinz, J.-C. Muñoz-Mateos, M. Cisternas, S. Erroz-Ferrer, R. Buta, E. Laurikainen, H. Salo, J. Laine, K. Menéndez-Delmestre, M. W. Regan, B. de Swardt, A. Gil de Paz, M. Seibert, and T. Mizusawa. Unveiling the Structure of Barred Galaxies at 3.6 μm with the Spitzer Survey of Stellar Structure in Galaxies (S^4G). I. Disk Breaks. *ApJ*, 782(2):64, Feb. 2014. doi: 10.1088/0004-637X/782/2/64. 4.4.2, 4.8, 5.3, 3

T. Kim, D. A. Gadotti, E. Athanassoula, A. Bosma, K. Sheth, and M. G. Lee. Evidence of bar-induced secular evolution in the inner regions of stellar discs in galaxies: what shapes disc galaxies? *MNRAS*, 462(4):3430–3440, Nov. 2016. doi: 10.1093/mnras/stw1899. 1.2.4, 4.5.2

T. Kim, E. Athanassoula, K. Sheth, A. Bosma, M.-G. Park, Y. H. Lee, and H. B. Ann. Cosmic Evolution of Barred Galaxies up to z 0.84. *ApJ*, 922(2):196, Dec. 2021. doi: 10.3847/1538-4357/ac2300. 1.2.4, 2.5, 3.1, 3.7, 3.5.2, 3.5.2, 3.8, 3.6, 3.11, 3.6.2, 3.7, 4.4.2, 4.6, 4.4.2, 6

T. Kim, D. A. Gadotti, M. Querejeta, I. Pérez, A. Zurita, J. Neumann, G. van de Ven, J. Méndez-Abreu, A. de Lorenzo-Cáceres, P. Sánchez-Blázquez, F. Fragkoudi, L. P. Martins, L. A. Silva-Lima, W.-T. Kim, and M.-G. Park. Impacts of Bar-driven Shear and Shocks on Star Formation. *ApJ*, 968(2):87, June 2024. doi: 10.3847/1538-4357/ad410e. 1.3.2

T. Kim, D. A. Gadotti, M.-g. Park, Y. H. Lee, F. Fragkoudi, M. Kim, and W.-T. Kim. Dark Gaps and Resonances in Barred Galaxies. *ApJ*, 994(1):105, Nov. 2025. doi: 10.3847/1538-4357/ae113a. 4.5.2

J. H. Knapen, J. E. Beckman, C. H. Heller, I. Shlosman, and R. S. de Jong. The Central Region in M100: Observations and Modeling. *ApJ*, 454:623, Dec. 1995. doi: 10.1086/176516. 1.3.2, 1.3.5

J. H. Knapen, I. Shlosman, and R. F. Peletier. A Subarcsecond Resolution Near-Infrared Study of Seyfert and "Normal" Galaxies. II. Morphology. *ApJ*, 529(1): 93–100, Jan. 2000. doi: 10.1086/308266. 1.3.5, 6.1.4

A. M. Koekemoer, S. M. Faber, H. C. Ferguson, N. A. Grogin, D. D. Kocevski, D. C. Koo, K. Lai, J. M. Lotz, R. A. Lucas, E. J. McGrath, S. Ogaz, A. Rajan, A. G. Riess, S. A. Rodney, L. Strolger, S. Casertano, M. Castellano, T. Dahlen, M. Dickinson, T. Dolch, A. Fontana, M. Giavalisco, A. Grazian, Y. Guo, N. P. Hathi, K.-H. Huang, A. van der Wel, H.-J. Yan, V. Acquaviva, D. M. Alexander, O. Almaini, M. L. N. Ashby, M. Barden, E. F. Bell, F. Bournaud, T. M. Brown, K. I. Caputi, P. Cassata, P. J. Challis, R.-R. Chary, E. Cheung, M. Cirasuolo, C. J. Conselice, A. Roshan Cooray, D. J. Croton, E. Daddi, R. Davé, D. F. de Mello, L. de Ravel, A. Dekel, J. L. Donley, J. S. Dunlop, A. A. Dutton, D. Elbaz, G. G. Fazio, A. V. Filippenko, S. L. Finkelstein, C. Frazer, J. P. Gardner, P. M. Garnavich, E. Gawiser, R. Gruetzbauch, W. G. Hartley, B. Häussler, J. Herrington, P. F. Hopkins, J.-S. Huang, S. W. Jha, A. Johnson, J. S. Kartaltepe, A. A. Khostovan, R. P. Kirshner, C. Lani, K.-S. Lee, W. Li, P. Madau, P. J. McCarthy, D. H. McIntosh, R. J. McLure, C. McPartland, B. Mobasher, H. Moreira, A. Mortlock, L. A. Moustakas, M. Mozena, K. Nandra, J. A. Newman, J. L. Nielsen, S. Niemi, K. G. Noeske, C. J. Papovich, L. Pentericci, A. Pope, J. R. Primack, S. Ravindranath, N. A. Reddy, A. Renzini, H.-W. Rix, A. R. Robaina, D. J. Rosario, P. Rosati, S. Salimbeni, C. Scarlata, B. Siana, L. Simard, J. Smidt, D. Snyder, R. S. Somerville, H. Spinrad, A. N. Straughn, O. Telford, H. I. Teplitz, J. R. Trump, C. Vargas, C. Villforth, C. R. Wagner, P. Wandro, R. H. Wechsler, B. J. Weiner, T. Wiklind, V. Wild, G. Wilson, S. Wuyts, and M. S. Yun. CANDELS: The Cosmic Assembly Near-infrared Deep Extragalactic Legacy Survey—The Hubble Space Telescope Observations, Imaging Data Products, and Mosaics. *ApJS*, 197(2):36, Dec. 2011. doi: 10.1088/0067-0049/197/2/36. 2.2

J. Kormendy. Rotation of the bulge components of barred galaxies. *ApJ*, 257: 75–88, June 1982. doi: 10.1086/159964. 1.3.3

J. Kormendy. Elliptical Galaxies and Bulges of Disc Galaxies: Summary of Progress and Outstanding Issues. In E. Laurikainen, R. Peletier, and D. Gadotti, editors, *Galactic Bulges*, volume 418 of *Astrophysics and Space Science Library*, page 431, Jan. 2016. doi: 10.1007/978-3-319-19378-6_16. 4.5.1

J. Kormendy and J. Kennicutt, Robert C. Secular Evolution and the Formation of Pseudobulges in Disk Galaxies. *ARA&A*, 42(1):603–683, Sept. 2004. doi: 10.1146/annurev.astro.42.053102.134024. 1.3.3, 4.5.4

K. Kraljic, F. Bournaud, and M. Martig. The Two-phase Formation History of Spiral Galaxies Traced by the Cosmic Evolution of the Bar Fraction. *ApJ*, 757(1): 60, Sept. 2012. doi: 10.1088/0004-637X/757/1/60. 1.2.3

D. Krishnarao, Z. J. Pace, E. D'Onghia, J. A. L. Aguerri, R. L. McClure, T. Peterken, J. G. Fernández-Trincado, M. Merrifield, K. L. Masters, L. Garma-Oehmichen, N. F. Boardman, M. Bershady, N. Drory, and R. R. Lane. Photometric Signature of Ultraharmonic Resonances in Barred Galaxies. *ApJ*, 929(2):112, Apr. 2022. doi: 10.3847/1538-4357/ac5d55. 4.5.2

P. Kroupa. On the variation of the initial mass function. *Monthly Notices of the Royal Astronomical Society*, 322(2):231–246, 2001. 5.2.5

A. La Marca, M. T. Nardone, L. Wang, B. Margalef-Bentabol, S. Kruk, and S. C. Trager. Galactic bars and active galactic nucleus fuelling in the second half of cosmic history. *A&A*, 707:A152, Mar. 2026. doi: 10.1051/0004-6361/202556236. 6.1.4

G. Lamé. *Examen des différentes méthodes employées pour résoudre les problèmes de géométrie*. Vve Courcier, 1818. 4.3

Z. A. Le Conte, D. A. Gadotti, L. Ferreira, C. J. Conselice, C. de Sá-Freitas, T. Kim, J. Neumann, F. Fragkoudi, E. Athanassoula, and N. J. Adams. A JWST investigation into the bar fraction at redshifts $1 \leq z \leq 3$. *MNRAS*, 530(2):1984–2000, May 2024. doi: 10.1093/mnras/stae921. 1.2.3, 2

Z. A. Le Conte, D. A. Gadotti, L. Ferreira, C. J. Conselice, C. de Sá-Freitas, T. Kim, J. Neumann, F. Fragkoudi, E. Athanassoula, and N. J. Adams. The evolution of the bar fraction and bar lengths in the last 12 billion years. *MNRAS*, 545(1):staf2010, Jan. 2026. doi: 10.1093/mnras/staf2010. 1.2.3, 3, 4.6, 5

Y. H. Lee, H. B. Ann, and M.-G. Park. Bar Fraction in Early- and Late-type Spirals. *ApJ*, 872(1):97, Feb. 2019. doi: 10.3847/1538-4357/ab0024. 1.2.3, 2.5

J. Leja, A. C. Carnall, B. D. Johnson, C. Conroy, and J. S. Speagle. How to measure galaxy star formation histories. ii. nonparametric models. *The Astrophysical Journal*, 876(1):3, 2019. 5.2.5

X. Liang, S.-Y. Yu, T. Fang, and L. C. Ho. The robustness in identifying and quantifying high-redshift bars using JWST observations. *arXiv e-prints*, art. arXiv:2311.04019, Nov. 2023. doi: 10.48550/arXiv.2311.04019. 2.5

X. Liang, S.-Y. Yu, T. Fang, and L. C. Ho. The robustness in identifying and quantifying high-redshift bars using JWST observations. *A&A*, 688:A158, Aug. 2024. doi: 10.1051/0004-6361/202348539. 3.6.1, 3.6.1, 3.6.5, 3.12

L. Lin, C. Li, Y. He, T. Xiao, and E. Wang. Bar-induced Central Star Formation as Revealed by Integral Field Spectroscopy from CALIFA. *ApJ*, 838(2):105, Apr. 2017. doi: 10.3847/1538-4357/aa657a. 1.3.2

E. L. Łokas. Formation of Tidally Induced Bars in Galactic Flybys: Prograde versus Retrograde Encounters. *ApJ*, 857(1):6, Apr. 2018. doi: 10.3847/1538-4357/aab4ff. 1.2.1

E. L. Łokas. High-redshift Merger-induced Bar-like Galaxies in IllustrisTNG. *ApJ*, 991(2):L52, Oct. 2025. doi: 10.3847/2041-8213/ae07c2. 1.2.1, 4.5.3

E. L. Łokas, E. Athanassoula, V. P. Debattista, M. Valluri, A. d. Pino, M. Semczuk, G. Gajda, and K. Kowalczyk. Adventures of a tidally induced bar. *MNRAS*, 445 (2):1339–1350, Dec. 2014. doi: 10.1093/mnras/stu1846. 1.2.1

E. L. Łokas, I. Ebrová, A. del Pino, A. Sybilska, E. Athanassoula, M. Semczuk, G. Gajda, and S. Fouquet. Tidally Induced Bars of Galaxies in Clusters. *ApJ*, 826 (2):227, Aug. 2016. doi: 10.3847/0004-637X/826/2/227. 1.2.1, 3.6.3, 3.6.4

P. D. López, F. Fragkoudi, S. A. Cora, C. Scannapieco, R. Pakmor, R. J. J. Grand, F. Gómez, and F. Marinacci. Formation and evolution of boxy/peanut bulges in the Auriga cosmological simulations. *MNRAS*, 540(3):2031–2048, July 2025. doi: 10.1093/mnras/staf818. 4.5.3

D. Lynden-Bell and A. J. Kalnajs. On the generating mechanism of spiral structure. *MNRAS*, 157:1, Jan. 1972. doi: 10.1093/mnras/157.1.1. 1.3, 1.3.1

F. Maeda, F. Egusa, K. Ohta, Y. Fujimoto, and A. Habe. Statistical Study of the Star Formation Efficiency in Bars: Is Star Formation Suppressed in Gas-rich Bars? *ApJ*, 943(1):7, Jan. 2023. doi: 10.3847/1538-4357/aca664. 6.1.3

D. F. Malin. Unsharp masking. *AAS Photo Bulletin*, 16:10–13, Jan. 1977. 5.2.2

I. Marinova and S. Jogee. Characterizing Bars at z ~0 in the Optical and NIR: Implications for the Evolution of Barred Disks with Redshift. *ApJ*, 659(2):1176–1197, Apr. 2007. doi: 10.1086/512355. 1.2, 1.2.3, 1.2.3, 3.1, 3.6.1

I. Marinova, S. Jogee, A. Heiderman, F. D. Barazza, M. E. Gray, M. Barden, C. Wolf, C. Y. Peng, D. Bacon, M. Balogh, E. F. Bell, A. Böhm, J. A. R. Caldwell, B. Häußler, C. Heymans, K. Jahnke, E. van Kampen, K. Lane, D. H. McIntosh, K. Meisenheimer, S. F. Sánchez, R. Somerville, A. Taylor, L. Wisotzki, and X. Zheng. Barred Galaxies in the Abell 901/2 Supercluster with Stages. *ApJ*, 698 (2):1639–1658, June 2009. doi: 10.1088/0004-637X/698/2/1639. 4.4.2

G. Martin, S. Kaviraj, J. E. G. Devriendt, Y. Dubois, and C. Pichon. The role of mergers in driving morphological transformation over cosmic time. *MNRAS*, 480 (2):2266–2283, Oct. 2018. doi: 10.1093/mnras/sty1936. 1.3.5

K. L. Masters, R. C. Nichol, B. Hoyle, C. Lintott, S. P. Bamford, E. M. Edmondson, L. Fortson, W. C. Keel, K. Schawinski, A. M. Smith, and D. Thomas. Galaxy Zoo: bars in disc galaxies. *MNRAS*, 411(3):2026–2034, Mar. 2011. doi: 10.1111/j.1365-2966.2010.17834.x. 1.2.4, 1.3.2, 1.4, 2.4, 2.10, 2.5, 3.4

S. McAlpine, C. M. Harrison, D. J. Rosario, D. M. Alexander, S. L. Ellison, P. H. Johansson, and D. R. Patton. Galaxy mergers in EAGLE do not induce a significant amount of black hole growth yet do increase the rate of luminous AGN. *MNRAS*, 494(4):5713–5733, June 2020. doi: 10.1093/mnras/staa1123. 1.3.5

T. Melvin, K. Masters, C. Lintott, R. C. Nichol, B. Simmons, S. P. Bamford, K. R. V. Casteels, E. Cheung, E. M. Edmondson, L. Fortson, K. Schawinski, R. A. Skibba, A. M. Smith, and K. W. Willett. Galaxy Zoo: an independent look at the evolution of the bar fraction over the last eight billion years from HST-COSMOS. *MNRAS*, 438(4):2882–2897, Mar. 2014. doi: 10.1093/mnras/stt2397. 1.2.3, 2.4, 2.10, 2.5, 3.4, 3.5.1

K. Menéndez-Delmestre, K. Sheth, E. Schinnerer, T. H. Jarrett, and N. Z. Scoville. A Near-Infrared Study of 2MASS Bars in Local Galaxies: An Anchor for High-Redshift Studies. *ApJ*, 657(2):790–804, Mar. 2007. doi: 10.1086/511025. 1.2.3, 1.3

K. Menéndez-Delmestre, T. S. Gonçalves, K. Sheth, T. Düringer Jacques de Lima, T. Kim, D. A. Gadotti, E. Schinnerer, E. Athanassoula, A. Bosma, D. M. Elmegreen, J. H. Knapen, R. E. G. Machado, and H. Salo. Bar properties as a function of wavelength: a local baseline with S^4G for high-redshift studies. *MNRAS*, 527(4):11777–11800, Feb. 2024. doi: 10.1093/mnras/stad3662. 1.2.3, 1.5, 3.6.1, 5.3

D. Merritt and J. A. Sellwood. Bending Instabilities in Stellar Systems. *ApJ*, 425: 551, Apr. 1994. doi: 10.1086/174005. 4.4.2

A. Merrow, F. Fragkoudi, R. J. J. Grand, and M. Martig. What drives bar rotation? The effect of internal properties and galaxy interactions on bar pattern speeds. *MNRAS*, Feb. 2026. doi: 10.1093/mnras/stag371. 4.5.2

M. Morris and E. Serabyn. The Galactic Center Environment. *ARA&A*, 34:645–702, Jan. 1996. doi: 10.1146/annurev.astro.34.1.645. 1.3.4

P. B. Nair and R. G. Abraham. On the Fraction of Barred Spiral Galaxies. *ApJ*, 714(2):L260–L264, May 2010. doi: 10.1088/2041-8205/714/2/L260. 1.2.3, 2.4

D. Nelson, V. Springel, A. Pillepich, V. Rodriguez-Gomez, P. Torrey, S. Genel, M. Vogelsberger, R. Pakmor, F. Marinacci, R. Weinberger, L. Kelley, M. Lovell, B. Diemer, and L. Hernquist. The IllustrisTNG simulations: public data release. *Computational Astrophysics and Cosmology*, 6(1):2, May 2019. doi: 10.1186/s40668-019-0028-x. 1.2.3, 2.5

E. J. Nelson, K. A. Suess, R. Bezanson, S. H. Price, P. van Dokkum, J. Leja, B. Wang, K. E. Whitaker, I. Labbé, L. Barrufet, G. Brammer, D. J. Eisenstein, J. Gibson, A. I. Hartley, B. D. Johnson, K. E. Heintz, E. Mathews, T. B. Miller, P. A. Oesch, L. Sandles, D. J. Setton, J. S. Speagle, S. Tacchella, K.-i. Tadaki, H. Übler, and J. R. Weaver. JWST Reveals a Population of Ultrared, Flattened Galaxies at $2 \lesssim z \lesssim 6$ Previously Missed by HST. *ApJ*, 948(2):L18, May 2023. doi: 10.3847/2041-8213/acc1e1. 2.3.2

M. Ness and D. Lang. The X-shaped Bulge of the Milky Way Revealed by WISE. *AJ*, 152(1):14, July 2016. doi: 10.3847/0004-6256/152/1/14. 1.3.3

J. Neumann, D. A. Gadotti, L. Wisotzki, B. Husemann, G. Busch, F. Combes, S. M. Croom, T. A. Davis, M. Gaspari, M. Krumpe, M. A. Pérez-Torres, J. Scharwächter, I. Smirnova-Pinchukova, G. R. Tremblay, and T. Urrutia. The Close AGN Reference Survey (CARS). Comparative analysis of the structural properties of star-forming and non-star-forming galaxy bars. *A&A*, 627:A26, July 2019. doi: 10.1051/0004-6361/201834441. 1.3.2, 6.1.3

J. Neumann, F. Fragkoudi, I. Pérez, D. A. Gadotti, J. Falcón-Barroso, P. Sánchez-Blázquez, A. Bittner, B. Husemann, F. A. Gómez, R. J. J. Grand, C. E. Donohoe-Keyes, T. Kim, A. de Lorenzo-Cáceres, M. Martig, J. Méndez-Abreu, R. Pakmor, M. K. Seidel, and G. van de Ven. Stellar populations across galaxy bars in the MUSE TIMER project. *A&A*, 637:A56, May 2020. doi: 10.1051/0004-6361/202037604. 1.3.2

J. Neumann, D. Thomas, C. Maraston, D. R. Gleis, C. Mao, E. Schinnerer, and S. K. Stuber. Azimuthal variations of stellar populations in barred galaxies. *MNRAS*, 534(3):2438–2457, Nov. 2024. doi: 10.1093/mnras/stae2252. 3.5.2

M. Noguchi. Close encounter between galaxies - II. Tidal deformation of a disc galaxy stabilized by massive halo. *MNRAS*, 228:635–651, Oct. 1987. doi: 10.1093/mnras/228.3.635. 1.2.1

K. Ormerod, C. J. Conselice, N. J. Adams, T. Harvey, D. Austin, J. Trussler, L. Ferreira, J. Caruana, G. Lucatelli, Q. Li, and W. J. Roper. EPOCHS VI: the size and shape evolution of galaxies since z 8 with JWST Observations. *MNRAS*, 527(3):6110–6125, Jan. 2024. doi: 10.1093/mnras/stad3597. 3.3.3, 3.3.3, 4.4.1

J. P. Ostriker and P. J. E. Peebles. A Numerical Study of the Stability of Flattened Galaxies: or, can Cold Galaxies Survive? *ApJ*, 186:467–480, Dec. 1973. doi: 10.1086/152513. 1.2.1

S. Pastras, R. Genzel, L. J. Tacconi, K. Schuster, R. Neri, N. M. Förster Schreiber, T. Naab, C. Barfety, A. Burkert, Y. Cao, J. Chen, F. Combes, R. Davies, F. Eisenhauer, J. M. Espejo Salcedo, S. García-Burillo, R. Herrera-Camus, J.-B. Jolly, L. L. Lee, M. M. Lee, D. Liu, D. Lutz, A. Nestor Shachar, E. Parlanti, S. H. Price, C. Pulsoni, A. Renzini, L. Scaloni, T. T. Shimizu, V. Springel, A. Sternberg, E. Sturm, G. Tozzi, S. Wuyts, and H. Übler. NOEMA^{3D}: A first kpc resolution study of a $z \sim 1.5$ main sequence barred galaxy channeling gas into a growing bulge. *arXiv e-prints*, art. arXiv:2505.07925, May 2025. doi: 10.48550/arXiv.2505.07925. 3.1

P. A. Patsis, C. Skokos, and E. Athanassoula. Orbital dynamics of three-dimensional bars - III. Boxy/peanut edge-on profiles. *MNRAS*, 337(2):578–596, Dec. 2002. doi: 10.1046/j.1365-8711.2002.05943.x. 1.2.2

C. Y. Peng, L. C. Ho, C. D. Impey, and H.-W. Rix. Detailed Structural Decomposition of Galaxy Images. *AJ*, 124(1):266–293, July 2002. doi: 10.1086/340952. 1.2.4

M. D. Perrin, A. Sivaramakrishnan, C.-P. Lajoie, E. Elliott, L. Pueyo, S. Ravindranath, and L. Albert. Updated point spread function simulations for JWST with WebbPSF. In J. M. Oschmann, Jr., M. Clampin, G. G. Fazio, and H. A. MacEwen, editors, *Space Telescopes and Instrumentation 2014: Optical, Infrared, and Millimeter Wave*, volume 9143 of *Society of Photo-Optical Instrumentation Engineers (SPIE) Conference Series*, page 91433X, Aug. 2014. doi: 10.1117/12.2056689. 4.3.1

N. Peschken and E. L. Łokas. Tidally induced bars in Illustris galaxies. *MNRAS*, 483(2):2721–2735, Feb. 2019. doi: 10.1093/mnras/sty3277. 2.5

Planck Collaboration, N. Aghanim, Y. Akrami, M. Ashdown, J. Aumont, C. Baccigalupi, M. Ballardini, A. J. Banday, R. B. Barreiro, N. Bartolo, S. Basak, R. Battye, K. Benabed, J. P. Bernard, M. Bersanelli, P. Bielewicz, J. J. Bock, J. R. Bond, J. Borrill, F. R. Bouchet, F. Boulanger, M. Bucher, C. Burigana, R. C. Butler, E. Calabrese, J. F. Cardoso, J. Carron, A. Challinor, H. C. Chiang, J. Chluba, L. P. L. Colombo, C. Combet, D. Contreras, B. P. Crill, F. Cuttaia, P. de Bernardis, G. de Zotti, J. Delabrouille, J. M. Delouis, E. Di Valentino, J. M. Diego, O. Doré, M. Douspis, A. Ducout, X. Dupac, S. Dusini, G. Efstathiou, F. Elsner, T. A. Enßlin, H. K. Eriksen, Y. Fantaye, M. Farhang, J. Fergusson, R. Fernandez-Cobos, F. Finelli, F. Forastieri, M. Frailis, A. A. Fraisse, E. Franceschi, A. Frolov, S. Galeotta, S. Galli, K. Ganga, R. T. Génova-Santos, M. Gerbino, T. Ghosh, J. González-Nuevo, K. M. Górski, S. Gratton, A. Gruppuso, J. E. Gudmundsson, J. Hamann, W. Handley, F. K. Hansen, D. Herranz, S. R. Hildebrandt, E. Hivon, Z. Huang, A. H. Jaffe, W. C. Jones, A. Karakci, E. Keihänen, R. Keskitalo, K. Kiiveri, J. Kim, T. S. Kisner, L. Knox, N. Krachmalnicoff, M. Kunz, H. Kurki-Suonio, G. Lagache, J. M. Lamarre, A. Lasenby, M. Lattanzi, C. R. Lawrence, M. Le Jeune, P. Lemos, J. Lesgourgues, F. Levrier, A. Lewis, M. Liguori, P. B. Lilje, M. Lilley, V. Lindholm, M. López-Caniego, P. M. Lubin, Y. Z. Ma, J. F. Macías-Pérez, G. Maggio, D. Maino, N. Mandolesi, A. Mangilli, A. Marcos-Caballero, M. Maris, P. G. Martin, M. Martinelli, E. Martínez-González, S. Matarrese, N. Mauri, J. D. McEwen, P. R. Meinhold, A. Melchiorri, A. Mennella, M. Migliaccio, M. Millea, S. Mitra, M. A. Miville-Deschênes, D. Molinari, L. Montier, G. Morgante, A. Moss, P. Natoli, H. U. Nørgaard-Nielsen, L. Pagano, D. Paoletti, B. Partridge, G. Patanchon, H. V. Peiris, F. Perrotta, V. Pettorino, F. Piacentini, L. Polastri, G. Polenta, J. L. Puget, J. P. Rachen, M. Reinecke, M. Remazeilles, A. Renzi, G. Rocha, C. Rosset, G. Roudier, J. A. Rubiño-Martín, B. Ruiz-Granados, L. Salvati, M. Sandri, M. Savelainen, D. Scott, E. P. S. Shellard, C. Sirignano, G. Sirri, L. D. Spencer, R. Sunyaev, A. S. Suur-Uski, J. A. Tauber, D. Tavagnacco, M. Tenti, L. Toffolatti, M. Tomasi, T. Trombetti, L. Valenziano, J. Valiviita, B. Van Tent, L. Vibert,

P. Vielva, F. Villa, N. Vittorio, B. D. Wandelt, I. K. Wehus, M. White, S. D. M. White, A. Zacchei, and A. Zonca. Planck 2018 results. VI. Cosmological parameters. *A&A*, 641:A6, Sept. 2020. doi: 10.1051/0004-6361/201833910. 2.1

M. Querejeta, E. Schinnerer, S. Meidt, J. Sun, A. K. Leroy, E. Emsellem, R. S. Klessen, J. C. Muñoz-Mateos, H. Salo, E. Laurikainen, I. Bešlić, G. A. Blanc, M. Chevance, D. A. Dale, C. Eibensteiner, C. Faesi, A. García-Rodríguez, S. C. O. Glover, K. Grasha, J. Henshaw, C. Herrera, A. Hughes, K. Kreckel, J. M. D. Kruijssen, D. Liu, E. J. Murphy, H.-A. Pan, J. Pety, A. Razza, E. Rosolowsky, T. Saito, A. Schruba, A. Usero, E. J. Watkins, and T. G. Williams. Stellar structures, molecular gas, and star formation across the PHANGS sample of nearby galaxies. *A&A*, 656:A133, Dec. 2021. doi: 10.1051/0004-6361/202140695. 6.1.3

J. Randolph. Free-marginal multirater kappa (multirater κfree): An alternative to fleiss fixed-marginal multirater kappa. In *Joensuu University Learning and Instruction Symposium 2005*, volume 4, 01 2010. 3.3.3

M. W. Regan, M. D. Thornley, S. N. Vogel, K. Sheth, B. T. Draine, D. J. Hollenbach, M. Meyer, D. A. Dale, C. W. Engelbracht, R. C. Kennicutt, L. Armus, B. Buckalew, D. Calzetti, K. D. Gordon, G. Helou, C. Leitherer, S. Malhotra, E. Murphy, G. H. Rieke, M. J. Rieke, and J. D. Smith. The Radial Distribution of the Interstellar Medium in Disk Galaxies: Evidence for Secular Evolution. *ApJ*, 652(2):1112–1121, Dec. 2006. doi: 10.1086/505382. 1.3

D. Reynaud and D. Downes. Kinematics of the gas in a barred galaxy: do strong shocks inhibit star formation? *A&A*, 337:671–680, Sept. 1998. 4.4.2

F. E. Rosas, P. A. M. Mediano, A. I. Luppi, T. F. Varley, J. T. Lizier, S. Stramaglia, H. J. Jensen, and D. Marinazzo. Disentangling high-order mechanisms and high-order behaviours in complex systems. *Nature Physics*, 18(5):476–477, May 2022. doi: 10.1038/s41567-022-01548-5. 1.2

Y. Rosas-Guevara, S. Bonoli, M. Dotti, D. Izquierdo-Villalba, A. Lupi, T. Zana, M. Bonetti, D. Nelson, V. Springel, L. Hernquist, and M. Vogelsberger. The evolution of the barred galaxy population in the TNG50 simulation. *MNRAS*, 512(4): 5339–5357, June 2022. doi: 10.1093/mnras/stac816. 1.2.1, 1.2.3, 1.4, 2.5

M. Roshan, A. Habibi, J. A. L. Aguerri, V. Cuomo, C. Bottrell, L. Costantin, E. M. Corsini, T. Kim, Y. H. Lee, J. Mendez-Abreu, M. Frosst, A. de Lorenzo-Cáceres, L. Morelli, and A. Pizzella. The Tremaine-Weinberg method at high redshifts. *A&A*, 701:A160, Sept. 2025. doi: 10.1051/0004-6361/202555547. 6.1.2

K. Saha and B. Elmegreen. Why Are Some Galaxies Not Barred? *ApJ*, 858(1):24, May 2018. doi: 10.3847/1538-4357/aabacd. 1.2.1

K. Sakamoto, S. K. Okumura, S. Ishizuki, and N. Z. Scoville. Bar-driven Transport of Molecular Gas to Galactic Centers and Its Consequences. *ApJ*, 525(2):691–701, Nov. 1999. doi: 10.1086/307910. 1.3.2

H. Salo, P. Rautiainen, R. Buta, G. B. Purcell, M. L. Cobb, D. A. Crocker, and E. Laurikainen. The Structure and Dynamics of the Early-Type Resonance Ring Galaxy IC 4214. II. Models. *AJ*, 117(2):792–810, Feb. 1999. doi: 10.1086/300726. 4.5.2

H. Salo, E. Laurikainen, J. Laine, S. Comerón, D. A. Gadotti, R. Buta, K. Sheth, D. Zaritsky, L. Ho, J. Knapen, E. Athanassoula, A. Bosma, S. Laine, M. Cisternas, T. Kim, J. C. Muñoz-Mateos, M. Regan, J. L. Hinz, A. Gil de Paz, K. Menendez-Delmestre, T. Mizusawa, S. Erroz-Ferrer, S. E. Meidt, and M. Querejeta. The Spitzer Survey of Stellar Structure in Galaxies (S^4G): Multi-component Decomposition Strategies and Data Release. *ApJS*, 219(1):4, July 2015. doi: 10.1088/0067-0049/219/1/4. 1.8

P. Sánchez-Blázquez, P. Ocvirk, B. K. Gibson, I. Pérez, and R. F. Peletier. Star formation history of barred disc galaxies. *MNRAS*, 415(1):709–731, July 2011. doi: 10.1111/j.1365-2966.2011.18749.x. 3.1

R. H. Sanders and A. D. Tubbs. Gas as a tracer of barred spiral dynamics. *ApJ*, 235:803–820, Feb. 1980. doi: 10.1086/157683. 1.3.2

L. Scaloni, G. Rodighiero, A. Enia, C. Gruppioni, F. Annibali, L. Bisigello, P. Cassata, E. M. Corsini, V. Casasola, C. M. Lofaro, and A. Bianchetti. The impact of stellar bars on star-formation quenching: Insights from a spatially resolved analysis in the local Universe. *A&A*, 687:A255, July 2024. doi: 10.1051/0004-6361/202449894. 6.1.3

M. Schultheis, M. C. Sormani, and D. A. Gadotti. Nuclear stellar discs. *A&ARv*, 33(1):7, Nov. 2025. doi: 10.1007/s00159-025-00163-6. 1.3.4

M. P. Schwarz. The response of gas in a galactic disk to bar forcing. *ApJ*, 247: 77–88, July 1981. doi: 10.1086/159011. 4.5.2

J. A. Sellwood and A. Wilkinson. Dynamics of barred galaxies. *Reports on Progress in Physics*, 56(2):173–256, Feb. 1993. doi: 10.1088/0034-4885/56/2/001. 1.2, 1.2.4

W.-Y. Seo, W.-T. Kim, S. Kwak, P.-Y. Hsieh, C. Han, and P. F. Hopkins. Effects of Gas on Formation and Evolution of Stellar Bars and Nuclear Rings in Disk Galaxies. *ApJ*, 872(1):5, Feb. 2019. doi: 10.3847/1538-4357/aafc5f. 1.3.4, 2.6, 5.4

K. Sheth, M. W. Regan, N. Z. Scoville, and L. E. Strubbe. Barred Galaxies at z ¿ 0.7: NICMOS Hubble Deep Field-North Observations. *ApJ*, 592(1):L13–L16, July 2003. doi: 10.1086/377329. 1.2.3

K. Sheth, S. N. Vogel, M. W. Regan, M. D. Thornley, and P. J. Teuben. Secular Evolution via Bar-driven Gas Inflow: Results from BIMA SONG. *ApJ*, 632(1): 217–226, Oct. 2005. doi: 10.1086/432409. 1.3.2

K. Sheth, D. M. Elmegreen, B. G. Elmegreen, P. Capak, R. G. Abraham, E. Athanassoula, R. S. Ellis, B. Mobasher, M. Salvato, E. Schinnerer, N. Z. Scoville, L. Spalsbury, L. Strubbe, M. Carollo, M. Rich, and A. A. West. Evolution of

the Bar Fraction in COSMOS: Quantifying the Assembly of the Hubble Sequence. *ApJ*, 675(2):1141–1155, Mar. 2008. doi: 10.1086/524980. 1.2.3, 1.4, 2.4, 2.10, 2.5, 3.4, 3.5.1

K. Sheth, M. Regan, J. L. Hinz, A. Gil de Paz, K. Menéndez-Delmestre, J.-C. Muñoz-Mateos, M. Seibert, T. Kim, E. Laurikainen, H. Salo, D. A. Gadotti, J. Laine, T. Mizusawa, L. Armus, E. Athanassoula, A. Bosma, R. J. Buta, P. Capak, T. H. Jarrett, D. M. Elmegreen, B. G. Elmegreen, J. H. Knapen, J. Koda, G. Helou, L. C. Ho, B. F. Madore, K. L. Masters, B. Mobasher, P. Ogle, C. Y. Peng, E. Schinnerer, J. A. Surace, D. Zaritsky, S. Comerón, B. de Swardt, S. E. Meidt, M. Kasliwal, and M. Aravena. The Spitzer Survey of Stellar Structure in Galaxies (S4G). *PASP*, 122(898):1397, Dec. 2010. doi: 10.1086/657638. 1.2.4

K. Sheth, J. Melbourne, D. M. Elmegreen, B. G. Elmegreen, E. Athanassoula, R. G. Abraham, and B. J. Weiner. Hot Disks and Delayed Bar Formation. *ApJ*, 758(2):136, Oct. 2012. doi: 10.1088/0004-637X/758/2/136. 3.6.3

T. W. Shimwell, H. J. A. Röttgering, P. N. Best, W. L. Williams, T. J. Dijkema, F. de Gasperin, M. J. Hardcastle, G. H. Heald, D. N. Hoang, A. Horneffer, H. Intema, E. K. Mahony, S. Mandal, A. P. Mechev, L. Morabito, J. B. R. Oonk, D. Rafferty, E. Retana-Montenegro, J. Sabater, C. Tasse, R. J. van Weeren, M. Brüggen, G. Brunetti, K. T. Chyży, J. E. Conway, M. Haverkorn, N. Jackson, M. J. Jarvis, J. P. McKean, G. K. Miley, R. Morganti, G. J. White, M. W. Wise, I. M. van Bemmel, R. Beck, M. Brienza, A. Bonafede, G. Calistro Rivera, R. Cassano, A. O. Clarke, D. Cseh, A. Deller, A. Drabent, W. van Driel, D. Engels, H. Falcke, C. Ferrari, S. Fröhlich, M. A. Garrett, J. J. Harwood, V. Heesen, M. Hoeft, C. Horellou, F. P. Israel, A. D. Kapińska, M. Kunert-Bajraszewska, D. J. McKay, N. R. Mohan, E. Orrú, R. F. Pizzo, I. Prandoni, D. J. Schwarz, A. Shulevski, M. Sipior, D. J. B. Smith, S. S. Sridhar, M. Steinmetz, A. Stroe, E. Varenius, P. P. van der Werf, J. A. Zensus, and J. T. L. Zwart. The LOFAR Two-metre Sky Survey. I. Survey description and preliminary data release. *A&A*, 598:A104, Feb. 2017. doi: 10.1051/0004-6361/201629313. 6.1.1

I. Shlosman, J. Frank, and M. Begelman. Bars within bars: a mechanism for fuelling active galactic nuclei. *Nature*, 338, 1989. doi: 10.1038/338045a0. 1.3.4, 5.4

L. A. Silva-Lima, L. P. Martins, P. R. T. Coelho, and D. A. Gadotti. Revisiting the role of bars in AGN fuelling with propensity score sample matching. *A&A*, 661:A105, May 2022. doi: 10.1051/0004-6361/202142432. 1.3.5, 6.1.4

B. Silverman. *Density Estimation for Statistics and Data Analysis*. Chapman & Hall/CRC Monographs on Statistics and Applied Probability, 1986. 4.6, 4.4.2

B. D. Simmons, T. Melvin, C. Lintott, K. L. Masters, K. W. Willett, W. C. Keel, R. J. Smethurst, E. Cheung, R. C. Nichol, K. Schawinski, M. Rutkowski, J. S. Kartaltepe, E. F. Bell, K. R. V. Casteels, C. J. Conselice, O. Almaini, H. C. Ferguson, L. Fortson, W. Hartley, D. Kocevski, A. M. Koekemoer, D. H. McIntosh, A. Mortlock, J. A. Newman, J. Ownsworth, S. Bamford, T. Dahlen, S. M. Faber, S. L. Finkelstein, A. Fontana, A. Galametz, N. A. Grogin, R. Grützbauch, Y. Guo,

B. Häußler, K. J. Jek, S. Kaviraj, R. A. Lucas, M. Peth, M. Salvato, T. Wiklind, and S. Wuyts. Galaxy Zoo: CANDELS barred discs and bar fractions. *MNRAS*, 445(4):3466–3474, Dec. 2014. doi: 10.1093/mnras/stu1817. 1.2.3, 1.2.3, 1.4, 2.10, 2.5, 3.4, 4.5.4

I. Smail, U. Dudzeviciute, M. Gurwell, G. G. Fazio, S. P. Willner, A. M. Swinbank, V. Arumugam, J. Summers, S. H. Cohen, R. A. Jansen, R. A. Windhorst, A. Meena, A. Zitrin, W. C. Keel, D. Coe, C. J. Conselice, J. C. J. D'Silva, S. P. Driver, B. Frye, N. A. Grogin, A. M. Koekemoer, M. A. Marshall, M. Nonino, N. Pirzkal, A. Robotham, M. J. Rutkowski, R. E. R. J. au2, S. Tompkins, C. N. A. Willmer, H. Yan, T. J. Broadhurst, C. Cheng, J. M. Diego, P. Kamieneski, and M. Yun. Hidden giants in jwst's pearls: An ultra-massive z=4.26 sub-millimeter galaxy that is invisible to hst, 2023. 2.5, 2.6

R. J. Smethurst, R. S. Beckmann, B. D. Simmons, A. Coil, J. Devriendt, Y. Dubois, I. L. Garland, C. J. Lintott, G. Martin, and S. Peirani. Evidence for non-merger co-evolution of galaxies and their supermassive black holes. *MNRAS*, 527(4):10855–10866, Feb. 2024. doi: 10.1093/mnras/stad1794. 1.3.5

L. S. Sparke and J. S. Gallagher, III. *Galaxies in the universe : an introduction*. Cambridge University Press, 2000. 1.4

E. R. Stanway and J. Eldridge. Re-evaluating old stellar populations. *Monthly Notices of the Royal Astronomical Society*, 479(1):75–93, 2018. 5.2.5

M. Stefanon, H. Yan, B. Mobasher, G. Barro, J. L. Donley, A. Fontana, S. Hemmati, A. M. Koekemoer, B. Lee, S.-K. Lee, H. Nayyeri, M. Peth, J. Pforr, M. Salvato, T. Wiklind, S. Wuyts, M. L. N. Ashby, M. Castellano, C. J. Conselice, M. C. Cooper, A. R. Cooray, T. Dolch, H. Ferguson, A. Galametz, M. Giavalisco, Y. Guo, S. P. Willner, M. E. Dickinson, S. M. Faber, G. G. Fazio, J. P. Gardner, E. Gawiser, A. Grazian, N. A. Grogin, D. Kocevski, D. C. Koo, K.-S. Lee, R. A. Lucas, E. J. McGrath, K. Nandra, J. A. Newman, and A. van der Wel. CANDELS Multi-wavelength Catalogs: Source Identification and Photometry in the CANDELS Extended Groth Strip. *ApJS*, 229(2):32, Apr. 2017. doi: 10.3847/1538-4365/aa66cb. 2.5

R. Storn and K. Price. Differential evolution – a simple and efficient heuristic for global optimization over continuous spaces. *Journal of Global Optimization*, 11, 1997. doi: 10.1023/A:1008202821328. 4.3.2

R. Storn and K. Price. Differential evolution - a simple and efficient heuristic for global optimization over continuous spaces. *Journal of Global Optimization*, 11: 341–359, 01 1997. doi: 10.1023/A:1008202821328. 3.3.3

A. Toomre. On the gravitational stability of a disk of stars. *ApJ*, 139:1217–1238, May 1964. doi: 10.1086/147861. 1.2.1

A. Toomre. Mergers and Some Consequences. In B. M. Tinsley and R. B. G. Larson, D. Campbell, editors, *Evolution of Galaxies and Stellar Populations*, page 401, Jan. 1977. 4.5.4

S. Tremaine and M. D. Weinberg. A kinematic method for measuring the pattern speed of barred galaxies. *ApJ*, 282:L5–L7, July 1984. doi: 10.1086/184292. 6.1.2

I. Trujillo, C. J. Conselice, K. Bundy, M. C. Cooper, P. Eisenhardt, and R. S. Ellis. Strong size evolution of the most massive galaxies since z $\sim$ 2. *MNRAS*, 382(1): 109–120, Nov. 2007. doi: 10.1111/j.1365-2966.2007.12388.x. 2.5

T. Tsukui, E. Wisnioski, J. Bland-Hawthorn, Y. Mai, S. Iguchi, J. Baba, and K. Freeman. Detecting a disk bending wave in a barred-spiral galaxy at redshift 4.4, 2023. 2.5, 2.6

T. Tsukui, E. Wisnioski, J. Bland-Hawthorn, Y. Mai, S. Iguchi, J. Baba, and K. Freeman. Detecting a disc bending wave in a barred-spiral galaxy at redshift 4.4. *MNRAS*, 527(3):8941–8949, Jan. 2024. doi: 10.1093/mnras/stad3588. 3.1

A. van der Wel, M. Franx, P. G. van Dokkum, R. E. Skelton, I. G. Momcheva, K. E. Whitaker, G. B. Brammer, E. F. Bell, H. W. Rix, S. Wuyts, H. C. Ferguson, B. P. Holden, G. Barro, A. M. Koekemoer, Y.-Y. Chang, E. J. McGrath, B. Häussler, A. Dekel, P. Behroozi, M. Fumagalli, J. Leja, B. F. Lundgren, M. V. Maseda, E. J. Nelson, D. A. Wake, S. G. Patel, I. Labbé, S. M. Faber, N. A. Grogin, and D. D. Kocevski. 3D-HST+CANDELS: The Evolution of the Galaxy Size-Mass Distribution since z = 3. *ApJ*, 788(1):28, June 2014. doi: 10.1088/0004-637X/788/1/28. 2.5

S. Verley, F. Combes, L. Verdes-Montenegro, G. Bergond, and S. Leon. Star formation in isolated AMIGA galaxies: dynamical influence of bars. *A&A*, 474(1): 43–53, Oct. 2007. doi: 10.1051/0004-6361:20077650. 4.4.2

M. Walmsley, M. Huertas-Company, L. Quilley, K. L. Masters, S. Kruk, K. A. Rem-melgas, J. J. Popp, E. Romelli, D. O'Ryan, H. J. Dickinson, C. J. Lintott, S. Ser-jeant, R. J. Smethurst, B. Simmons, J. S. Makechemu, I. L. Garland, H. Roberts, K. Mantha, L. F. Fortson, T. Géron, W. Keel, E. M. Baeten, C. Macmillan, J. Bovy, S. Casas, C. D. Leo, H. D. Sánchez, J. Katona, A. Kovács, N. Aghanim, B. Al-tieri, A. Amara, S. Andreon, N. Auricchio, H. Aussel, C. Baccigalupi, M. Baldi, A. Balestra, S. Bardelli, A. Basset, P. Battaglia, R. Bender, A. Biviano, A. Bonchi, E. Branchini, M. Brescia, J. Brinchmann, S. Camera, G. Cañas-Herrera, V. Capo-bianco, C. Carbone, J. Carretero, F. J. Castander, M. Castellano, G. Castignani, S. Cavuoti, K. C. Chambers, A. Cimatti, C. Colodro-Conde, G. Congedo, C. J. Conselice, L. Conversi, Y. Copin, F. Courbin, H. M. Courtois, M. Cropper, A. D. Silva, H. Degaudenzi, G. D. Lucia, A. M. D. Giorgio, C. Dolding, H. Dole, F. Du-bath, C. A. J. Duncan, X. Dupac, S. Dusini, A. Ealet, S. Escoffier, M. Fabricius, M. Farina, R. Farinelli, F. Faustini, F. Finelli, P. Fosalba, S. Fotopoulou, M. Frailis, E. Franceschi, S. Galeotta, K. George, B. Gillis, C. Giocoli, P. Gómez-Alvarez, J. Gracia-Carpio, B. R. Granett, A. Grazian, F. Grupp, S. Gwyn, S. V. H. Hau-gan, H. Hoekstra, W. Holmes, I. M. Hook, F. Hormuth, A. Hornstrup, P. Hudelot, K. Jahnke, M. Jhabvala, B. Joachimi, E. Keihänen, S. Kermiche, A. Kiessling, R. Kohley, B. Kubik, K. Kuijken, M. Kümmel, M. Kunz, H. Kurki-Suonio, O. La-hav, Q. L. Boulc'h, A. M. C. L. Brun, D. L. Mignant, P. Liebing, S. Ligori,

P. B. Lilje, V. Lindholm, I. Lloro, G. Mainetti, D. Maino, E. Maiorano, O. Mansutti, S. Marcin, O. Marggraf, M. Martinelli, N. Martinet, F. Marulli, R. Massey, S. Maurogordato, H. J. McCracken, E. Medinaceli, S. Mei, M. Melchior, Y. Mellier, M. Meneghetti, E. Merlin, G. Meylan, A. Mora, M. Moresco, L. Moscardini, R. Nakajima, C. Neissner, R. C. Nichol, S. M. Niemi, J. W. Nightingale, C. Padilla, S. Paltani, F. Pasian, K. Pedersen, W. J. Percival, V. Pettorino, S. Pires, G. Polenta, M. Poncet, L. A. Popa, L. Pozzetti, F. Raison, R. Rebolo, A. Renzi, J. Rhodes, G. Riccio, M. Roncarelli, B. Rusholme, R. Saglia, Z. Sakr, A. G. Sánchez, D. Sapone, B. Sartoris, J. A. Schewtschenko, P. Schneider, T. Schrabback, M. Scodeggio, A. Secroun, G. Seidel, M. Seiffert, S. Serrano, P. Simon, C. Sirignano, G. Sirri, L. Stanco, J. Steinwagner, P. Tallada-Crespí, D. Tavagnacco, A. N. Taylor, H. I. Teplitz, I. Tereno, N. Tessore, S. Toft, R. Toledo-Moreo, F. Torradeflot, I. Tutusaus, E. A. Valentijn, L. Valenziano, J. Valiviita, T. Vassallo, G. V. Kleijn, A. Veropalumbo, Y. Wang, J. Weller, A. Zacchei, G. Zamorani, F. M. Zerbi, I. A. Zinchenko, E. Zucca, V. Allevato, M. Ballardini, M. Bolzonella, E. Bozzo, C. Burigana, R. Cabanac, A. Cappi, D. D. Ferdinando, J. A. E. Vigo, L. Gabarra, J. Martín-Fleitas, S. Matthew, N. Mauri, R. B. Metcalf, A. Pezzotta, M. Pöntinen, C. Porciani, I. Risso, V. Scottez, M. Sereno, M. Tenti, M. Viel, M. Wiesmann, Y. Akrami, I. T. Andika, S. Anselmi, M. Archidiacono, F. Atrio-Barandela, C. Benoist, K. Benson, D. Bertacca, M. Bethermin, L. Bisigello, A. Blanchard, L. Blot, H. Böhringer, M. L. Brown, S. Bruton, F. Buitrago, A. Calabro, B. C. Quevedo, F. Caro, C. S. Carvalho, T. Castro, F. Cogato, A. R. Cooray, O. Cucciati, S. Davini, F. D. Paolis, G. Desprez, A. Díaz-Sánchez, J. J. Diaz, S. D. Domizio, J. M. Diego, P. A. Duc, A. Enia, Y. Fang, A. G. Ferrari, A. Finoguenov, A. Fontana, A. Franco, K. Ganga, J. García-Bellido, T. Gasparetto, V. Gautard, E. Gaztanaga, F. Giacomini, G. Gozaliasl, M. Guidi, C. M. Gutierrez, A. Hall, W. G. Hartley, S. Hemmati, C. Hernández-Monteagudo, H. Hildebrandt, J. Hjorth, J. J. E. Kajava, Y. Kang, V. Kansal, D. Karagiannis, K. Kiiveri, C. C. Kirkpatrick, J. L. Graet, L. Legrand, M. Lembo, F. Lepori, G. Leroy, G. F. Lesci, J. Lesgourgues, L. Leuzzi, T. I. Liaudat, A. Loureiro, J. Macias-Perez, G. Maggio, M. Magliocchetti, F. Mannucci, R. Maoli, C. J. A. P. Martins, L. Maurin, M. Miluzio, P. Monaco, C. Moretti, G. Morgante, C. Murray, S. Nadathur, K. Naidoo, A. Navarro-Alsina, S. Nesseris, F. Passalacqua, K. Paterson, L. Patrizii, A. Pisani, D. Potter, S. Quai, M. Radovich, P. F. Rocci, G. Rodighiero, S. Sacquegna, M. Sahlén, D. B. Sanders, E. Sarpa, C. Scarlata, J. Schaye, A. Schneider, M. Schultheis, D. Sciotti, E. Sellentin, F. Shankar, L. C. Smith, K. Tanidis, G. Testera, R. Teyssier, S. Tosi, A. Troja, M. Tucci, C. Valieri, A. Venhola, D. Vergani, G. Verza, P. Vielzeuf, N. A. Walton, E. Soubrie, and D. Scott. Euclid quick data release (q1): First visual morphology catalogue, 2025. URL `https://arxiv.org/abs/2503.15310`. 3.4

Y. Wang, E. Athanassoula, P. Patsis, and S. Mao. Periodic orbits of multiplicity higher than one in an N-body barred galaxy potential. *A&A*, 668:A55, Dec. 2022. doi: 10.1051/0004-6361/202243699. 1.2.2

C. Wegg and O. Gerhard. Mapping the three-dimensional density of the Galactic bulge with VVV red clump stars. *MNRAS*, 435(3):1874–1887, Nov. 2013. doi: 10.1093/mnras/stt1376. 1.3.3

C. Wegg, O. Gerhard, and M. Portail. The structure of the Milky Way's bar outside the bulge. *MNRAS*, 450(4):4050–4069, July 2015. doi: 10.1093/mnras/stv745. 1.2.4

A. Whitney, C. J. Conselice, R. Bhatawdekar, and K. Duncan. Unbiased Differential Size Evolution and the Inside-out Growth of Galaxies in the Deep CANDELS GOODS Fields at $1 \leq z \leq 7$. *ApJ*, 887(2):113, Dec. 2019. doi: 10.3847/1538-4357/ab53d4. 2.5

H. Wozniak, D. Friedli, L. Martinet, P. Martin, and P. Bratschi. Disc galaxies with multiple triaxial structures. I. BVRI and Hα surface photometry. *A&AS*, 111:115, May 1995. 1.2.3

S. M. Wylie, J. P. Clarke, and O. E. Gerhard. The Milky Way's middle-aged inner ring. *A&A*, 659:A80, Mar. 2022. doi: 10.1051/0004-6361/202142343. 3.11, 3.6.2

W.-B. G. Zee, S. Paudel, J.-S. Moon, and S.-J. Yoon. Unraveling Joint Evolution of Bars, Star Formation, and Active Galactic Nuclei of Disk Galaxies. *ApJ*, 949 (2):91, June 2023. doi: 10.3847/1538-4357/acc79a. 6.1.4

Y. F. Zhou, Z. Li, and H. Li. N-body Simulations of Galaxy Bars Generated by Satellite Collisions: Effects of the Impact Geometry. *ApJ*, 988(2):205, Aug. 2025. doi: 10.3847/1538-4357/aded87. 1.2.1